BIBLIOGRAPHIC INFORMATION

PB95-174025

Report Nos: CU/SR-94/6

Title: Performance of Masonry-Infilled R/C Frames under In-Plane Lateral Loads.

Date: Oct 94

Authors: A. B. Mehrabi, P. B. Shing, M. P. Schuller, and J. L. Noland.

Performing Organization: Colorado Univ. at Boulder. Dept. of Civil, Environmental, and Architectural Engineering.**Atkinson-Noland and Associates, Inc., Boulder, CO.

Sponsoring Organization: *National Science Foundation, Arlington, VA.

Contract Nos: NSF-MSM-8914008, NSF-MSM-9011065

Type of Report and Period Covered: Structural engineering and structural mechanics research series.

NTIS Field/Group Codes: 89D (Structural Analyses), 89G (Construction Materials, Components, & Equipment), 50C (Construction Equipment, Materials, & Supplies)

Price: PC A12/MF A03

Availability: Available from the National Technical Information Service, Springfield, VA. 22161

Number of Pages: 259p

Keywords: *Masonry, *Concrete structures, *Reinforced concrete, *Frames, *Wall loading, *Dynamic response, *Earthquake engineering, Cyclic loads, Finite element method, Cracks, Prototypes, Algorithms, Cracking(Fracturing), Structural failure, Structural analysis, Structural components, Displacement, Failure modes, Shear stresses, Stress strain relations, Strain gages, Earthquake damage, *Lateral loads, *Infilled panels.

Abstract: A comprehensive study has been conducted to evaluate the safety of existing masonry infilled reinforced concrete structures under earthquake loadings. Fourteen 1/2-scale frame specimens were tested to evaluate the influence of the relative strength and stiffness of an infill with respect to those of the bounding frame, the lateral load history, the panel aspect ratio, the magnitude and distribution of vertical loads, and the adjacent infilled bays on the performance of these structures. The experimental results show that the addition of infill panels results in a major improvement in the strength and energy-dissipation capability of these frames. The test results have been extrapolated to obtain the dynamic properties of the prototype structure and, thereby, to study its performance under seismic loadings. The results have demonstrated a remarkable improvement of structural performance due to the infill.

STRUCTURAL ENGINEERING AND STRUCTURAL MECHANICS
RESEARCH SERIES

REPORT CU/SR-94/6

PERFORMANCE OF MASONRY-INFILLED R/C FRAMES UNDER IN-PLANE LATERAL LOADS

by

Armin B. Mehrabi

P. Benson Shing

University of Colorado

Michael P. Schuller

James L. Noland

Atkinson-Noland & Associates, Inc.

Sponsor:

National Science Foundation

October 1994

DEPARTMENT OF CIVIL, ENVIRONMENTAL,
& ARCHITECTURAL ENGINEERING
UNIVERSITY OF COLORADO AT BOULDER

PERFORMANCE OF MASONRY-INFILLED R/C FRAMES UNDER IN-PLANE LATERAL LOADS

by

Armin B. Mehrabi

P. Benson Shing

University of Colorado

Michael P. Schuller

James L. Noland

Atkinson-Noland & Associates, Inc.

Sponsor:

National Science Foundation

Department of Civil, Environmental,

& Architectural Engineering

University of Colorado

Boulder, CO 80309-0428

Research Series No. CU/SR-94/6

October 1994

ABSTRACT

A comprehensive study has been conducted to evaluate the safety of existing masonry infilled R/C structures under earthquake loadings. Fourteen 1/2-scale frame specimens were tested to evaluate the influence of the relative strength and stiffness of an infill with respect to those of the bounding frame, the lateral load history, the panel aspect ratio, the magnitude and distribution of vertical loads, and the adjacent infilled bays on the performance of these structures. The experimental results show that the addition of infill panels results in a major improvement in the strength and energy-dissipation capability of these frames. The test results have been extrapolated to obtain the dynamic properties of the prototype structure and, thereby, to study its performance under seismic loadings. The results have demonstrated a remarkable improvement of structural performance due to the infill. Furthermore, simple analytical methods have been developed in this study to predict the lateral strength and stiffness of infilled frames. The predictive value of these methods has been validated by the experimental results. Finite element analyses have been conducted on the frame specimens. To this end, two interface models have been developed in this study. One simulates the behavior of the interface between the frame and masonry infill and that of the mortar joints, and the other is to model the bond-slip behavior of reinforcing bars in concrete. The resulting finite element models are able to capture both the failure mechanisms and lateral strengths of the infilled frame specimens.

ACKNOWLEDGMENTS

The financial support for this study was provided by the National Science Foundation under Grant Nos. MSM-8914008 and MSM-9011065. However, opinions expressed in this report are those of the writers and do not necessarily represent those of the sponsor.

The dedicated involvement of undergraduate assistants, Rebecca Matkins, Daniel Ott, Matthew Schmidt, William Lips, Jon Gray, Mark Jurgemeyer, and Dean Frank in the experimental work is gratefully acknowledged.

TABLE OF CONTENTS

LIST OF FIGURES

FIGURE

LIST OF TABLES

CHAPTER 1

INTRODUCTION

1.1 Statement of Problems and Objectives

Masonry infill panels can be frequently found as interior and exterior partitions in R/C structures. Since they are normally treated as architectural elements, their presence is often ignored by engineers. However, even though they are considered non-structural, they may interact with the bounding frames when the structure is subjected to strong lateral loads induced by earthquake ground motions. Such interaction may or may not be beneficial to the performance of a structure, and has been a subject of many debates. In some countries, masonry infill has been used as a means to strengthen existing moment-resisting frames, and there is evidence that they improved the performance of structures in past earthquakes (Rosenblueth et al. 1986; Amrhein et al. 1985). On the other hand, infill walls have been related to catastrophic failures (Glogau 1974; Uzsoy et al. 1972), such as the development of soft stories and the brittle shear failure of columns induced by the short-column effect. As many reinforced concrete structures located in seismically active areas have masonry infills, their safety has become a major concern among engineers, and there are no code provisions or rational guidelines available for the design and safety assessment of such structures. Even though a number of studies (e.g., Fiorato and Sozen 1970; Brokken and Bertero 1981; Klinger and Bertero 1976; Mander et al. 1993; Angel et al. 1994) have been conducted on

infilled frames, experimental data which can be used to assess the performance of such structures are still very limited. Furthermore, many of the early tests were conducted on small-scale structures.

To assess the lateral strength and stiffness of infilled frames, several analytical models have been proposed (Stafford Smith 1966; Fiorato et al. 1970; Liauw and Kwan 1985). However, none of these models is capable of capturing all the major failure mechanisms. The finite element method has been used by several investigators (Dhanasekar and Page 1986; Liauw and Lo 1988; Schmidt 1989) to analyze the behavior of infilled frames. In all these analyses, relatively simple models have been used for the frames and infill panels. Except for Schmidt's work, most of the studies have been devoted to steel frames with masonry infill. Work on the analysis of R/C infilled frames has been very limited.

To further our understanding of the behavior of R/C infilled frames, a comprehensive experimental and analytical study has been conducted. The study focuses on the performance and safety of existing masonry-infilled R/C constructions in the United States. It includes the identification of critical design parameters, experimental investigation with 1/2-scale models, seismic analysis of a prototype structure, development of analytical methods, development and calibration of finite element models, and validation of these models with experimental results.

1.2 Organization of the Report

Chapter 2 presents a literature review of experimental and analytical research conducted on infilled frames. A number of possible failure mechanisms and the governing parameters are identified.

Chapter 3 summarizes the experimental program and observations. Tests were conducted on fourteen 1/2-scale masonry-infilled R/C frame specimens to investigate the influence of the relative strength and stiffness of the infill with respect to those of the frame, the lateral load history, the vertical load level and distribution, the panel aspect ratio, and the adjacent infilled bays on the behavior of these structures.

Chapter 4 studies the seismic performance of a prototype structure. Test results of single-story, single-bay specimens have been extrapolated to deduce the load resistance properties of the corresponding prototype frames. The frames have been analyzed under short- and long-duration pulses as well as earthquake ground motions.

Chapter 5 reviews some of the existing simple analytical methods developed for infilled frames. A new method has been developed in this study for predicting the lateral strength of infilled frames. It accounts for the diagonal/sliding shear failure of the infill and the shear failure of the columns. The applicability of this method has been examined by comparing the analytical results with those of the experiments. The applicability of existing methods for assessing the lateral stiffness of masonry-infilled R/C frames has also been evaluated.

In Chapter 6, the finite element models which have been developed in this study to model the bond-slip behavior between the reinforcing steel and concrete and the behavior of cementitious interfaces are presented. The models have been implemented in a finite element program and analyses have been conducted on some of the infilled frame specimens that were tested.

Chapter 7 summarizes the results of the experimental, analytical, and

numerical investigations. The important conclusions and the needs in future studies are also identified.

CHAPTER 2

LITERATURE REVIEW

2.1 Experimental Research

Experimental investigations of the behavior of infilled frames have been carried out by a number of researchers. Some of these studies are highlighted here. Stafford Smith (1963,1966) has subjected 6-in.-by-6-in. steel frames infilled with mortar to diagonal compression and racking forces, and has found that increasing the stiffness of the bounding frames with respect to that of the infill can significantly increase the strength of infilled frames. Based on the results of these tests, he has proposed an equivalent diagonal strut model for evaluating the strength and stiffness of infilled frames. In a study conducted by Fiorato et. al (1970), 1/8-scale non-ductile reinforced concrete frames infilled with brick masonry have been subjected to monotonic as well as cyclic lateral loads. They have observed that the horizontal sliding failure of masonry infill introduces a short-column effect, with plastic hinges and sometimes brittle shear failure developed at the mid-height of the columns. They have concluded that masonry infill can increase the strength but reduce the ductility of concrete frames. Liauw and Kwan (1983, 1985), based on the tests of small steel frames infilled with relatively stiff concrete panels, have identified failure mechanisms characterized by the formation of plastic hinges in the columns and beams, which are accompanied by the crushing of the infill at compression corners. Schmidt (1989) has tested reinforced concrete frames

with brick infills that had relatively weak mortar joints. In these tests, the increase of the lateral strength due to infill is not very significant. His test specimens exhibited a large amount of slip along the mortar joints that was followed by the formation of plastic hinges at the top and bottom sections of the columns. The failure mechanisms of infilled frames observed from prior experimental studies can be classified into five major types, as shown in Fig. 2.1, depending on the relative strength and stiffness of the bounding frame with respect to those of the infill, the geometric configuration of the frame, as well as the loading condition. Frames dominated by mechanisms B and C identified in the figure tend to exhibit a brittle behavior. However, the load and design conditions that lead to these mechanisms remain to be studied.

Klingner and Bertero (1976), and Brokken and Bertero (1981) have tested 1/3-scale, three-story-high, reinforced concrete frames infilled with fully grouted hollow concrete masonry under monotonic and cyclic lateral loadings. The infill panels were reinforced with standard deformed bars in both vertical and horizontal directions, and the shear strength of the concrete columns was enhanced with additional shear steel that was beyond the minimum requirements of the ACI code. They have concluded from these studies that infill panels can be effectively used to enhance the seismic performance of reinforced concrete frames in terms of strength and ductility. They have shown that the lateral stiffness and strength deteriorate with cyclic load reversals, the degree of which depends on the panel reinforcement and interface condition. The peak strength under cyclic loading is, in general, somewhat smaller than that obtained under monotonic loading, but it is always higher than that of a bare frame. Hobbs and Samai (1985) have investigated the effect of the stiffness

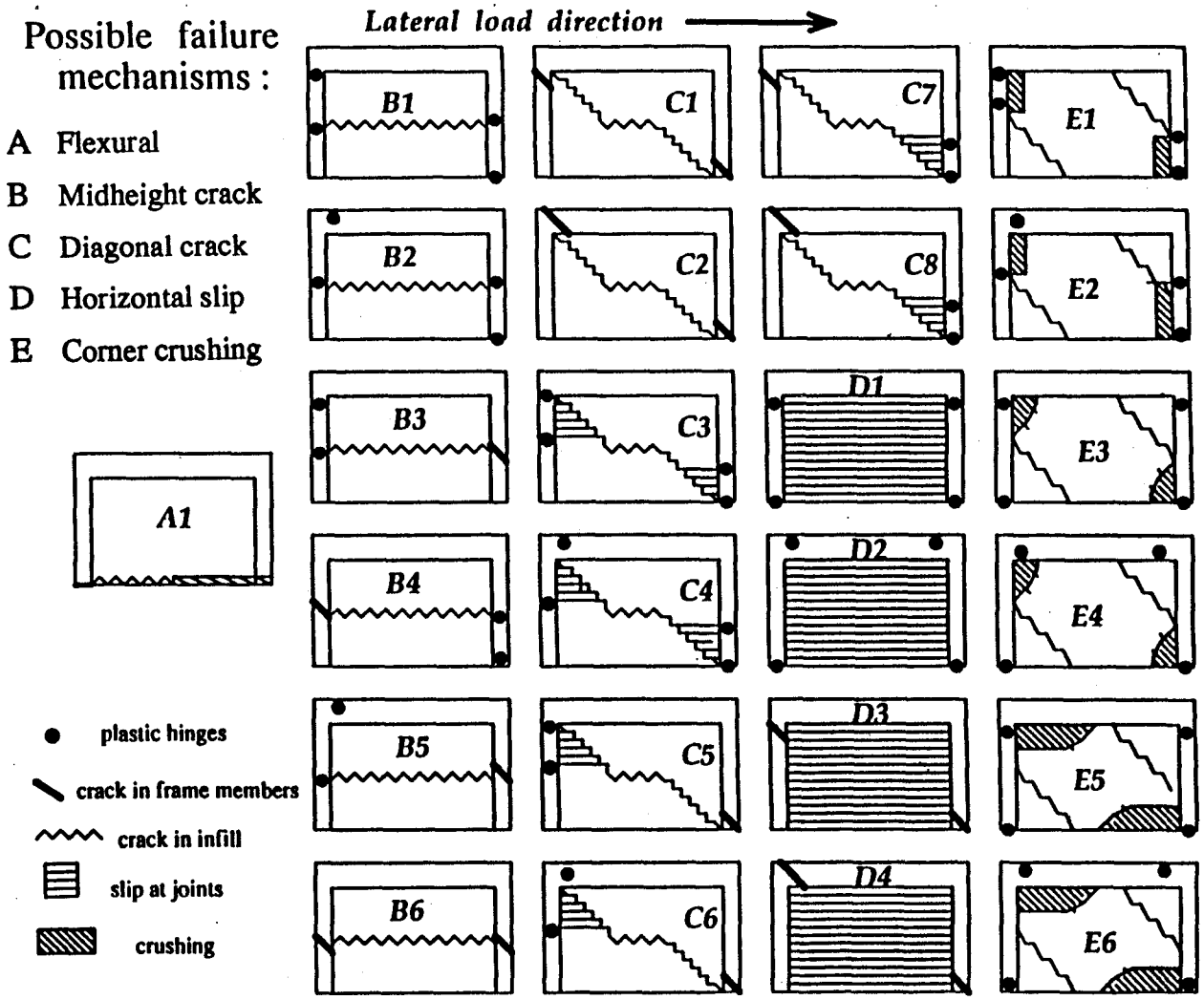

Figure 2.1. Failure Mechanisms of Infilled Frames.

of an infill wall with respect to that of the frame on structural performance, and have concluded that a weak infill give a smooth behavior close to an ideal elastic-perfectly plastic response, whereas a moderately strong or strong infill leads to a more brittle behavior due to the development of shear failure in frame members. Kahn and Hanson (1979) have reached the same conclusion in their tests of R/C frames with reinforced concrete panels as infills. They have found that separating the infill from the bounding columns and enchancing the shear transfer between the beam and the infill can prevent the brittle shear failure of the columns and, therefore, significantly enhance the ductility of a structure. They have found that the failure of an infill panel transfers a big shear force to the columns, whose failure in shear will result in a fast degradation of the lateral load resistance of the system. The shear failure of the columns could be prevented if the columns were confined with adequate shear reinforcement.

Fiorato et. al (1970) have observed that the presence of vertical loads increases the strength and stiffness due to the stiffening and strengthening of the columns as well as to the increase of the shear capacity of the infill. Their test results show that the presence of an opening reduces the strength and stiffness of a structure. However, this reduction is not proportional to the reduction of the area of the wall due to the openings. Liauw and Lo (1988), in their tests of small (11.8-in.-tall) steel frames with microconcrete infills, have noticed that the strength of a two-bay infilled frame is only about 1.5 times of that of a single-bay infilled frame, which shows that the strength of adjacent infilled bays in a multi-bay frame is not additive. Zarnic and Tomazevic (1990) have found that introducing horizontal steel into a masonry infill has a little influence on the performance of R/C frames, except for cases

where there are openings in the infill. For the latter cases, the horizontal steel improves the ductility of infilled frames. They have examined the applicability of different repair and strengthening methods and have concluded that infilled frames damaged by earthquakes can be efficiently repaired and strengthened.

McDowel et al. (1956), Lefter and Colville (1974), Angel et al. (1994), and Seah (1988) have investigated the out-of-plane resistance of infills. They have noticed that the arching action has a beneficial influence on the out-of-plane resistance. In these studies, some analytical methods have also been proposed to determine the maximum out-of-plane pressure that a masonry infill can resist.

In spite of the aforementioned studies, quantity information on the safety and performance of masonry-infilled R/C structures that are representative of the current construction in the U.S. is still lacking. In particular, the effects of the relative strength and stiffness of an infill with respect to those of the columns, the lateral load history, the panel aspect ratio, the vertical load and its distribution, and the adjacent infilled bays on the performance of these structures are not well understood.

2.2 Analytical Models

Fiorato et. al (1970) have used an equivalent beam model to estimate the precracked stiffness and cracking strength of an infilled frame, and have proposed a knee-braced frame model to simulate the short-column effect observed in their experiments. Polyakov (1960) has proposed a diagonal strut model, in which the infill panel is substituted by an equivalent diagonal strut. Analytical techniques have been developed by Holmes (1961), Stafford Smith (1963,1967), and Mainstone and Weeks (1970) to estimate the effective width

of a diagonal strut. Schmidt (1989) has used an additional strut to induce column failure. To find the collapse loads of infilled frames, Wood (1978) has used the plastic analysis method. Liauw and Kwan (1985) have proposed a unified plastic analysis method to define the maximum lateral resistances and failure mechanisms of infilled frames. In this method, they have identified four types of failure mechanisms, which involve plastic hinges in frame members and the crushing of infill at loaded corners.

To develop a general model for the failure analysis of infilled frames, the finite element method has been used by Dhanasekar and Page (1986) and Liauw and Lo (1988). In their analyses, linear and nonlinear beam elements have been used to model the behavior of steel frames, and simple interface elements have been developed to model the interaction between the infill and the frame. Dhanasekar and Page have used a nonlinear orthotropic model to simulate the behavior of brick panels, while Liauw and Lo have used a simple smeared crack model to simulate the behavior of microconcrete infills. Schmidt (1989) has used smeared crack elements for both reinforced concrete frames and brick infills. In all these analyses, infill panels have been modeled as homogeneous materials, and the effects of mortar joints have been smeared out. The performance of these models has been validated with limited test results.

CHAPTER 3

EXPERIMENTAL STUDY

3.1 Introduction

The performance of infilled frames under lateral loadings has been experimentally investigated by a number of researchers. Stafford Smith (1966), and Liauw and Kwan (1985) have studied the behavior of steel frames with mortar infills. Dawe et al. (1992) and Mander et al. (1993) have studied the behavior of masonry-infilled steel frames. The behavior of masonry-infilled R/C frames under in-plane loads has been examined by Fiorato et al. (1970), Klinger and Bertero (1976), Brokken and Bertero (1981), Schmidt (1989), Hobbs and Samai (1985), Zarnic and Tomazevic (1990), and others. Angel et al. (1994) have conducted an extensive study on the out-of-plane resistance of masonry infill. Based on results of prior studies, one can classify the failure mechanisms of infilled frames into five major types, as illustrated in Fig. 2.1. It has been shown that the failure mechanisms are very much determined by the relative strength and stiffness of the infill with respect to those of the bounding frame, as well as the loading condition. However, in spite of these studies, information on the safety and performance of existing infilled structures in the U.S. is still very limited. This is partly due to the complexity of the problem, which involves a large number of design parameters and complicated frame-panel interaction mechanisms. Furthermore, many of the infilled specimens used in prior studies did not reflect the current construction practice in the U.S.

3.2 Experimental Program

The objective of the experimental program reported here is two-fold. First, it is intended as a parametric study for evaluating the performance of masonry-infilled R/C frames that are representative of current construction practice. Secondly, it is intended to provide a data base for the validation of the finite element models which have been developed in this project for predictive analysis as well as simple analytical models. To this end, extensive material tests were conducted on individual components and subassemblies, in conjunction with the frame specimens, for the calibration of these models.

3.2.1 Prototype Structure and Test Specimens. A six-story, three-bay, reinforced concrete moment-resisting frame, which is shown in Fig. 3.1, has been selected as a prototype structure. It represents an interior frame of a typical office building. The height/length ratio for each bay is 1/1.5. The design loads comply with the specifications of the Uniform Building Code (UBC) (1991). The service live load was taken to be 50 psf, and the dead load was estimated to be 130 psf. For the purpose of parametric study, two types of frames were designed with respect to lateral loadings. One is a "weak" frame, which was designed for a lateral wind pressure of 26 psf, corresponding to a basic wind speed of 100 mph. The other is a "strong" frame, which was designed for a set of equivalent static forces stipulated for Seismic Zone 4 in the UBC. The former represents some existing R/C frames which do not meet the current seismic resistance standards. The frames were designed to satisfy the provisions of ACI 318-89 (1989). In either case, the load resistance contributed by infill panels was ignored, as in standard design practice.

The single-bay test specimens, Specimens 1 through 12, were chosen

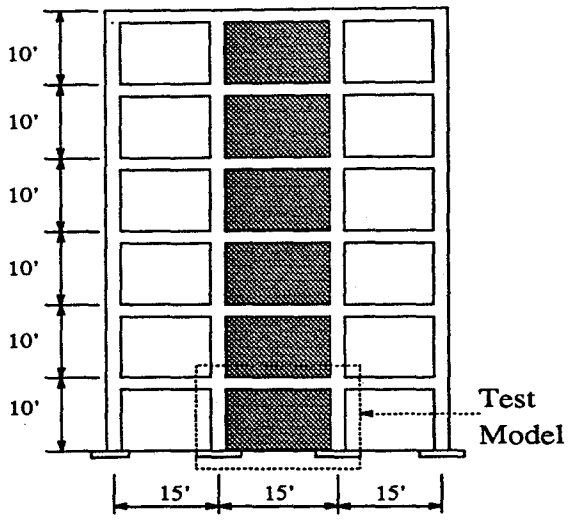

Figure 3.1. Prototype Frame.

to be 1/2-scale models representing the interior bay at the bottom story of the prototype frame. The design of the weak frame is shown in Figs. 3.2 and 3.3, which had weak columns and a strong beam, comparatively. As shown in Figs. 3.4 and 3.5, in the strong frame, the columns were heavier and had closer ties near the ends, and yielding was expected to initiate in the beam. The design of the beam in the strong frame is identical to that in the weak frame, except that the former had more shear reinforcement in the critical regions. Each beam-to-column joint in the strong frame had four horizontal stirrups to prohibit brittle shear failure, in accordance with the seismic provisions of ACI 318-89 (1989). While the strong frame had a height/length (h/l) ratio of about 1/1.5, two h/l ratios were considered for the weak frame. They are approximately 1/1.5 and 1/2. The design details of a weak frame with the lower h/l ratio is shown in Figs. 3.6 and 3.7. The two-bay specimens, Specimens 13 and 14, were intended to study the influence of adjacent infilled bays. As shown in Fig. 3.8, the aspect ratio for each panel of these specimens was 1/1.5 and the frames

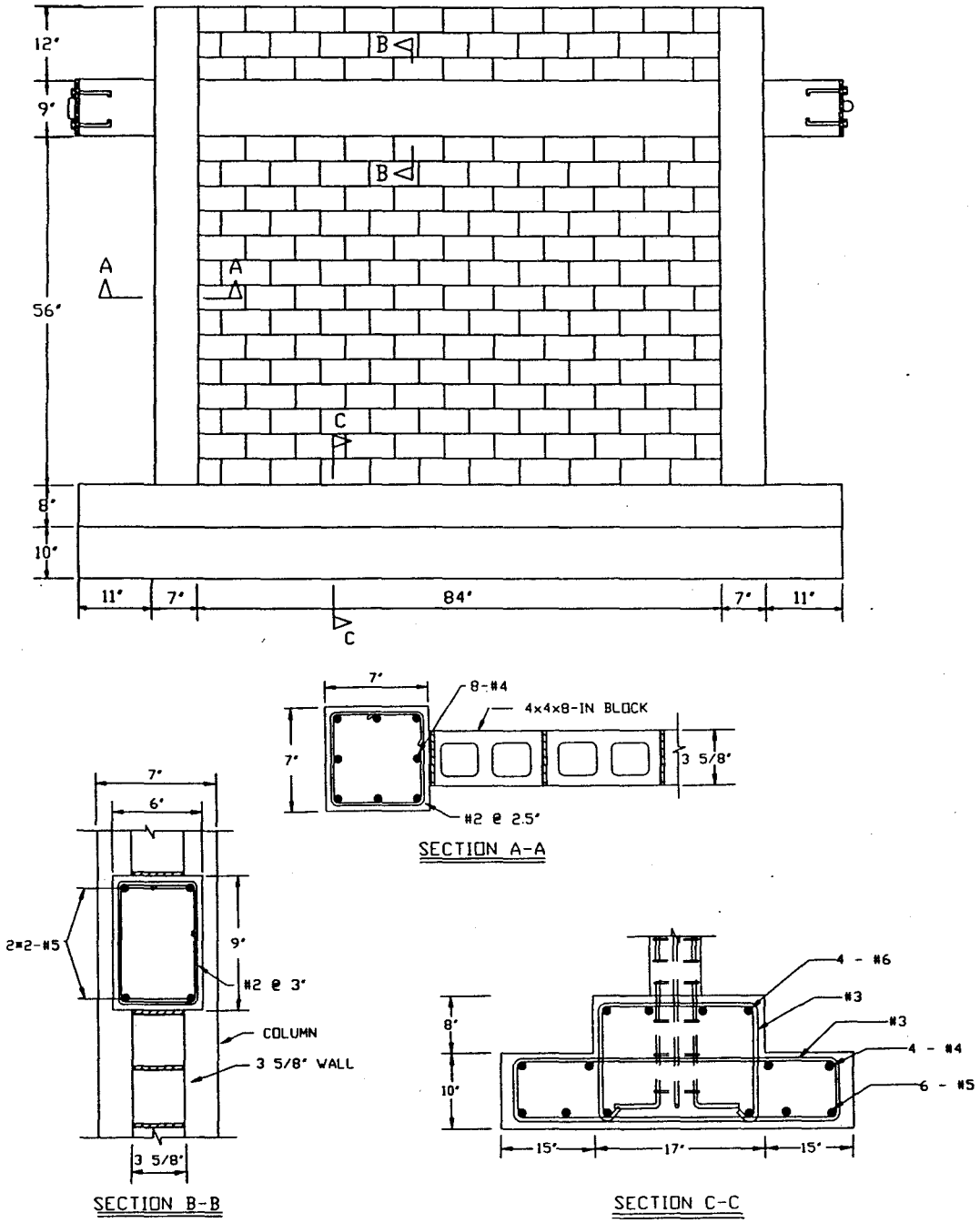

Figure 3.2. Design Details of Weak Frame with Panel Aspect Ratio of 0.67.

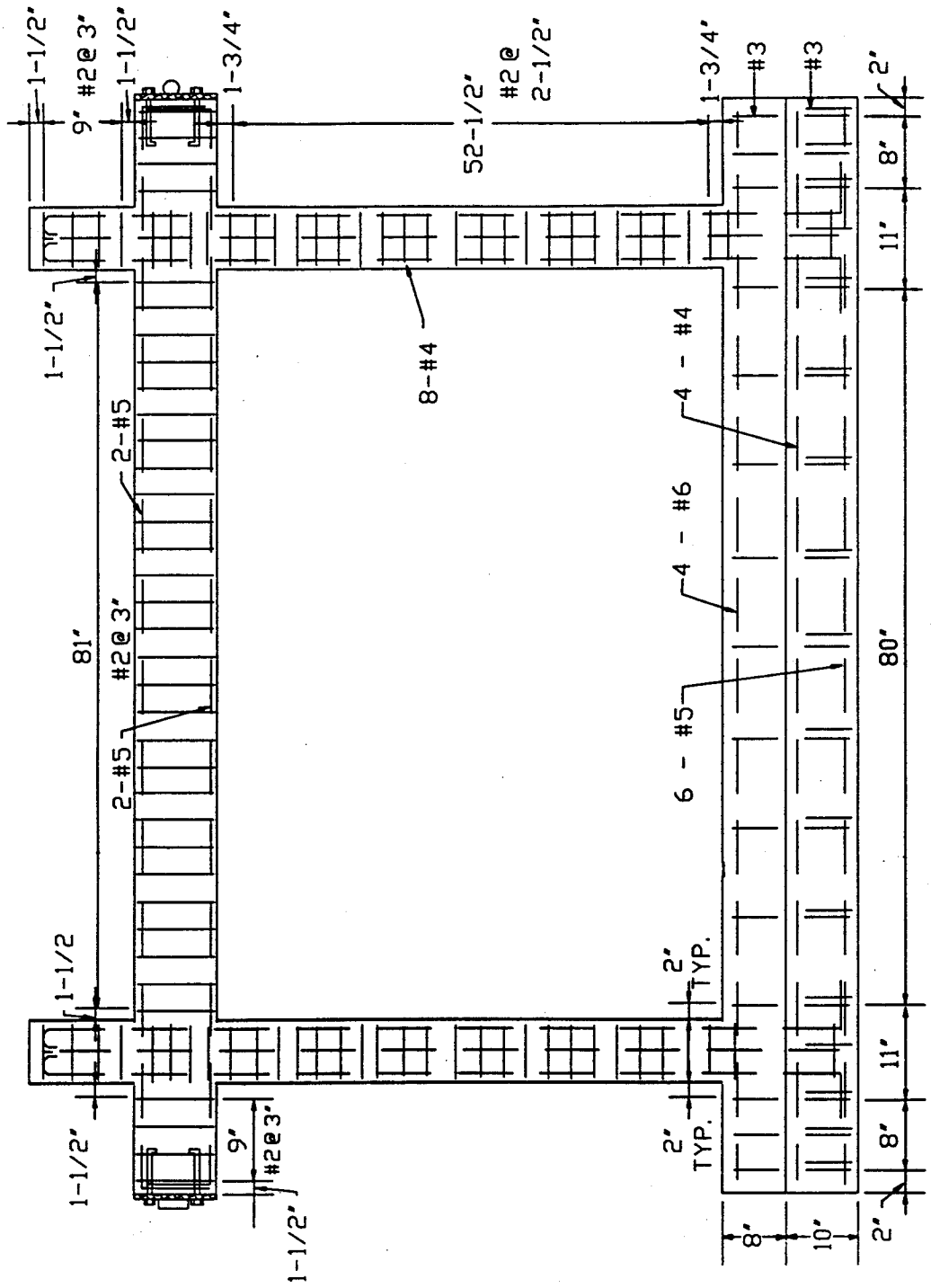

Figure 3.3. Reinforcement of Weak Frame with Panel Aspect Ratio of 0.67.

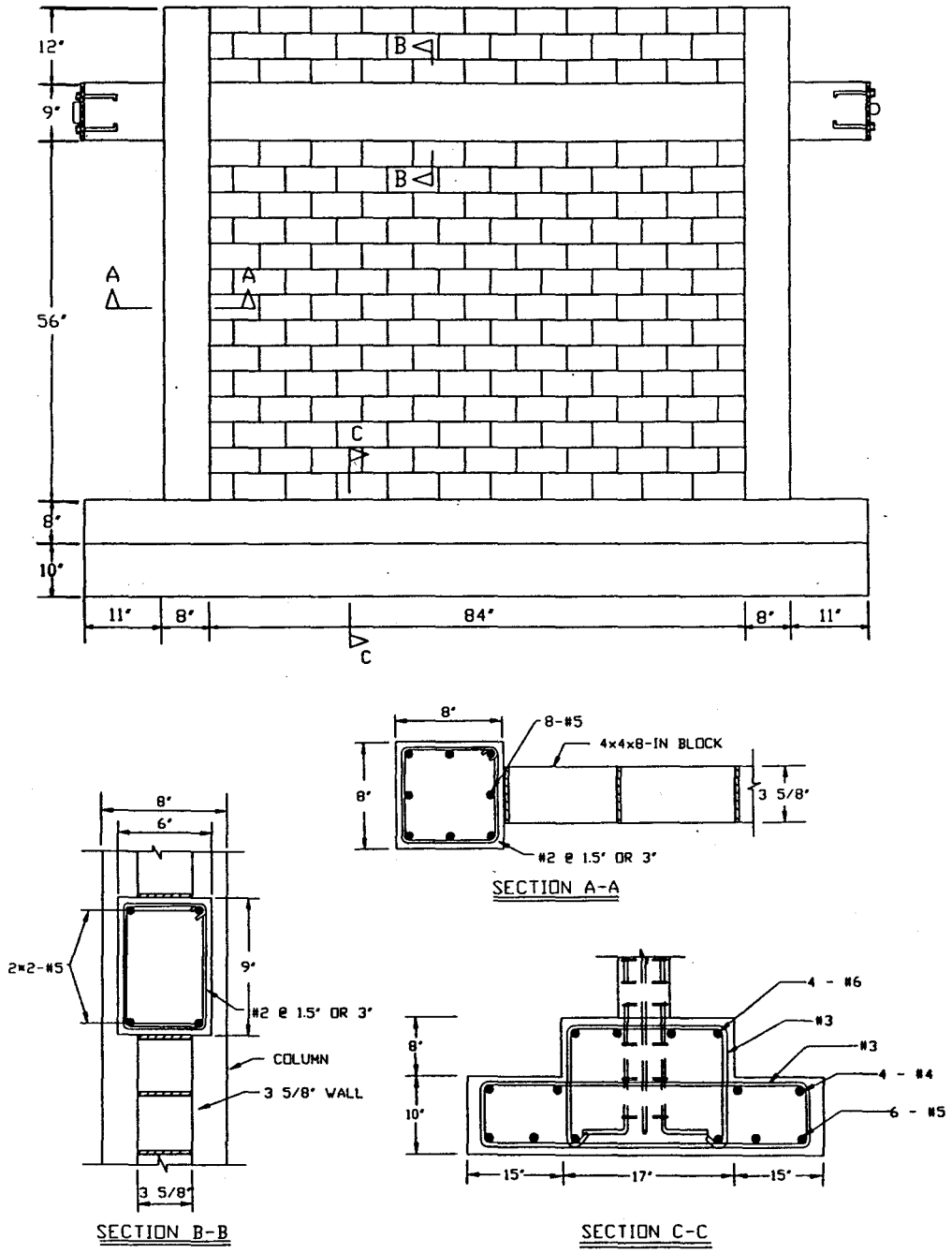

Figure 3.4. Design Details of Strong Frame with Panel Aspect Ratio of 0.67.

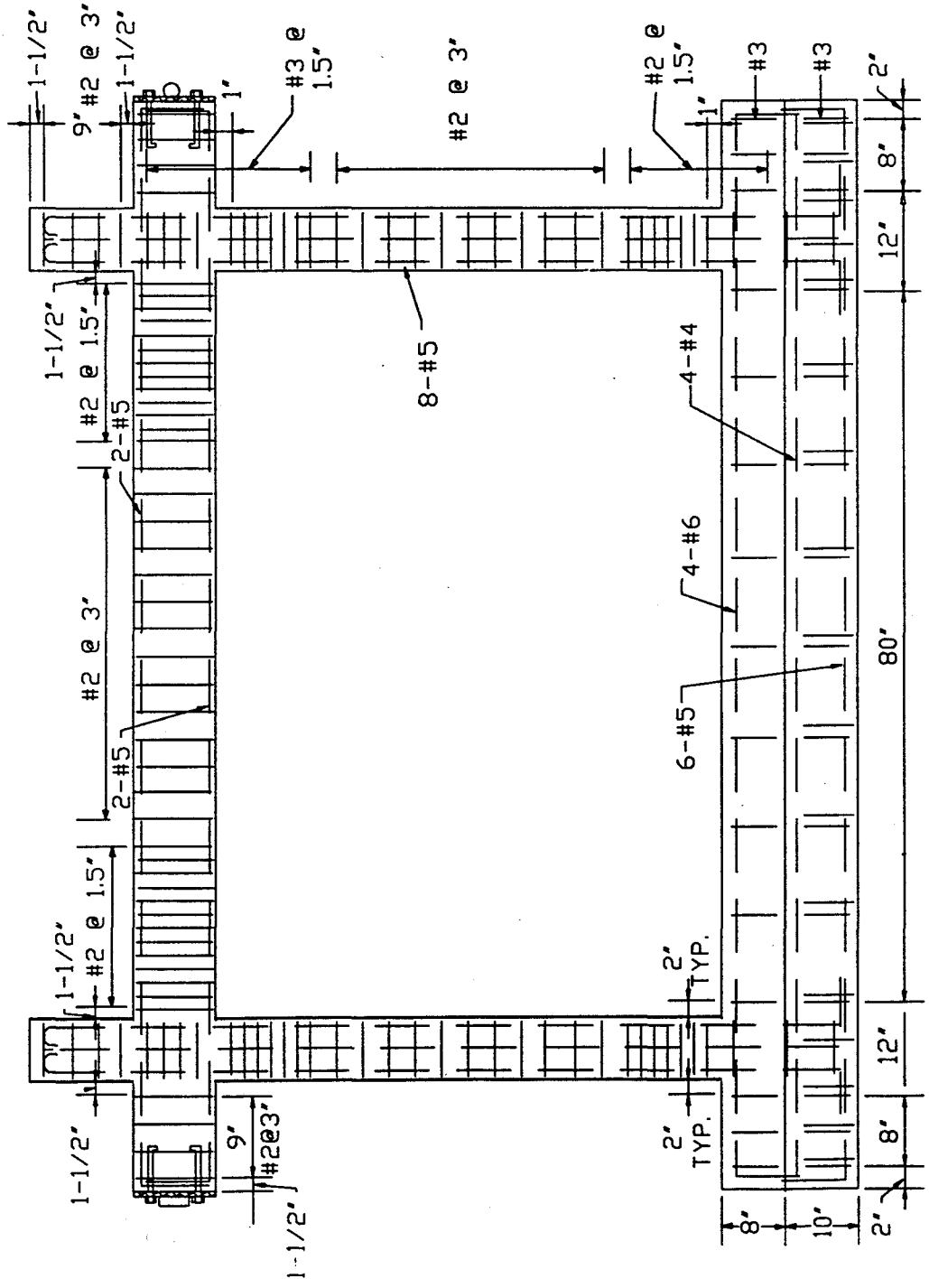

Figure 3.5. Reinforcement of Strong Frame with Panel Aspect Ratio of 0.67.

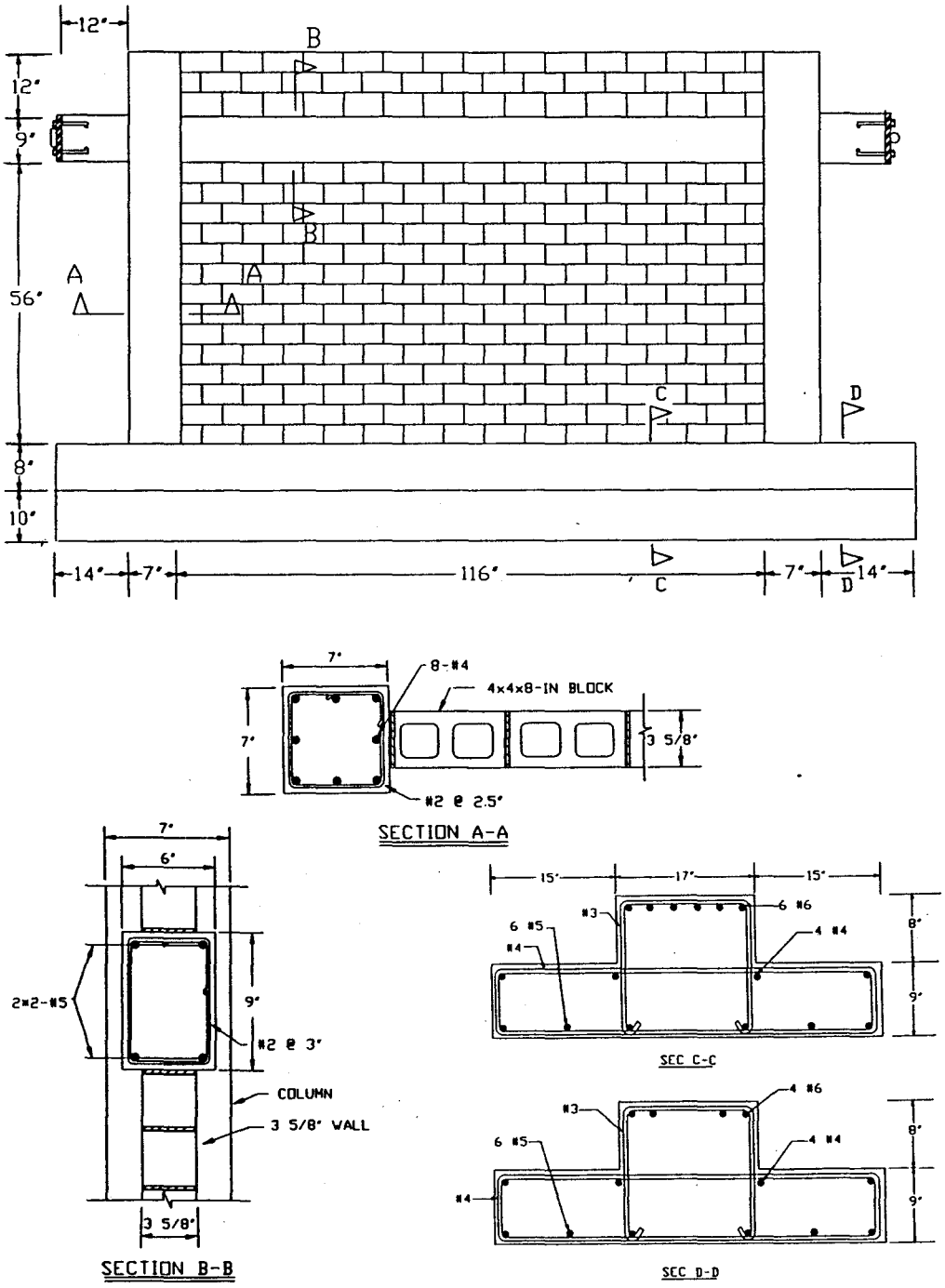

Figure 3.6. Design Details of Weak Frame with Panel Aspect Ratio of 0.48.

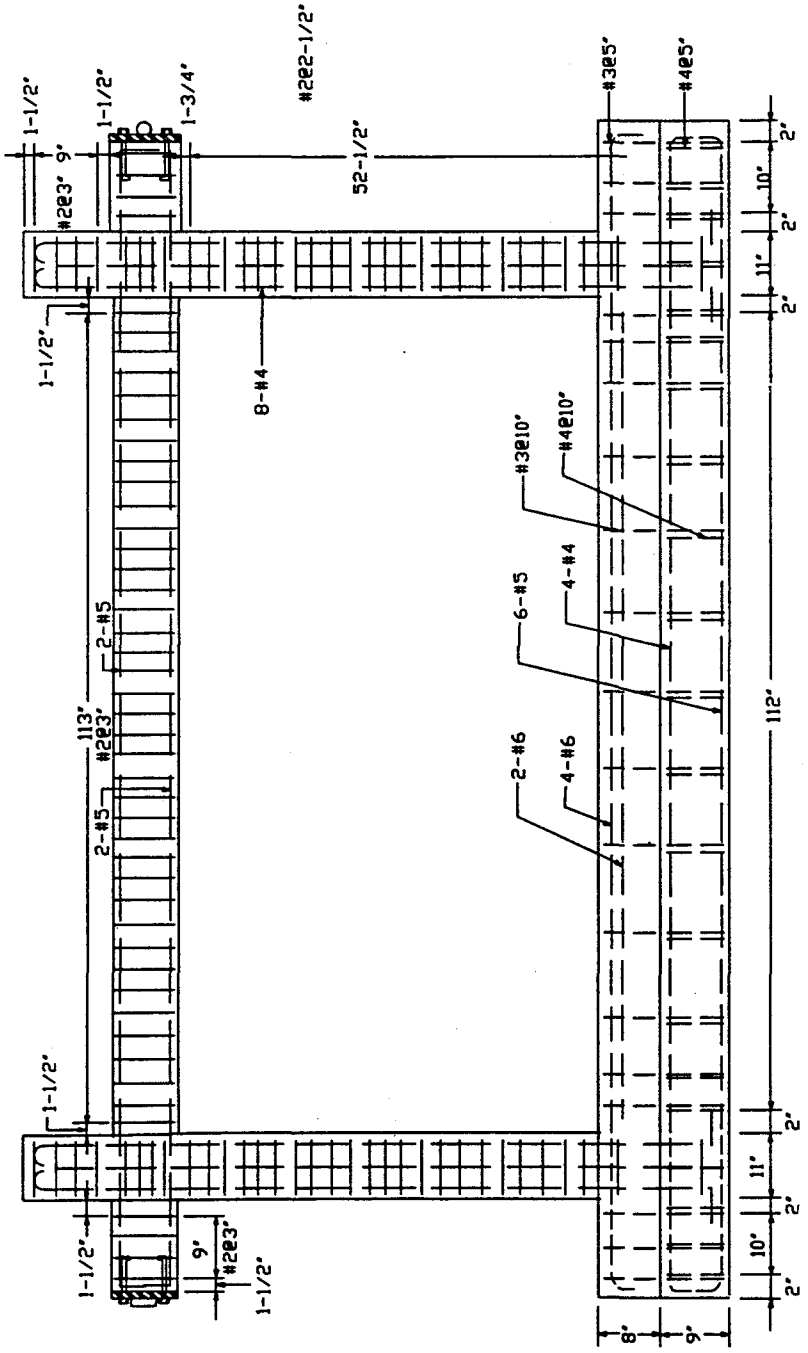

Figure 3.7. Reinforcement of Weak Frame with Panel Aspect Ratio of 0.48.

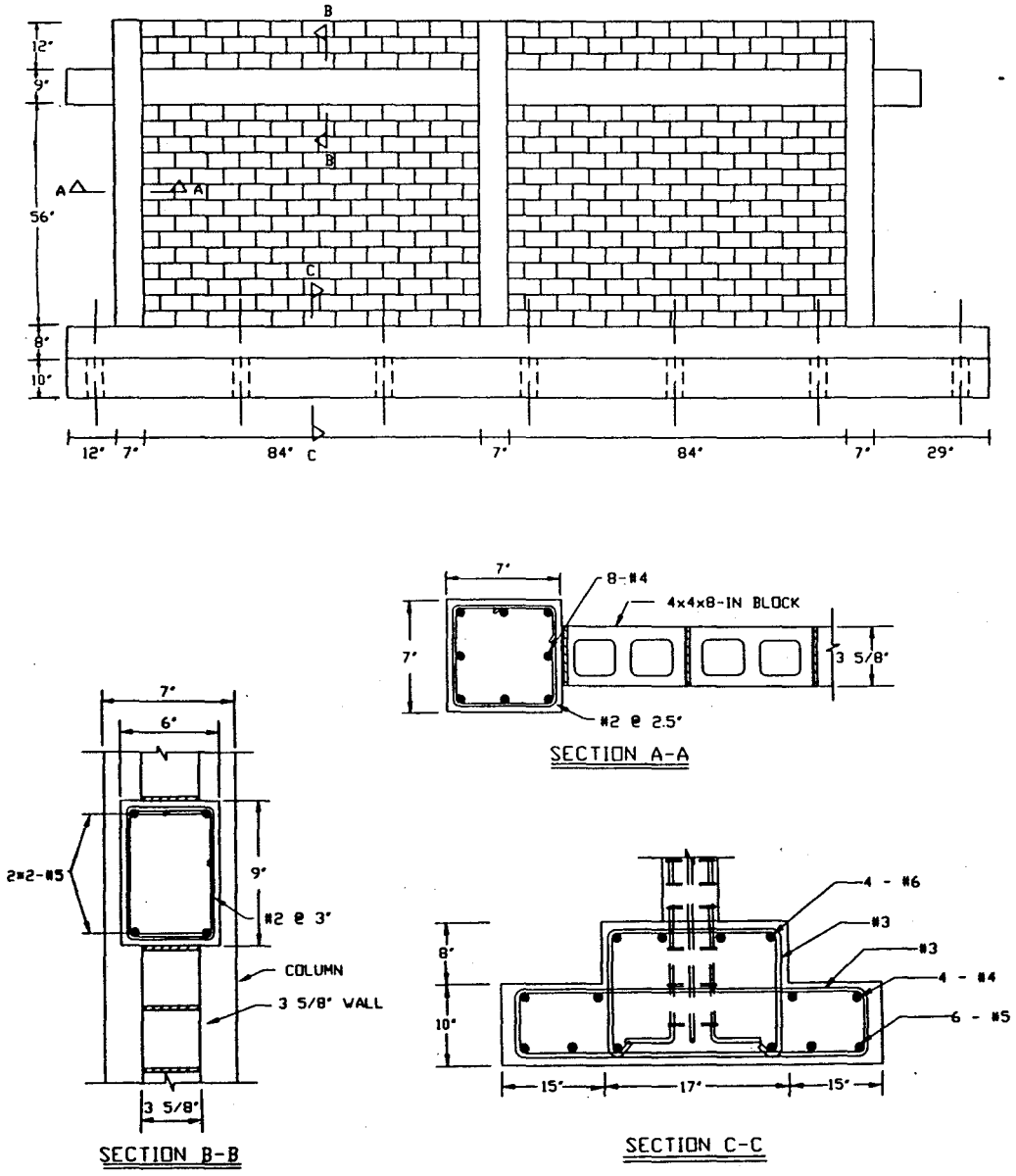

Figure 3.8. Design Details of Two-Bay Weak Frame with Panel Aspect Ratio of 0.67.

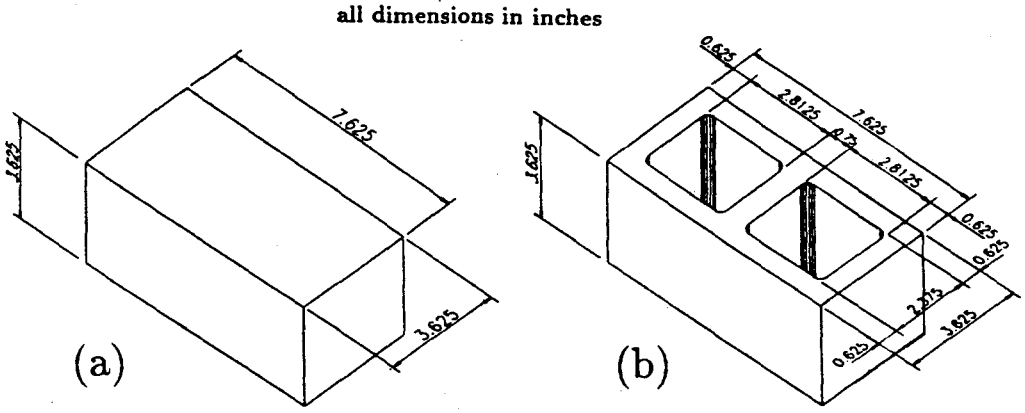

Figure 3.9. Concrete Masonry Units; a) Hollow Block; b) Solid Block.

had the weak design. For infill panels, 4 × 4 × 8-in. hollow and solid concrete masonry blocks were used in respective specimens. Their configurations are shown in Fig. 3.9.

The concrete base slab of each specimen was cast at least one week ahead of the frame. The concrete in each frame specimen had a specified compressive strength of 3,000 psi. The concrete mix consisted of 564 lbs of cement, 1400 lbs of sand, 1400 lbs of size #8 aggregate, and 340 lbs of water per cubic yard. The infill was constructed by a professional mason after the frame had been cast. Type S masonry mortar was used. It had a cement:lime:sand ratio of 1:0.5:4.5 by volume. Special attention was paid to the wall-frame interfaces to avoid any gap between the infill and the frame. In the bed joints of the hollow blocks, mortar was applied onto the face shells only, whereas the solid blocks had mortar applied onto the entire bed joint. The head joints were filled partially with mortar as in practice. The bed and head joints were 3/8-in. thick.

Table 3.1 summarizes the characteristics of the test specimens. Some of the frame specimens were tested more than once. In these cases, the damaged frames were repaired with epoxy injection into the cracks, and the crushed regions were patched up with cement paste of strength comparable to that of the original concrete. A new infill panel was used for each test. The specimens were tested at least 28 days after the construction of the infill.

3.2.2 Test Setup and Instrumentation. The test setup is shown in Fig. 3.10. The lateral load was applied by means of two servo-controlled hydraulic actuators, each of which has a load capacity of 110 kips and a stroke of ± 5 inches. To avoid any tensile force on the R/C beam, four stiff steel rods were used to transmit the pulling force to the specimen. The vertical loads were exerted by manually controlled hydraulic jacks, whose forces were directly monitored by strain gages attached to the vertical loading rods. The reaction frame and the specimen were anchored onto a two-foot-thick strong floor.

Strain gages and displacement transducers (LVDT's) were installed in each test to monitor the strains in the reinforcing bars and the deformations of the specimen at different locations, as shown in Fig. 3.11. LVDT's 1, 2, and 13 in the figure were used to measure the lateral displacement of the frame, LVDT's 5, 6, 7, and 8 were used to calculate the bending curvatures at the column sections, and LVDT's 9, 10, 11, and 12 were used to measure the overall shear distortion of the infill panel. The data from strain gages 15 to 26 were used to derive the moments, curvatures, and axial forces developed at critical beam and column sections.

Table 3.1. Test Specimens.

Spec. No.	Type of Frame	Type of Masonry Units	Panel Aspect Ratio (h/l)	Lateral Load	Vertical Load Distribution (Kips)		No. of Bays
					Columns	Beam	
1	weak	no infill	0.67	monotonic	66	---	1
2	weak - repaired (1)*	hollow	0.67	monotonic	66	---	1
3	weak - repaired (2)*	solid	0.67	monotonic	66	---	1
4	weak	hollow	0.67	cyclic	44	22	1
5	weak	solid	0.67	cyclic	44	22	1
6	strong	hollow	0.67	cyclic	44	22	1
7	strong	solid	0.67	cyclic	44	22	1
8	weak - repaired (4)*	hollow	0.67	monotonic	44	22	1
9	weak - repaired (8)*	solid	0.67	monotonic	44	22	1
10	weak	hollow	0.48	cyclic	44	22	1
11	weak	solid	0.48	cyclic	44	22	1
12	weak - repaired (10)*	solid	0.48	cyclic	66	33	1
13	weak	hollow	0.67	cyclic	99	---	2
14	weak - repaired (13)*	solid	0.67	cyclic	99	---	2

* Specimen repaired

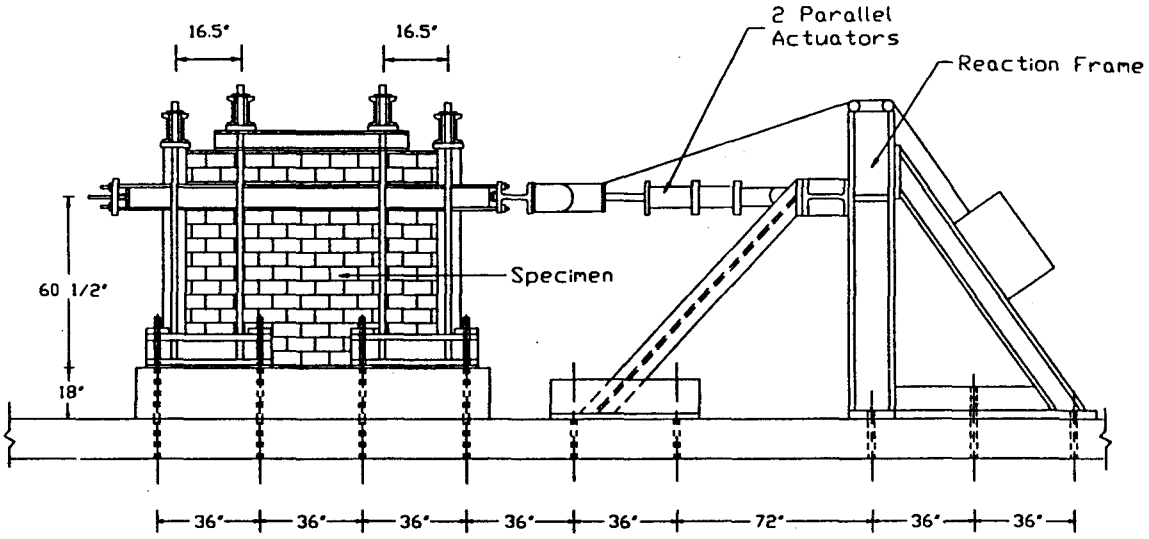

Figure 3.10. Test Setup.

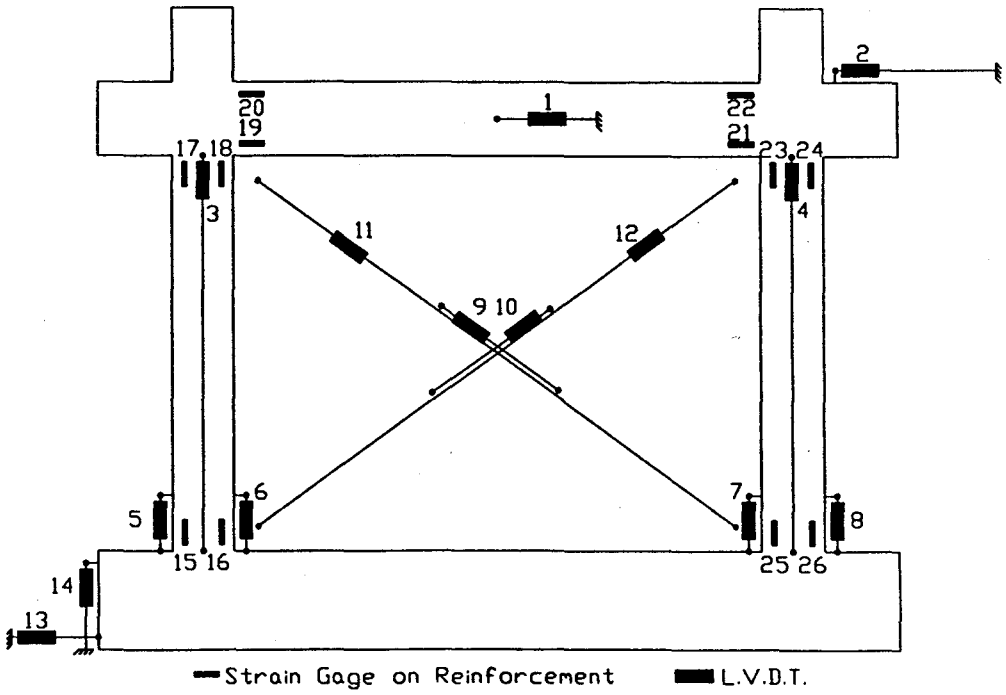

Figure 3.11. Typical Instrumentation.

3.2.3 Load Patterns and Histories. As shown in Table 3.1, the specimens were subjected to different combinations of vertical and lateral loads. A constant vertical load was applied onto each specimen. Two different vertical load distributions were employed: one with vertical loads applied onto the columns only, and the other with 1/3 of total vertical load applied onto the beam and 2/3 onto the columns. The vertical load distribution is shown for a one-bay specimen in Fig. 3.12. The load was distributed along the R/C beam by a steel wide-flanged beam (see Fig. 3.12). For this purpose, a W5×16 beam was used for specimens with an aspect ratio of 2/3 and a W6×15 was used for specimens with an aspect ratio of 1/2. In the two-bay specimens, a total vertical load of 99 kips was exerted onto the columns, with 33 kips applied onto each column. Two types of in-plane lateral displacement histories were selected. They were monotonic and cyclic loads. The cyclic load tests started with five cycles of load control, in which the amplitude of the load was increased gradually until the lateral load was slightly lower than the level at which a major crack was expected to occur in the infill. Results of monotonic tests were used to estimate the cracking load for the infill. For the single-bay specimens, the maximum load applied under load control was 24 kips for the weak-panel specimens and 40 kips for the strong-panel specimens. For the two-bay specimens, these loads were 40 and 60 kips for the weak-panel and strong-panel specimens, respectively. The load controlled cycles for the weak-panel, single-bay, specimens are shown in Fig. 3.13a. The load controlled cycles were followed by displacement controlled cycles of gradually increasing displacement amplitudes. As shown in Fig 3.13b, the displacement controlled cycles started from an amplitude of 0.15 in., which was increased with increments of 0.15

in. Each specimen was subjected to three fully reversed displacement cycles at each amplitude level. The 0.15-in. displacement is the level about which a major crack was expected to initiate in the panels of different specimens. Usually, a test was terminated when excessive damage was observed in the specimen.

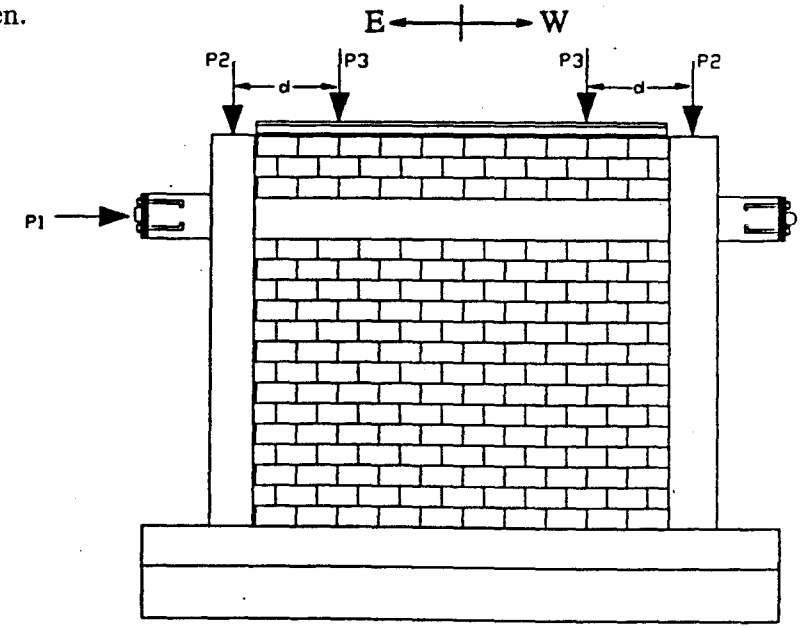

Figure 3.12. Vertical Load Distribution on Columns and Beam in Single-Bay Specimens (d = 16.5").

3.2.4 Material Properties. Material tests were conducted on the reinforcing steel, and concrete and masonry samples for each specimen. These include the modulus of rupture tests on $2 \times 2 \times 7$ in. concrete prisms, the split-cylinder tests of concrete, the compression tests of standard 6-in-diameter concrete cylinders, the compression tests of masonry units, the compression tests of 2-in.-diameter mortar cylinders and 2-in. mortar cubes, and the compression tests of 3-course masonry prisms. At least three samples were tested in each case and the results were averaged. Figures A.1 to A.3 (in Appendix A) show typical stress-strain curves from the compression tests of concrete

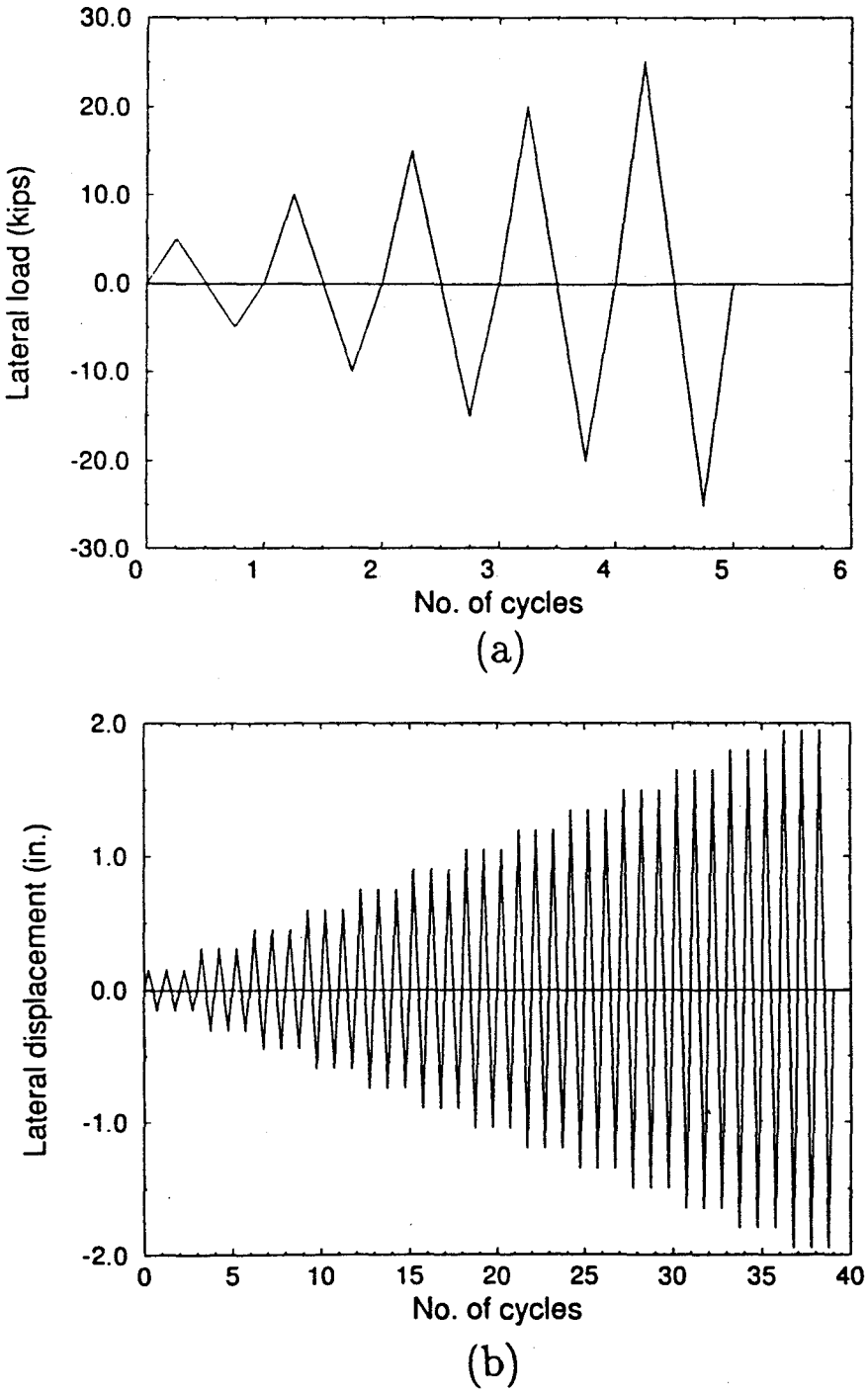

Figure 3.13. Typical Cyclic Lateral Load and Displacement Histories Applied to Weak-Panel Specimens; a) Load Controlled Cycles; b) Displacement Controlled Cycles.

cylinders. These tests were conducted for Specimen 11. Typical stress-strain curves from the compression tests of masonry prisms are shown in Figs. A.4 to A.6. These were tests carried out for Specimen 12. The average strengths of concrete and masonry samples are presented in Table 3.2. It can be noted from the table that the compressive strengths of 3-course hollow masonry prisms are considerably lower than those of individual units and mortar specimens. This can be attributed to the lack of stability of the face shells of the hollow prisms.

The tensile strengths of the reinforcing bars are summarized in Table 3.3. These are based on the nominal diameters of the bars. Two of the stress-strain curves obtained from the tension tests conducted on #5 rebars are shown in Figs. A.7 and A.8. Furthermore, direct shear tests were conducted on single mortar joints to obtain their cyclic shear behavior under different compression forces. As it is shown in Table 3.4, the shear strengths of the bed joints in the hollow and solid specimens are almost identical. They are computed based on the net cross-sectional area of mortar joints. It must be pointed out that, in some of the shear tests, the peak shear strength was not captured accurately due to measurement problems. Hence, some of these results were adjusted based on the results of well conducted tests and the assumption that the cohesive force remained the same. Typical shear stress-shear displacement curves and normal displacement-shear displacement curves under normal compressive stresses of 50, 75, 100, 150 psi are shown in Figs. A.9 to A.24.

3.3 Experimental Results

The specimens were aligned in the east-west direction (see Fig. 3.12). The sign convention adopted for the lateral displacement and force is that they are positive when they are towards west and negative when towards east. The

Table 3.2. Average Strengths of Concrete and Masonry Materials.

Spec. No.	Frame Concrete					Three-Course Masonry Prisms			Compressive Strength of Masonry Units (ksi)	Compressive Strength of Mortar Cylinders (ksi)
	Secant Modulus * (ksi)	Compressive Strength (ksi)	Strain at Peak Stress	Modulus of Rupture (ksi)	Tensile Strength (Split-Cylinder Test) (ksi)	Secant Modulus * (ksi)	Compressive Strength (ksi)	Strain at Peak Stress		
1	3180	4.48	0.0018	0.980	0.477	---	---	---	---	---
2	3180	4.48	0.0018	0.980	0.477	457	1.40	0.0036	2.39	2.30
3	3180	4.48	0.0018	0.980	0.477	1381	2.19	0.0029	2.26	2.32
4	2500	3.89	0.0027	0.705	0.401	667	1.54	0.0030	2.39	1.62
5	2620	3.03	0.0026	0.635	0.263	1298	2.01	0.0023	2.26	1.94
6	2880	3.75	0.0024	0.712	0.455	609	1.47	0.0032	2.39	2.43
7	2700	4.85	0.0030	0.744	0.328	1316	1.97	0.0026	2.26	2.25
8	2500	3.89	0.0027	0.705	0.401	740	1.38	0.0027	2.39	2.25
9	2500	3.89	0.0027	0.705	0.401	1195	2.06	0.0026	2.26	1.81
10	2920	3.90	0.0021	0.689	0.432	572	1.54	0.0036	2.39	1.73
11	2630	3.73	0.0028	0.617	0.448	1393	1.66	0.0025	2.26	1.89
12	2920	3.90	0.0021	0.689	0.432	1064	1.97	0.0029	2.26	2.59
13	2830	3.95	0.0027	0.734	0.504	823	1.99	0.0026	2.39	2.08
14	2830	3.95	0.0027	0.734	0.504	933	1.68	0.0034	2.26	2.08

* At 45% of the Compressive Strength

Table 3.3. Average Tensile Strengths of Reinforcing Steel.

Bar Size	Type of Bar	Nominal Diameter (in.)	Yield Stress (ksi)	Ultimate Stress (ksi)
No. 2	Plain	0.250	53.3	65.2
No. 4	Deformed	0.500	61.0	96.0
No. 5	Deformed	0.625	60.0	96.0

Table 3.4. Average Shear Strengths of Mortar Joints.

Type of Masonry Units	Average Compressive Strength of Mortar Cylinders (psi)	Compressive Stress (psi)	Peak Shear Strength (psi)	Residual Shear Strength (psi)
Hollow	1980	25	----	27
		50	72	48
		75	99	70
		100	136	89
		150	198	135
Solid	1950	50	70	44
		75	----	63
		100	138 *	89
		150	186	133

* Adjusted

lateral load-lateral displacement curves of the fourteen frame specimens are shown in Figs. 3.14 through 3.27. The final damage patterns of the specimens are shown in Figs. 3.28 through 3.41. The bare frame, which was a weak frame, exhibited a fairly ductile behavior with, however, some significant shear cracks developed in the beam-to-column joints. In the case of an infilled frame, the major nonlinearity in the behavior was usually initiated by the cracking of the infill. These cracks often initiated in the form of inclined cracks at the diagonal compression corners, with an approximately 45-degree angle, which were connected by horizontal sliding cracks developed along the bed joints near the midheight of the panel. This type of crack will be referred to as diagonal/sliding cracks in the following discussions. However, as shown by the failure patterns of the test specimens, the failure mechanism of an infilled frame depends very much on the relative strengths of the frame and the infill. In general, a frame with a weak panel had its lateral resistance governed by the sliding of the panel along its bed joints, as shown by Specimen 4 in Fig. 3.31. In such a case, the resistance of the panel does not seem to be influenced by the frame, and the total strength of the specimen is equal to the flexural resistance of a bare frame plus the sliding-shear strength of the panel. This is also true for the two-bay specimen which had weak panels and a weak frame. In the case of a strong infill and a weak frame, the ultimate resistance and failure were very much dominated by the diagonal/sliding crack and the shear failure of the east column, as shown by Specimen 5 in Fig. 3.32. This type of failure mode was also observed in the test of Specimen 14, which had strong panels and a two-bay weak frame. However, the cracking patterns of the panels were slightly different in two-bay and one-bay specimens. In the case of a strong

infill and a strong frame, as shown by Specimen 7 in Fig. 3.34, the ultimate resistance was governed by the corner crushing in the infill. In this case, the diagonal compression strut mechanism was fully developed, and the infill was most effective in enhancing the lateral resistance of the frame. It must be noted that in most of the weak-panel specimens (with hollow blocks), the lower courses of the masonry infill were strengthened by the mortar spilled from the upper courses. In these cases, the damage developed in the lower parts of the infills was less severe.

The initial stiffness, critical loads, critical displacements, and failure mechanisms of the fourteen specimens are summarized in Table 3.5. In the table, for monotonically loaded specimens, the secant stiffness is defined as the slope of a line joining the origin of the lateral load-vs.-lateral displacement curve and the point at which 50% of the maximum resistance was first reached. For the case of cyclic loading, the secant stiffness is the slope of a line connecting the extreme points of a small-amplitude displacement cycle in which the peak load is about 50% of the maximum lateral resistance. As shown by Specimens 1, 4, and 5, the stiffness of a weak frame-weak panel specimen can be 15 times as large as that of a bare frame, while that of a weak frame-strong panel specimen can be 50 times. However, for the repaired specimens, such as Specimens 8 and 9, the increase in stiffness appears to be much smaller. The maximum load resistance of a weak frame-weak panel specimen can be 1.5 times that of a bare frame, while the resistance of a weak frame-strong panel specimen can be 2.3 times. No test has been conducted on a strong frame without an infill panel. However, the lateral resistance of the strong frame is estimated to be 32.7 kips. This is based on the theoretical strength after being increased

by 15% to account for the expected discrepancy between the actual strength and theoretical prediction, as reflected by Specimen 1. Comparing this to the strengths developed by Specimens 6 and 7 indicates that the maximum resistances of the strong frames were increased by the weak and strong infills by factors of 1.4 and 3.2, respectively. Furthermore, frames with strong panels exhibited a much better hysteretic energy dissipation than those with weak panels.

The resistance of an infilled frame does not seem to depend on the aspect ratio of the specimen. Furthermore, the distribution of the vertical load between the columns and the beam does not affect the resistance of an infilled frame very much. Nevertheless, increasing the total vertical load by 50% can increase the stiffness by 30% and the maximum resistance by 25%, as shown by Specimens 11 and 12. Specimen 13, which had a two-bay weak frame with weak panels, was about 1.8 times stronger and 1.9 times stiffer than Specimen 4, which had a one-bay weak frame and a weak panel. Specimen 14, which had a two-bay weak frame with strong panels, was about 1.7 times stronger and 1.1 times stiffer than Specimen 5, which had a one-bay weak frame and a strong panel. The difference between the strengths and stiffnesses of the two-bay and one-bay specimens is mainly due to the contribution of the third column and the additional infill panel to the load resistance of the two-bay specimens. The total vertical load applied onto the two-bay specimens was 50% higher than those on Specimens 4 and 5. No test has been conducted on a bare two-bay frame. Its resistance is estimated to be 36 kips based on the resistance of Specimen 1. Comparing this to the resistances of the two-bay infilled specimens, it can be noticed that the resistance of a two-bay bare frame

Table 3.5. Summary of Test Results.

Spec. No.	Secant Stiffness (Kips/in.)	Load at First Major Crack in Panel *(Kips)	Disp. at First Major Crack (in.)	Max. Lateral Load (Kips)	Disp. at Max. Load (in.)	Failure Mechanism**
1	24	----	----	23.9	2.57	flexural
2	----	----	----	----	----	D1
3	740	62.4	0.13	62.4	0.13	C7
4	430	-30. 0, +20.7	-0.14 , +0.04	-34.5 , +36.5	-0.28 , +0.47	D1 + E3
5	1280	-46. 0, +49.2	-0.18 , +0.08	-52.2 , +60.0	-0.60 , +0.36	C7
6	480	-41.1, +46.2	-0.19 , +0.22	-42.3 , +46.6	-0.35 , +0.38	D1
7	1460	-90.2, +93.8	-0.24 , +0.20	-110 , +100	-0.45 , +0.40	E3
8	330	30.0	0.14	42.7	0.55	C3 + E3
9	590	58.7	0.20	65.8	0.29	C7
10	400	-35.1, +42.6	-0.24 , +0.24	-35.1 , +42.6	-0.24 , +0.24	D1 + E3
11	1470	-59.0, +65.8	-0.23 , +0.22	-62.0 , +65.8	-0.67 , +0.22	C7
12	1950	-74.6, +74.1	-0.19 , +0.14	-79.9 , +81.5	-0.32 , +0.28	C7
13	830	-55.0, +61.0	-0.10 , +0.15	-67.7 , +65.7	-0.36 , +0.30	D1
14	1450	-90.4, +91.0	-0.21 , +0.19	-101 , +91.0	-0.34 , +0.19	C7

* Diagonal/Sliding Crack

** Defined in Fig. 2.1

could be increased by the strong and weak panels by factors of 2.8 and 1.9, respectively. In general, the specimens subjected to cyclic loads exhibited a lower resistance and a faster load degradation with respect to the level of lateral displacement than those subjected to monotonically increasing loads. Detailed experimental observations are summarized in the following paragraphs.

3.3.1 Single-Bay Specimens with Weak Frames. Specimens 1 through 5 and 8 through 12 had weak frames. Some of them were subjected to monotonically increasing lateral displacements, while the others were subjected to fully reversed displacement cycles. The total vertical loads applied to these specimens were 66 kips, except for Specimen 12, which was subjected to a vertical load of 99 kips. Specimens 1 through 3 had vertical loads applied onto the columns only, while the rest had vertical loads distributed between the columns and the beam. Specimens 10 through 12 had a h/l ratio of approximately 1/2, while all other specimens had a h/l ratio of about 1/1.5.

Monotonically Loaded Specimens

Specimen 1. Specimen 1 was a bare frame, which exhibited a fairly ductile behavior with plastic hinges developed in the columns. The load-displacement curve of Specimen 1 is shown in Fig. 3.14. Flexural cracks initiated at the bottom sections of both columns at a lateral load of about 11 kips. Major shear cracks developed in the beam-to-column joints at about 16 kips. The longitudinal reinforcement at the bottom sections of the columns yielded at a lateral load of about 14 kips and a lateral displacement of 0.58 in., while the flexural reinforcement at the end sections of the beam yielded at about 17 kips and 0.78-in. displacement. Concrete crushing was observed at the upper end of the east column and the lower end of the west column

at the maximum load of 24 kips and a lateral displacement of about 1.9 in., after which the lateral resistance remained more or less constant. The failure pattern of Specimen 1 is shown in Fig. 3.28.

Specimen 2. The frame used in Specimen 1 was repaired and installed with a weak infill panel, and tested as Specimen 2. At the very beginning of the test, the control on one of the two horizontal actuators was lost due to a broken wire connection, and a large lateral force was applied to the specimen before any data were recorded. This force was large enough to crack the infill. Hence, the load-displacement curve shown in Fig. 3.15 corresponds to the post-cracked behavior of the specimen. At the maximum lateral load of about 32 kips, large slips occurred along the initially cracked bed joints, after which the lateral resistance remained almost constant. The longitudinal reinforcement at the bottom sections of the columns yielded at a lateral displacement of about 0.7 in. and that at the end sections of the beam yielded at about 1.8 in. Concrete crushing was observed at the bottom of the west column and the top of the east column at a lateral displacement of about 2 in. The failure pattern of Specimen 2 is shown in Fig. 3.29.

Specimen 3. The frame used in Specimen 2 was repaired for the second time and infilled with solid blocks to be tested as Specimen 3. The first diagonal/sliding crack occurred in the infill at the maximum lateral load of 62.4 kips and a lateral displacement of 0.13 in., after which the lateral load dropped to 48.3 kips and shear cracks appeared at the top of the east column. The lateral load reached 62.4 kips again at a lateral displacement of 0.23 in. The shear crack at the top of the east column widened at a lateral displacement of about 0.4 in. The test was terminated when concrete crushing was observed at

the bottom section of the west column. Since the strain gages in the frame were damaged in the previous tests, no strain data were recorded. As it is shown in Fig. 3.16, the lateral load-lateral displacement curve levels off at 42.5 kips when the lateral displacement is close to 1 in. The failure pattern of Specimen 3 is shown in Fig. 3.30.

Specimen 8. Specimen 8 was constructed with a repaired frame that was tested previously as Specimen 4. It was similar to Specimen 2 in design, except that the vertical load was distributed between the columns and the beam. At a lateral load of 30 kips and a lateral displacement of 0.14 in., the first diagonal/sliding crack occurred in the infill. The lateral resistance did not drop at this point and increased with displacement up to 42.5 kips at 0.32-in. displacement, at which the load dropped to 39.5 kips due to a major slip in the bed joint of the infill. The maximum lateral resistance reached was 42.7 kips at 0.55-in. displacement. It was followed by a gradual decrease in lateral load. At about a lateral displacement of 0.8 in. and a lateral load of 39 kips, a large slip was observed along the top bed joints in the infill. Subsequently, the opening of inclined cracks and the crushing in the infill led to a rapid decline of the lateral load as shown in Fig. 3.21. Crushing of concrete occurred at the bottom section of the west column at about 1.2-in. displacement. As shown in Fig. 3.35, the failure mode is very similar to that of Specimen 2.

Specimen 9. The frame used in Specimen 8 was repaired again and infilled with solid blocks and it was tested as Specimen 9. It was similar to Specimen 3 in design, except that the vertical load was distributed between the columns and the beam. At about a lateral load of 53 kips, an inclined crack developed in the infill. This was followed by a horizontal crack at about

59 kips, after which the lateral load dropped immediately to 54 kips. A major diagonal/sliding crack developed in the infill at the maximum load of 65.8 kips and at a lateral displacement of 0.29 in. This was followed immediately by a significant shear crack at the top of the east column. At 1.7-in. displacement, minor concrete crushing was observed at the bottom section of the west column. Some crushing and spalling occurred in the infill at 1.25-in. displacement. The load-displacement curve and the failure mode of this specimen, as shown in Figs. 3.22 and 3.36, are similar to those of Specimen 3. However, the resistance of Specimen 9 is slightly higher than that of Specimen 3. This might be due to the fact that a part of the vertical load in Specimen 9 was directly applied onto the beam. This could have enhanced the shear resistance of the infill.

Cyclically Loaded Specimens

Specimens 4 and 5, and Specimens 10 through 12 were subjected to cyclic lateral loads.

Specimen 4. Specimen 4 had a weak panel. The first diagonal/sliding crack in the infill occurred at a lateral load of 30 kips and a lateral displacement of 0.13 in. in the negative direction, and at 20 kips and 0.04-in. displacement in the positive direction. The maximum lateral resistances were detected at 36.5 kips and 0.47-in. displacement in the positive direction and 34.5 kips and 0.28-in. displacement in the other. Considerable slip was observed along the bed joints at about 0.6-in. displacement. The slip progressed with the crushing and degradation of mortar at the bed joints. Crushing started inside the infill at about 0.75-in. displacement. At about a lateral displacement of 1.35 in., concrete crushing was observed at the bottom section of the west column in each loading direction. The yielding of the flexural reinforcement in

the columns could not be monitored because of bad strain gages. The load-displacement hysteresis curves of the specimen are shown in Fig. 3.17. The failure pattern of Specimen 4 is shown in Fig. 3.31.

Specimen 5. Specimen 5 had a strong panel. As shown by the hysteresis curves in Fig. 3.18, the load degradation in this specimen was much faster than that of Specimen 4, which had a weak panel. However, the energy dissipation of this specimen appears to be better than that of Specimen 4. The first diagonal/sliding cracks in the infill were observed at a lateral load of 49.2 kips in the positive direction and 46 kips in the negative direction. The corresponding lateral displacements were 0.08 in. and 0.18 in., respectively. This led to a drop of the lateral resistance. At this point, shear cracks appeared at the top of the east column in each direction. The shear cracks widened significantly at the maximum lateral resistance of 60 kips in the positive direction and 52.2 kips in the other. Slips along the horizontal cracks and the openings of the diagonal cracks were observed in the infill at about 0.8-in. displacement. Crushing of infill started at about a lateral displacement of 0.85 in. in both directions. The longitudinal reinforcement at the bottom sections of the columns yielded at about a lateral displacement of 0.9 in., but no yielding was detected for the longitudinal reinforcement in the beam. Due to the spalling of crushed masonry inside the infill, the lateral resistance dropped considerably at about 1-in. displacement. Concrete crushing started at the bottom section of the leeward column at about 1.2-in. displacement in each direction. The failure pattern is shown in Fig. 3.32.

Specimen 10. Specimen 10 had a weak infill and a panel aspect ratio of 0.48. The hysteresis curves and the failure mode of Specimen 10, as shown

in Figs. 3.23 and 3.37, are quite similar to those of Specimen 4, but the maximum lateral resistance is 17% higher. The first major diagonal/sliding cracks developed in infill at a lateral load of 42.6 kips and a lateral displacement of 0.24 in. in the positive direction, and 35.1 kips and 0.24 in. in the negative direction. The cracking loads coincided with maximum lateral resistances in both directions. Corner crushing was observed in the infill at about a lateral displacement of 0.55 in. The longitudinal reinforcement at the bottom sections of the columns yielded at about a lateral displacement of 1.0 in. Due to bad strain gages, no strain data were recorded for the steel bars in the beam. At about a lateral displacement of 1.4 in., minor crushing of concrete was observed at bottom sections of the columns in both directions.

Specimen 11. Specimen 11 had a strong infill and a panel aspect ratio of 0.48. The hysteresis curves and the failure mode of Specimen 11, as shown in Figs. 3.24 and 3.38, are similar to those of Specimen 5. However, its maximum lateral resistance is 10% higher than that of Specimen 5, which had a panel aspect ratio of 0.67. The first diagonal/sliding crack was observed at 65.8 kips and 0.22-in. displacement in the positive direction, and 59 kips and 0.23-in. displacement in the negative direction. The first cracking load and the maximum resistance coincide in the positive direction. The maximum lateral resistance in the negative direction occurred at 62-kips load and 0.67-in. displacement after the first major crack. These cracks were followed immediately by shear cracks at the top sections of the east column. The shear cracks in the columns widened at about 0.8-in. displacement. Yielding occurred in the longitudinal reinforcement at the bottom sections of the columns at about 0.7-in displacement, but the bars in the beam did not yield. At about 61 kips

and 0.4-in. displacement, crushing started inside the infill. At about 1.3-in. displacement, crushing was observed at the bottom section of the west column in the negative direction.

Specimen 12. The frame used in Specimen 10 was repaired and installed with a strong panel and tested as Specimen 12. It was similar to Specimen 11, except that the vertical load was 50% higher in this case. At a lateral load of 55 kips in the positive direction and 60 kips in the negative direction, 45-degree inclined cracks developed in the infill from the middle of the beam-wall interface and propagated to the bottom corners of the wall in both directions. They did not affect the lateral resistance. The first major diagonal/sliding cracks occurred at 74 kips and 0.14-in. displacement in the positive direction, and 75 kips and 0.18 in. in the other. These were followed immediately by a small drop of lateral resistance and the initiation of shear cracks at the top of the east column in each direction. The maximum lateral resistances reached were 81.5 kips in the positive direction and 79.9 kips in the negative direction. The corresponding displacements were 0.28 in. and 0.32 in., respectively. At about 75 kips and 0.3-in. displacement in the positive direction, crushing started inside the infill. As shown by the hysteresis curves in Fig. 3.25, the lateral resistance dropped significantly at about 0.5-in. displacement due to the spalling of the infill in the previously crushed areas. The shear cracks at the top of the east column widened at about 43 kips and 0.7-in. displacement in the positive direction. Similar shear failure was also observed in the other column. At a lateral displacement of about 1.0 in., crushing started at the bottom section of the west column in the negative direction. The failure mode of Specimen 12 shown in Fig. 3.39 was very similar to that of Specimen 11,

but the lateral resistance increased by 25%.

3.3.2 Single-Bay Specimens with Strong Frames. Specimens 6 and 7, which had strong frames, were intended to study the influence of the strength and stiffness of the columns on the lateral resistance of an infilled frame. Specimen 6 had a weak panel and Specimen 7 a strong panel. The panel aspect ratio was 0.67 for both specimens.

Specimen 6. As shown by the hysteresis curves in Fig. 3.19, the behavior of Specimen 6 was quite similar to that of Specimen 4, but the lateral strength is 28% higher than that of Specimen 4. The first diagonal/sliding crack occurred at 46.2 kips and 0.218-in. displacement in the positive direction, and 41.1 kips and 0.192-in. in the other. At about a displacement of 0.24 in., a major slip was observed along the top bed joint at the wall-beam interface. The maximum lateral resistance of 46.6 kips was reached at 0.38-in. displacement in the positive direction, and 42.3 kips at 0.35-in. displacement in the negative direction. At about 0.5-in. displacement and a lateral load of 44 kips, crushing started in the infill. No major opening was observed in the diagonal cracks in the infill. The failure mode of this specimen is shown in Fig. 3.33. Unlike the specimens with weak frames, the yielding of the longitudinal reinforcement in the beam occurred prior to that in the columns, at 0.34-in. displacement.

Specimen 7. The first crack in the infill developed along the bed joint at the beam-wall interface at about 77 kips and 0.14-in. displacement in the positive direction. The first diagonal/sliding crack in the infill occurred at 93.8 kips and 0.2-in. displacement in the positive direction, and 90.2 kips and 0.24 in. in the negative direction. These led to a drop of the lateral resistance. Shear cracks also appeared at the top of the windward column at this point.

The maximum lateral resistances reached were 100 kips in the positive direction and 110 kips in the negative direction. The corresponding displacements were 0.4 and 0.45 in., respectively. The corner crushing of the infill was observed at about a displacement of 0.5 in., and the internal crushing occurred at about 0.7 in. The longitudinal reinforcement at the bottom section of the columns yielded at about 0.9-in. displacement. No shear failure was observed in the columns. However, the shear cracks in the columns opened slightly at about 1.1-in. displacement. The hysteresis curves and the failure pattern of Specimen 7 are shown in Figs. 3.20 and 3.34, respectively.

3.3.3 Two-Bay Specimens. A two-bay frame with a weak-frame design was constructed for Specimens 13 and 14. Each panel had an aspect ratio of 0.67. A total vertical load of 99 kips was applied onto these specimens, and it was divided equally among the columns. The specimens were subjected to fully reversed displacement cycles.

Specimen 13. Specimen 13 had weak panels. As shown in Fig. 3.40, the failure mode of this specimen is similar to that of Specimen 4, which was a one-bay specimen having the same design. However, as shown by the hysteresis curves in Fig. 3.26, the maximum lateral resistance of Specimen 13 is about 85% higher than that of Specimen 4, and it exhibited a more severe strength degradation than Specimen 4. It must be pointed out that the total vertical load applied on this specimen was 50% higher than that applied on Specimen 4. The first diagonal/sliding cracks were observed in both panels at 55-kip lateral load and 0.1-in. displacement in the negative direction, and 61 kips and 0.15-in. displacement in the positive direction. The maximum lateral resistances were 67.7 kips in the negative direction and 65.7 kips in the positive

direction at lateral displacements of 0.37 and 0.29 in., respectively. Shear and flexural cracks were observed in the columns and the beams as well as in the column-to-beam joints. However, they did not widen considerably. Crushing started inside the infill at about 0.45-in. displacement and at corners at about 0.6-in. Major slidings along the bed joints were observed at about 0.6-in. displacement. No yielding was observed in the longitudinal reinforcement, and no crushing was observed in the concrete columns in the test.

Specimen 14. The frame of Specimen 13 was repaired and installed with strong panels and tested as Specimen 14. In general, as shown in Fig. 3.41, the failure of this specimen is similar to that of Specimen 5, which was a one-bay specimen having the same design. However, as shown by the hysteresis curves in Fig. 3.27, the lateral resistance of Specimen 14 is about 68% higher than that of Specimen 5, and its strength degradation is more severe than that of Specimen 5. The levels of damage in the columns and the panels of this specimen are different in the two different bays. As shown in Fig. 3.41, one panel exhibited a sliding shear failure mode, while the other severe corner crushing. Severe shear crack developed only in one of the two exterior columns. The first diagonal/sliding cracks were observed in both panels at 90.4-kip lateral load and 0.21-in. displacement in the negative direction, and at 91.0 kips and 0.19-in. displacement in the positive direction. The cracking load and the maximum load coincided in the positive direction; whereas, in the negative direction, a maximum lateral load of 101.0 kips was reached at 0.34-in. displacement. The shear crack widened in the west exterior column at 0.46-in. displacement. Corner crushing was observed in the west infill panel at 0.46-in. displacement. Within the maximum lateral displacement of 1.14

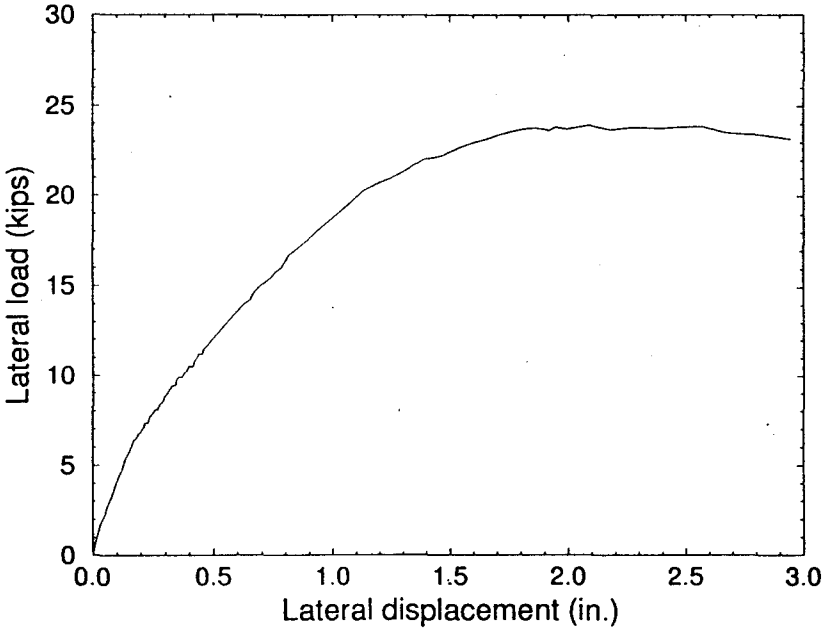

Figure 3.14. Load-Displacement Curve for Specimen 1.

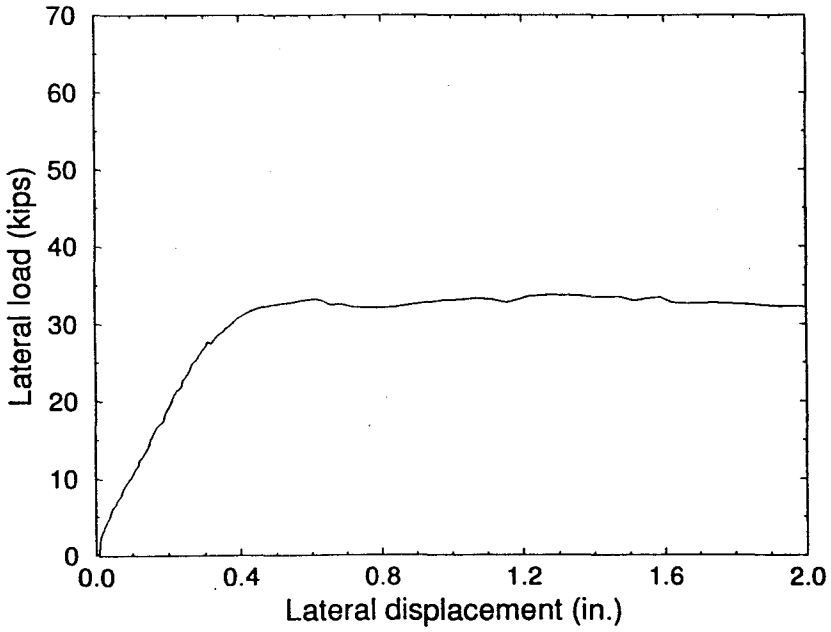

Figure 3.15. Load-Displacement Curve for Specimen 2.

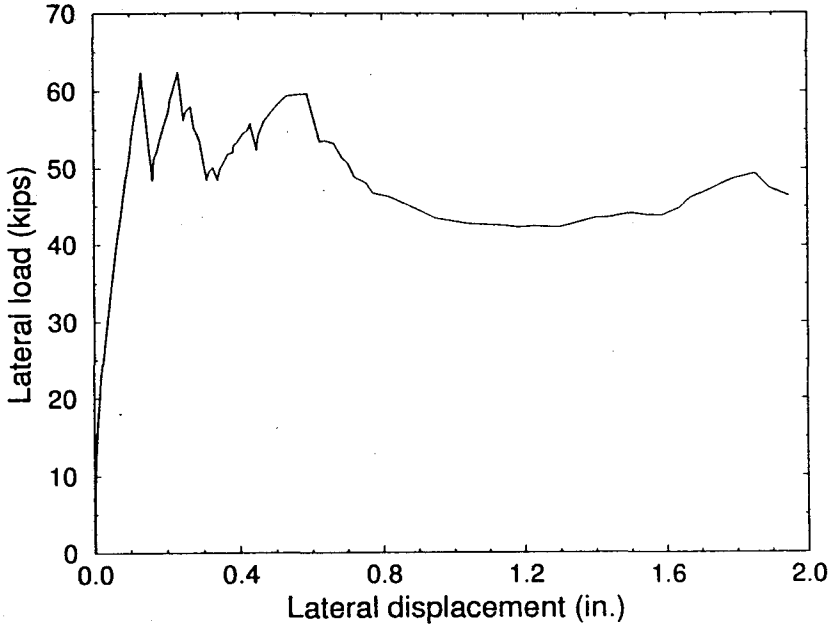

Figure 3.16. Load-Displacement Curve for Specimen 3.

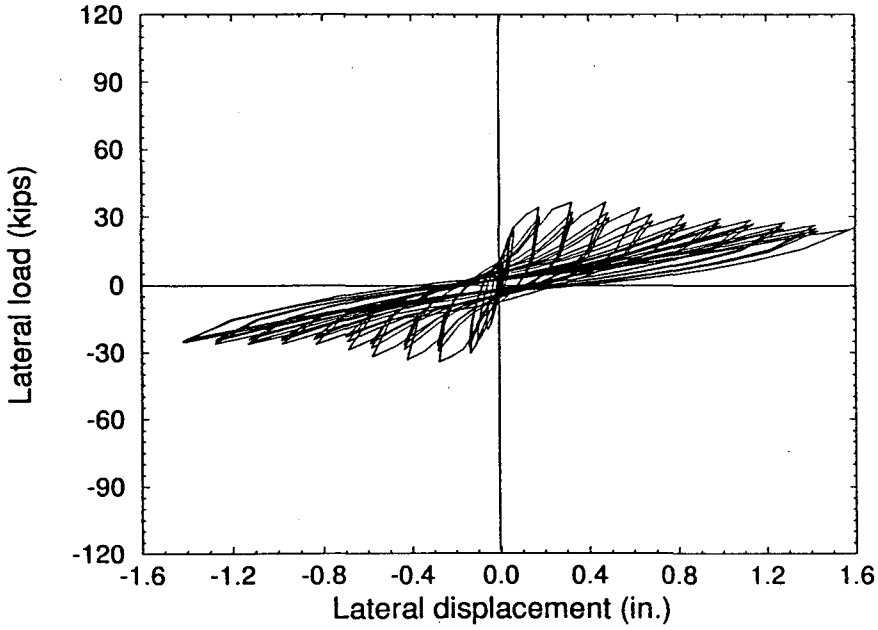

Figure 3.17. Load-Displacement Hysteresis Curves for Specimen 4.

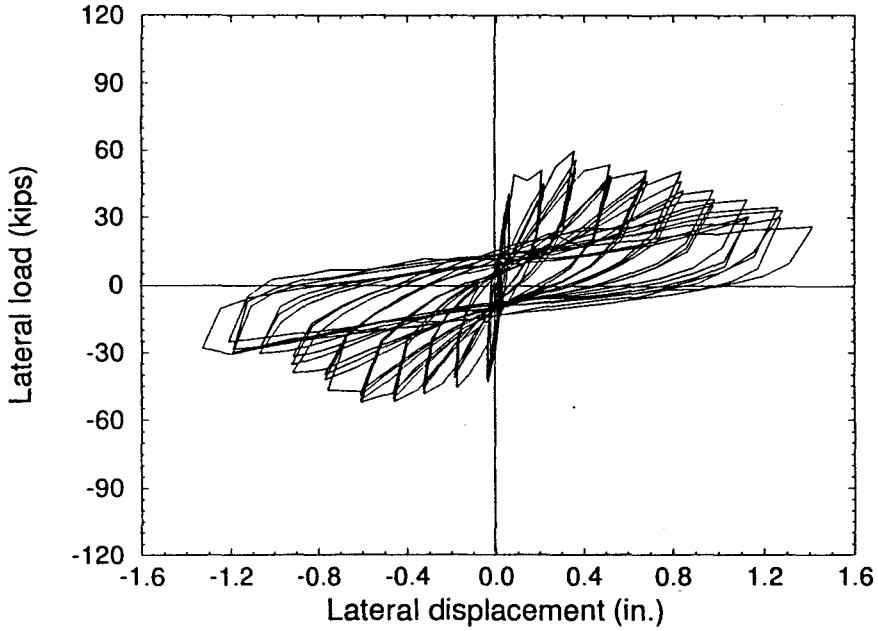

Figure 3.18. Load-Displacement Hysteresis Curves for Specimen 5.

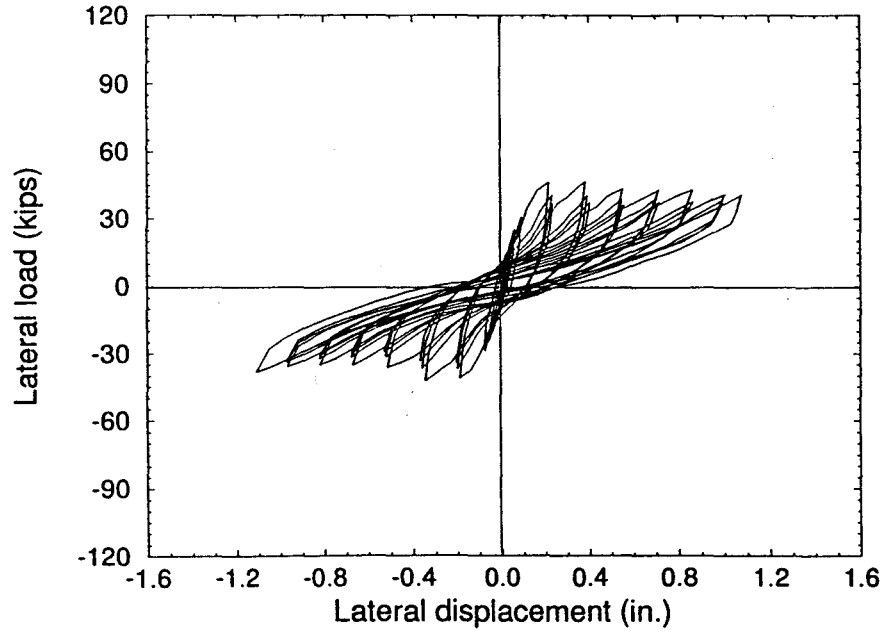

Figure 3.19. Load-Displacement Hysteresis Curves for Specimen 6.

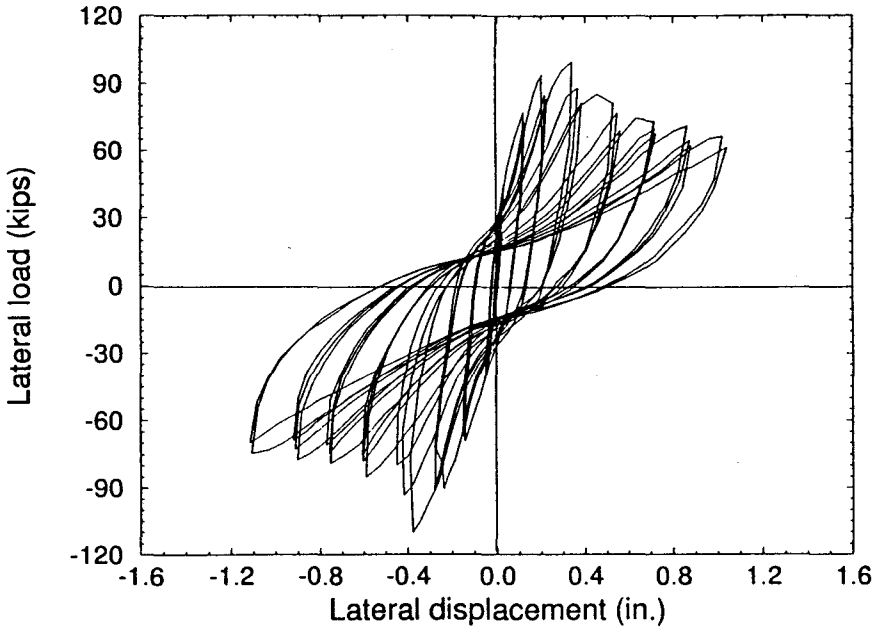

Figure 3.20. Load-Displacement Hysteresis Curves for Specimen 7.

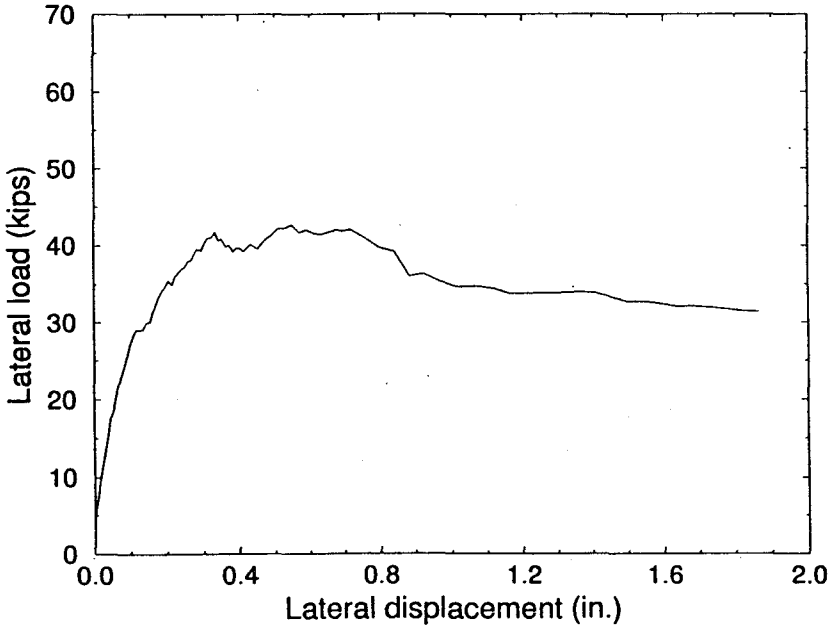

Figure 3.21. Load-Displacement Curve for Specimen 8.

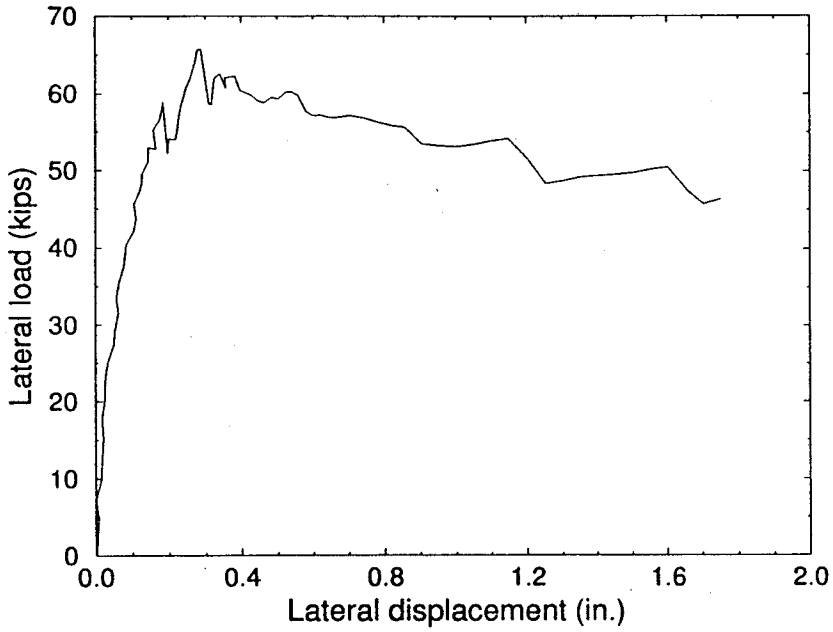

Figure 3.22. Load-Displacement Curve for Specimen 9.

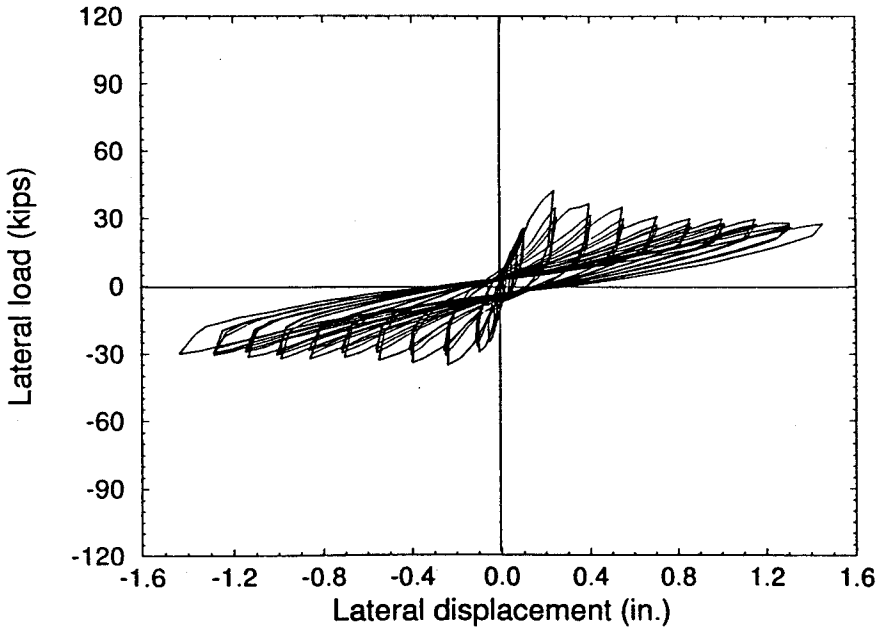

Figure 3.23. Load-Displacement Hysteresis Curves for Specimen 10.

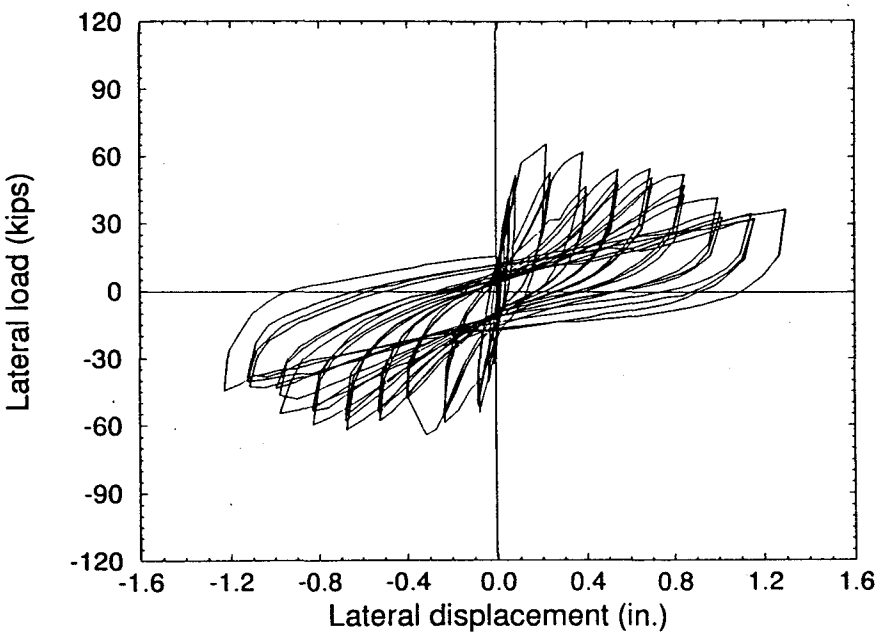

Figure 3.24. Load-Displacement Hysteresis Curves for Specimen 11.

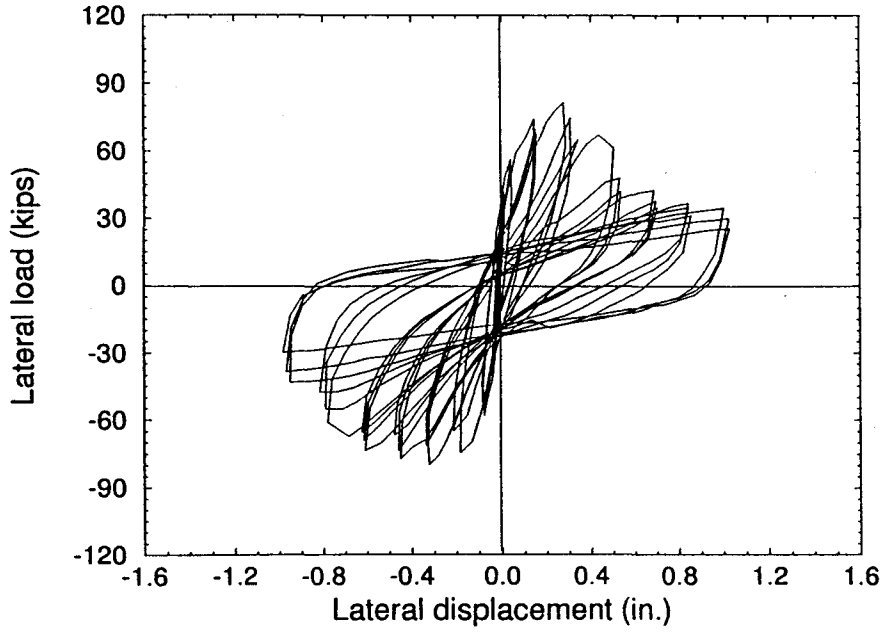

Figure 3.25. Load-Displacement Hysteresis Curves for Specimen 12.

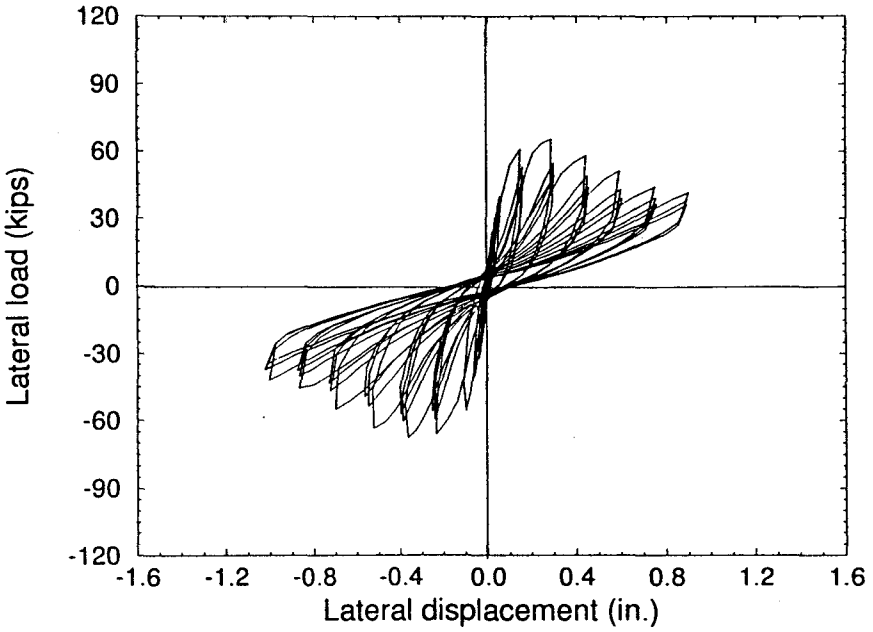

Figure 3.26. Load-Displacement Hysteresis Curves for Specimen 13.

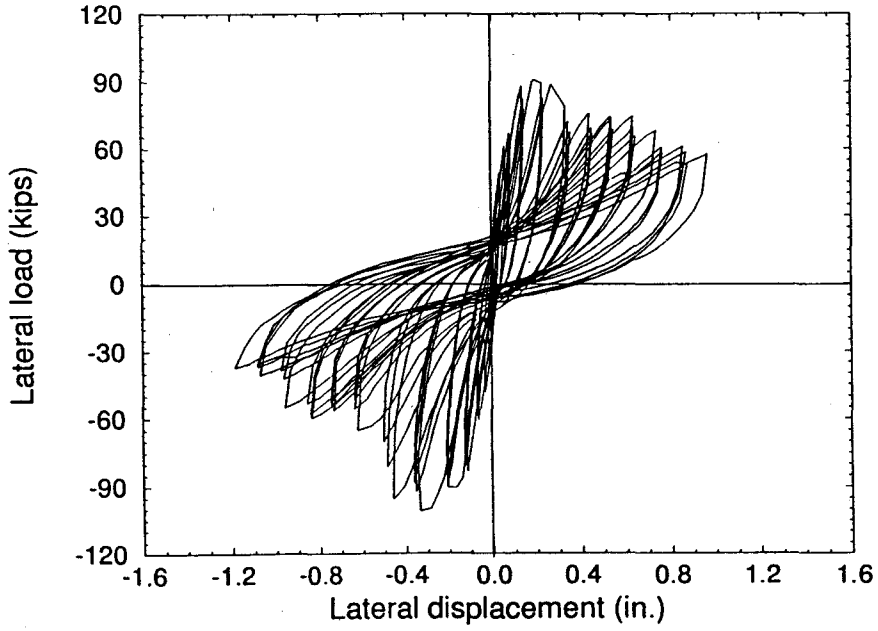

Figure 3.27. Load-Displacement Hysteresis Curves for Specimen 14.

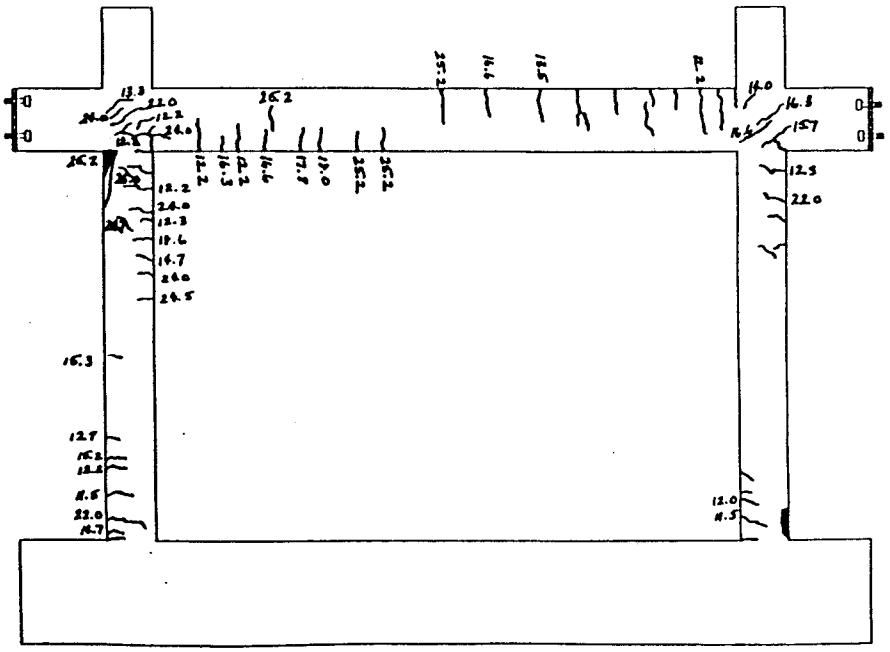

Figure 3.28. Failure Pattern of Specimen 1.

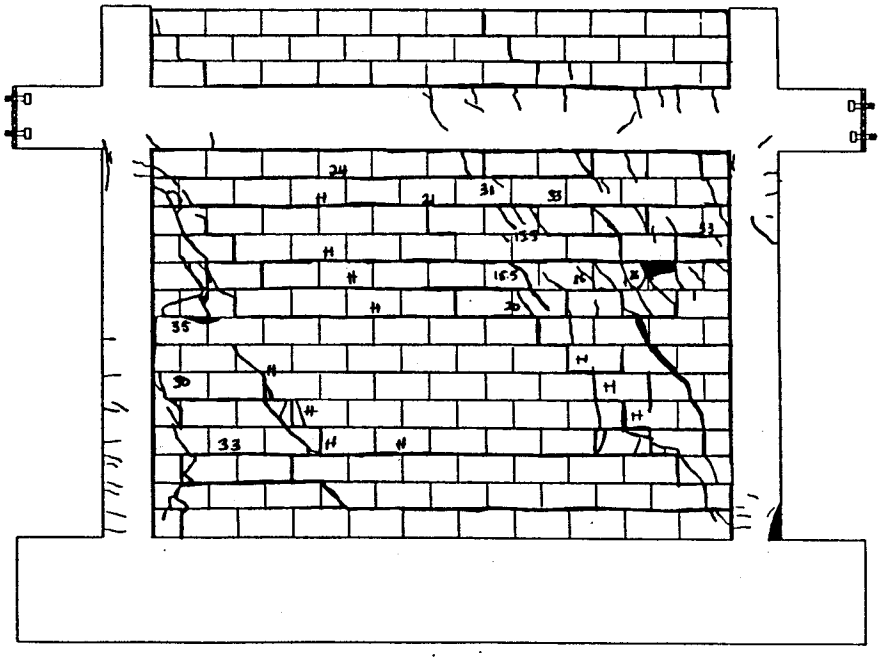

Figure 3.29. Failure Pattern of Specimen 2.

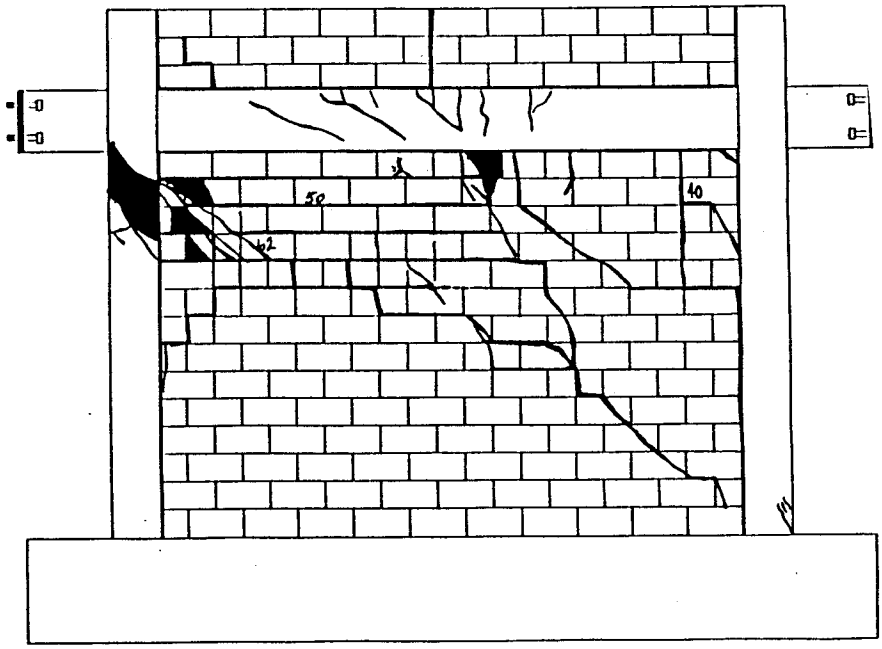

Figure 3.30. Failure Pattern of Specimen 3.

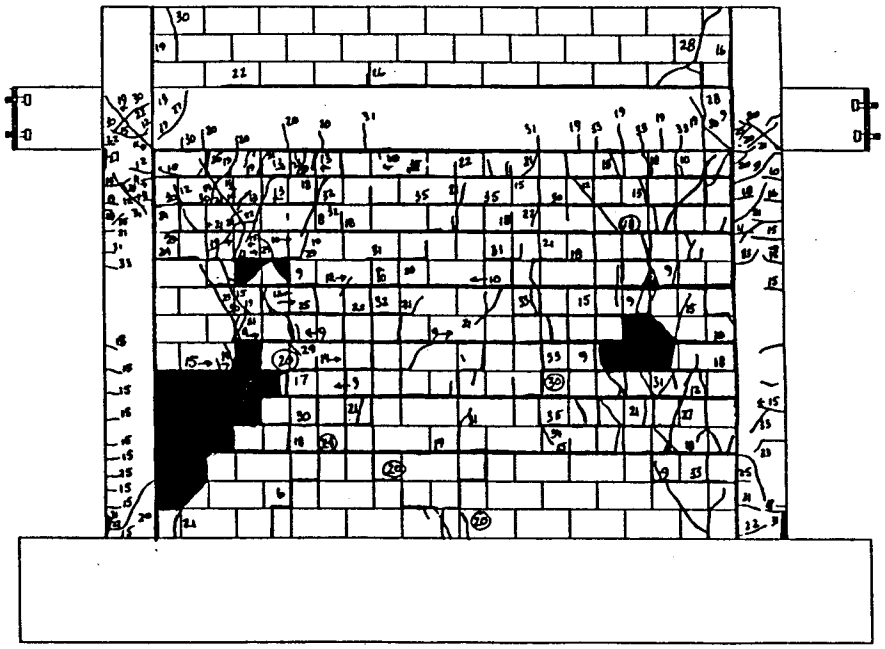

Figure 3.31. Failure Pattern of Specimen 4.

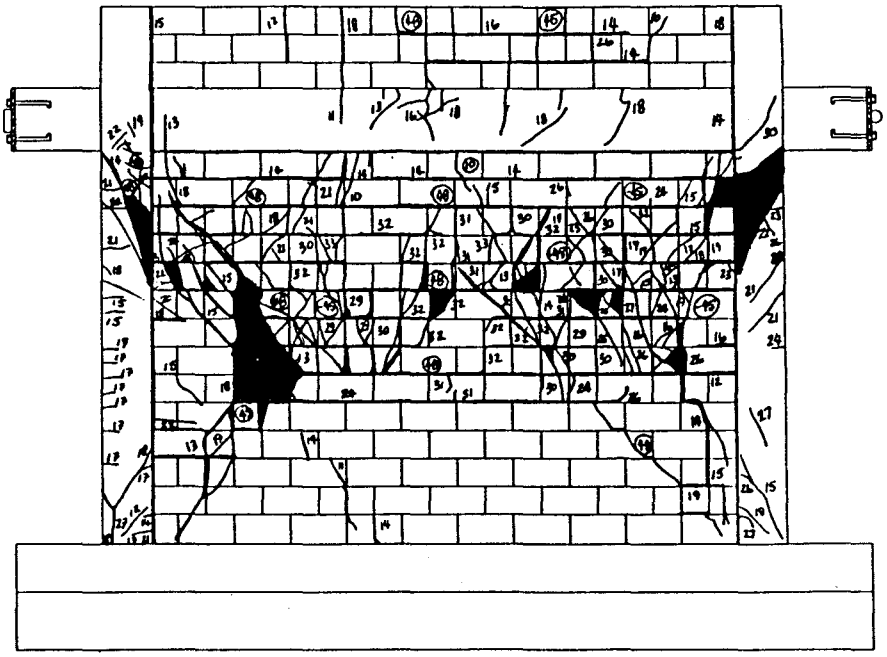

Figure 3.32. Failure Pattern of Specimen 5.

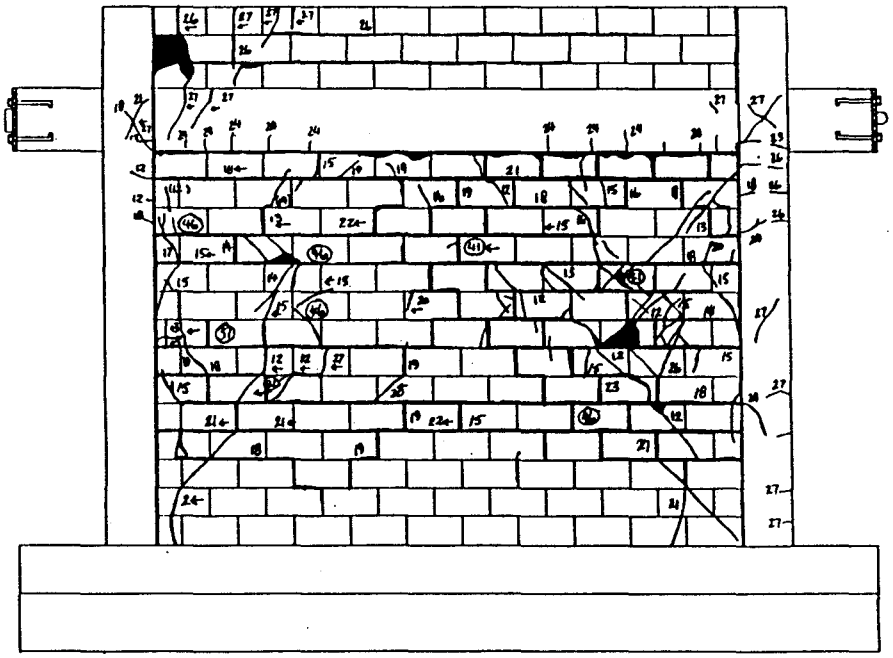

Figure 3.33. Failure Pattern of Specimen 6.

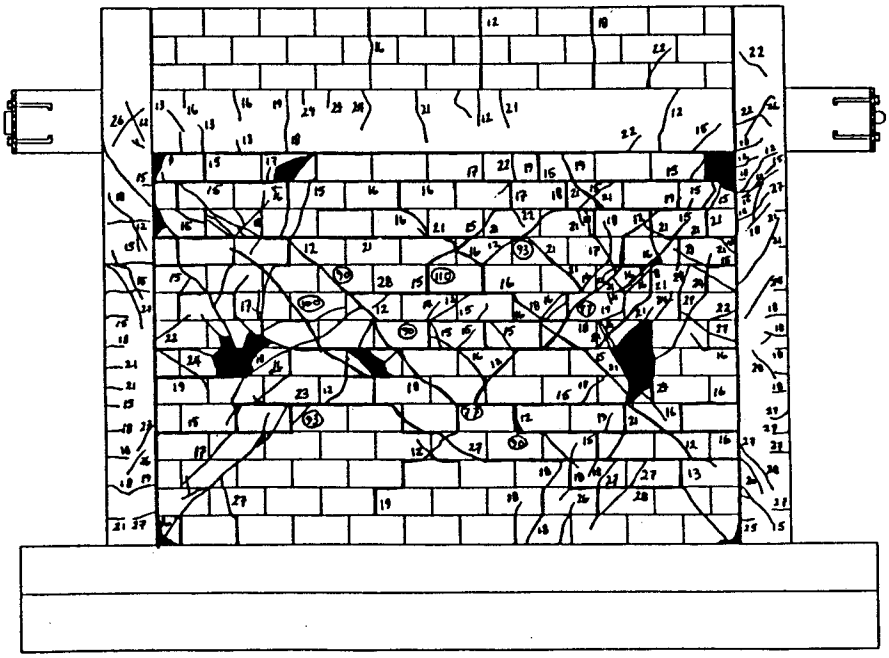

Figure 3.34. Failure Pattern of Specimen 7.

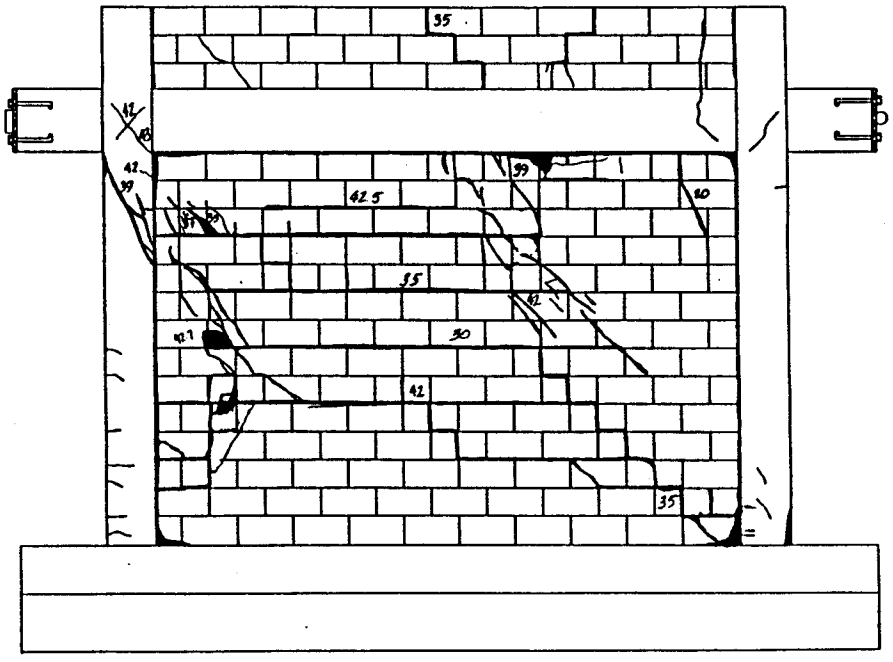

Figure 3.35. Failure Pattern of Specimen 8.

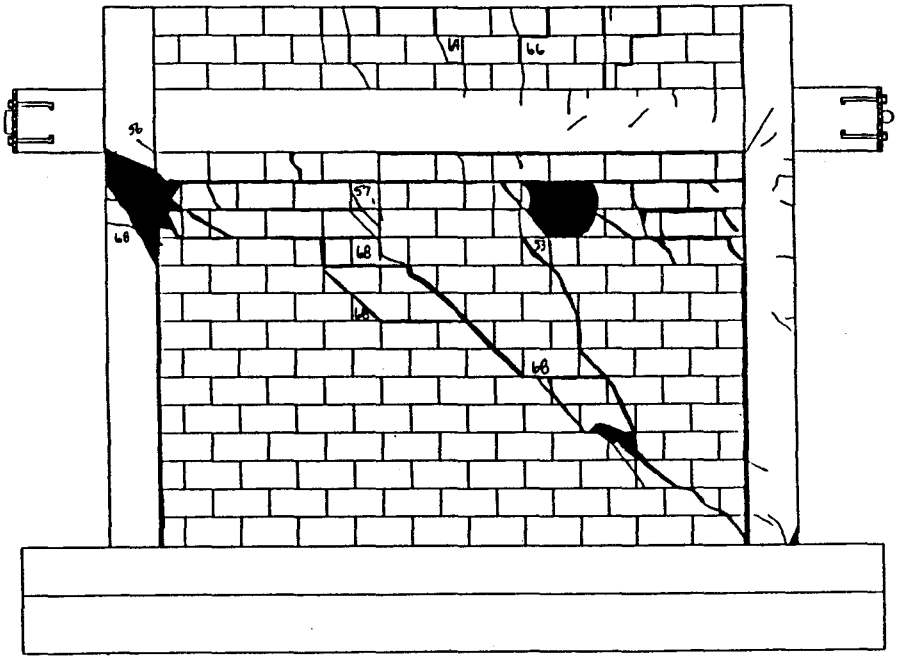

Figure 3.36. Failure Pattern of Specimen 9.

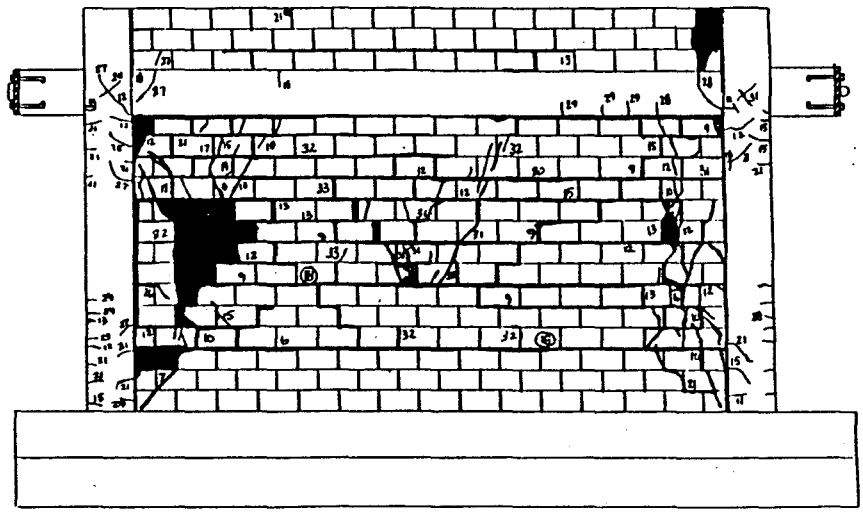

Figure 3.37. Failure Pattern of Specimen 10.

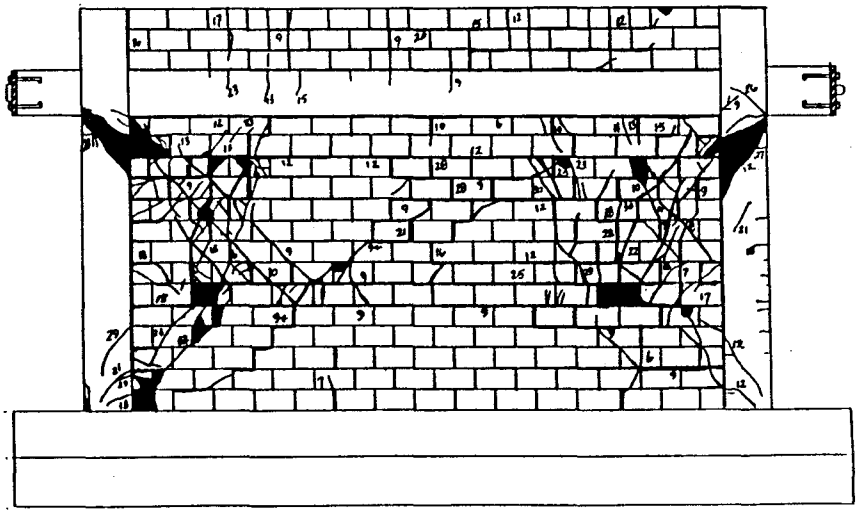

Figure 3.38. Failure Pattern of Specimen 11.

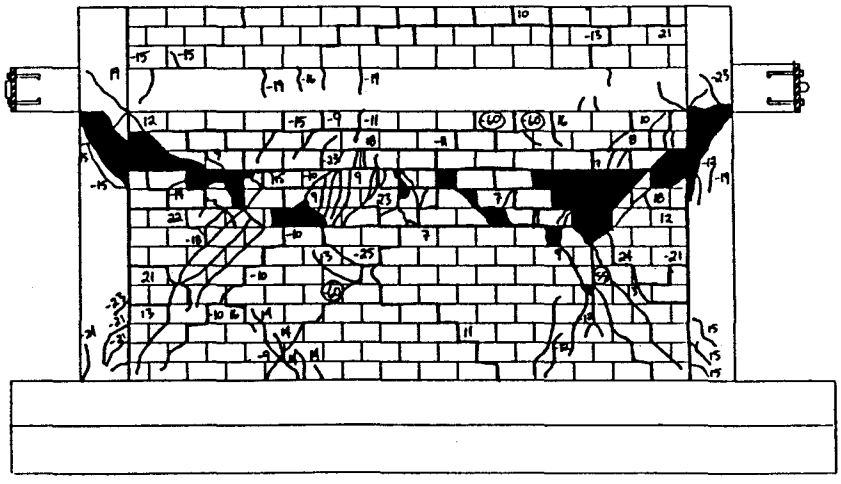

Figure 3.39. Failure Pattern of Specimen 12.

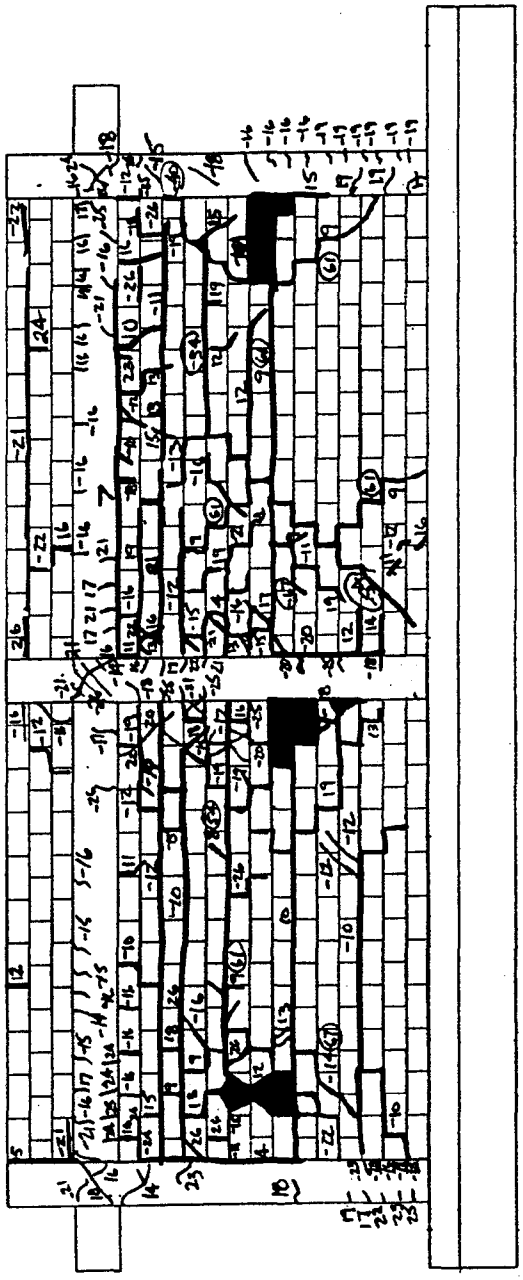

Figure 3.40. Failure Pattern of Specimen 13.

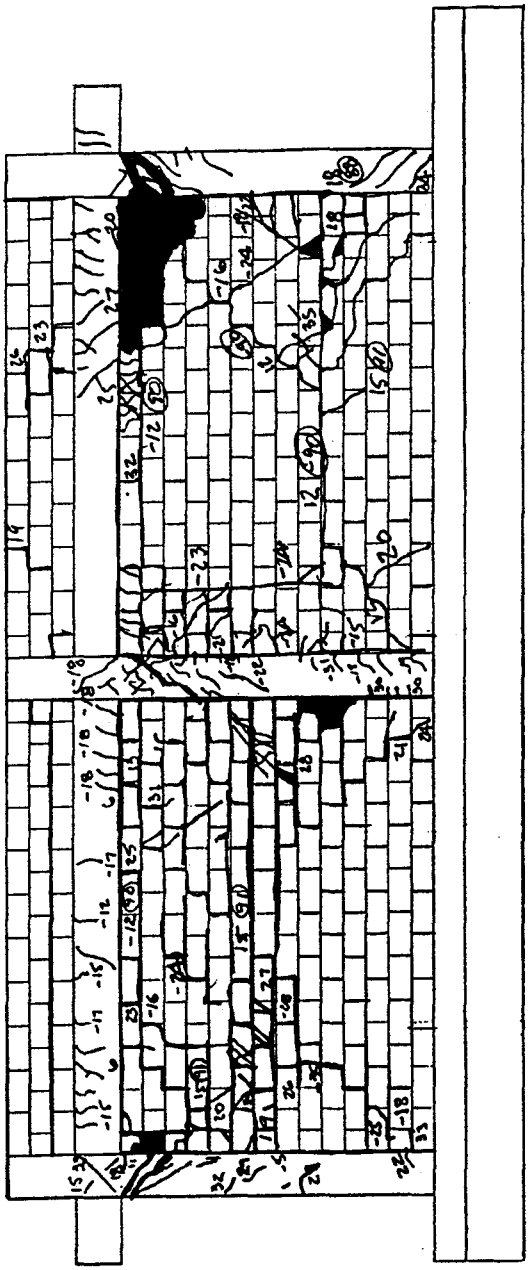

Figure 3.41. Failure Pattern of Specimen 14.

in., the yielding of the longitudinal reinforcement occurred only at the bottom section of the east exterior column at 0.46-in. displacement.

3.4 Interpretation of Experimental Results

3.4.1 Influence of Panel Strength. As shown in Fig. 3.42, an infill panel can significantly increase both the lateral stiffness and load resistance of a reinforced concrete frame. The stronger the panel is, the larger is the increase. The strength of Specimen 9, which had a weak frame and a strong infill, is about 54% higher than that of Specimen 8, which had a hollow infill, and 175% higher than the maximum resistance of the weak bare frame (Specimen 1). Specimen 5, which had a strong infill and was subjected to cyclic loads, had a lateral resistance 64% higher than that of Specimen 4, which had a weak panel. Specimens 6 and 7 had strong frames and were subjected to cyclic loads. Specimen 7, which had a strong infill, had a resistance 136% higher than that of Specimen 6, which had a weak infill. Nevertheless, the degradation of post-peak resistance with respect to displacement was faster in the case of the strong infill than the case of the weak infill. This is more evident under cyclic lateral loads as is indicated by the hysteresis envelope curves of Specimens 4 and 5, and those of Specimens 6 and 7 in Fig. 3.43. This can be partly attributed to the brittle shear failure that was induced in the columns by the solid infill in the case of a weak frame, and partly to compression failure of the solid infill itself. However, as the hysteresis curves of the specimens with weak and strong panels show, a strong infill resulted in a much better energy-dissipation capability than a weak infill.

3.4.2 Influence of Column Strength. The specimens with a strong frame design had a substantially higher load resistance than those with

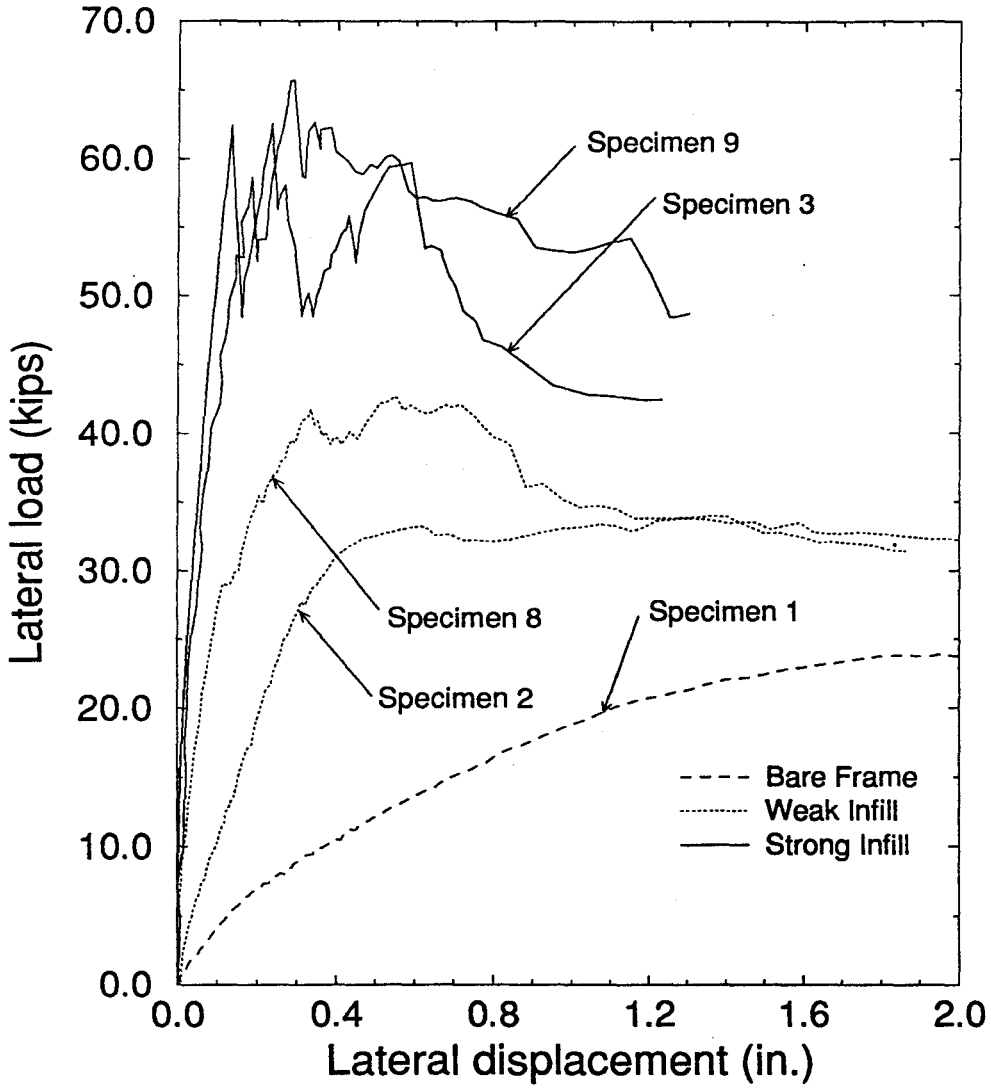

Figure 3.42. Load-Displacement Curves for Monotonically Loaded Specimens.

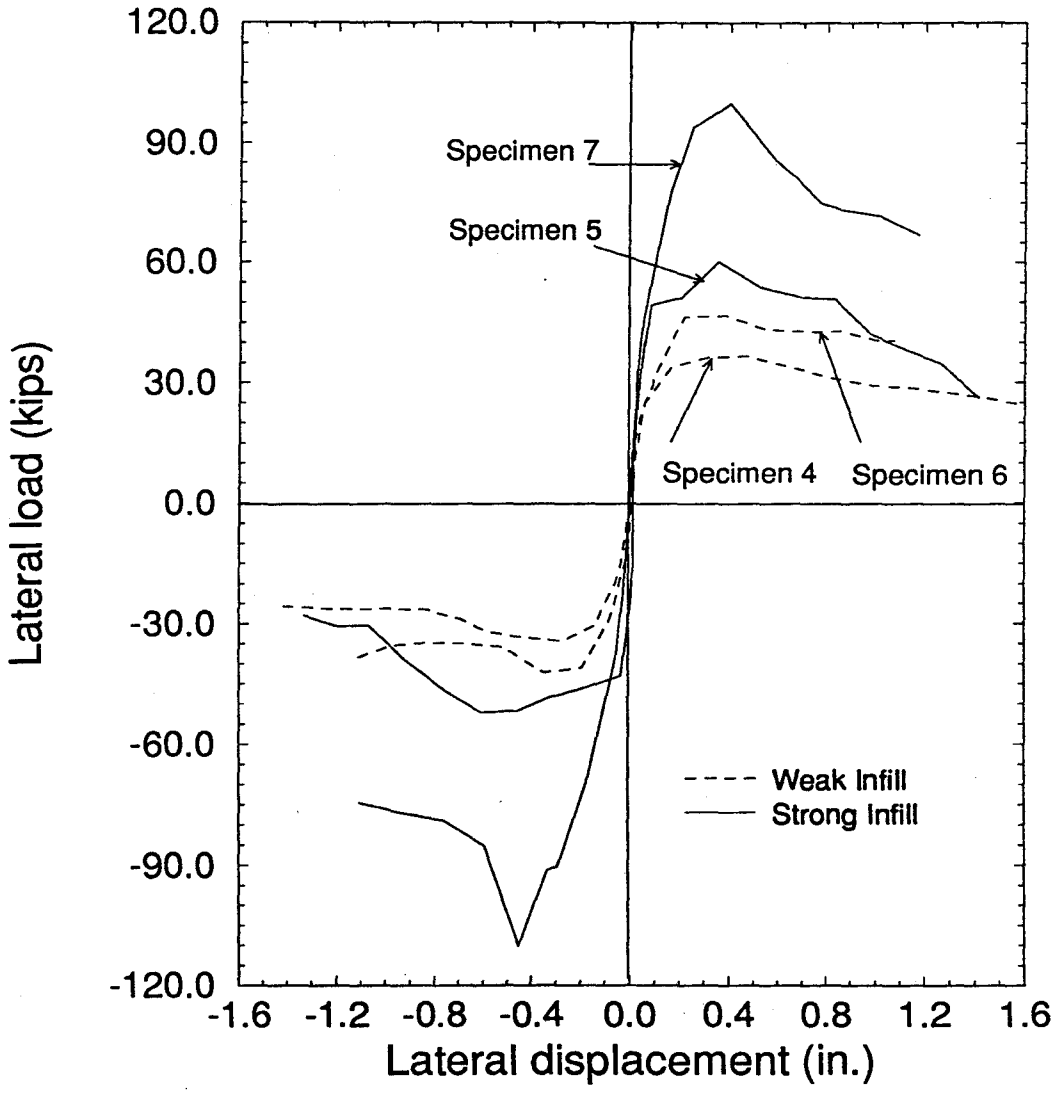

Figure 3.43. Hysteresis Envelopes for Single-Bay Specimens with Aspect Ratio of 0.67.

a weak frame design. The strength of Specimen 7, which had a strong frame and a strong infill, was 83% higher than that of Specimen 5, which had a weak frame and a strong infill; whereas, the strength of Specimen 6, which had a strong frame and a weak infill, was only 28% higher than that of Specimen 4, which had a weak frame and a weak infill. On the other hand, the theoretical load carrying capacities of the weak and strong bare frames are 21.4 and 28.5 kips, respectively. In the case of a weak infill, where the sliding shear was the dominant failure mode, the frame and the panel actions were more or less independent and their strengths were additive. In the case of a strong panel, the lateral resistance was governed by the shear strength of the columns and the diagonal compression mechanism in the infill. In the case of a strong frame, the higher frame stiffness resulted in a more efficient compression strut mechanism and, thereby, a higher resistance.

3.4.3 Influence of Aspect Ratio. The panel aspect ratio has little influence on the lateral strength and stiffness of a specimen. This can be seen by comparing the hysteresis envelope curves of Specimens 10 and 11, which had a h/l ratio of 0.48, with those of Specimens 4 and 5, which had a h/l ratio of 0.67, as shown in Fig. 3.44. The increase in lateral strength due to the decrease of the aspect ratio from 0.67 to 0.48 is only 17% for the specimens with weak panels, and 10% for those with strong panels.

3.4.4 Influence of Vertical Load. Vertical load distribution had only a small influence on the lateral resistance of the specimens as shown by Specimens 3 and 9 in Fig. 3.42. Specimen 9, which had vertical loads applied onto the beam as well as the columns, was about 5% stronger than Specimen 3, which had the same design and had vertical loads applied on

the columns only. The total vertical loads in both cases were the same. The increase in the lateral strength can be attributed to the increase of the panel shear strength resulting from the higher compressive stress in the bed joints. An increase in the total vertical load resulted in a substantial increase in both the lateral strength and stiffness of infilled frames. As shown in Fig. 3.44, Specimen 12, which had the vertical load 50% higher than that of Specimen 11, had its lateral resistance and stiffness 25% and 33% higher than those of Specimen 11.

3.4.5 Influence of Horizontal Load History. The influence of lateral load history can be observed from the comparison of the monotonic load-displacement curves of Specimens 8 and 9 with the hysteresis envelopes of Specimens 4 and 5 in Fig. 3.45. All these specimens had weak frames. Specimens 8 and 4 were infilled with hollow blocks, while Specimens 9 and 5 were infilled with solid blocks. The monotonically loaded specimens, Specimens 8 and 9, had lateral resistances 17% and 10% higher than those of Specimens 4 and 5, which were loaded cyclically. Cyclic loads induced a lower resistance and a faster degradation of the post-peak resistance. The latter was more evident for the case of strong infills.

3.4.6 Influence of Two Adjacent Infilled Bays. In Fig. 3.46, the hysteresis envelopes of Specimens 13 and 14, which had two infilled bays, are compared to those of Specimens 4 and 5, which were single-bay specimens. Specimens 13 and 4 had the same frame design and weak infill panels, while Specimens 14 and 5 had strong infill panels. It can be observed from Fig. 3.46 that for the case of weak panels, the two-bay frame had a resistance 85% higher than that of the single-bay frame. In the case of strong panels, the

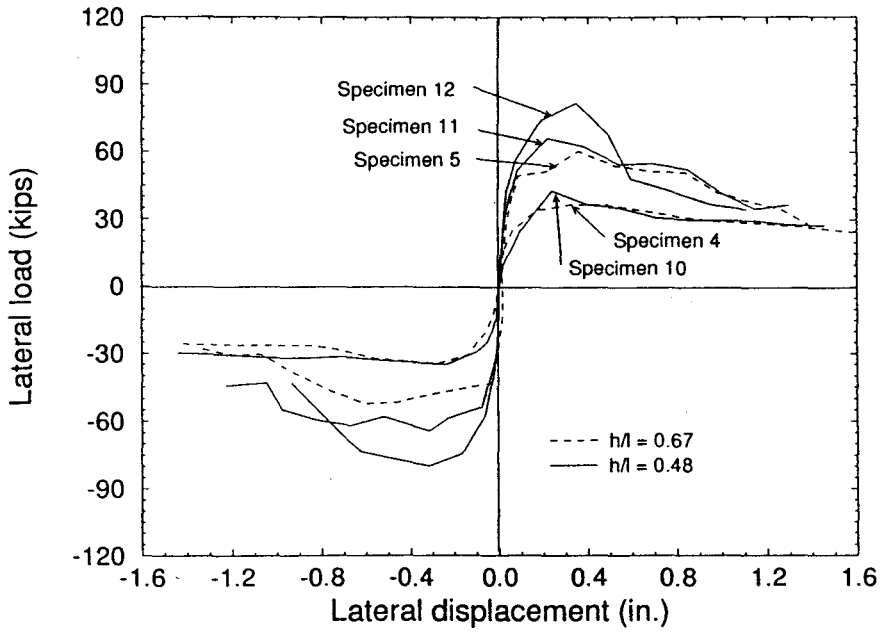

Figure 3.44. Hysteresis Envelopes for Weak Frames with Different Aspect Ratios.

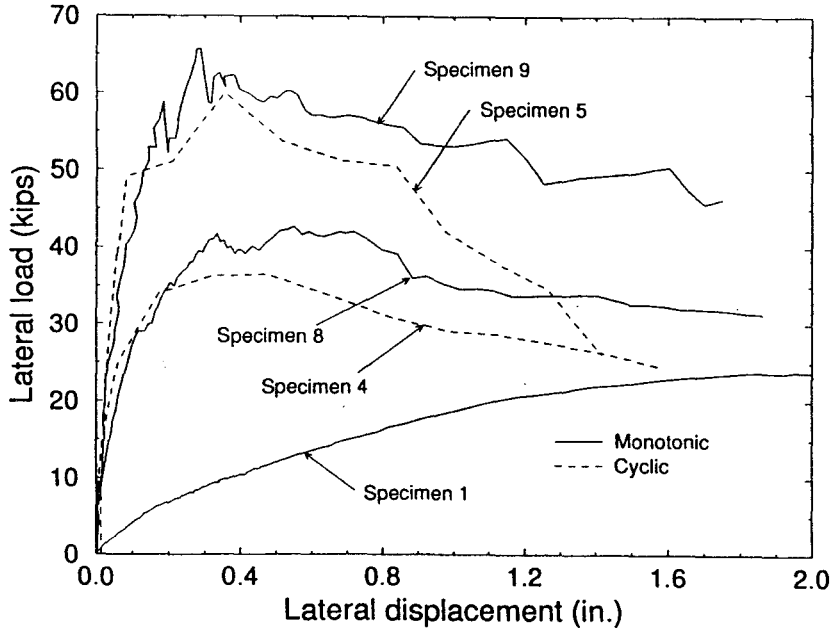

Figure 3.45. Comparison of Monotonically and Cyclically Loaded Specimens.

two-bay frame was 68% stronger than the single-bay frame. The small increase of lateral resistance in the latter case could be due to the fact that the peak resistance of each bay of the two-bay frame did not occur at the same moment. By comparing the lateral resistances of Specimens 11, 12, and 14 (see Table 3.5), it can be observed that both the total vertical load and the number of infilled bays have an influence on the lateral resistance.

3.5 Drift Limits

In design, drift limits can be used to control the extent of structural and non-structural damage in a building. Hence, the drift corresponding to the onset of a major damage in the test specimens is summarized in Table 3.6. As can be observed from the table, for all the specimens tested, the first major crack in an infill occurred at a drift between 0.17 and 0.46%. This is usually the first significant damage in the specimens and corresponds more or less to the elastic limit of a specimen. Therefore, it can be regarded as the serviceability limit for this type of structures. Specimens with strong frames or panels demonstrated a comparatively high serviceability limit. The drift at which the lateral resistance was reduced to 80% of the maximum resistance ranges from 0.8 to 2%. This can be considered as the ultimate limit state. The ratio of the drift at the ultimate limit state to that at the serviceability limit state can be regarded as a ductility measure. For the specimens tested, this ductility measure ranges from 2.3 to 11. Specimens with strong frames or panels had a lower ductility than those with weak frames or panels because of the relatively large drift at the serviceability limit state of the former. The two-bay specimens were less ductile than the one-bay specimens which had similar design details. Furthermore, Specimen 12, which had a higher vertical

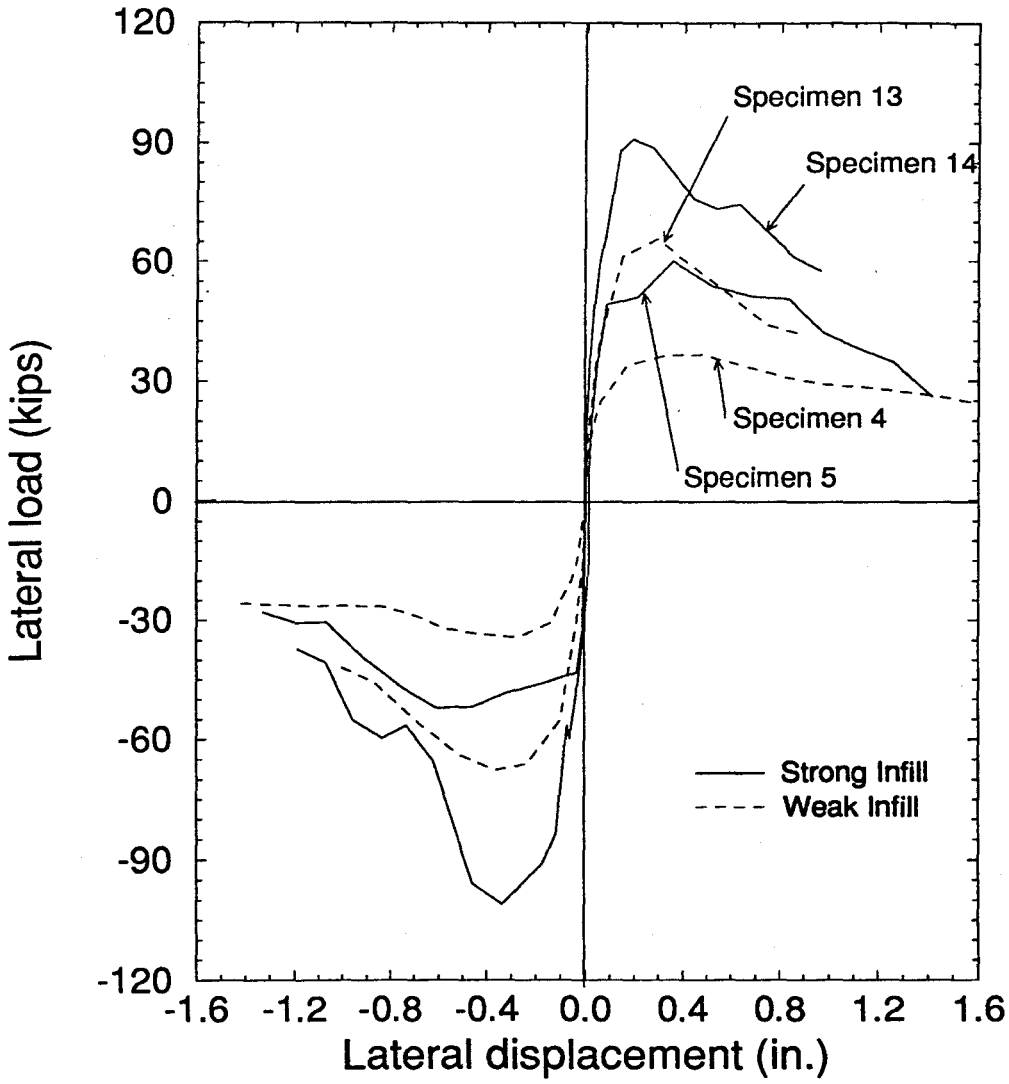

Figure 3.46. Comparison of Hysteresis Envelopes for Single-Bay and Two-Bay Specimens.

Table 3.6. Drift Limits.

Spec. No.	Drift at (Percentage of Story Height)											
	I	II	III	IV	V	VI	VII	VIII	IX	X	XI	XII
1	N	3.1	6.8	N	1.32	N	N	N	0.96	1.29	3.1	4.9
2	--	--	--	N	--	--	N	N	1.19	2.98	--	3.7
3	0.21	0.21	1.16	0.71	N	N	N	N	N	--	--	3.2
4	0.17	0.63	1.45	1.82	1.40	0.99	1.24	N	--	N	2.23	2.6
5	0.33	0.79	1.42	1.32	2.07	1.32	1.40	N	1.54	N	1.90	2.3
6	0.36	0.61	1.78	N	1.73	0.40	0.91	N	N	0.56	N	1.8
7	0.46	0.71	1.04	1.82	1.65	0.46	1.16	0.82	1.42	N	N	1.9
8	0.20	0.91	1.82	1.98	N	1.49	1.59	1.98	--	--	2.48	3.1
9	0.33	0.48	1.98	0.66	N	0.82	2.07	N	--	--	2.81	2.9
10	0.17	0.40	1.88	N	N	0.41	1.40	0.91	1.65	--	2.31	2.4
11	0.36	0.74	1.50	1.32	N	0.91	0.91	N	1.15	N	2.15	2.1
12	0.17	0.55	1.02	0.95	N	0.66	0.66	N	--	--	1.65	1.7
13	0.17	0.55	1.06	N	N	1.00	0.74	1.00	N	N	N	1.7
14	0.31	0.44	0.84	0.76	N	1.80	0.83	0.76	0.76	N	N	1.9

N = Not happened, not major, or not applicable

-- = No data

I. First major crack in infill: diagonal or diagonal/sliding.
II. Maximum lateral load.
III. Reduction to 80% of maximum lateral load.
IV. Major shear crack in column.
V. Shear crack in beam-column joint.
VI. Sliding of mortar joints.
VII. Interior crushing of infill.
VIII. Corner crushing of infill.
IX. Yielding of reinforcement in column.
X. Yielding of reinforcement in beam.
XI. Crushing of concrete in columns.
XII. Maximum lateral displacement imposed on specimen.

load, exhibited a higher ductility than Specimen 11. The drift level at which a severe shear crack developed in a column ranges from 0.7 to 2%. In general, shear cracks occurred earlier in specimens with strong panels than those with weak panels. The crushing of concrete in the columns occurred at drift levels ranging from 1.7 to 2.8%. The lower bound corresponds to Specimen 12, which had a relatively high axial load.

3.6 Conclusions

The test results have demonstrated that infill panels can significantly enhance the load resistance capabilities of R/C frames. Strong panels provide a better energy-dissipation capability and are more effective in enhancing the load resistance of a frame than weak panels. This improvement is more significant for strong frames than for weak frames.

Generally, three different failure modes have been observed from masonry-infilled R/C frames. In the case of a weak panel, slip along the bed joints and plastic hinges in the frame governed. In the case of a weak frame infilled with a strong panel, the interaction between the infill and the frame resulted in a brittle shear failure of the columns. However, in spite of the shear failure, an infilled frame can sustain a lateral load that is much higher than that of a bare frame up to a drift level of 2%. Furthermore, the results of this study indicate that the shear failure of the columns can be prevented if they are provided with adequate shear reinforcement. In the case of a strong frame and a strong panel, the lateral strength was governed by the crushing of the infill.

Specimens subjected to cyclic loads showed a lower resistance and a faster strength degradation than those subjected to monotonic loads. Increasing the total vertical load resulted in a higher resistance, but the influence of

the distribution of the vertical load between the columns and the beam was insignificant. The panel aspect ratio (h/l) in the range of 0.48 to 0.67 had only a small effect on the lateral stiffness and resistance. Finally it has been observed that the two-bay infilled frames were about 1.7 to 1.85 times stronger than a similar one-bay infilled frame.

CHAPTER 4

SEISMIC PERFORMANCE OF PROTOTYPE STRUCTURE

4.1 Introduction

It has been always a challenging problem as to how the information required for the seismic analysis of structures can be derived from the experimental results of small-scale substructures. To this end, a simple and rational analytical method is proposed in this study. For this method, the experimental results presented in Chapter 3 are analyzed to assess the load resistance properties of the test specimens. Results of this analysis are extrapolated to obtain the ductility and yield resistance of the three-bay, six-story, prototype frame based on an approximate modal analysis. The natural period of the prototype frame is computed with the eigenvalue analysis. Based on the period, ductility, and yield resistance of the prototype frame, with and without infill, response spectrum analyses are conducted to compute the seismic resistances of the prototype frame at different limit states. In the analyses, the El Centro and Pacoima Dam ground motion records, and short- and long-duration acceleration pulses are used as input excitations.

4.2 Load Resistance Properties of Test Specimens

The experimental results from the test specimens have been discussed in Chapter 3. These results are analyzed here to quantify the yield resistance, ductility, and energy-dissipation capability of the specimens.

4.2.1 Ductility and Yield Resistance. The ductility and yield resistance, along with the natural period, are the necessary information for a seismic response analysis. For elastic-perfectly plastic systems, ductility is often defined as the ratio of the maximum allowable displacement to the displacement at which the first yield occurs. For infilled frames, the first noticeable nonlinearity occurs with the separation at the infill-to-frame interfaces. This introduces a small reduction of the lateral stiffness. After that, the initiation of major cracks in the infill or the compressive crushing of the infill induces a major inelastic behavior. This point can be considered as the first yield. In this study, the ultimate limit state of an infilled frame is taken as the displacement at which the maximum resistance is developed, or the displacement at which the lateral resistance is reduced to 80% of the maximum lateral resistance. The latter is the displacement at which the degradation of the structural resistance begins to accelerate in most of the infilled frame specimens. To define the ductility in a more consistent manner, an infilled frame is idealized by an equivalent elastic-perfectly plastic system, as shown in Fig. 4.1. Based on this, the ductility can be defined as

$$\mu_{rm} = \frac{\Delta_{rm}}{\Delta_y} \tag{4.1}$$

or

$$\mu_{80} = \frac{\Delta_{80}}{\Delta_y} \tag{4.2}$$

in which Δ_{rm} is the displacement at the maximum lateral resistance, Δ_{80} is the displacement at which the lateral resistance is reduced to 80% of the maximum resistance, and Δ_y is the yield displacement of the equivalent elastic-perfectly

plastic system as shown in Fig. 4.1. In this study, the yield resistance, r_y, of the equivalent system is selected to be 80% of the ultimate resistance in both cases. This results in a conservative approximation. In the case of fully reversed cyclic loading, the yield resistance is evaluated as the average of the yield resistances in the two loading directions. For a monotonically loaded specimen, the elastic stiffness, k, of the equivalent system is approximated by the secant stiffness between the origin and 50% of the maximum resistance in the ascending branch of the load-displacement curve, as shown in Fig. 4.1. For the case of cyclic loading, the elastic stiffness is approximated by the slope of the line connecting the extreme points of a small amplitude displacement cycle in which the peak load is about 50% of the maximum lateral resistance.

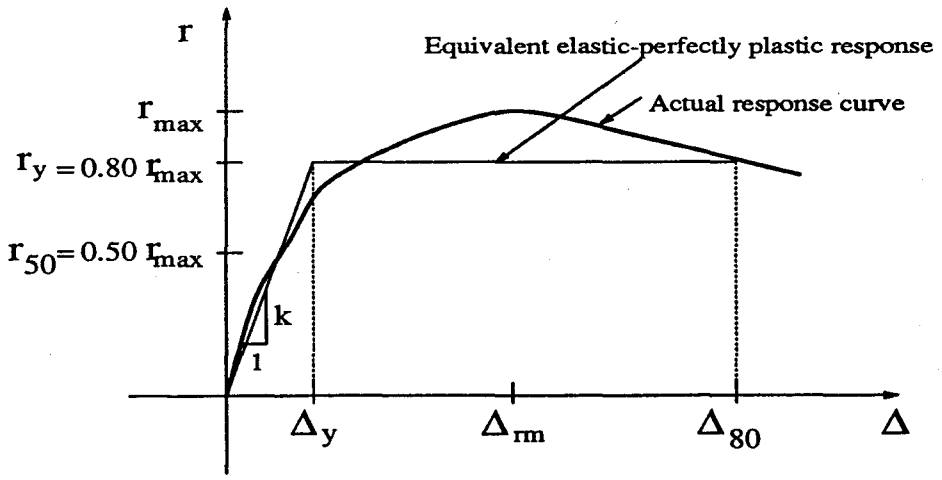

Figure 4.1. Idealized Response Curve for a Single-Degree-of-Freedom System.

For the bare frame, the assumption of an elastic-perfectly plastic behavior is very close to the response curve obtained from the test. Unlike infilled frames, the bare frame did not exhibit a significant load degradation after the

maximum lateral resistance had been reached. As can be seen from the load-displacement curve of the bare frame specimen in Fig. 3.14, to attain an 80% reduction of the lateral strength, a displacement far beyond an acceptable drift level is required. As a result, the maximum allowable drift for the bare frame is taken to be 2%, which is intended to prevent significant structural and non-structural damage. On the other hand, for the infilled specimens, the drift levels corresponding to the maximum allowable displacements defined previously are lower than 2% in all cases, as shown in Table 4.1. Based on the 2% drift limit, the maximum allowable displacement for the bare frame specimen is 1.2 in. The yield displacement, Δ_y, of the bare frame is 0.8 in., which is computed by dividing the yield resistance by the elastic stiffness. With these allowable and yield displacements, a ductility of 1.5 is obtained for the bare frame. The yield and maximum allowable displacements of all the specimens as well as the resulting ductilities are summarized in Table 4.1. The results show that the ductility of infilled frames is higher than that of the bare frame. This is due to the higher elastic stiffness and, consequently, the lower yield displacement of an infilled frame, when compared to those of the bare frame. In most cases, the single-bay specimens that had strong panels are more ductile than those with weak panels. On the other hand, the two-bay specimen that had strong panels was slightly less ductile than the one with weak panels. At the ultimate limit state corresponding to 80% of the maximum resistance, two-bay specimens were considerably less ductile than one-bay specimens.

4.2.2 Energy-Dissipation Capability. For the case of cyclic loadings, the cumulative energy dissipation for a specific damage state is defined as

Table 4.1. Load Resistance Properties of Test Specimens.

Test No.	Maximum Resistance r_{max} (Kips)	Equivalent Elastic-Plastic System			At Maximum Resistance			At 80% of Maximum Resistance		
		Yield Resistance $r_y = 0.8r_{max}$ (Kips)	Stiffness k ** (Kips/in.)	Yield Displacement Δ_y (in.)	Displacement Δ_{rm} (in.)	Ductility μ_{rm}	Energy Dissipated U (Kip-in)	Displacement Δ_{80} (in.)	Ductility μ_{80}	Energy Dissipated U (Kip-in)
1	23.9	19.1	24	0.800	---	---	---	1.20 +	1.5 +	12 +
2	---	---	---	---	---	---	---	---	---	---
3	62.4	49.9	740	0.068	0.13	1.5	3	0.70	10.3	35
4	35.5 *	28.4	430	0.066	0.37	4.5	63	0.88	13.3	169
5	56.1 *	44.9	1280	0.035	0.48	10.9	88	0.86	24.6	290
6	44.5 *	35.6	480	0.074	0.36	3.9	46	1.08	14.6	253
7	105.0 *	84.0	1460	0.058	0.42	7.2	241	0.63	10.9	420
8	42.7	34.2	330	0.103	0.55	4.3	16	1.10	10.7	39
9	65.8	52.6	590	0.089	0.29	2.6	9	1.20	13.5	63
10	38.9 *	31.1	395	0.079	0.24	2.4	22	1.14	14.4	289
11	65.0 *	52.0	1470	0.035	0.27	6.1	57	0.91	26.0	398
12	80.7 *	64.6	1950	0.033	0.30	7.3	93	0.62	18.8	198
13	66.7 *	53.4	834	0.064	0.33	5.2	70	0.64	10.0	176
14	96.0 *	76.8	1447	0.053	0.26	4.9	140	0.51	9.6	315

* Average of two directions

** Based on the secant stiffness as defined in the text

\+ Based on 2% drift limit

$$U = \sum_{i=1}^{n} U_i \tag{4.3}$$

in which U_i is the energy dissipated in cycle i and n is the number of cycles to arrive at the damage state, which can correspond to the development of the maximum lateral resistance or the state at which the lateral resistance is reduced to 80% of the maximum resistance.

Similarly, for the case of monotonic loadings, U can be defined as the energy dissipated by plastic work at a specific damage state. Based on the idealized response curve shown in Fig. 4.1, this can be expressed as

$$U = r_y(\Delta_a - \Delta_y) \tag{4.4}$$

in which Δ_a is the maximum allowable displacement, which can be defined either as Δ_{rm} or Δ_{80}. The values of U calculated for the different test specimens are shown in Table 4.1. Among the cyclically loaded specimens, those which had a strong panel were stronger and dissipated more energy than those which had a weak panel. The specimens with a smaller aspect ratio dissipated less energy at the maximum resistance and more energy at 80% of the maximum resistance than the specimens with a higher aspect ratio. Increasing the vertical load resulted in a higher energy dissipation at the maximum resistance and a lower energy dissipation at 80% of the maximum resistance. The two-bay infilled specimens dissipated more energy than the one-bay specimens of the same design.

4.3 Prototype Frame

The prototype frame is a three-bay, six-story, R/C frame, representing an internal frame of an office building (see Fig. 3.1). For the case with infill,

this frame is assumed to have an infill panel in the middle bay of every story. As discussed in Chapter 3, the frames have been designed for two types of lateral loadings: a moderate wind load, which results in a weak frame design, and a severe earthquake load, which results in a strong frame design. The test specimens represent the middle bay of the first story of the prototype frame. Under lateral loadings, three types of failure mechanisms can be conceived for the prototype frame, as illustrated in Fig. 4.2. For the strong bare frame, which has a strong-column-weak-beam design, the failure tends to be governed by the plastic hinges at the bottom sections of the columns in the first story and at the end sections of the beams, as shown in Fig. 4.2a. The weak bare frame has a weak-column-strong-beam design. As shown in Fig. 4.2b, the failure of this frame tends to be dominated by the plastic hinges at the end sections of the columns in the first story. For an infilled frame, the failure is expected to initiate with a diagonal/sliding crack in the infill in the first story, which is followed by the failure of the surrounding columns, as shown in Fig. 4.2c. The last two cases (Figs. 4.2b and 4.2c) correspond to the soft-story mechanisms.

4.4 Modal Analysis of Prototype Frame

The prototype frame is idealized as a six-degree-of-freedom system, with each degree of freedom corresponding to the lateral displacement at each story. Modal analysis is conducted on the idealized prototype frame to have its response represented by that of an equivalent single-degree-of-freedom system.

The equations of motion for the idealized multiple-degree-of-freedom system is

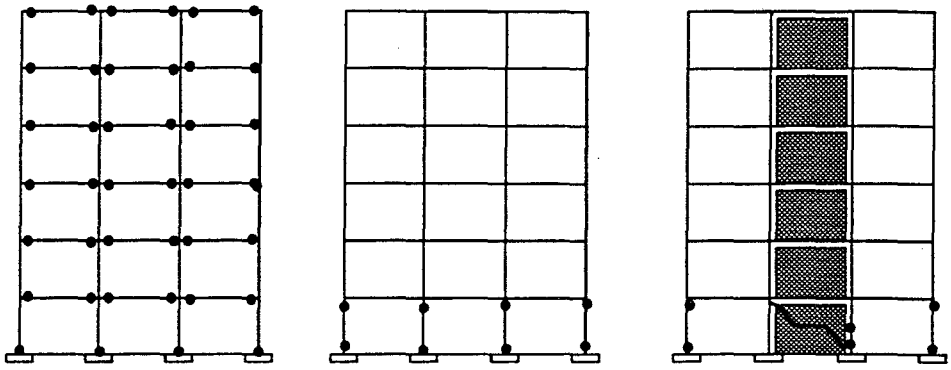

Figure 4.2. Failure Mechanisms of Prototype Frames; a) Strong Bare Frame; b) Weak Bare Frame; c) Infilled Frame.

$$\mathbf{m}\ddot{\mathbf{v}} + \mathbf{r} = -\mathbf{m}\{1\}\ddot{v}_g \tag{4.5}$$

in which $\mathbf{m}$ is the mass matrix, $\mathbf{v}$ is the displacement vector, $\mathbf{r}$ is the restoring force vector, $\{1\}$ is a vector of unity, and $\ddot{v}_g$ is the ground acceleration. The displacement vector in the geometric coordinates, $\mathbf{v}$, can be expressed in terms of the modal displacements as

$$\mathbf{v} = \boldsymbol{\Phi}\mathbf{Y} \tag{4.6}$$

in which $\boldsymbol{\Phi}$ is a matrix that consists of the modal vectors in its columns, and $\mathbf{Y}$ is the displacement vector in the modal coordinates. Combining Eqs. 4.5 and 4.6, and premultiplying Eq. 4.5 by $\boldsymbol{\Phi}^T$, one has

$$\mathbf{M}\ddot{\mathbf{Y}} + \mathbf{R} = -\mathbf{L}\ddot{v}_g \tag{4.7}$$

in which $\mathbf{M} = \boldsymbol{\Phi}^T\mathbf{m}\boldsymbol{\Phi}$ is the modal mass matrix, $\mathbf{L} = \boldsymbol{\Phi}^T\mathbf{m}\{1\}$, and $\mathbf{R} = \boldsymbol{\Phi}^T\mathbf{r}$

is the modal force vector. In this study, the response of the prototype frame is approximated by the fundamental mode of vibrations. With this assumption, Eq. 4.7 becomes

$$M_1\ddot{Y}_1 + R_1 = -L_1\ddot{v}_g \tag{4.8}$$

in which $M_1 = \phi_1^T \mathbf{m}\phi_1$ is the modal mass, $L_1 = \phi_1^T \mathbf{m}\{1\}$, $R_1 = \phi_1^T \mathbf{r}$ is the modal force, and Y_1 is the modal response corresponding to the fundamental mode of the structure. By assuming that each story of the structure has a mass m, one has

$$M_1 = m\phi_1^T\phi_1 = m\sum_{i=1}^{N}\phi_{1i}^2 \tag{4.9}$$

$$L_1 = m\phi_1^T\{1\} = m\sum_{i=1}^{N}\phi_{1i} \tag{4.10}$$

in which N is the number of stories and ϕ_{1i} is the i-th component of the fundamental mode. The effective modal mass, M_e, corresponding to the fundamental mode is defined as

$$M_e = \frac{L_1^2}{M_1} = \frac{m(\phi_1^T\{1\})^2}{\phi_1^T\phi_1} = \frac{m(\sum_{i=1}^{N}\phi_{1i})^2}{\sum_{i=1}^{N}\phi_{1i}^2} \tag{4.11}$$

With the above assumption, one can characterize the response of the prototype frame in terms of the base shear and first-story displacement by carrying out the following operations.

$$< 1 > \mathbf{m}\phi_1\ddot{Y}_1 + < 1 > \mathbf{r}_1 = - < 1 > \mathbf{m}\{1\}\ddot{v}_g \tag{4.12}$$

in which $< 1 >$ is a row vector of unity and r_1 is the restoring force vector due to the fundamental mode of vibrations. By normalizing the fundamental

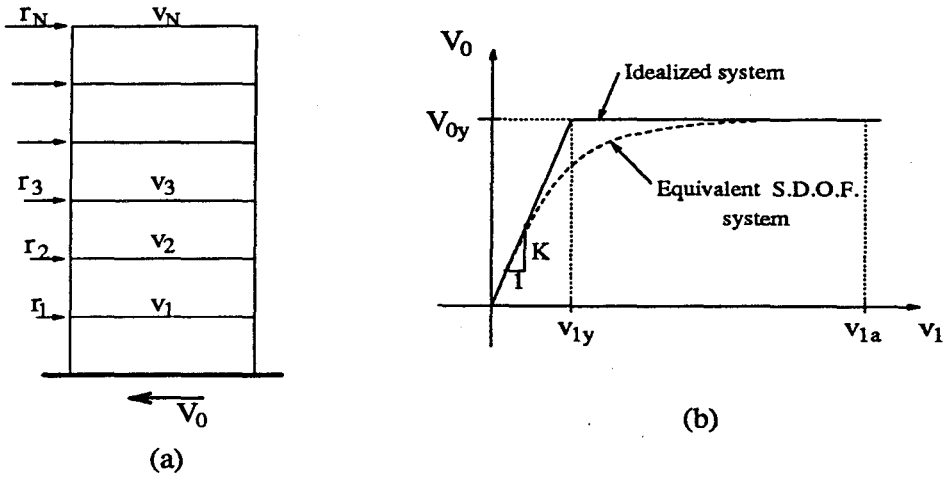

Figure 4.3. Equivalent Single-Degree-of-Freedom System; a) the Structure; b) Response of the Equivalent System.

mode shape so that $\phi_{11} = 1$ and $Y_1 = v_1$, which is the displacement at the first story, Eq. 4.12 becomes

$$L_1\ddot{v}_1 + V_0 = -M_t\ddot{v}_g \tag{4.13}$$

in which $M_t =< 1 > \mathbf{m}\{1\}$ is the total mass of the frame and $V_0 =< 1 > \mathbf{r_1}$ is the base shear. The above equation represents the equation of motion for an equivalent single-degree-of-freedom system.

For a nonlinear structure, one can idealize the response by an elastic-perfectly plastic system, as shown in Fig. 4.3b. In accordance with the idealized response, one has the yield resistance V_{0y} and yield displacement v_{1y}. Furthermore, the maximum allowable displacement of the structure can be denoted as v_{1a}. In the linearly elastic range,

$$V_0 =< 1 > \mathbf{r}_1 =< 1 > \mathbf{k}\phi_1 Y_1 = \omega_1^2 L_1 v_1 \tag{4.14}$$

in which ω_1 is the modal frequency, and L_1 and $K = \omega_1^2 L_1$ are the mass and elastic stiffness of the equivalent system. If one knows the yield resistance V_{0y}, the yield displacement can, therefore, be determined as

$$v_{1y} = \frac{V_{0y}}{\omega_1^2 L_1} \tag{4.15}$$

and the ductility becomes v_{1a}/v_{1y}. In summary, to characterize the equivalent system, one needs to find ϕ_1, ω_1, V_{0y}, and v_{1a}. These can be extracted from the behavior of the scaled models that were tested.

4.5 Seismic Performance Analysis

To study the influence of infill panels on the seismic performance of R/C structures, seismic analyses are carried out with the prototype frame using the response spectrum method. To this end, the properties of the equivalent single-degree-of-freedom systems must be defined. These include the frequency or the period of the fundamental mode, the yield base shear, and the ductility of the system. In the derivation of these properties, the properties of the single-bay test specimens are used. To be consistent with the experimental loadings, two types of input excitations are used. Those frames which have their properties determined from the cyclically loaded specimens are analyzed with earthquake loadings, while the frames with properties determined from the monotonically loaded specimens are analyzed with short- and long-duration pulse accelerations. For a ductile bare frame, the inelastic behavior is not influenced very much by the load history. Therefore, the weak and strong prototype bare frames are also analyzed with the earthquake loadings. For each loading type, three limit states are considered: the elastic limit, the inelastic state at which the maximum lateral resistance is reached, and the post-peak ultimate

limit state at which the lateral resistance drops to 80% of the maximum. However, as mentioned before, for the bare frames, the 2% drift limit is considered as the ultimate limit state.

4.5.1 Properties of Prototype Frame.

Period

Eigenvalue analysis has been conducted with SAP90 program (Habibullah and Wilson 1991) to obtain the eigenvector, ϕ_1, and the corresponding period, T, of the fundamental mode of the prototype frame with different designs. The comparison of experimental and numerical results have shown that the actual stiffness of a R/C frame specimen is much lower than the analytical stiffness that is based on uncracked sections. As a result, an effective moment of inertia, I_e, is used in the analysis. The effective moment of inertia, I_e, is taken as a fraction of the moment of inertia, I_g, of the member gross section, i.e.,

$$I_e = \alpha I_g \tag{4.16}$$

in which the reduction factor, α, has been found such that the stiffness of a single-bay, single-story, 1/2-scale, bare frame obtained from SAP90 matches the experimental stiffness of the specimen. For the weak bare frame, α has been found to be 0.44. This value is used in the eigenvalue analysis for all cases because of the absence of other data.

The complicated interaction of the infill with the surrounding frame cannot be modeled with SAP90. Therefore, an infilled bay is modeled by an equivalent beam that has an effective shear modulus G_e. The value of G_e has been found such that the lateral stiffness of a cantilever beam obtained from

the elastic analysis is equal to the stiffness of the corresponding infilled frame specimen. The bending stiffness EI of this beam has been assumed to be equal to that of the uncracked infilled specimen.

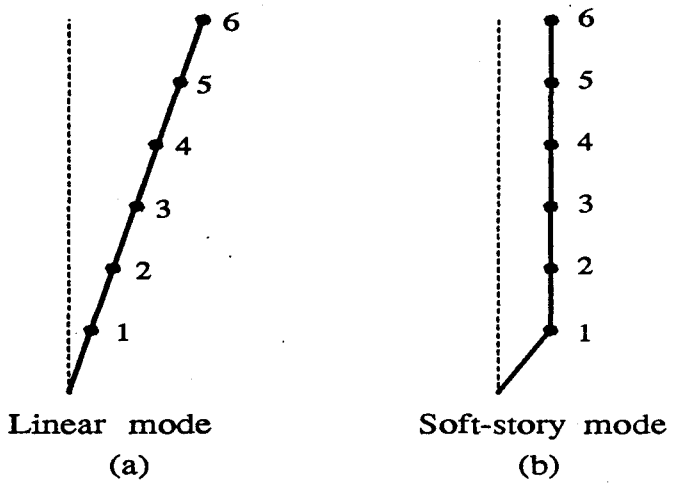

Figure 4.4. Idealized Mode Shapes for Inelastic Response; a) Linear Mode; b) Soft-Story Mode.

Yield Base Shear

The yield base shear, V_{0y}, is governed by the failure mechanism of the prototype frame. With the failure mechanisms assumed in Fig. 4.2, the inelastic response of the strong bare frame is approximated by a linear mode, as shown in Fig. 4.4a, and those of the weak bare frame and infilled frames by a soft-story mode, as shown in Fig. 4.4b.

To obtain the yield base shear of the strong bare frame, a collapse analysis has been conducted using the failure mechanism shown in Fig. 4.2a. The distribution of the lateral forces along the height of the frame is assumed to be linearly proportional to the height. For the collapse analysis, the plastic moments of the frame members have been calculated theoretically in accordance with the ACI provisions (1989), and they have been increased by 15%

to account for the discrepancy between the actual and theoretical strengths, as reflected by the test results from Specimen 1. The sum of the lateral forces corresponding to the collapse of the frame is defined as the ultimate base shear, V_{0u}, 80% of which is considered as the yield base shear, V_{0y}, to be consistent with the yield resistance defined previously (Sec. 4.2).

In the case of the weak bare frame and infilled frames, where the failure is concentrated in the first story, the yield base shear, V_{0y}, is approximately equal to the yield resistance of the first story. For the weak bare frame, based on the failure mechanism shown in Fig. 4.2b, the yield resistance of the first story can be calculated with the plastic moment capacity of the columns. However, in this study, it is taken to be twice the yield resistance of the middle bay, by assuming that the interior and exterior columns have the identical design. The yield resistance of the middle bay of the prototype frame is calculated by applying the similitude rules to the yield resistance of Specimen 1 (see Table 4.1). To obtain the yield resistance of the first story of the infilled frames, the lateral forces resisted by the bending of the exterior columns at the first story can be added to the yield resistance of the middle bay. The yield resistance of the middle bay of the prototype frame is obtained by applying the similitude rules to the yield resistance of the corresponding test specimen. In this study, the scaling factor is 2. Hence, the resistances of the specimens are multiplied by 4 to obtain those of the prototype. Furthermore, it must be pointed out that in the case of the infilled frames, the exterior columns are much more flexible than the middle bay of the frame. The yielding of these columns may occur way after the peak resistance has been reached by the middle bay. Hence, to be conservative, the resistances of the exterior columns are calculated at the

yield displacement of the middle bay for all the three limit states.

Ductility

The ductility of the equivalent single-degree-of-freedom system has been defined as the ratio of the allowable displacement, v_{1a}, to the yield displacement, v_{1y}. For the weak and strong bare frames, v_{1a} is calculated based on the 2% drift limit as discussed before. In the infilled frame, the allowable displacement of the first story is approximated by that of the middle bay. This is obtained from the experimental results of the infilled frame specimens (see Table 4.1) by applying the similitude rules.

4.5.2 Earthquake Excitations. The elastic and ductility response spectra of the NS component of the 1940 El Centro record and the derived 1971 Pacoima Dam record are used in the analyses. They have peak ground accelerations, $\tilde{v}_{gmax}$, of 0.35g and 0.4g, respectively. A damping ratio of 5% of the critical is considered for all cases. The structures are evaluated based on the maximum ground acceleration that can be sustained without exceeding the prescribed limit state.

Elastic Range

The maximum allowable peak ground acceleration, $\tilde{v}_{ga}$, which can be resisted by the prototype frame at the elastic limit is obtained from the elastic response spectra shown in Fig. 4.5. Based on Eq. 4.14, one has the following expression for the maximum base shear.

$$V_{0,max} = L_1 \omega_1^2 v_{1,max} \tag{4.17}$$

where, based on Eq. 4.13,

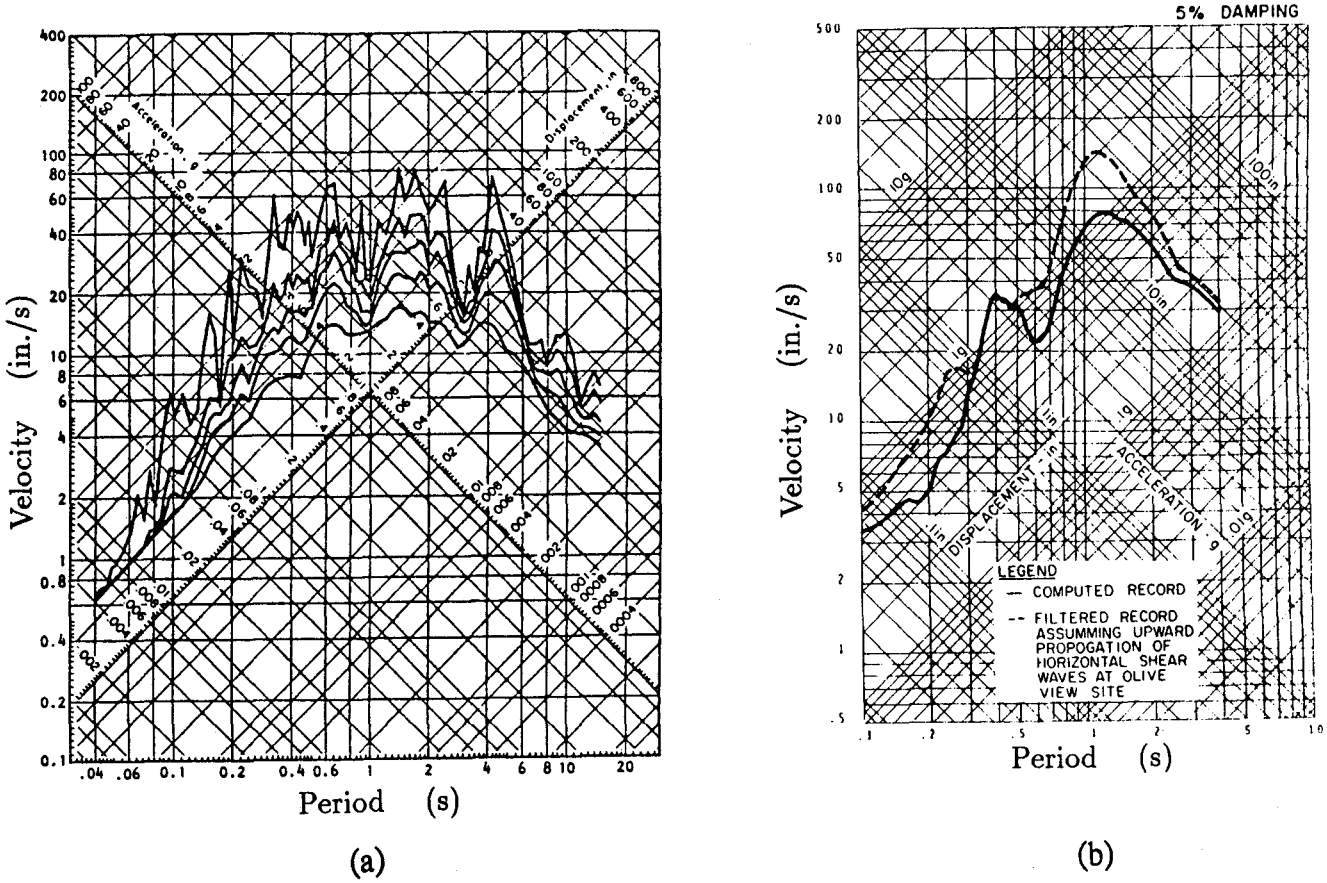

Figure 4.5. Elastic Response Spectra; a) El Centro (Housner and Jennings 1982); b) Pacoima Dam (Mahin et al. 1976).

$$v_{1,max} = \frac{M_t}{L_1} S_d \tag{4.18}$$

in which S_d is the spectral displacement. Combining Eqs. 4.17 and 4.18, one has

$$V_{0,max} = \omega_1^2 M_t S_d = M_t P S_a \tag{4.19}$$

in which $PS_a = \omega_1^2 S_d$ is the pseudo-spectral acceleration.

For the prototype frame, one can obtain the maximum allowable peak ground acceleration, $\ddot{v}_{ga}$, as

$$\ddot{v}_{ga} = \frac{V_{0y}}{V_{0,max}} \ddot{v}_{gmax} \tag{4.20}$$

Substituting Eq. 4.19 in Eq. 4.20 results in the following relation for $\ddot{v}_{ga}$.

$$\ddot{v}_{ga} = \frac{V_{0y}}{M_t P S_a} \ddot{v}_{gmax} \tag{4.21}$$

Inelastic Range

In the inelastic range, seismic analyses are conducted using the ductility spectra shown in Fig. 4.6. The development of these spectra has been discussed by Bertero et al. (1978) and is only briefly summarized here. With damping, the equation of motion for the equivalent single-degree-of-freedom system is given by

$$L_1 \ddot{v}_1 + 2L_1 \omega_1 \xi \dot{v}_1 + V_0 = -M_t \ddot{v}_g \tag{4.22}$$

in which ξ is the damping ratio. By introducing the dimensionless variables $\gamma = \frac{v_1}{v_{1y}}$ and $\rho = \frac{V_0}{V_{0y}}$ and using Eq. 4.15, one can rewrite the above equation in the non-dimensional form:

$$\ddot{\gamma} + 2\omega_1 \xi \dot{\gamma} + \omega_1^2 \rho = -\frac{\omega_1^2}{\eta} \frac{\ddot{v}_g}{\ddot{v}_{gmax}} \tag{4.23}$$

in which the resistance factor, η, is defined as

$$\eta = \frac{V_{0y}}{\ddot{v}_{gmax} M_t} \tag{4.24}$$

Based on the above equation, Bertero et al. (1978) have computed the ductility demand, γ_{max}, for structures of different frequencies and resistance factors, η, using the El Centro and Pacoima Dam records. With these spectra, one can obtain η for a given elastic period and ductility, and calculate the maximum allowable ground acceleration with Eq. 4.24.

4.5.3 Short-Duration Pulse Excitation. A short-duration pulse is a relatively high acceleration which is applied in a very short period of time when compared to the natural period of a structure, as shown in Fig. 4.7. The allowable impulse that an elastic-perfectly plasticly plastic single-degree-of-freedom system can resist can be calculated, based on the conservation of energy principle, as

$$I = \frac{V_{0y}}{\omega_1} \sqrt{(2\mu - 1)} \tag{4.25}$$

in which $I = M_t \int_0^{t_d} \ddot{v}_g dt$ is the impulse and μ is the displacement ductility of the system.

4.5.4 Long-Duration Pulse Excitation. A long-duration pulse is a ground acceleration applied for a relatively long duration, as shown in Fig. 4.8. It is assumed that the duration of the pulse, t_d, is much larger than the natural period of the structure, T, and the amplitude is more or less constant.

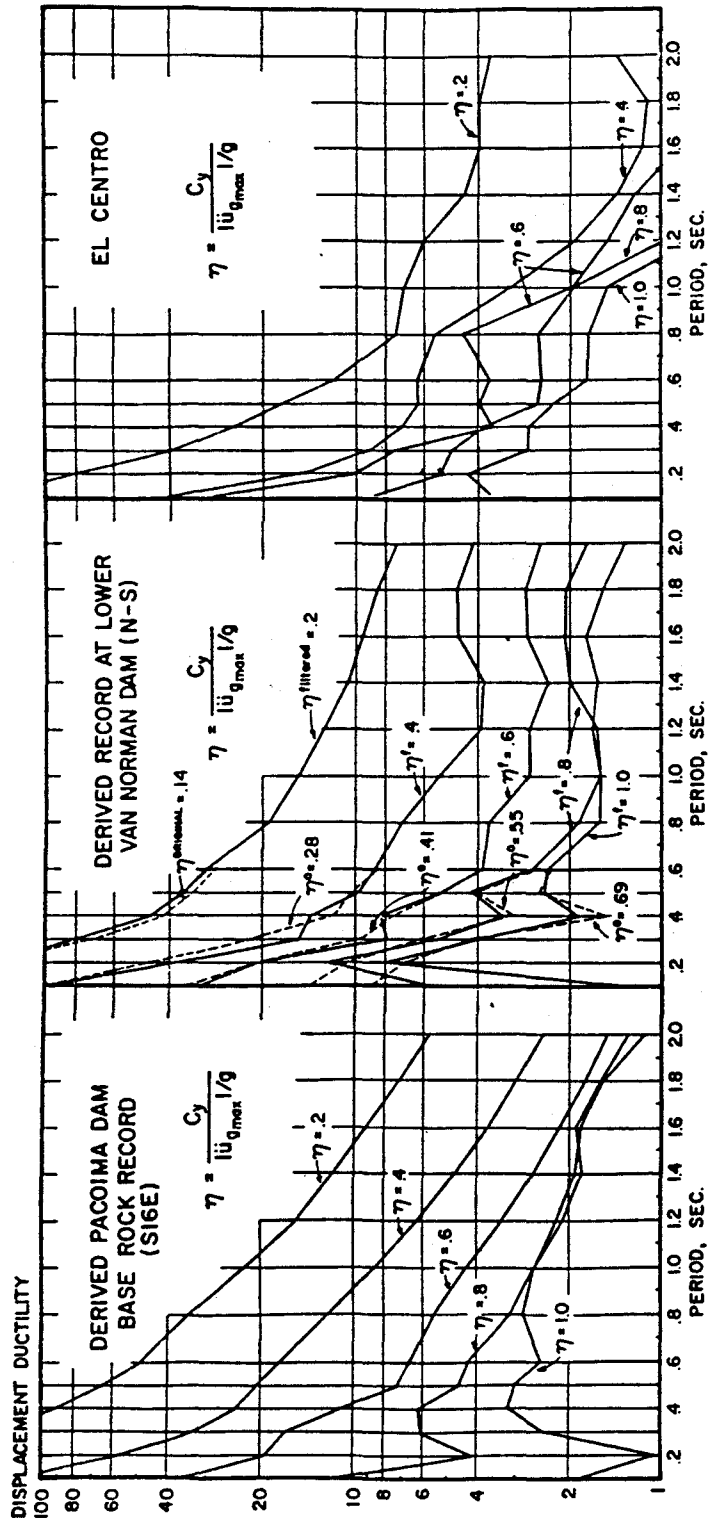

Figure 4.6. Ductility Spectra for 5% Damping (Bertero et al. 1978).

The maximum allowable pulse acceleration, $\ddot{v}_{ga}$, that an elastic-perfectly plastic single-degree-of-freedom system can resist can be calculated, based on the conservation of energy principle, as

$$\ddot{v}_{ga} = \frac{V_{0y}}{M_t}(1 - \frac{1}{2\mu}) \tag{4.26}$$

4.6 Comparison of Results

With the period, yield base shear, and ductility calculated with the methods presented in the previous sections, the performance of the prototype frame has been analyzed under the aforementioned dynamic loadings with different design conditions. The results are presented in Tables 4.2 and 4.3. The maximum allowable ground accelerations that the prototype frame can resist at different limit states are summarized in Table 4.2. In this table, v_{rm} and v_{80} are the lateral displacements at the level of the first story corresponding to the maximum resistance and 80% of the maximum resistance, respectively. These results are also shown in Fig. 4.9 for the El Centro ground motion and in Fig. 4.10 for the Pacoima Dam record. The mass of the infill panels is also included in the analyses. However, the influence of the additional mass on the results is insignificant. The comparison of the results shows that, in the elastic range, the addition of the infill has reduced the maximum allowable ground acceleration that can be resisted by the frame in most of the cases. On the other hand, increasing the vertical load has increased the maximum allowable ground acceleration for the elastic limit state.

At the limit state corresponding to the maximum resistance, only the strong infill has improved the performance of the frame. At the ultimate limit state corresponding to 80% of the maximum resistance, the addition of an infill

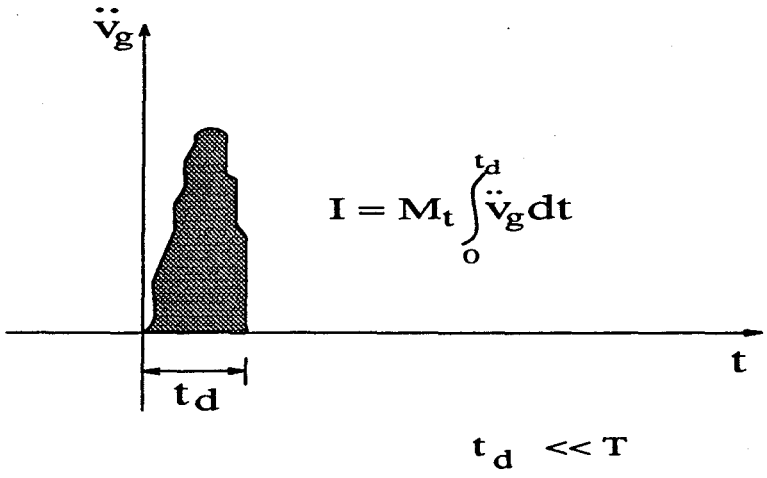

Figure 4.7. Short-Duration Pulse.

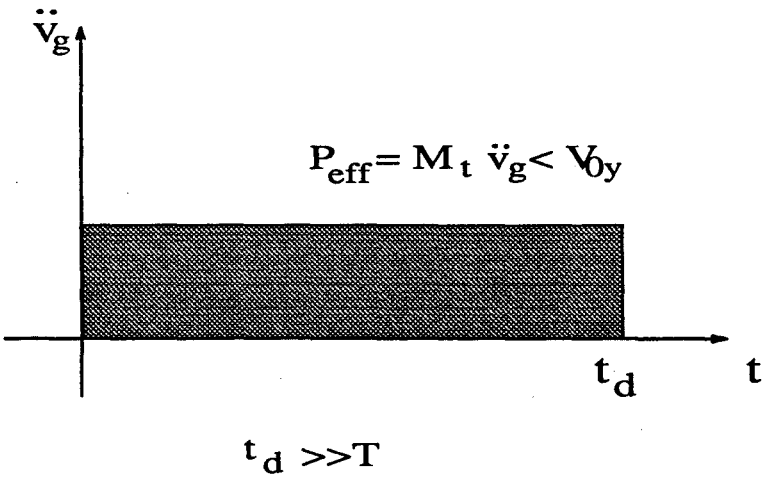

Figure 4.8. Long-Duration Pulse.

Table 4.2. Allowable Peak Ground Accelerations Resisted by Prototype Frame.

Specimen					Equivalent SDOF System for Prototype Frame													
Test No.	Frame	Aspect Ratio	Vert. Load (Kips)	Infill	Period T (sec)	K (Kips/in.)	V_{0y} (Kips)	V_{1y} (in.)	At Max. Resistance		At 80% of Resistance		Max. Allowable Peak Ground Acceleration (g)					
									V_{rm} (in.)	μ_{rm}	V_{80} (in.)	μ_{80}	$V_{1a}=V_{1y}$		$V_{1a}=V_{rm}$		$V_{1a}=V_{80}$	
													Pacoima Dam	El Centro	Pacoima Dam	El Centro	Pacoima Dam	El Centro
1	weak	0.67	66	no	1.50	98	154	1.57	--	--	2.4	1.5	0.2	0.5	--	--	0.25*	0.8*
4			66	weak	0.54	774	123	0.16	0.74	4.6	1.76	11.0	0.15	0.1	0.30	0.45	0.45	0.85
5			66	strong	0.41	1812	189	0.10	0.96	9.6	1.72	17.2	0.15	0.2	0.55	0.95	0.65	1.30
--	strong	0.67	66	no	1.32	125	190	1.52	--	--	2.4	1.6	0.2	0.65	--	--	0.30*	0.90*
6			66	weak	0.49	899	155	0.17	0.72	4.3	2.16	12.7	0.15	0.15	0.35	0.55	0.60	1.05
7			66	strong	0.37	2225	349	0.15	0.82	5.6	1.26	8.4	0.2	0.35	0.75	1.05	0.90	1.65
10	weak	0.48	66	weak	0.50	752	134	0.18	0.48	2.7	2.28	12.7	0.15	0.1	0.25	0.35	0.50	1.0
11			66	strong	0.33	2320	218	0.09	0.54	6.0	1.82	20.1	0.2	0.2	0.45	0.65	0.75	1.4
12			99	strong	0.33	2320	268	0.11	0.6	5.4	1.24	11.3	0.25	0.25	0.55	0.75	0.75	1.35

* Based on 2% drift limit

Table 4.3. Maximum Pulse Levels Resisted by Prototype Frame.

Specimen			Equivalent SDOF System for Prototype Frame							
Test No.	Frame	Infill Panel	Modal Quantities		Level of Maximum Ground Motion					
					$V_{1a} = V_{1y}$		$V_{1a} = V_{rm}$		$V_{1a} = V_{80}$	
			V_{1y} (in.)	Mass M_t (Kip-sec^2/in.)	I* (Kip-sec)	$(\ddot{v}_{ga}/g)$**	I* (Kip-sec)	$(\ddot{v}_{ga}/g)$**	I* (Kip-sec)	$(\ddot{v}_{ga}/g)$**
1	weak	none	1.42	1.36	13.7	0.15	--	--	26.7+	0.2+
3	weak	strong	0.08	1.46	5.1	0.19	11.3	0.33	28.0	0.37
8	weak	weak	0.16	1.40	5.7	0.14	20.4	0.25	29.5	0.26
9	weak	strong	0.09	1.46	5.3	0.20	18.6	0.36	38.8	0.39

* Short-Duration Pulse, $I = M_t \int_0^{t_d} \ddot{v}_g(t)\, dt$

**Long-Duration Pulse

+ Based on 2% drift limit

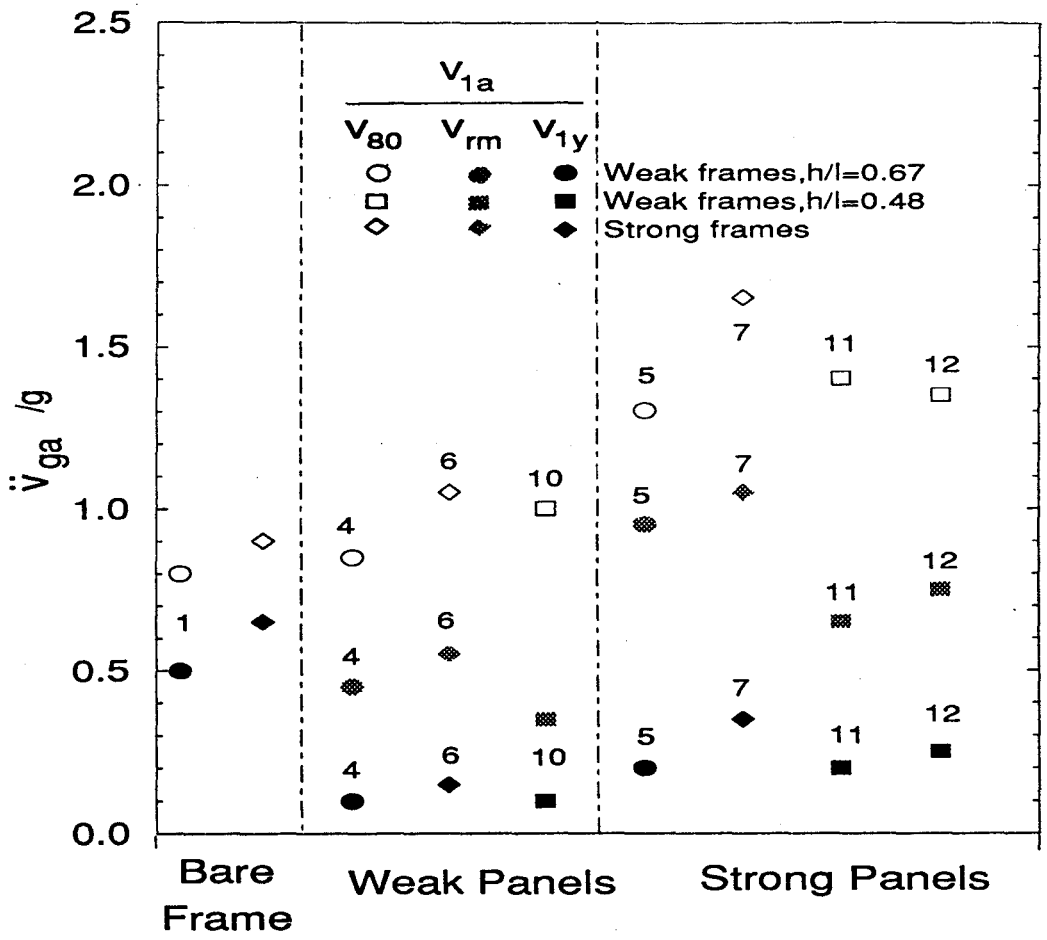

Figure 4.9. Allowable Peak Ground Accelerations for Prototype Frame with El Centro Record.

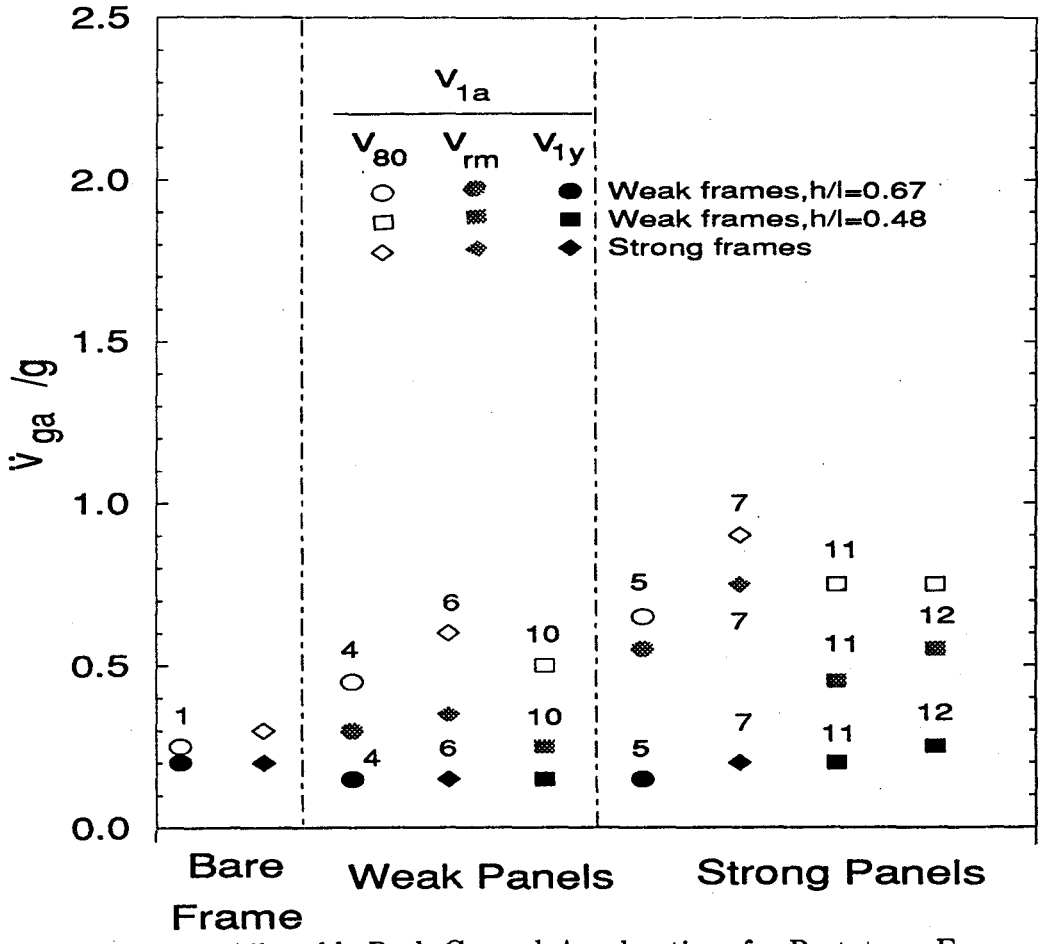

Figure 4.10. Allowable Peak Ground Accelerations for Prototype Frame with Pacoima Dam Record.

has improved the performance of the frame in all cases. For this limit state, the stronger the frame or the infill is, the higher is the seismic resistance.

The prototype frame, whose properties have been derived based on the monotonically loaded specimens, has been analyzed under short- and long-duration pulses. The results, presented in Table 4.3, show that with the limit states based on the elastic limit and the maximum resistance, the bare frame can resist a bigger impulse than the infilled frames. At the ultimate limit state corresponding to 80% of the maximum resistance, infilled frames can resist a stronger impulse than a bare frame. For the case of a long-duration pulse, the results indicate that the infilled frames perform considerably better than the bare frame. Furthermore, it is observed that the strength of an infill panel has a significant influence on the seismic resistance.

The seismic analyses have been conducted with the assumption that only the middle bay of the prototype frame is infilled. However, if the frame is infilled in two adjacent bays in every story, the test results from the two-bay specimens can be used. As shown in Table 4.1, the difference between the stiffnesses of the one-bay and two-bay specimens of identical design is not large enough to create a big difference in the fundamental period of the prototype frame. On the other hand, the yield resistances of the two-bay specimens are much higher than those of the one-bay specimens. Therefore, the seismic resistance of a prototype frame which has infills in two bays would be higher than the frame with only one infilled bay. Nevertheless, in the case of strong panels, the ductility of the two-bay frame is considerably lower than those of the one-bay frames (see Table 4.1). In this case, it is possible that the seismic resistance of the former could be lower than that of the latter.

CHAPTER 5

SIMPLE ANALYTICAL METHODS

5.1 Introduction

As demonstrated by the experimental results, the lateral stiffness and strength of an infilled frame depend, to a large extent, on how the frame and panel may interact with one another. This is an extremely complicated behavior. A complete analysis of this requires a detailed finite element model which accounts for the cracking of the frame and the infill as well as the separation of the frame-panel interface, which will be considered in Chapter 6. However, a number of simplified methods, which consider one type of frame-panel interaction mechanism or the other, have been proposed previously (Stafford Smith 1966; Fiorato et al. 1970; Liauw and Kwan 1985) for practical reasons. These methods are reviewed in this study. In addition, based on recent experimental observations, new methods have been developed in this study to account for the sliding and diagonal shear failure of the infill and the shear failure of the columns. To examine the predictive value of these formulas, they are compared to the experimental results presented previously.

To assess the lateral strength in a realistic manner, it is necessary to have a means to identify the failure mechanism of an infilled frame. For this purpose, some of the most likely failure mechanisms have been identified for single-bay, single-story infilled frames, and corresponding analytical formulas have been derived for strength predictions. The strength formulas have been

used to evaluate the lateral resistances of the single- and two-bay infilled-frame specimens that were tested in this study. Predictive formulas for lateral stiffness have also been examined.

For convenience in the following discussions, the design of a test specimen is denoted by a three-letter label. For the first letter, "w" refers to a weak frame and "s" to a strong frame. For the second letter, "w" refers to a weak infill and "s" to a strong infill. For the third letter, "l" refers to the aspect ratio of 2/3 and "s" to the aspect ratio of 1/2. For example, a weak frame specimen infilled with a weak panel of aspect ratio equal to 2/3 is designated by "wwl".

5.2 Lateral Stiffness

One well recognized method for assessing the lateral stiffness of an infilled frame is based on the equivalent diagonal strut concept (Polyakov 1960; Holmes 1961; Stafford Smith 1966), which is shown in Fig. 5.1a. Stafford Smith (1966) has shown that the effective width, w, of an equivalent strut that represents an infill depends on the contact length between the frame and the infill, which, in turn, depends on the relative stiffness of the two components. Based on the analogy of a beam on an elastic foundation, Stafford Smith has proposed the following relation between the contact length, α, and the relative stiffness.

$$\frac{\alpha}{h} = \frac{\pi}{2\lambda h} = \frac{\pi}{h}\sqrt[4]{\frac{E_f I_c h}{4E_w t \sin\theta}} \tag{5.1}$$

in which λh is a non-dimensional parameter representing the relative stiffness of the infill with respect to that of the frame, E_f and E_w are the moduli of elasticity of the frame members and the infill, respectively, I_c is the moment

of inertia of the uncracked column section, h is the height of the frame, t is the thickness of the infill, and θ is the angle of the frame diagonal with respect to a horizontal axis. Assuming a linear as well as a parabolic distribution of the contact stress, Stafford Smith has calculated the average strain along the diagonal, based on theory of elasticity and the finite difference approximation. The contact lengths calculated with the aforementioned distributions were in good agreement with the experimental results. Based on this, the width of an equivalent diagonal strut has been established to arrive at the same diagonal strain. However, the theoretical results based on the above contact length do not show a good correlation with Stafford Smith's experimental data with respect to the effective width of the equivalent diagonal strut. Therefore, a set of empirical curves, as shown in Fig. 5.2, relating the relative stiffness (λh) to the effective width of an equivalent diagonal strut have been proposed (Stafford Smith 1967). These curves are used here to evaluate the effective width of the equivalent strut and, thereby, the lateral stiffness of the infilled frame specimens presented previously. However, it must be pointed out that these curves are based on experimental data derived from small-scale specimens of steel frames infilled with mortar panels, with the relative stiffness, λh, ranges from about 4 to 14. The relative stiffness of the masonry-infilled R/C frame specimens tested in this study ranges from 2 to 3.6. Therefore, these curves may not be applicable to the specimens considered here.

Mainstone and Weeks (1970) have proposed some empirical relations to find the effective width of an equivalent strut based on similar ideas. The relation proposed for R/C frames infilled with masonry is

$$w = 0.175(2L_w \sin\theta)(\lambda h)^{-0.4} \tag{5.2}$$

in which L_w is the length of the infill, and w is the effective width of the equivalent strut, both in inches. This relation results in a lower value for the effective width than the empirical curves discussed above.

With the equivalent strut concept, an infilled frame is represented by a diagonally braced structure, whose lateral stiffness is calculated by the following relations depending on the rigidity of the joints. These relations have been derived by Stafford Smith (1966) by considering the strain energy due to the tension column, the equivalent diagonal strut, and the bending of the frame. In the case of hinged joints, the lateral stiffness is given by

$$K_s = \frac{1}{(A+B)} \tag{5.3}$$

In the case of rigid joints, with the assumption that the flexural resistance of the frame and the resistance of the braced frame with hinged joints are parallel, he has proposed that

$$K_s = \frac{A+B+C}{C(A+B)} \tag{5.4}$$

In Eqs. 5.3 and 5.4,

$$A = \frac{h(\tan\theta)^2}{A_c E_f} \qquad B = \frac{d}{wtE_w(\cos\theta)^2} \qquad C = \frac{h^3(3I_b h + 2I_c L)}{12E_f I_c(6I_b h + I_c L)} \tag{5.5}$$

in which I_b is the moment of inertia of the beam section, d is the diagonal length of the infill, and L is the span length of the frame as shown in Fig. 5.1a. A represents the lateral flexibility related to the axial deformation of

the tension column, B accounts for the lateral flexibility due to the diagonal strut, and C is the lateral flexibility due to the flexural deformation of the rigid frame.

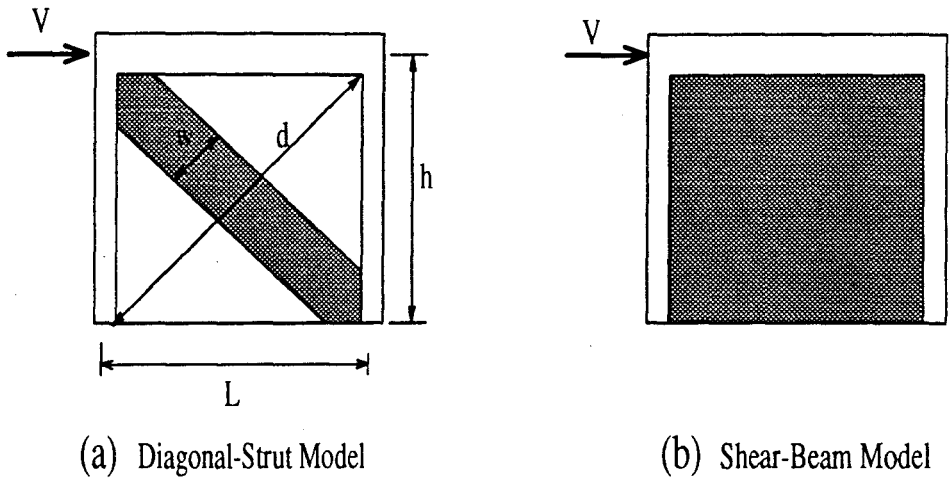

Figure 5.1. Diagonal-Strut and Shear-Beam Models.

With the above formulas, Stafford Smith has found that the joint rigidity does not have a significant influence on the lateral stiffness.

Another simple method for assessing the lateral stiffness of an infilled frame is based on a shear-beam model (Fiorato et al. 1970), which is shown in Fig. 5.1b. In this model, one can obtain the following expression for the lateral stiffness.

$$K_b = \frac{1}{\frac{1}{K_{sh}} + \frac{1}{K_{fl}}} \tag{5.6}$$

in which K_{sh} and K_{fl} are the shear and flexural stiffnesses of a cantilever beam. In this case, the beam is assumed to be a composite section consisting of a masonry panel and R/C columns. However, for shear stiffness, K_{sh}, only the wall section is considered with the assumption that shear is uniform across

the wall; whereas, for flexural stiffness, K_{fl}, the whole composite section is used. As a result, these stiffnesses are given as

$$K_{sh} = \frac{A_w G_w}{h_w} \qquad K_{fl} = \frac{3E_c I}{h^3} \tag{5.7}$$

in which h_w, A_w, and G_w are the height, horizontal cross-sectional area, and shear modulus of the infill, E_c is the modulus of elasticity of concrete, and h and I are the height and moment of inertia of the composite beam.

The methods described above were used to calculate the lateral stiffness of some of the infilled frame specimens which were tested in this study. The results are summarized in Table 5.1. The experimental stiffness in this table is the secant stiffness. For the case of cyclic loading, the secant stiffness is defined as the slope of a line connecting the extreme points of a small-amplitude displacement cycle in which the peak load is about 50% of the maximum lateral resistance. The stiffness of the frame members influences the effective width of the equivalent strut and, consequently the lateral stiffness of the infilled frame. However, as shown by the results in Table 5.1, the contribution of the flexural resistance of the frame itself to the total lateral stiffness is insignificant. The elastic moduli of concrete and masonry used for the above calculations are based on the average of the material test results, which are shown in Table 3.2. The moment of inertia of the R/C beams and columns, I_b and I_c, are based on gross uncracked sections.

For a better evaluation of the formulas, the ratio of the secant stiffness, K, of the infilled frames obtained from the experiments to stiffness K_s evaluated with the Stafford Smith's equivalent strut model, considering only

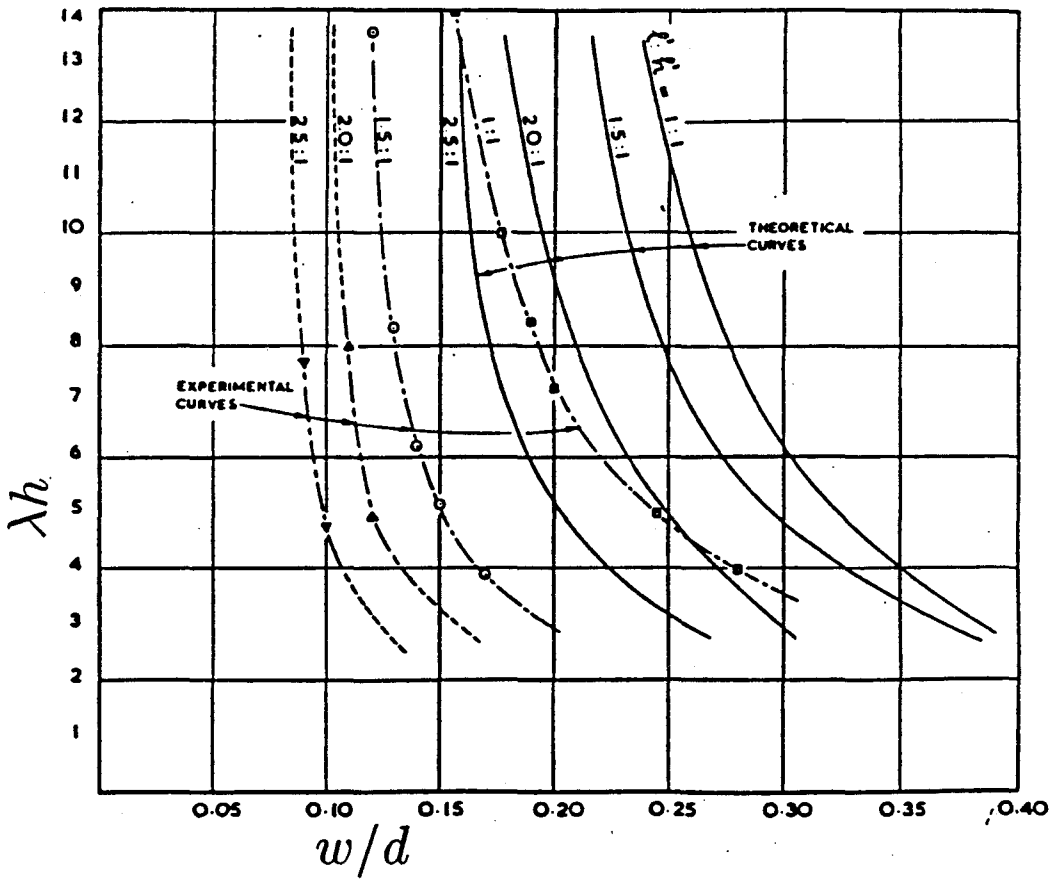

Figure 5.2. Effective Width-vs-Relative Stiffness Curves for Frames of Different Aspect Ratios (Stafford Smith 1967).

Table 5.1: Lateral Stiffness of Test Specimens.

Specimen		Lateral Stiffness (kips/in.)					
		Experimental	Stafford Smith's Method			Mainstone's Method Strut Only	Fiorato's Shear Beam Method
No.	Label		Strut Only	Columns & Strut	Rigid Frame & Strut		
4	wwl	430	127	126	180	62	495
5	wsl	1280	585	537	591	314	2533
6	swl	480	144	143	218	66	502
7	ssl	1460	624	584	661	330	2652
10	wws	395	135	132	182	64	693
11	wss	1470	563	512	562	322	3729

the flexibility of the diagonal strut, are presented in Fig. 5.3. It can be observed that the secant stiffness obtained from the tests, in general, is a lot higher than that predicted by the strut model. The trend is quite consistent for specimens with a virgin frame. Specimens 3, 8, and 9, which had repaired frames, exhibited a much lower stiffness ratio than the rest. This indicates the influence of the stiffness of the frame on the overall stiffness of an infilled frame. Furthermore, Fig. 5.3 indicates that the stiffness ratio for Specimen 12 is a lot higher than that for Specimen 11. This is due to the fact that the strut model does not consider the influence of axial loads, which, in reality, have an important influence on the behavior of R/C frames and masonry infills.

The ratios of the secant stiffness, K, of the infilled frames to stiffness K_b evaluated with the shear-beam model are presented in Fig. 5.3 as well. Generally, the shear-beam model overestimates the stiffness. This can be attributed to the lack of a perfect bond in the frame-panel interface in reality.

Under seismic excitation, a higher stiffness usually attracts larger lateral forces. Therefore, the method based on the shear-beam model, which overestimates the stiffness, is conservative in this respect.

5.3 Lateral Strength

From the experimental results presented in Chapter 3, it can be observed that the lateral strength of an infilled frame strongly depends on the type of the failure mechanism developed, which, in turn, is dependent on how the frame and the infill interact with one another.

5.3.1 Interaction between Infill and Frame. To assess the nature of the interaction between a frame and the infill in the single-bay specimens, two simple mechanisms are considered here as baselines for comparison.

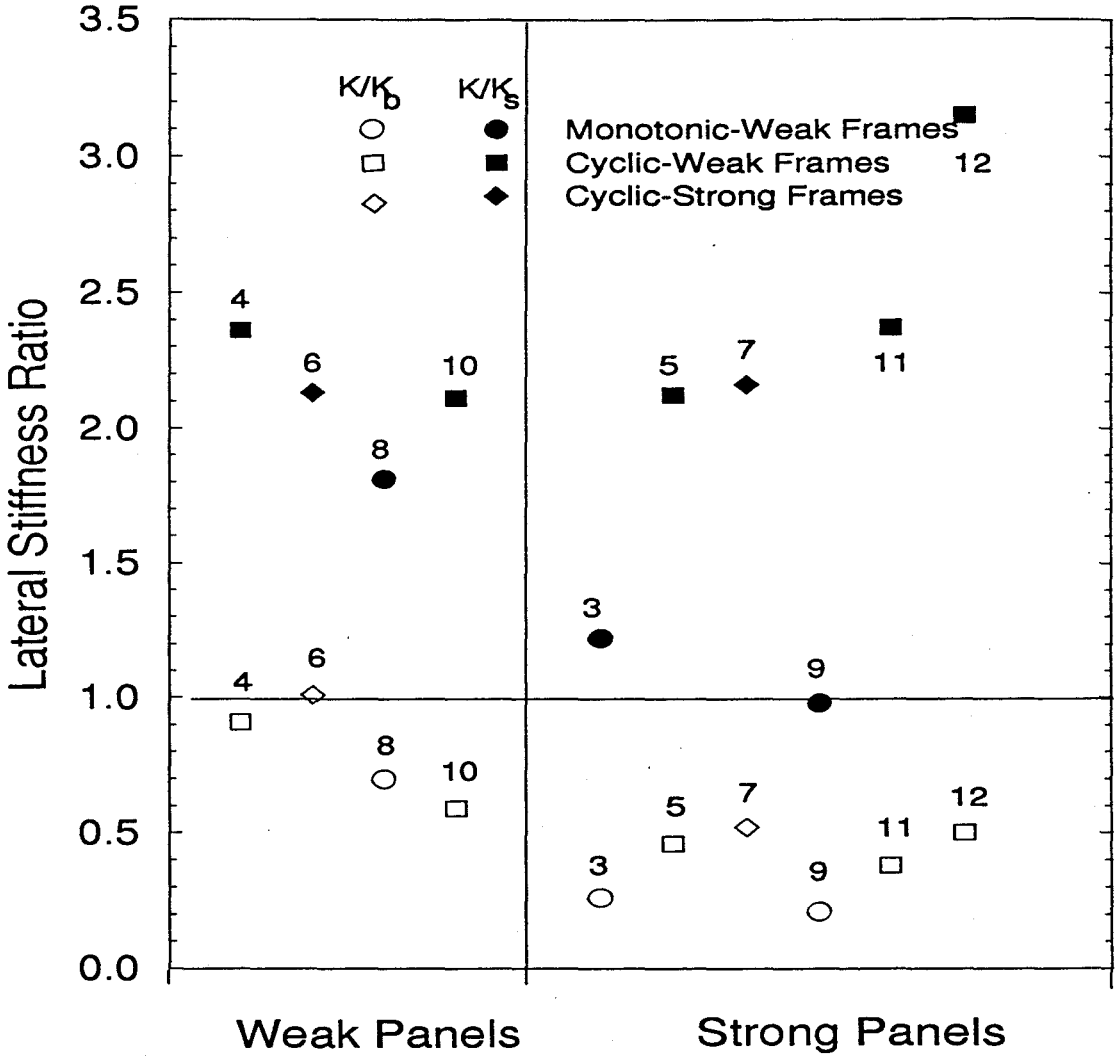

Figure 5.3. Lateral Stiffness Ratios.

These are the flexural mechanism of a bare frame and the simple resistance mechanism governed by the sliding-shear failure of an infill. The ratios of the actual lateral resistance V_{ua} developed by an infilled specimen to the resistances provided by these mechanisms can provide some information on the nature of the frame-panel interaction. To evaluate the lateral resistance of an infilled frame based on the simple sliding-shear mechanism, the vertical load was distributed between the frame and infill in accordance with their axial stiffnesses. Based on the Mohr-Coulomb Criterion, the sliding-shear strength V_w of an infill can be expressed as

$$V_w = CA_w + \mu_0 P_w \tag{5.8}$$

in which A_w is the horizontal cross-sectional area of the infill, and P_w is the vertical load acting on the infill. The cohesive strength, C, and the initial coefficient of friction, μ_0, are determined to be to 50 psi and 0.9, respectively, based on the average results of the direct shear tests conducted on masonry mortar joints (see Table 3.4). The flexural resistance, F_f, of the weak frame is based on the actual strength of Specimen 1. The resistance of the strong frame was computed theoretically and increased by 15% to account for the possible discrepancy between the actual and theoretical strengths as reflected by Specimen 1 (see Chapter 4). The sliding-shear strength V_w of the infill is added to the flexural strength F_f of the bare frame to obtain the total strength.

The strength ratios ($V_{ua}/(V_w + F_f)$) are shown in Fig. 5.4. It can be observed that specimens that had weak frames and weak panels have a strength ratio of about one. On the other hand, specimens which had weak frames and strong panels exhibit ratios less than one. The failure mechanism of this type

of specimen (see Fig. 3.26) is very much dominated by the diagonal/sliding cracks in the infills and the shear failure of the columns. In this case, the shear failure of the columns prevented the development of an effective load-resisting mechanism. On the other hand, in Specimen 7, the strong columns led to the development of a diagonal strut mechanism (see Fig 3.28), which results in a high strength ratio. This reflects a complicated frame-panel interaction mechanism. Figure 5.4 also contains the ratio of the maximum lateral strength, V_{ua}, of the specimens to the flexural strength, F_f, of the corresponding bare frame. These ratios show the effectiveness of an infill in increasing the lateral strength of a frame.

In summary, it can be concluded that in a weak-panel specimen, the interaction of the infill and the frame introduces no significant influence on the lateral strength. In this type of specimens, the lateral strength is almost equal to the sum of the strengths of the individual components. For a strong-panel specimen, the interaction can significantly enhance the lateral strength, provided the frame is sufficiently strong. However, if a frame is weak, the interaction of the frame and the infill can lead to the shear failure of the windward column. This prevents the development of a diagonal strut mechanism, which is believed to be the most effective load carrying mechanism of an infilled frame.

Most of the analytical models proposed for infilled frames are based on one type of the frame-panel interaction mechanism or the other. Some of these models and the corresponding formulas for the lateral strength are discussed in the next section.

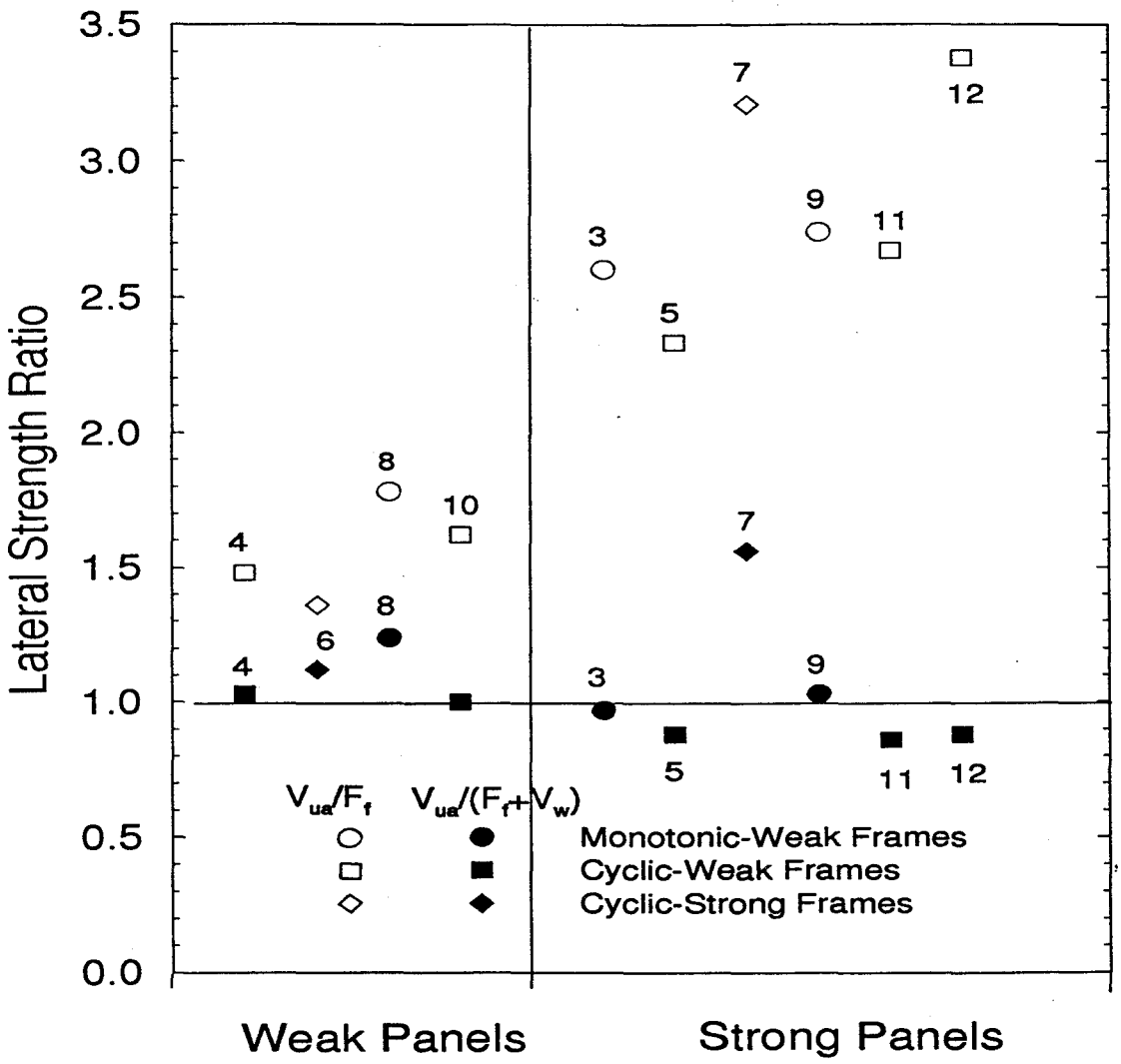

Figure 5.4. Lateral Strength Ratios.

5.3.2 Analytical Models. Different analytical models have been proposed for predicting the strength of a single-story, single-bay infilled frame. Fiorato et al. (1970) have used an equivalent beam model to estimate the precracked stiffness and the cracking strength of an infilled frame. To estimate the ultimate strength of an infilled frame, they have proposed a knee-braced frame model to simulate the short-column effect observed in their experiments. In this model, it is assumed that failure is dominated by a horizontal fracture developed at the mid-height of an infill (which is mechanism B1 in Fig. 2.1), and the resistance of an infilled frame is governed by the bending resistance of two short columns. Polyakov (1960) has proposed a diagonal strut model, in which the infill panel is substituted by an equivalent diagonal strut. Analytical techniques have been developed by Stafford Smith (1963,1969), Holmes (1961), and Mainstone and Weeks (1970) to estimate the effective width of the diagonal strut. This model is only capable of capturing the diagonal compression failure of infill panels (i.e., mechanism E in Fig. 2.1). Schmidt (1989) has used an additional strut to induce column failure. Wood (1978) has used plastic analysis to find the collapse loads of infilled frames. In his model, a failure criterion is adopted for brick infills. Liauw and Kwan (1985) have simplified this technique to analyze multi-story infilled frames by proposing four types of failure mechanisms, which involve plastic hinges in frame members and the crushing of infill at loaded corners.

Nevertheless, none of the aforementioned models can capture all possible failure mechanisms of infilled frames. Some of these models, such as the equivalent diagonal strut model, have been calibrated with test results obtained from steel frames with mortar infills. Most of these models preclude the shear

failure of columns, which are not uncommon in R/C infilled frames.

5.3.3 Failure Mechanisms. Among all the possible failure mechanisms shown in Fig. 2.1, five of them are selected as the most possible cases and are shown in Fig. 5.5. Mechanisms 1 and 2 can be represented by the knee-braced frame model proposed by Fiorato et al. (1970); Mechanisms 3 and 4 can be represented by the plastic models proposed by Liauw and Kwan (1988); and Mechanism 5 is dominated by the slip along bed joints. With the assumption that plastic hinges are developed in the columns only, these mechanisms are applicable to frames with a weak column-strong beam design. However, these mechanisms are also applicable to infilled specimens with a strong column-weak beam design. This is due to the fact that in these specimens, the infill panels restrained the beams from bending and, thereby, postpone the development of plastic hinges in the beams. It must be understood that the maximum lateral resistance of an infilled frame may occur long before the formation of a complete failure mechanism. For example, the maximum resistance can occur at the initiation of the first major crack in an infill or at the onset of the crushing of the diagonal strut.

Analytical methods proposed for assessing the ultimate resistance provided by the aforementioned mechanisms are presented in the following sections. Some of the methods have been proposed by other investigators. These include the method proposed by Fiorato et al. (1970) for predicting the first cracking load, the method proposed by Stafford Smith (1969) for estimating the diagonal crushing load, and the plastic analysis method proposed by Liauw and Kwan (1985) for calculating the failure loads of Mechanisms 3 and 4. In addition to these, methods have been developed in this study to compute

the resistance provided by Mechanisms 1, 2, and 5. Even though these mechanisms and the corresponding load resistance formulas are originally derived for single-bay infilled frames, they can also be used to approximate the lateral resistance of the two-bay specimens as reflected by the following results.

5.3.4 Cracking Load. The cracking load of an infilled frame is the lateral load at which the first major diagonal/sliding crack initiates in the infill. This load can be approximated with the sliding resistance of the wall as proposed by Fiorato et al. (1970). This approach is adopted here by using the model shown in Fig. 5.6. In this model, the beam is assumed to be rigid and the wall is represented by a diagonal strut and a vertical strut, which are connected by a hinge. As shown in Fig. 5.6, P is the total vertical load applied on the infilled frame and V is the lateral load, P_{c1} is the axial load in a column due to the applied vertical load P, P_{wl} is the vertical component of the load carried by the compression strut, and P_{wv} is the portion of the total vertical load carried by the wall (i.e. $P = 2P_{c1} + P_{wv}$). The cracking load of the infill, V_{wcr}, is estimated with the Mohr-Coulomb criterion as

$$V_{wcr} = CL_w t + \mu_0 P_w \tag{5.9}$$

where

$$P_w = P_{wv} + P_{wl} \tag{5.10}$$

It is assumed that the vertical load on an infilled frame is distributed between the horizontal cross section of the wall and the columns in accordance with their relative axial stiffnesses. The lateral load applied to an infilled frame results in a diagonal force in the strut. Based on these considerations, at cracking load,

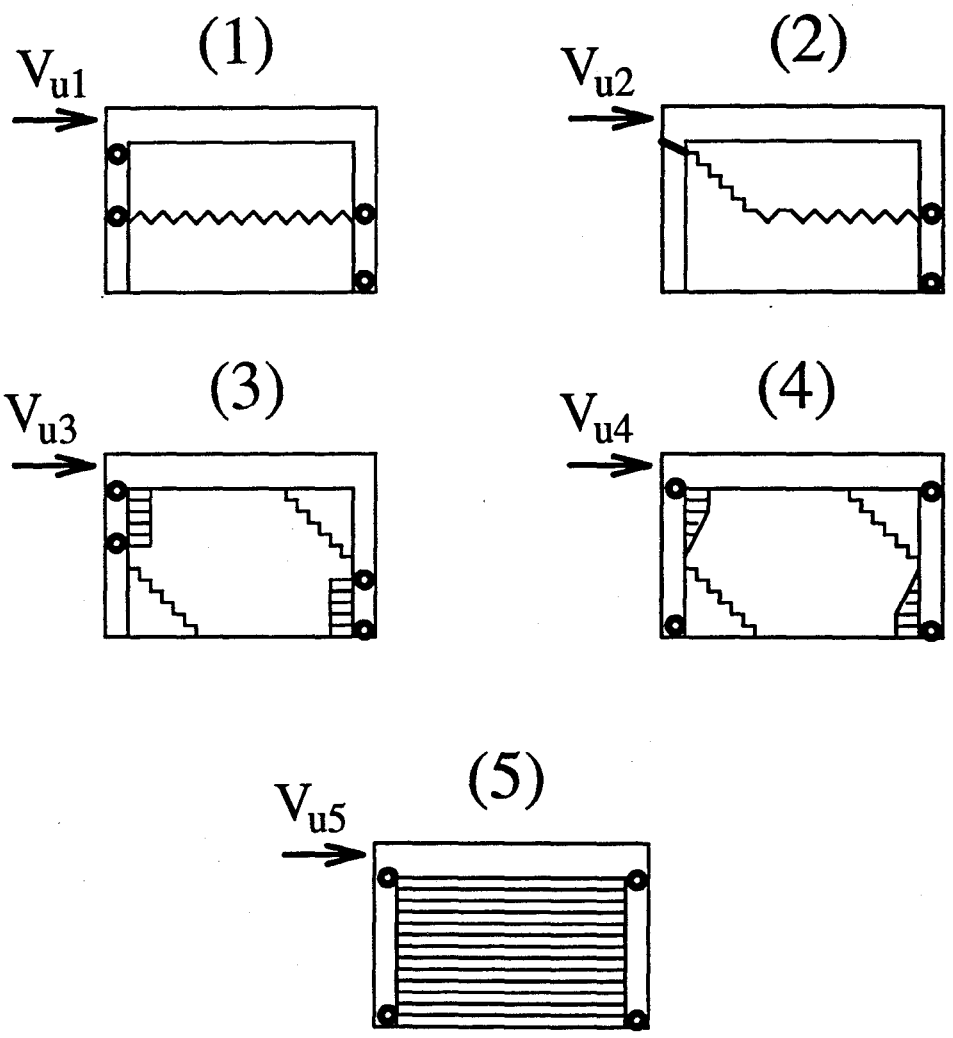

Figure 5.5. Selected Failure Mechanisms.

V_{wcr}, P_{wv} and P_{wl} are expressed as

$$P_{wv} = \frac{PA_w}{A_w + 2A_{ceq}} \tag{5.11}$$

$$P_{wl} = \frac{V_{wcr}h}{L} \tag{5.12}$$

where

$$A_w = L_w t$$

$$A_{ceq} = A_c \frac{E_c}{E_w}$$

$$A_c = h_c b_c + A_s(\frac{E_s}{E_c} - 1)$$

in which E_s is the elastic modulus of the reinforcing bars, h_c and b_c are the depth and the width of the concrete columns, A_c is the cross-sectional area of a R/C column, A_{ceq} is the equivalent area in masonry for the R/C columns, and A_s is the cross-sectional area of the longitudinal bars in a column. Combining these equations with Eqs. 5.9 and 5.10 results in

$$V_{wcr} = \frac{C + \frac{\mu_0 P}{A_w + 2A_{ceq}}}{1 - \frac{\mu_0 h}{L}} A_w \tag{5.13}$$

5.3.5 Crushing Load. The lateral load V_{crush} corresponding to the diagonal crushing of an infill can be calculated based on the equivalent diagonal strut concept proposed by Stafford Smith (1962) as

$$V_{crush} = wtf'_m \cos\theta \tag{5.14}$$

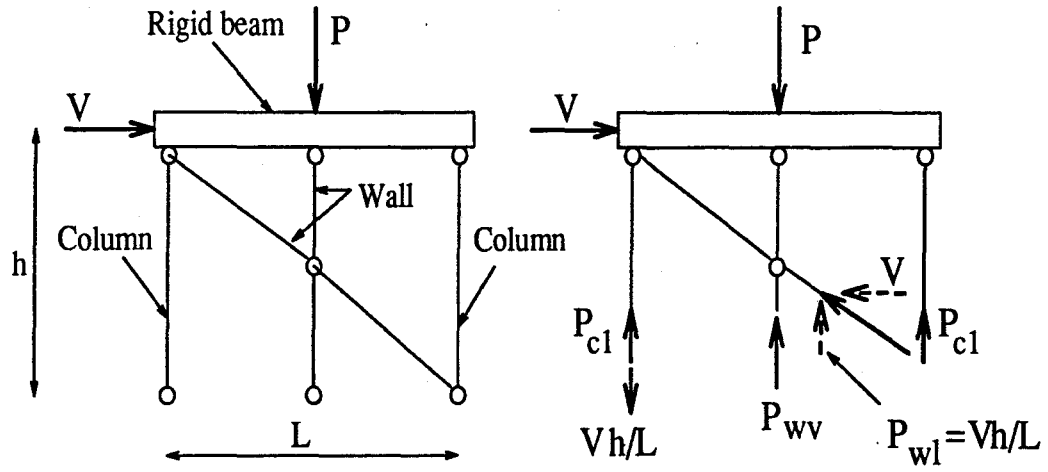

Figure 5.6. Vertical Load Components Acting on the Wall.

in which f'_m is the compressive strength of the masonry. The effective width, w, of the diagonal compressive strut (see Fig. 5.1) can be obtained from the empirical curves presented by Stafford Smith (1967) (see Fig. 5.2) based on the relative stiffness of the wall with respect to that of the frame.

5.3.6 Residual Shear Resistance of Cracked Wall. After the fracture of the infill, the cohesion is lost and the coefficient of friction is reduced due to wearing. Therefore, the residual shear force of the wall, V_{wr}, can be expressed as

$$V_{wr} = \frac{\frac{\mu_r P}{A_w + 2A_{ceq}}}{1 - \frac{\mu_r h}{L}} A_w \tag{5.15}$$

which is derived from Eq. 5.13. In this equation, μ_r is the residual coefficient of friction of the mortar joints, which is determined based on the average results of the direct shear tests (see Table 3.4).

5.3.7 Failure Mechanism 1. This mechanism and the corresponding model that is used for calculating the lateral resistance are quite

similar to those proposed by Fiorato et al. (1970). Nevertheless, the residual shear resistance of the infill, which has been neglected in Fiorato's method, is considered here. As shown in Fig 5.7, the lateral resistance corresponding to Mechanism 1 is the sum of the shear forces in the columns and the shear resistance of the wall. The resistance of the frame is governed by the plastic hinges formed at one end and the midheight of each column. However, the development of plastic hinges in the columns usually occurs at a relatively large lateral displacement. Therefore, the infill is assumed to be cracked at that time and the residual shear force of the cracked infill should be considered as the shear resistance of the wall. Hence, the lateral resistance is given as

$$V_{u1} = V_{wr} + F_{cc} + F_{ct} \tag{5.16}$$

in which V_{wr} is obtained from Eq. 5.15, and F_{cc} and F_{ct} are the shear forces in the leeward and windward columns, respectively. In Mechanism 1 (see Fig. 5.7), for the column segment AB, taking moment about A results in the following expression for F_{ct}.

$$F_{ct} = \frac{4M_{pct}}{h} \tag{5.17}$$

in which M_{pct} is the plastic moment developed in the windward column considering the effect of the axial force. Taking moment about D in column segment CD results in the following relation for F_{cc}.

$$F_{cc} = \frac{4M_{pc}}{h} \tag{5.18}$$

in which M_{pc} is the plastic moment of the leeward column for which the influence of the axial compressive load is ignored for simplicity.

5.3.8 Failure Mechanism 2. This mechanism has been identified in this study based on experimental observations. As shown in Fig. 5.7, the lateral resistance, V_{u2}, provided by Mechanism 2 is the sum of the ultimate shear resistance of the windward column, the shear force in the leeward column, and the residual shear resistance along the horizontal crack in the wall. Hence,

$$V_{u2} = V'_{wr} + F_{cc} + V_{ct} \tag{5.19}$$

in which V_{wr} is the residual shear resistance provided by the horizontal crack in the wall:

$$V'_{wr} = \frac{\frac{\mu_r P}{A_w + 2A_{ceq}}}{1 - \frac{\mu_r h}{2L}} A_w \tag{5.20}$$

The above equation is similar to Eq. 5.15. The difference is that only one-half of the vertical component of the diagonal force is considered here, assuming that the diagonal force is divided equally between the two segments of the wall separated by the diagonal crack. F_{cc} is the same as that described in Mechanism 1, and V_{ct} is the ultimate shear resistance of the windward column approximated by

$$V_{ct} = 0.8V_{cs} + V_{cc} \tag{5.21}$$

in which V_{cs} and V_{cc} are the shear resistances of the column provided by the shear reinforcement and the concrete, respectively. These are calculated based on the provisions of ACI 318-89 (1989) as

$$V_{cs} = f_{yv} A_v \frac{d}{s} \tag{5.22}$$

$$V_{cc} = 2(1 + \frac{N_{ct}}{500A_g})\sqrt{f'_c}b_c d \tag{5.23}$$

in which $A_g = h_c b_c$ is the gross cross-sectional area of the column, f_{yv} is the yield strength of shear reinforcement, s is the spacing of shear reinforcement in the columns near the beam-to-column joints, A_v is the area of shear reinforcement within a distance s. Furthermore,

$$N_{ct} = V_{u2}\frac{h}{L} + P_{c1} \tag{5.24}$$

is the tensile force in the windward columns, d is the distance form the centroid of tension reinforcement to the extreme compression fiber of concrete in the column section, and f'_c is the specified compressive strength of concrete. In Eq. 5.23, all dimensions are in inches, f'_c is in psi, and V_{cc} and N_{ct} are in pounds. The factor 0.8 in Eq. 5.21 is to reduce the shear capacity of the section due to the fact that not all the ties which intersect the diagonal crack in the column have the necessary development length to reach the yield capacity.

5.3.9 Failure Mechanism 3. In Mechanism 3, as shown in Fig. 5.8, masonry is assumed to reach the crushing strength along the length y at the wall-to-frame interface, and plastic hinges are assumed to develop in the columns near the beam-to-column joints and at points B in the columns. This mechanism, which is based upon the plastic analysis method, has been proposed by Liauw and Kwan (1985). It is assumed that there is no significant shear transfer between the beam and the wall. The contact stress is assumed uniform, which implies that the entire region has reached the plastic state. Point B in the windward column is the location at which the moment is maximum and the shear is zero. Taking moment about A in column segment AB

results in

$$f'_m t y^2/2 = 2M_{pc} \tag{5.25}$$

For simplicity, the plastic moment of the columns, M_{pc}, is evaluated without considering the influence of the axial load. Based on Eq. 5.25, the contact length can be evaluated as

$$y = \sqrt{\frac{4M_{pc}}{f'_m t}} \tag{5.26}$$

Considering the equilibrium of column segment AB, one obtains

$$V_{u3} = y f'_m t = \sqrt{\frac{4M_{pc}}{f'_m t}} f'_m t \tag{5.27}$$

Defining $m_c = \sqrt{\frac{4M_{pc}}{f'_m t h_c^2}}$ and substituting it in the above equation, one has

$$V_{u3} = m_c f'_m t h_c \tag{5.28}$$

5.3.10 Failure Mechanism 4. Mechanism 4 is based on the plastic analysis method proposed by Liauw and Kwan (1985). In Mechanism 4, as shown in Fig. 5.8, plastic hinges are assumed to develop at both ends of the columns and the masonry is assumed to reach crushing at the compression corners. No significant shear transfer is assumed between the beam and the infill. It is assumed that the contact stress at the wall-to-column interface has a parabolic distribution along the contact length αh with a maximum intensity of f'_m at the corner. This distribution of the compressive stress is based on the assumption that the rotation of the column induces a linear variation of compressive strain in the masonry panel. Taking moment about A in column AB results in

$$F_c h + \frac{2}{3} f'_m t \alpha h \frac{3}{8} \alpha h = 2M_{pc} \tag{5.29}$$

in which F_c is the shear force in each column. Again, for simplicity, the plastic moment of the column, M_{pc}, is evaluated without the consideration of the axial load. Hence, considering the equilibrium of column AB in the horizontal direction results in

$$V_{u4} = \frac{2}{3} f'_m t \alpha h + 2F_c = m_c^2 f'_m t h + (\frac{2\alpha}{3} - \frac{\alpha^2}{2}) f'_m t h \tag{5.30}$$

in which α is the ratio of the contact length to the height of the frame. The contact length is approximated by the analogy of a beam on elastic foundation and can be evaluated with Eq. 5.1 based on the relative stiffness of the wall with respect to that of the frame.

5.3.11 Failure Mechanism 5. As shown in Fig. 5.9, in Mechanism 5, the frame and the infill are considered as two parallel systems with a displacement compatibility at the compression corners. Hence, the lateral resistance of this mechanism is considered to be the sum of the flexural resistance of the frame and the residual shear resistance of the fractured wall as

$$V_{u5} = V_{wr} + F_f \tag{5.31}$$

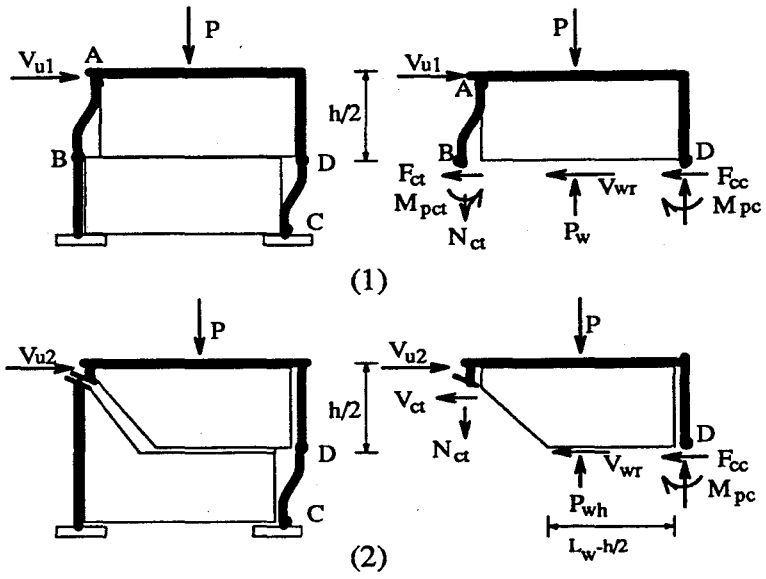

Figure 5.7. Failure Mechanisms 1 and 2.

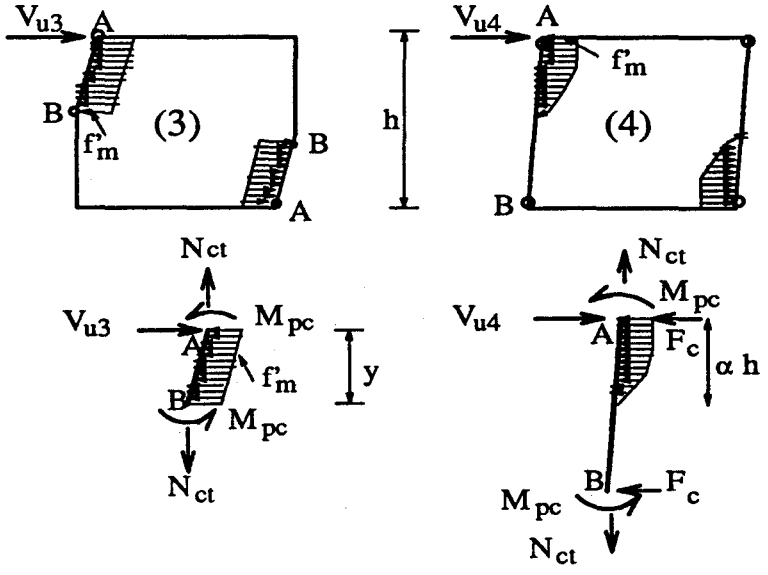

Figure 5.8. Failure Mechanisms 3 and 4.

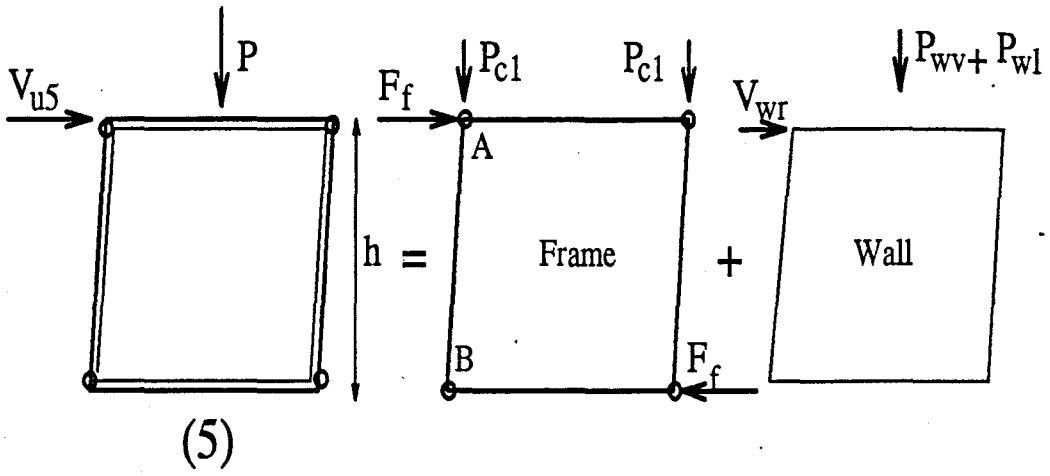

Figure 5.9. Failure Mechanism 5.

in which V_{wr} can be obtained from Eq. 5.15. The resistance of a bare frame, F_f, with plastic hinges at the end sections of the columns can be expressed as

$$F_f = \frac{4M_{pc}}{h} \tag{5.32}$$

In the calculation of M_{pc}, the influence of the axial loads is ignored. The vertical load distribution on the wall and the columns is based on the model shown in Fig. 5.6.

5.3.12 Two-Bay Infilled Frames. For two-bay infilled frames, it is assumed that both bays will fail with the same mode, which can be one of the five failure mechanisms introduced for single-bay infilled frames, as shown in Fig. 5.5. This assumption is used here to derive the formulas for the strength prediction of the two-bay specimens. However, with Mechanisms 1 through 3, the assumption of identical mechanisms in both bays results in two incompatible failure modes for the middle column. In the following derivations, this inconsistency is ignored. Furthermore, they are based on the assumption

that all the columns and infill panels are identical in a two-bay frame.

Cracking and Residual Shear Resistances

The vertical loads acting on the panels and the columns are calculated with a model similar to that shown in Fig. 5.6. Based on this, the cracking load of the infills is

$$V_{wcr} = \frac{C + \frac{\mu_0 P}{2A_w + 3A_{ceq}}}{1 - \frac{\mu_0 h}{L}} 2A_w \tag{5.33}$$

and the total residual shear resistance of cracked walls is

$$V_{wr} = \frac{\frac{\mu_r P}{2A_w + 3A_{ceq}}}{1 - \frac{\mu_r h}{L}} 2A_w \tag{5.34}$$

in which A_w is the cross-sectional area of a single panel, h and L are the height and length of a single bay, and A_{ceq} is the equivalent cross sectional area of a column.

Crushing Load

It is assumed that the effective width of the equivalent diagonal strut in a two-bay frame is the same as that in a single-bay frame. Based on this, the crushing load of the infills are calculated to be twice as large as the crushing load of each panel expressed by Eq. 5.14.

Failure Mechanism 1

In this case, the failure of an infilled frame is assumed to be similar to Mechanism 1 shown in Fig. 5.5. Hence,

$$V_{u1} = V_{wr} + 2F_{cc} + F_{ct} \tag{5.35}$$

in which F_{cc} and F_{ct} are computed by Eq. 5.18 and 5.17, respectively, and V_{wr} is calculated by Eq. 5.34.

Failure Mechanism 2

The failure of an infilled frame is assumed to be similar to Mechanism 2 shown in Fig. 5.5. Hence,

$$V_{u2} = V'_{wr} + 2F_{cc} + V_{ct} \tag{5.36}$$

in which V'_{wr} is the residual shear resistance provided by the horizontal crack in the infills:

$$V'_{wr} = \frac{\frac{\mu_r P}{2A_w + 3A_{ceq}}}{1 - \frac{\mu_r h}{2L}} 2A_w \tag{5.37}$$

Failure Mechanisms 3 and 4

With Mechanisms 3 and 4 and the assumption of simultaneous crushing in both panels, the lateral resistances of the two-bay infilled frames are twice as large as the loads computed by Eqs. 5.28 and 5.30, respectively.

Failure Mechanism 5

With Mechanism 5, which is governed by sliding along the bed joints and plastic hinges at the end sections of the columns, the lateral resistance of a two-bay frame is given by

$$V_{u5} = V_{wr} + F_f \tag{5.38}$$

in which V_{wr} can be obtained from Eq. 5.34. The resistance of a two-bay bare frame, F_f, with plastic hinges at the end sections of the columns can be expressed as

$$F_f = \frac{6M_{pc}}{h} \tag{5.39}$$

in which M_{pc} is the plastic moment developed by the columns with the influence of the axial loads ignored.

5.3.13 Comparison of Results. The values of the parameters, which are used for the calculation of the failure loads, are summarized in Tables 5.2. The lateral resistances based on the selected mechanisms as well as the cracking and crushing loads of the infill, are calculated for the specimens tested and are summarized in Table 5.3. The minimum of the lateral resistances calculated for different failure mechanisms defines the failure load, and the corresponding mechanism identifies the dominant failure mode of the infilled frame. The analytical results indicate that Mechanism 5 is the dominant failure mechanism of the specimens which had a weak panel. In this mechanism, large slips along the bed joints and the plastic hinges in the columns govern. On the other hand, for the specimens which had a strong panel, the results indicate that Mechanism 2 is dominant. This mechanism is governed by the diagonal/sliding shear failure of the infill and the shear failure of the windward column.

Table 5.3 also shows the actual failure loads and failure mechanisms of the specimens. The comparison of the experimental and analytical results shows that the failure mechanisms identified from the analysis agree with those obtained from the experiments in all cases, except for the strong frame-strong panel specimen, i.e., Specimen 7. For this specimen, Mechanism 2 has been identified by the analysis as the dominant failure mechanism, whereas the actual failure is similar to a combination of Mechanisms 4 and 5. For the specimens whose failure mechanisms match the experimental results, the analytical failure loads are in good agreement with the actual lateral resistances. The

Table 5.2. Parameters for Simple Analytical Models.

Specimen	L (in.)	L_w (in.)	t (in.)	h_c (in.)	b_c (in.)	E_w** (ksi)	θ (rad)	λh	w* (in.)	α	f'_m (ksi)	f_y+ (ksi)	d (in.)	s (in.)
wwl	91	84	1.31	7	7	610	33.62	2.29	23.	0.68	1.47	71.8	5.75	2.5
wsl	91	84	3.62	7	7	1330	33.62	3.56	18	0.44	2.06	71.8	5.75	2.5
swl	92	84	1.31	8	8	610	33.62	2.03	26	0.78	1.47	73.0	6.70	1.5
ssl	92	84	3.62	8	8	1330	33.62	3.14	19	0.50	2.06	73.0	6.70	1.5
wws	123	116	1.31	7	7	610	26.19	2.19	27	0.71	1.47	71.8	5.75	2.5
wss	123	116	3.62	7	7	1330	26.19	3.38	19	0.46	2.06	71.8	5.75	2.5

All Specimens	P (kips)	h (in.)	h_w (in.)	μ_0	μ_r	C (ksi)	E_c (ksi)	f'_c (ksi)	f_{yv} (ksi)
	66	60.5	56	0.9	0.89	0.05	3580	3.95	53.3

** Secant Modulus of Masonry Prisms

* Calculated based on Stafford Smith's method (Fig. 5.2)

+ Yield strength of longitudinal bars in columns

Table 5.3. Lateral Strength of Test Specimens Predicted by Simple Analytical Models.

Specimen No.	Specimen Label	V_{wcr} (kips)	V_{crush}^{+} (kips)	V_{u1} (kips)	V_{u2} (kips)	V_{u3} (kips)	V_{u4} (kips)	V_{u5} (kips)	Actual Load V_{ua}^{*} (kips)	Actual Failure Mode **
4	wwl	33.8	36.9	53.8	43.1	45.4	43.9	**36.8**	36.5	5
5	wsl	110.0	112	101.2	**67.4**	90.4	107.5	88.1	60.0	2
6	swl	29.1	41.7	75.5	63.4	59.4	55.7	**45.7**	46.6	5
7	ssl	99.0	118.1	119.0	**85.2**	117.5	124.7	90.8	110.0	4+5
8	wwl	33.8	36.9	53.8	43.1	45.4	43.9	**36.8**	42.7	4+5
9	wsl	110.0	112	101.2	**67.4**	90.4	107.5	88.1	65.8	2
10	wws	32.0	46.7	52.5	45.5	45.4	43.8	**35.3**	42.6	5
11	wss	96.7	127.3	91.6	**72.2**	90.4	108.8	75.4	65.8	2
13 ++	wwl	66.1	73.8	89.2	70.6	90.8	87.8	**63.7**	67.7	5
14 ++	wsl	200.8	224.0	170.4	**114.3**	180.8	215.0	148.8	101.0	2

* Maximum lateral resistance from experiment

\+ Based on Stafford Smith's method.

** Failure mode in Fig. 5.5 that is closest to the experimental observation

++ Two-bay frames

difference is within 17% for Specimen 10, 12% for Specimens 5, 11, and 14, 6% for Specimen 13, and 2% for the others. However, a 22% difference is observed between the analytical and experimental results for Specimen 7.

CHAPTER 6

FINITE ELEMENT ANALYSIS

6.1 Introduction

The finite element method can be a powerful analytical tool for evaluating the behavior of structures under different load and design conditions. Once a model has been calibrated with experimental data, it can be used for numerical parametric studies to further our understanding of the behavior of a structure under different conditions. It is particularly useful for infilled structures, whose behavior depends upon a large number of parameters.

Several investigators have used the finite element method to model the behavior of infilled frames. Dhanasekar and Page (1986), and Liauw and Lo (1988) have used linear and nonlinear beam elements to model the behavior of steel frames, and simple interface elements to model the interaction between the infill and the frame. Dhanasekar and Page have used a nonlinear orthotropic model to simulate the behavior of brick panels, while Liauw and Lo have used a simple smeared crack model to simulate the behavior of micro-concrete infills. Schmidt (1989) has used smeared crack elements for both reinforced concrete frames and brick infills. In all these analyses, infill panels have been modeled as homogeneous materials, and the effects of mortar joints have been smeared out. The performance of these models has only been validated with limited test results.

Shing et al. (1994) have furthered the above mentioned work by

modeling the R/C frame and masonry units with smeared crack elements, and developing a cohesive dilatant interface model to simulate the behavior of mortar joints between masonry units as well as the behavior of the frame-to-panel interface. In the above analysis, the shear reinforcement in a R/C frame has been represented by a smeared overlay, and the longitudinal bars in the frame have been modeled with bar elements. For the reinforcing steel, an elastic-hardening plastic behavior has been considered.

This study is a continuation of the aforementioned work. A new interface constitutive model has been developed for mortar joints to account for the behavior that has not been apprppriately considered in previous models. The capability of the new model has been validated by experimental results on mortar joints and rock joints. Furthermore, a bond-slip model has been developed to consider the relative displacement between reinforcing bars and concrete. The influence of bond slip on the behavior of R/C frames with and without infill is investigated. These models have been implemented in the finite element code FEAP (Zienkiewicz 1989), and have been validated with the experimental results presented in a previous chapter. In this study, the concrete frame and masonry units are modeled with the smeared crack model developed by Lotfi and Shing (1991), which is summarized in the following section.

6.2 Smeared Crack Model for Concrete and Masonry Units

The smeared crack model developed by Lotfi and Shing (1991) has the following features. A J_2-plasticity model with an isotropic strain-hardening/softening law is utilized for modeling an uncracked material. The plasticity model is combined with the Rankine tension-cutoff criterion to signal the onset of

cracking. The failure criteria are shown in terms of the principal stresses, σ_1 and σ_2, in Fig. 6.1a. The von Mises yield criterion can be expressed as

$$f = J_2 - \frac{1}{3}\sigma_e^2(\epsilon_p) = 0 \tag{6.1}$$

in which J_2 is the second invariant of the deviatoric stress, σ_e is the effective stress, and ϵ_p is the effective plastic strain. The isotropic strain-hardening/softening is governed by $\sigma_e = \sigma_e(\epsilon_p)$, which consists of a parabolic curve and an exponential tail as shown in Fig. 6.1d.

A crack initiates when the maximum principal stress reaches the tensile strength, f_t', in a direction normal to the maximum principle stress. The cracked material is assumed to be nonlinear orthotropic with the axes of orthotropy, $n-t$, normal and tangential to the direction of the crack (Fig. 6.1b). For a coaxial rotating crack model, which is considered in this study, the crack direction and the axes of orthotropy rotate with the principal axes of strain in such a way that the crack remains normal to the direction of the maximum principal strain. The incremental stress-strain relation for a cracked material in the local $n-t$ coordinates can be expressed as:

$$d\hat{\boldsymbol{\sigma}} = \hat{\mathbf{D}}^c d\hat{\epsilon} \tag{6.2}$$

in which $\hat{\boldsymbol{\sigma}} = \{\sigma_n\ \sigma_t\ \sigma_{nt}\}^T$, $\hat{\epsilon} = \{\epsilon_n\ \epsilon_t\ 2\epsilon_{nt}\}^T$, and $\hat{\mathbf{D}}^c = \text{Diag}[E_{nn}\ ,\ E_{tt}\ ,\ G_{nt}]$. In this study, E_{nn} is modeled as an exponentially decaying function of the normal strain (Fig. 6.1c). For the case of a coaxial rotating crack, the shear modulus is given by $G_{nt} = (\sigma_1 - \sigma_2)/2(\epsilon_1 - \epsilon_2)$, where σ_1 and σ_2 are the principal stresses, and ϵ_1 and ϵ_2 are the principal strains (Bazant 1983). The tangent modulus in the direction parallel to the crack is represented by E_{tt}.

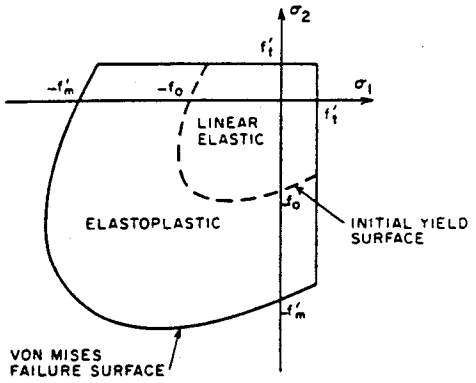

(a) Failure Criteria

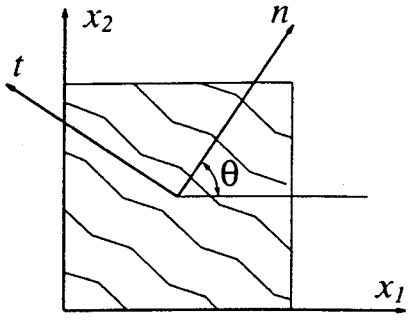

(b) Crack Orientation

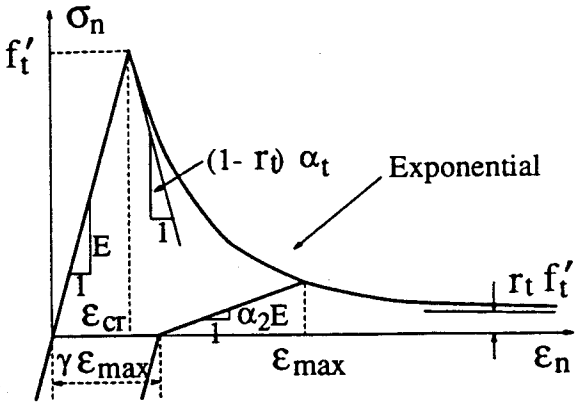

(c) Tension-Stiffening

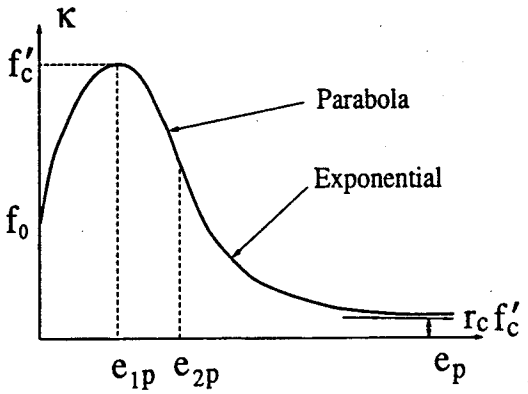

(d) Effective Stress-Effective Plastic Strain Curve

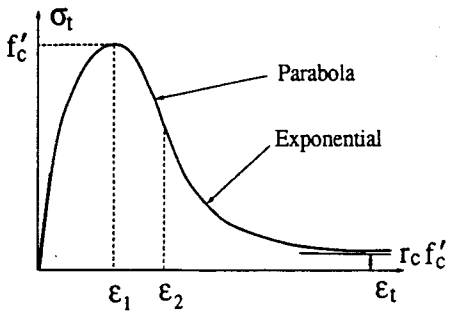

(e) Uniaxial Behavior Parallel to the Crack

Figure 6.1. Smeared Crack Constitutive Model.

The compression behavior in a direction parallel to the crack is modeled by a nonlinear hardening/softening law similar to the uniaxial compressive behavior given by the plasticity model for an uncracked material. Additional details of the crack model can be found in Lotfi and Shing (1991).

6.3 Dilatant Interface Constitutive Model

Among numerous constitutive models proposed for the modeling of the behavior of concrete, rock, and mortar joints, those capable of modeling the initiation and propagation of fracture under combined normal and shear stresses are limited. In this respect, the plasticity-based interface constitutive models proposed by Stankowski (1990), Carol and Prat (1991), Hohberg (1992), and Lotfi and Shing (1994) are among the few exceptions. Lotfi and Shing (1994) have developed a plasticity-based constitutive model for concrete and mortar joints. They used a Mohr-Coulomb-type failure surface, whose evolution is controlled by a set of internal variables. A non-associated flow rule is used in this model to properly account for the shear dilatancy effect, which can have a significant influence on the response of a confined interface. However, there are still some aspects of the physical behavior of interfaces which have not been considered properly in the aforementioned model. These include the compressive hardening behavior of interfaces, the reversal of shear dilatancy in the case of cyclic loading, and the normal contraction of an interface under shear sliding. These phenomena have been observed from experimental studies on rock and mortar joints, as described in the following paragraphs.

The study conducted on rock joints by Yow and Goodman (1987) has shown that an interface can exhibit a nonlinear hardening behavior under compression. This is similar to classical contact problems, in which the normal

force-normal displacement response can show a very large stiffness under a high compressive force. This can also be observed in mortar joints that have soft mortar fillings, such as the head joints in masonry and the joints at wall-to-frame interfaces.

Furthermore, experimental results on rock joints (Wibowo et al. 1991) and mortar joints (Amadei et al. 1989) have shown that a relative shear displacement results in a normal expansion which is called shear dilatancy. It has also been shown that this dilatancy is reversible, i.e., changing the direction of the relative shear displacement reverses the normal dilatation. In rock joints, the presence of asperities, as shown in Fig. 6.2, is the source of this kind of behavior. In mortar joints, this is usually caused by an inclined fracture plane.

Relative shear displacement under a high compressive stress can result in the crushing and wearing of asperities in an interface. The level of crushing depends on the quality of the material and the level of the compressive stress. This results in a normal contraction. The results of shear tests conducted on rock joints by Wibowo et al. (1991) and mortar joints by Amadei et al. (1989) have shown the compaction of interfaces under cyclic shear displacements and constant normal forces.

The aforementioned physical properties of interfaces are incorporated in the constitutive model proposed here.

6.3.1 Constitutive Model. The physical properties discussed in the previous section are modeled in the following manner. The nonlinear hardening behavior of an interface under a compressive stress is assumed to be an elastic phenomenon. No dilatation is assumed in the elastic regime. In the plastic regime, the total shear dilatation exhibited by an interface is considered

to be the sum of the normal compaction and the geometric dilatation. The latter is due to the wedging action of the asperities, as shown in Fig. 6.2. Owing to the reversible nature of this dilatation, it is conceived as a geometric phenomenon. This dilatation is thus represented as a function of the angle θ of the asperity and the shear displacement, as shown in Fig. 6.2. Although there is not a definite asperity angle for interfaces in general, the averaging method commonly used in rock mechanics (Rengers 1970) can be employed to define a representative angle for a finite length of an interface. On the other hand, the normal contraction of an interface, due to the loss of loose particles, is an irreversible phenomenon which can be modeled by the plasticity theory.

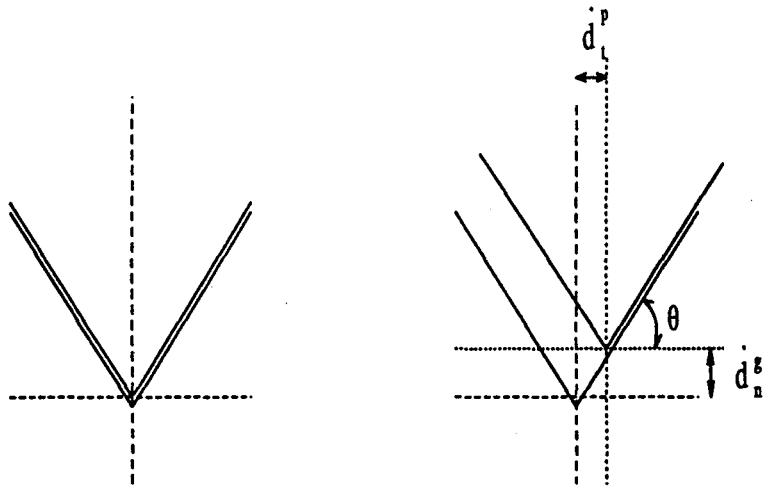

Figure 6.2. Interface Asperities.

Based on the above discussions, the relative displacements between the top and bottom faces of an interface is decomposed into an elastic part, a plastic part, and a geometric part as follows.

$$\dot{\mathbf{d}} = \dot{\mathbf{d}}^e + \dot{\mathbf{d}}^p + \dot{\mathbf{d}}^g \tag{6.3}$$

where

$$\mathbf{d}^e = \begin{Bmatrix} d_n^e \\ d_t^e \end{Bmatrix} \qquad \mathbf{d}^p = \begin{Bmatrix} d_n^p \\ d_t^p \end{Bmatrix} \qquad \mathbf{d}^g = \begin{Bmatrix} d_n^g \\ 0 \end{Bmatrix} \tag{6.4}$$

in which subscripts n and t denote the directions normal and tangential to the interface, as shown in Fig 6.3. The superscripts e, p, and g denote the elastic, plastic, and geometric portions of the relative displacements, respectively. The superposed dot represents differentiation with respect to time.

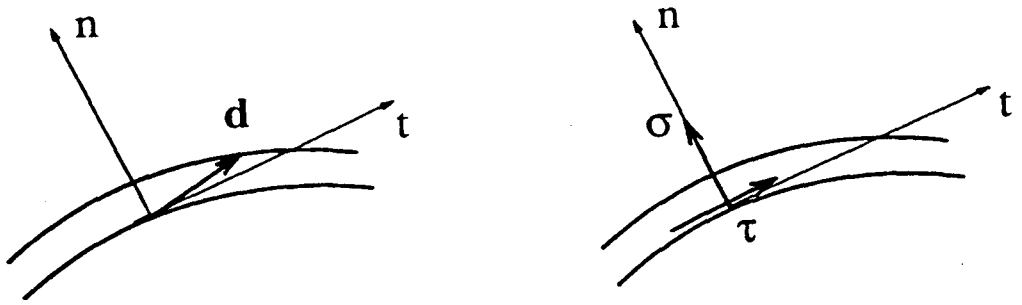

Figure 6.3. Local Coordinate System.

Elastic Regime

In this study, the elastic response is governed by

$$\boldsymbol{\sigma} = \mathbf{D}^e \mathbf{d}^e \tag{6.5}$$

in which $\boldsymbol{\sigma} = \{\sigma \quad \tau\}^T$, where σ is the normal stress and τ is the shear stress, and $\mathbf{D}^e$ =Diag $[D_{nn}\ ,\ D_{tt}]$, a diagonal matrix of elastic constants. Matrix $\mathbf{D}^e$ represents the linear or nonlinear elastic stiffness of an interface, which may

depend on the stress state. It may also serve as penalty parameters to enforce the impenetrability condition. In these respects, the elastic shear stiffness, D_{tt}, is assumed constant. The elastic normal stiffness, D_{nn}, is constant in tension and varies with respect to the normal relative displacement in compression, i.e.,

$$D_{nn} = \frac{K_{nn}\delta}{d_n^e + \delta} \qquad \text{for} \quad -\delta < d_n^e \leq 0 \tag{6.6}$$

in which K_{nn} is the initial normal stiffness of the interface, δ is the closing distance of the interface, and d_n^e is the normal component of the elastic relative displacement. This relation is illustrated in Fig. 6.4.

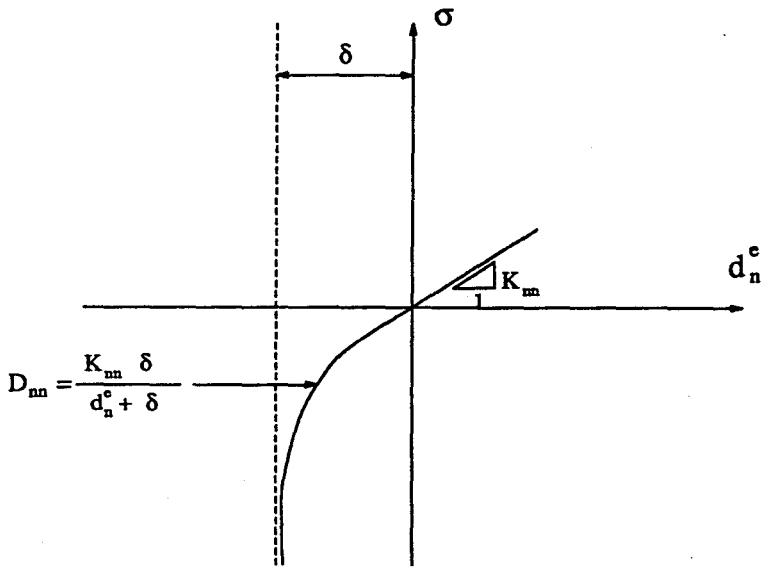

Figure 6.4: Nonlinear Elastic Compression Behavior.

Plastic Regime

Combining Eqs. 6.3 and 6.5, one can express the stresses in a rate form as

$$\dot{\boldsymbol{\sigma}} = \mathbf{D}^e(\dot{\mathbf{d}} - \dot{\mathbf{d}}^p - \dot{\mathbf{d}}^g) \tag{6.7}$$

Yield Criterion

A three-parameter hyperbolic yield criterion proposed by Lotfi and Shing (1994) for cohesive interfaces is adopted here. This is expressed as

$$F(\boldsymbol{\sigma}, \mathbf{q}) = \tau^2 - \mu^2(\sigma - s)^2 + 2r(\sigma - s) = 0 \tag{6.8}$$

in which r is the radius of curvature at the vertex of the hyperbola, s is the tensile resistance, and μ is the slope of the asymptotes, as shown in Fig. 6.5. It can be shown that $r = (c^2 - \mu^2 s^2)/2s$, where c represents cohesion. In the above formula, tensile stress is considered positive. The internal variables $\mathbf{q} = \{s \;\; r \;\; \mu\}^T$ control the evolution of the yield surface. As shown in Fig. 6.5, $\mathbf{q}_0 = \{s_0 \;\; r_0 \;\; \mu_0\}^T$ denotes the internal variables for an intact interface, while $\mathbf{q}_r = \{0 \;\; r_r \;\; \mu_r\}^T$ denotes the residual values characterizing the final state of an interface.

Non-Associated Flow Rule

To model the normal compaction of an interface due to the loss of materials and the opening of a fractured interface, a non-associated flow rule is proposed. Experimental results (e.g., Amadei et al. 1989) have indicated that the higher the compressive stress is, the larger is the compaction of the interface. To model this behavior, the plastic potential is defined as

$$Q(\boldsymbol{\sigma}) = \frac{1}{2}[\eta\tau^2 + (\sigma + a)^2] \tag{6.9}$$

in which η is a parameter that controls the loss of materials and a is a small

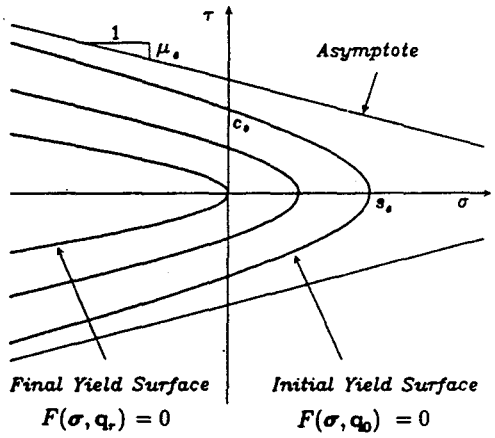

Figure 6.5. Hyperbolic Yield Criterion

positive constant used to define the direction of the plastic flow at $\sigma = \tau = 0$. The direction of the plastic relative displacement is governed by the flow rule as

$$\dot{\mathbf{d}}^p = \dot{\lambda}\frac{\partial Q}{\partial \boldsymbol{\sigma}} = \dot{\lambda}\mathbf{m} \tag{6.10}$$

in which $\dot{\lambda}$ is the plastic multiplier.

As illustrated in Fig. 6.6, as the compressive stress increases, the compaction increases as well. The proposed plastic potential also provides a lower compaction for materials with a higher shear strength. The contraction of the interface occurs only under a compressive stress that is bigger than a.

Dilatancy

As it has been discussed before, the shear dilatancy is considered as the sum of the geometric dilatation and normal plastic compaction. As shown in Fig. 6.2, the geometric dilatation occurs only after fracture and can be

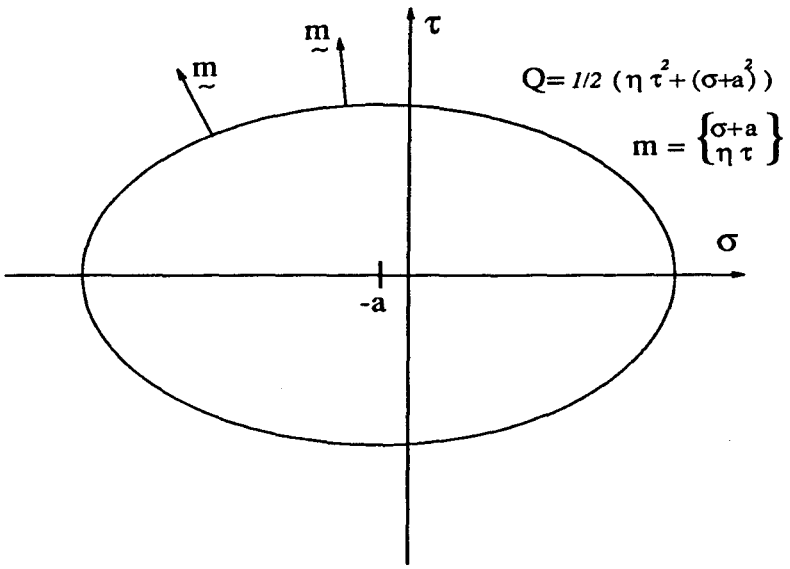

Figure 6.6. Non-Associated Flow Rule

expressed as a function of the plastic shear displacement as

$$\dot{d}_n^g = \text{sign}(d_t^p)\dot{d}_t^p\zeta \tag{6.11}$$

Hence,

$$\dot{\mathbf{d}}^g = \mathbf{A}\dot{\mathbf{d}}^p \tag{6.12}$$

where

$$\mathbf{A} = \begin{bmatrix} 0 & \text{sign}(d_t^p)\zeta \\ 0 & 0 \end{bmatrix} \tag{6.13}$$

in which $\zeta = \tan\theta$ and θ is the inclination angle of the asperities. Therefore, the total shear dilatancy, $\dot{d}_n^D$, is

$$\dot{d}_n^D = \text{sign}(d_t^p)\dot{d}_t^p\zeta + \dot{d}_n^p \tag{6.14}$$

With Eqs. 7, 10, and 12, one has

$$\dot{\boldsymbol{\sigma}} = \mathbf{D}^e(\dot{\mathbf{d}} - \dot{\lambda}\mathbf{B}\mathbf{m}) \tag{6.15}$$

where

$$\mathbf{B} = \mathbf{I} + \mathbf{A} = \begin{bmatrix} 1 & sign(d_t^p)\zeta \\ 0 & 1 \end{bmatrix} \tag{6.16}$$

Evolution of Internal Variables

The evolution of the internal variables $\mathbf{q}$ is governed by a set of work softening rules expressed as

$$s = s_0(1 - \frac{\dot{\kappa_1}}{G_1^f} - \frac{\dot{\kappa_2}}{G_2^f}) \tag{6.17}$$

$$r = r_r + (r_0 - r_r)e^{-\beta\kappa_3} \tag{6.18}$$

$$\mu = \mu_r + (\mu_0 - \mu_r)e^{-\alpha\kappa_3} \tag{6.19}$$

in which G_1^f and G_2^f represent Mode-I and Mode-II fracture energies, α and β are two material parameters that control the rate of softening, and κ_1, κ_2, and κ_3 are intermediate variables representing plastic work. They are computed with the following equations.

$$\dot{\kappa_1} = < \sigma > \dot{d_n^p} \tag{6.20}$$

$$\dot{\kappa_2} = (\tau - \tau_{r1}\text{sign}(\tau))\dot{d_t^p} \tag{6.21}$$

$$\dot{\kappa_3} = (\tau_{r1} - \tau_{r2})\text{sign}(\tau)\dot{d_t^p} \tag{6.22}$$

in which $< . >$ is the Macauley bracket (i.e., $< x >= (x + |x|)/2)$). For a given state, τ_{r1} corresponds to the shear capacity under the current normal stress when the tensile strength is exhausted, while τ_{r2} corresponds to the residual shear capacity given by the final yield surface under the same normal stress. The above equations can be written in a compact form as

$$\dot{\boldsymbol{\kappa}} = \mathbf{H}(\boldsymbol{\sigma})\dot{\mathbf{d}}^p = \dot{\lambda}\mathbf{H}(\boldsymbol{\sigma})\mathbf{m} \tag{6.23}$$

in which

$$\mathbf{H} = \begin{bmatrix} < \sigma > & 0 \\ 0 & \tau - \tau_{r1}\text{sign}(\tau) \\ 0 & (\tau_{r1} - \tau_{r2})\text{sign}(\tau) \end{bmatrix} \tag{6.24}$$

Hence,

$$\dot{\mathbf{q}} = (\frac{\partial \mathbf{q}}{\partial \boldsymbol{\kappa}})\dot{\boldsymbol{\kappa}} = \dot{\lambda}\mathbf{h}(\boldsymbol{\sigma}, \mathbf{q}) \tag{6.25}$$

where

$$\mathbf{h} = (\frac{\partial \mathbf{q}}{\partial \boldsymbol{\kappa}})\mathbf{H}\mathbf{m} \tag{6.26}$$

For the compression-shear region, it follows from the yield criterion that

$$\tau_{r1}^2 = \mu^2\sigma^2 - 2r\sigma \tag{6.27}$$

$$\tau_{r2}^2 = \mu^2\sigma^2 - 2r_r\sigma \tag{6.28}$$

It is assumed that τ_{r1} and τ_{r2} are zero in the tension-shear region. The tensile softening rules given by Eqs. 6.17 to 6.19 represent an enhancement of the original proposal of Stankowski (1990) (Lotfi and Shing 1994).

Furthermore, experimental results indicate that, for a given compressive stress, the change of dilatancy with respect to the shear displacement decreases with increasing cumulative tangential displacement (e.g., see Pande et al. 1990). This requires that the inclination slope of the asperities decreases with respect to the cumulative plastic work performed by shear. To this end, the following rule is proposed.

$$\zeta = \zeta_r + (\zeta_0 - \zeta_r)e^{-\gamma\kappa_3} \tag{6.29}$$

in which ζ_r and ζ_0 are the residual and initial values of ζ, and γ is a material parameter which controls the rate of decrease of ζ.

The loading and unloading satisfy the Kuhn-Tucker conditions:

$$F \leq 0 \quad , \quad \dot{\lambda} \geq 0 \quad , \quad F\dot{\lambda} = 0 \tag{6.30}$$

6.3.2 Stress Update Algorithm/Return Mapping. In the displacement-based finite element method, the incremental deformation is given and the update of the stress state is strain driven. Consequently, upon discretization in time, the problem of integrating the rate constitutive relation can be stated as follows: given $\boldsymbol{\sigma}_n$, $\boldsymbol{\kappa}_n$, and $\mathbf{d}_n$ at time $t = t_n$, evaluate $\boldsymbol{\sigma}_{n+1} = \boldsymbol{\sigma}_n + \Delta\boldsymbol{\sigma}_n$ and $\boldsymbol{\kappa}_{n+1} = \boldsymbol{\kappa}_n + \Delta\boldsymbol{\kappa}_n$ for a prescribed value of $\mathbf{d}_{n+1} = \mathbf{d}_n + \Delta\mathbf{d}_n$ at time $t = t_{n+1} = t_n + \Delta t_n$.

Splitting of Constitutive Relations

For the integration of the above constitutive relations, the return mapping algorithm based on the operator-splitting method proposed by Ortiz (1981) is adopted. The algorithm is based on the elastic prediction-plastic correction that satisfies the consistency requirement. The convergence and stability of the algorithm have been addressed by Simo and Ortiz (1985), and

Ortiz and Simo (1986). The rate constitutive relation to be considered here can be summarized as follows.

$$\begin{aligned}
\dot{\mathbf{d}} &= \dot{\mathbf{d}}^e + \dot{\mathbf{d}}^p + \dot{\mathbf{d}}^g \\
\dot{\boldsymbol{\sigma}} &= \mathbf{D}^e \dot{\mathbf{d}}^e \\
\dot{\mathbf{d}}^p &= \dot{\lambda}\mathbf{m}(\boldsymbol{\sigma}, \mathbf{q}) \\
\dot{\mathbf{q}} &= \dot{\lambda}\mathbf{h}(\boldsymbol{\sigma}, \mathbf{q}) \\
\dot{\mathbf{d}}^g &= \mathbf{A}\dot{\mathbf{d}}^p
\end{aligned} \tag{6.31}$$

According to the operator-splitting method, the rate equations are decomposed into an **elastic** part, a **plastic** part, and a **geometric** part as follows.

Elastic Part:

$$\begin{aligned}
\dot{\mathbf{d}} &= \dot{\mathbf{d}}^e + \dot{\mathbf{d}}^p + \dot{\mathbf{d}}^g \\
\dot{\boldsymbol{\sigma}} &= \mathbf{D}^e \dot{\mathbf{d}} \\
\dot{\mathbf{d}}^p &= 0 \\
\dot{\mathbf{q}} &= 0 \\
\dot{\mathbf{d}}^g &= 0
\end{aligned} \tag{6.32}$$

Plastic part:

$$\begin{aligned}
\dot{\mathbf{d}} &= 0 \\
\dot{\boldsymbol{\sigma}} &= -\mathbf{D}^e \dot{\mathbf{d}}^p \\
\dot{\mathbf{d}}^p &= \dot{\lambda}\mathbf{m}(\boldsymbol{\sigma}, \mathbf{q}) \\
\dot{\mathbf{q}} &= \dot{\lambda}\mathbf{h}(\boldsymbol{\sigma}, \mathbf{q}) \\
\dot{\mathbf{d}}^g &= 0
\end{aligned} \tag{6.33}$$

Geometric Part:

$$\begin{aligned} \dot{\mathbf{d}} &= 0 \\ \dot{\boldsymbol{\sigma}} &= -\mathbf{D}^e \dot{\mathbf{d}}^g \\ \dot{\mathbf{d}}^p &= 0 \\ \dot{\mathbf{q}} &= 0 \\ \dot{\mathbf{d}}^g &= 0 \end{aligned} \tag{6.34}$$

The sum of the right-hand sides of Eqs. 6.32, 6.33, and 6.34 will result in the right-hand side of Eq. 6.31. In Eq. 6.32 (elastic prediction), the plastic strains and internal variables are taken to be unchanged and the applied displacement increment is assumed to be totally elastic. For the other two parts, there is no additional displacement increment. The sum of Eqs. 6.33 and 6.34 represents the plastic correction:

$$\begin{aligned} \dot{\mathbf{d}} &= 0 \\ \dot{\boldsymbol{\sigma}} &= -\mathbf{D}^e(\dot{\mathbf{d}}^p + \dot{\mathbf{d}}^g) = -\dot{\lambda}\mathbf{D}^e\mathbf{B}\mathbf{m}(\boldsymbol{\sigma}, \mathbf{q}) \\ \dot{\mathbf{d}}^p &= \dot{\lambda}\mathbf{m}(\boldsymbol{\sigma}, \mathbf{q}) \\ \dot{\mathbf{q}} &= \dot{\lambda}\mathbf{h}(\boldsymbol{\sigma}, \mathbf{q}) \\ \dot{\mathbf{d}}^g &= \mathbf{A}\dot{\mathbf{d}}^p \end{aligned} \tag{6.35}$$

Linearization of Yield Function

The plastic correction for stresses and internal variables is carried out in an iterative fashion. In every iteration, the yield function $\mathbf{F}$ is linearized around the current states, $\boldsymbol{\sigma}_{n+1}^{(i)}$ and $\mathbf{q}_{n+1}^{(i)}$, to obtain

$$F \approx F(\boldsymbol{\sigma}_{n+1}^{(i)}, \mathbf{q}_{n+1}^{(i)}) + (\frac{\partial F}{\partial \boldsymbol{\sigma}})^T_{(\boldsymbol{\sigma}_{n+1}^{(i)}, \mathbf{q}_{n+1}^{(i)})} (\boldsymbol{\sigma} - \boldsymbol{\sigma}_{n+1}^{(i)}) + (\frac{\partial F}{\partial \mathbf{q}})^T_{(\boldsymbol{\sigma}_{n+1}^{(i)}, \mathbf{q}_{n+1}^{(i)})} (\mathbf{q} - \mathbf{q}_{n+1}^{(i)}) = 0$$

or

$$F \approx F_{n+1}^{(i)} + (\boldsymbol{\nu}_{n+1}^{(i)})^T(\boldsymbol{\sigma} - \boldsymbol{\sigma}_{n+1}^{(i)}) + (\boldsymbol{\xi}_{n+1}^{(i)})^T(\mathbf{q} - \mathbf{q}_{n+1}^{(i)}) = 0 \tag{6.36}$$

where

$$\boldsymbol{\nu} = \frac{\partial F}{\partial \boldsymbol{\sigma}} \qquad \boldsymbol{\xi} = \frac{\partial F}{\partial \mathbf{q}}$$

For iterative correction, the rate equations for stress and internal variables (Eq. 6.35) can be expressed by the following approximations.

$$\begin{aligned} \boldsymbol{\sigma}_{n+1}^{(i+1)} - \boldsymbol{\sigma}_{n+1}^{(i)} &= -\Delta\lambda \mathbf{D}_{n+1}^{(i)} \mathbf{B}_{n+1}^{(i)} \mathbf{m}_{n+1}^{(i)} \\ \mathbf{q}_{n+1}^{(i+1)} - \mathbf{q}_{n+1}^{(i)} &= \Delta\lambda \mathbf{h}_{n+1}^{(i)} \end{aligned} \tag{6.37}$$

in which $\Delta\lambda$ is an incremental plastic parameter, and $\mathbf{D}_{n+1}^{(i)}$,$\mathbf{B}_{n+1}^{(i)}$,$\mathbf{m}_{n+1}^{(i)}$,and $\mathbf{h}_{n+1}^{(i)}$ are the values of $\mathbf{D}$,$\mathbf{B}$,$\mathbf{m}$,and $\mathbf{h}$ at the state $(\boldsymbol{\sigma}_{n+1}^{(i)}, \mathbf{q}_{n+1}^{(i)})$. By substituting Eq. 6.37 into Eq. 6.36, the value of $\Delta\lambda$ can be obtained as

$$\Delta\lambda = \frac{F_{n+1}^{(i)}}{(\boldsymbol{\nu}_{n+1}^{(i)})^T \mathbf{D}_{n+1}^{(i)} \mathbf{B}_{n+1}^{(i)} \mathbf{m}_{n+1}^{(i)} - (\boldsymbol{\xi}_{n+1}^{i})^T \mathbf{h}_{n+1}^{(i)}} \tag{6.38}$$

where

$$\mathbf{h}_{n+1}^{(i)} = (\frac{\partial \mathbf{q}}{\partial \boldsymbol{\kappa}})_{n+1}^{(i)} \mathbf{H}_{n+1}^{(i)} \mathbf{m}_{n+1}^{(i)} \tag{6.39}$$

in which $\mathbf{H}$ is defined in Eq. 6.24.

In each iteration, evaluating matrix $\mathbf{H}$ based on the current stress state, which can be far beyond the yield surface, can result in excessive plastic work. Consequently, this causes an unrealistic change of the internal variables. Therefore, in this model, the expression for $\mathbf{h}_{n+1}^{(i)}$ has been changed to

$$\mathbf{h}_{n+1}^{(i)} = (\frac{\partial \mathbf{q}}{\partial \boldsymbol{\kappa}})_{n+1}^{(i)} \mathbf{H}_n \mathbf{m}_{n+1}^{(i)} \tag{6.40}$$

in which $\mathbf{H}_n$ denotes matrix $\mathbf{H}$ that is based on the converged stress state in the previous incremental step.

Substitution of $\Delta\lambda$ into Eq. 6.37 gives the stresses, $\boldsymbol{\sigma}_{n+1}^{(i+1)}$, and internal variables, $\mathbf{q}_{n+1}^{(i+1)}$. The process is repeated until $F_{n+1}^{(i)}$ converges to 0 within a prescribed tolerance.

The Algorithm

Step 1: Displacement Update

$$\mathbf{d}_{n+1} = \mathbf{d}_n + \Delta\mathbf{d}_n$$

Step 2: Elastic Predictor

$$\mathbf{d}_{n+1}^{p(0)} = \mathbf{d}_n^p$$

$$\mathbf{d}_{n+1}^{g(0)} = \mathbf{d}_n^g$$

$$\mathbf{d}_{n+1}^{e(0)} = \mathbf{d}_{n+1} - \mathbf{d}_{n+1}^{p(0)} - \mathbf{d}_{n+1}^{g(0)}$$

$$\mathbf{q}_{n+1}^{(0)} = \mathbf{q}_n$$

$$\zeta_{n+1}^{(0)} = \zeta_n$$

$$\boldsymbol{\sigma}_{n+1}^{(0)} = \boldsymbol{\sigma}(\mathbf{d}_{n+1}^{e(0)})$$

Step 3: Check for Yielding

$$\text{If} \qquad F_{n+1}^{(0)} \leq 0 \quad , \quad \text{then}$$

$$\mathbf{d}_{n+1}^{p} = \mathbf{d}_{n+1}^{p(0)},\ \mathbf{d}_{n+1}^{g} = \mathbf{d}_{n+1}^{g(0)},\ \mathbf{d}_{n+1}^{e} = \mathbf{d}_{n+1}^{e(0)}$$

$$\boldsymbol{\sigma}_{n+1} = \boldsymbol{\sigma}_{n+1}^{(0)},\ \mathbf{q}_{n+1} = \mathbf{q}_{n+1}^{(0)},\ \zeta_{n+1} = \zeta_{n+1}^{(0)}$$

go to Step 1.

Otherwise, set $i = 0$ and go to the next step.

Step 4: Update Stresses and Internal Variables

$$\Delta\lambda^{(i)} = \frac{F_{n+1}^{(i)}}{(\boldsymbol{\nu}_{n+1}^{(i)})^T \mathbf{D}_{n+1}^{(i)} \mathbf{B}_{n+1}^{(i)} \mathbf{m}_{n+1}^{(i)} - (\boldsymbol{\xi}_{n+1}^{(i)})^T \mathbf{h}_{n+1}^{(i)}}$$

$$\boldsymbol{\sigma}_{n+1}^{(i+1)} = \boldsymbol{\sigma}_{n+1}^{(i)} - \Delta\lambda^{(i)} \mathbf{D}_{n+1}^{(i)} \mathbf{B}_{n+1}^{(i)} \mathbf{m}_{n+1}^{(i)}$$

$$\mathbf{q}_{n+1}^{(i+1)} = \mathbf{q}_{n+1}^{(i)} + \Delta\lambda^{(i)} \mathbf{h}_{n+1}^{(i)}$$

$$\zeta_{n+1}^{(i+1)} = \zeta_{n+1}^{(i)} + (\zeta_0 - \zeta_r) e^{-\gamma \dot{\kappa}_3}$$

Step 5: Check Convergence

If $\quad | F_{n+1}^{(i+1)} | \leq Tol. \quad ,$ then

$$\boldsymbol{\sigma}_{n+1} = \boldsymbol{\sigma}_{n+1}^{(i+1)},\ \mathbf{q}_{n+1} = \mathbf{q}_{n+1}^{(i+1)},\ \zeta_{n+1} = \zeta_{n+1}^{(i+1)},\ \mathbf{d}_{n+1}^{e} = (\mathbf{D}^{e})^{-1} \boldsymbol{\sigma}_{n+1}$$

$$d_{tn+1}^{p} = d_{tn+1} - d_{tn+1}^{e},\ d_{nn+1}^{g} = d_{nn+1}^{g} + (d_{tn+1}^{p} - d_{tn}^{p}) \zeta_{n+1}$$

$$d_{nn+1}^{p} = d_{nn+1} - d_{nn+1}^{e} - d_{nn+1}^{g}$$

Otherwise, set $i = i + 1$ and go to step 4.

6.3.3 Numerical Verifications. Three sets of direct shear tests have been selected to validate the capability of the proposed interface model for simulating the behavior of different types of interfaces. For the calibration of the model, data from three shear tests under different levels of normal stress are required. In the case of mortar joints, the interface has a finite thickness and the elastic properties can be computed directly from the properties of the mortar

itself. However, experimental results on mortar joints show that the actual elastic stiffness is always much lower than the calculated value. Therefore, the elastic shear and normal stiffnesses, D_{nn} and D_{tt}, of mortar joints and rock joints are both found based on experimental results. Furthermore, it is desirable to have data from a tension test and a shear test to deduce the values of G_f^I and G_f^{II}. However, in the absence of data from such tests, the values of these parameters are obtained by trial and error in the calibration process.

The shear tests conducted by Amadei et al. (1989) on clay bricks have been chosen to provide one set of experimental data. In these tests, the clay bricks are 92 x 55 x 193 mm in size, and the mortar has a cement:lime:sand ratio of 1:1.5:4.5 by volume. The results of three tests, under constant normal forces of 18, 49, and 158 kN, have been used to calibrate the model. The values of the parameters obtained from the calibration are shown in Table 6.1. Figures 6.7 and 6.8 show the shear force-shear displacement curves obtained from the test and finite element analysis, respectively. As the results show, the model was able to capture the peak and residual shear resistances, and the decline of the shear strength. Figures 6.9 and 6.10 show the normal displacement-shear displacement curves obtained from the test and numerical analysis, respectively. The specimen under a 18-kN normal force is also analyzed to show the capability of the calibrated model for simulating the shear behavior under different normal forces. The experimental and numerical results of shear force-vs.-shear displacement for this specimen are shown in Figs. 6.11 and 6.12. Figures 6.13 and 6.14 show the normal displacement-shear displacement curves obtained from the test and the numerical analysis, respectively. The numerical results are in good agreement with the experimental curves. As it can be seen in Fig.

6.9, the normal displacement drops considerably at every turning point of the relative shear displacement. This is due to loss of materials during the shear cycles.

Table 6.1. Material Parameters for Mortar Joints in Clay Brick Masonry.

K_{nn} (psi)	δ (in.)	D_{tt} (psi)	s_0 (psi)	G_f^I (psi-in.)	G_f^{II} (psi-in.)	μ_0	μ_r
12000	0.3	42000	95	1.61	16.1	0.79	0.65

α	r_0	r_r	β	ζ_0	ζ_r	γ	η
0.5	42	5	2	0.6	0.025	2.3	300

Shear tests conducted in this study on mortar joints of hollow and solid concrete block specimens have been used to calibrate the interface model for the analysis of infilled frames later on. In these tests, the concrete blocks are 4 x 4 x 8 in. in size, and the mortar has a cement:lime:sand ratio of 1:0.5:4.5 by volume. The results of three tests, under constant normal stresses of 75, 100, and 150 psi, have been used to calibrate the model. The value of the parameters obtained from the calibration are shown in Tables 6.2 and 6.3 for hollow and solid concrete blocks, respectively. The experimental and numerical results for the hollow block specimen under a 100-psi normal stress are shown in Figs. 6.15 to 6.18. Figures 6.15 and 6.16 show the shear force-shear displacement curves for this specimen obtained from the test and finite element analysis, respectively. Figures 6.17 and 6.18 show the normal displacement-shear displacement curves of the same specimen obtained from the test and analysis, respectively. The results for the solid block specimen subjected to a

150-psi normal stress are shown in Figs. 6.19 to 6.22. Figures 6.19 and 6.20 show the shear force-shear displacement curves for the solid block specimen obtained from the test and analysis, respectively. The normal displacement-shear displacement curves of this specimen are shown in Figs. 6.21 and 6.22 for the test and analysis, respectively. The results show the capability of the model to simulate the cyclic behavior of a mortar joint under a constant normal pressure.

Table 6.2. Material Parameters for Mortar Joints in Hollow Concrete Block Masonry.

K_{nn} (psi)	δ (in.)	D_{tt} (psi)	s_0 (psi)	G_f^I (psi-in.)	G_f^{II} (psi-in.)	μ_0	μ_r
27820	0.2	35000	40	1.61	16.1	0.9	0.75

α	r_0	r_r	β	ζ_0	ζ_r	γ	η
4	10	5	2	0.45	0.0003	3	15.7

Table 6.3. Material Parameters for Mortar Joints in Solid Concrete Block Masonry.

K_{nn} (psi)	δ (in.)	D_{tt} (psi)	s_0 (psi)	G_f^I (psi-in.)	G_f^{II} (psi-in.)	μ_0	μ_r
27820	0.2	35000	40	1.61	16.1	0.9	0.75

α	r_0	r_r	β	ζ_0	ζ_r	γ	η
2	10	5	2	0.15	0.0003	3	55

Wibowo et al. (1991) subjected a block of welded tuff (3 x 3 x 6 in. in size) to tensile splitting to create a rock joint. They made several replicas of this joint using gypsum cement with a water-to-gypsum cement ratio of 20% and an unconfined compressive strength of 4000 psi. The results of three tests conducted on the manufactured rock joints, under constant normal forces of 2.95, 5.9, and 11.8 kips, have been used to calibrate the model. The values of the parameters obtained from the calibration are shown in Table 6.4. The result of the test under the 2.95-kip normal force has been simulated by the calibrated model. Figures 6.23 and 6.24 show the shear force-shear displacement curves obtained from the test and analysis, respectively. The normal displacement-shear displacement curves obtained from the test and analysis are shown in Figs. 6.25 and 6.26, respectively. As shown in Fig. 6.25, the specimen behaved unsymmetrically in the test. However, the numerical model can only assume a symmetric behavior. The simulated shear behavior of the rock joints under different normal forces are compared to the test results in Fig. 6.27 in terms of the shear force-shear displacement curves, and in Fig. 6.28 in terms of the normal displacement-shear displacement curves. In all cases, good agreement is observed between the experimental and analytical results.

To examine the capability of the model to simulate a nonlinear elastic behavior under compression, a mortar joint in a solid concrete block specimen has been subjected to an increasing compressive stress. Figure 6.29 shows the experimental and numerical results. For the interface model, the initial stiffness has been estimated from the experimental results and the closing distance has been adjusted to match the experimental curve. It can be seen that the

Table 6.4. Material Parameters for Rock Joint.

K_{nn} (psi)	δ (in.)	D_{tt} (psi)	s_0 (psi)	G_f^I (psi-in.)	G_f^{II} (psi-in.)	μ_0	μ_r
60000	0.03	30000	25	161	1610	0.7	0.36

α	r_0	r_r	β	ζ_0	ζ_r	γ	η
0.1	20	0	0.1	0.265	0.091	0.1	150

numerical normal stress-normal displacement curve agrees with the experimental response. However, it must be noted that the compression test could be influenced by the flexibility of the loading apparatus. Therefore, the results might not represent the actual behavior of an interface.

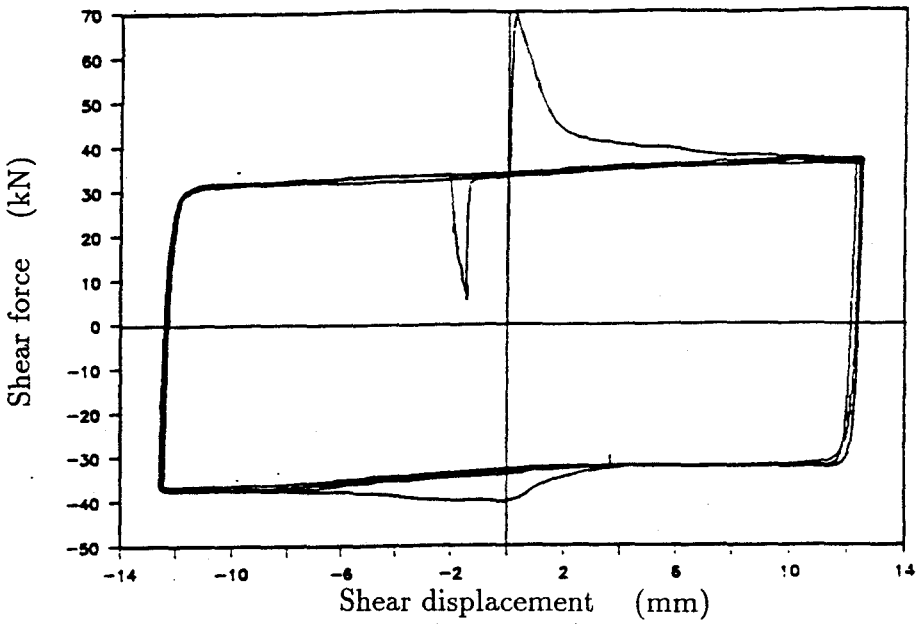

Figure 6.7. Shear force-Shear Displacement Curve for Mortar Joint in Clay Brick Masonry under 49-kN Normal Force (Experiment).

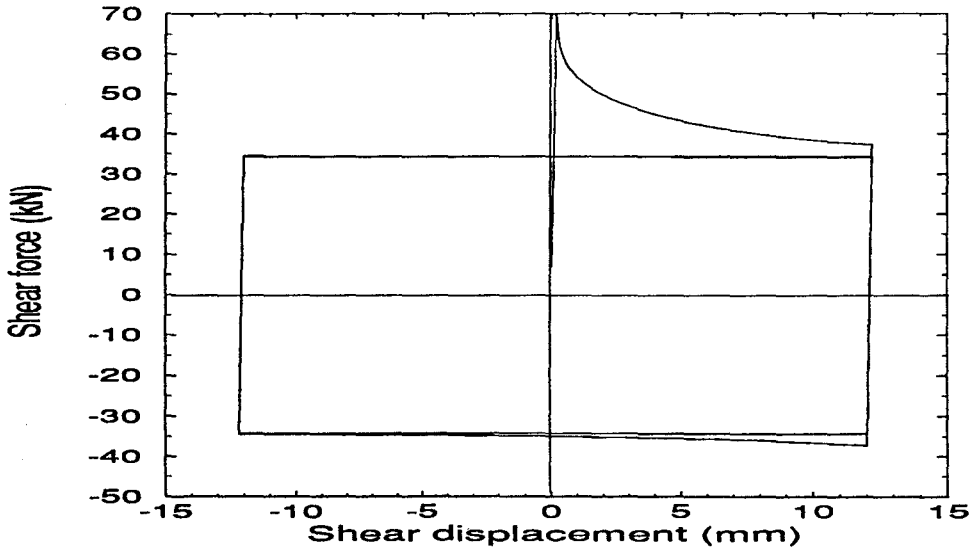

Figure 6.8. Shear Force-Shear Displacement Curve for Mortar Joint in Clay Brick Masonry under 49-kN Normal Force (Numerical Result).

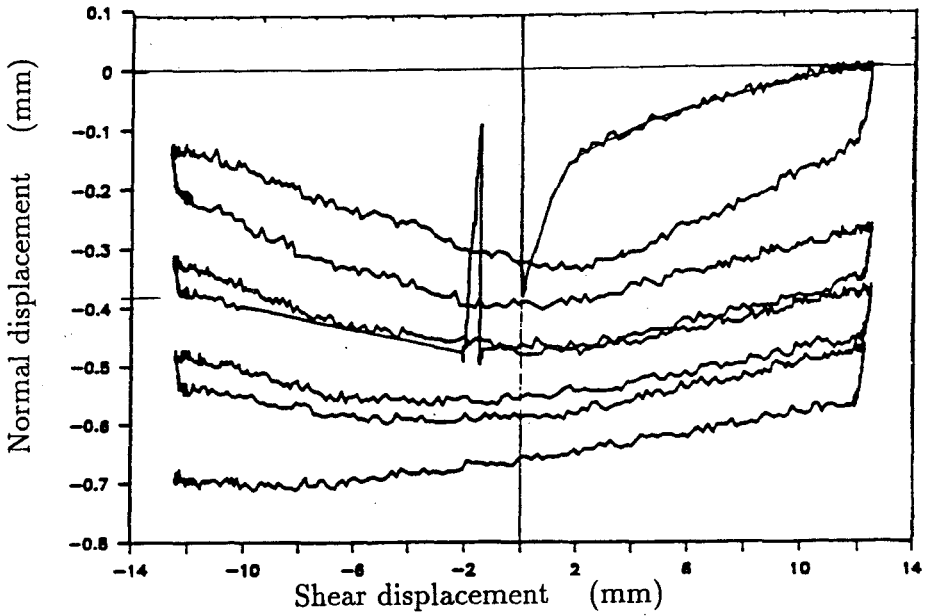

Figure 6.9. Normal Displacement-Shear Displacement Curve for Mortar Joint in Clay Brick Masonry under 49-kN Normal Force (Experiment).

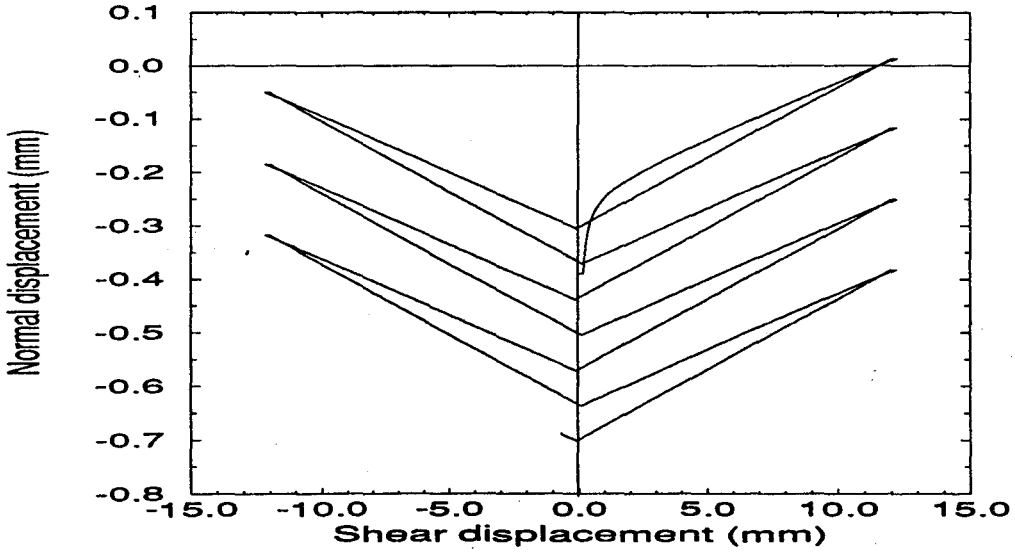

Figure 6.10. Normal Displacement-Shear Displacement Curve for Mortar Joint in Clay Bricks Masonry under 49-kN Normal Force (Numerical Result).

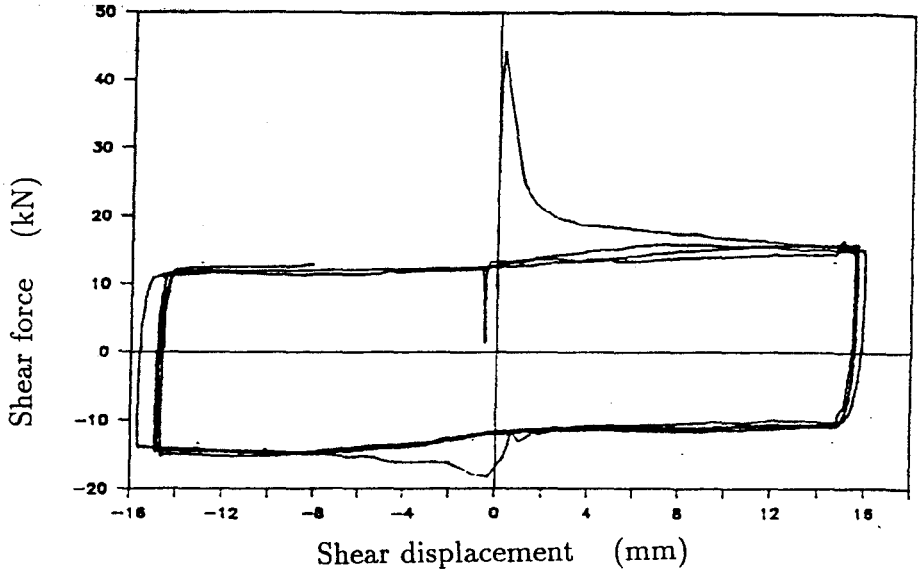

Figure 6.11. Shear force-Shear Displacement Curve for Mortar joint in Clay Brick Masonry under 18-kN Normal Force (Experiment).

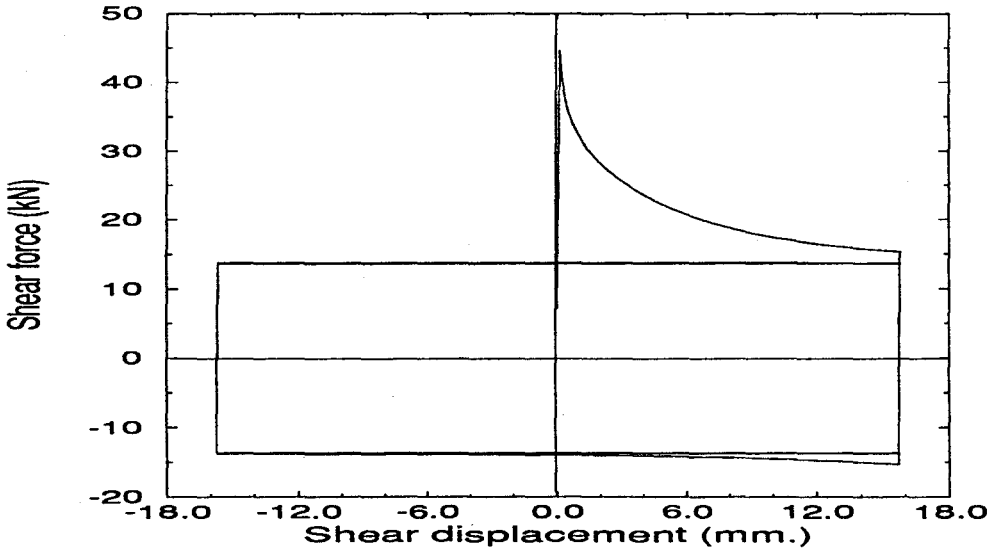

Figure 6.12. Shear Force-Shear Displacement Curve for Mortar Joint in Clay Brick Masonry under 18-kN Normal Force (Numerical Result).

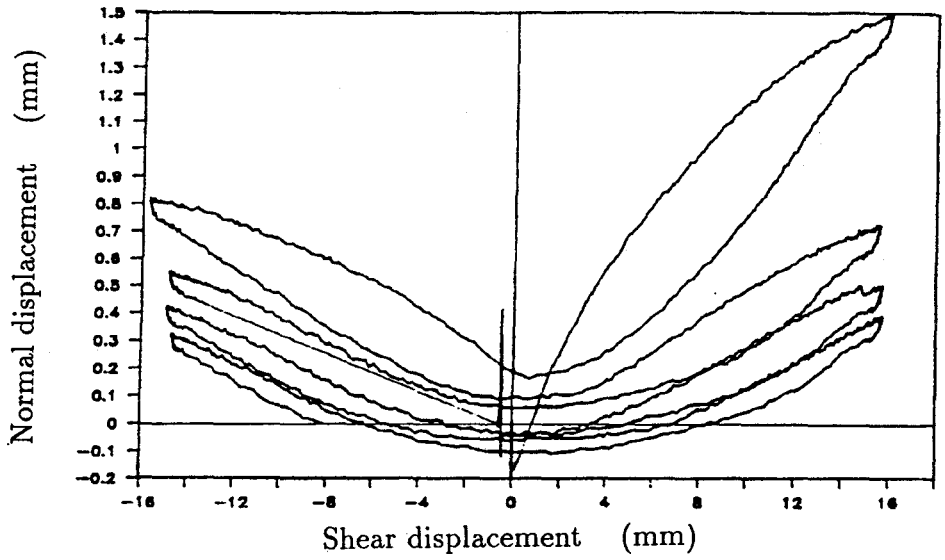

Figure 6.13. Normal Displacement-Shear Displacement Curve for Mortar Joint in Clay Brick Masonry under 18-kN Normal Force (Experiment).

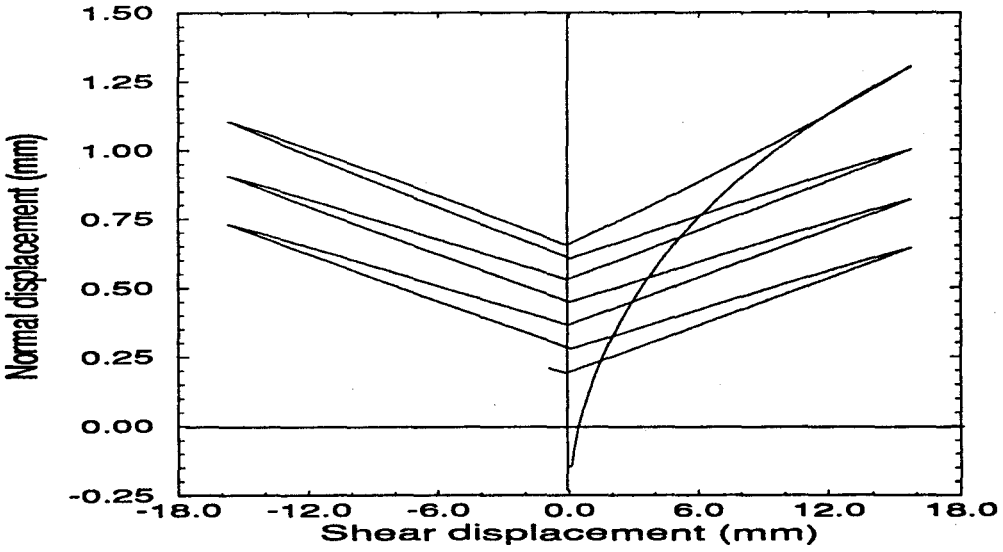

Figure 6.14. Normal Displacement-Shear Displacement Curve for Mortar Joint in Clay Brick Masonry under 18-kN Normal Force (Numerical Result).

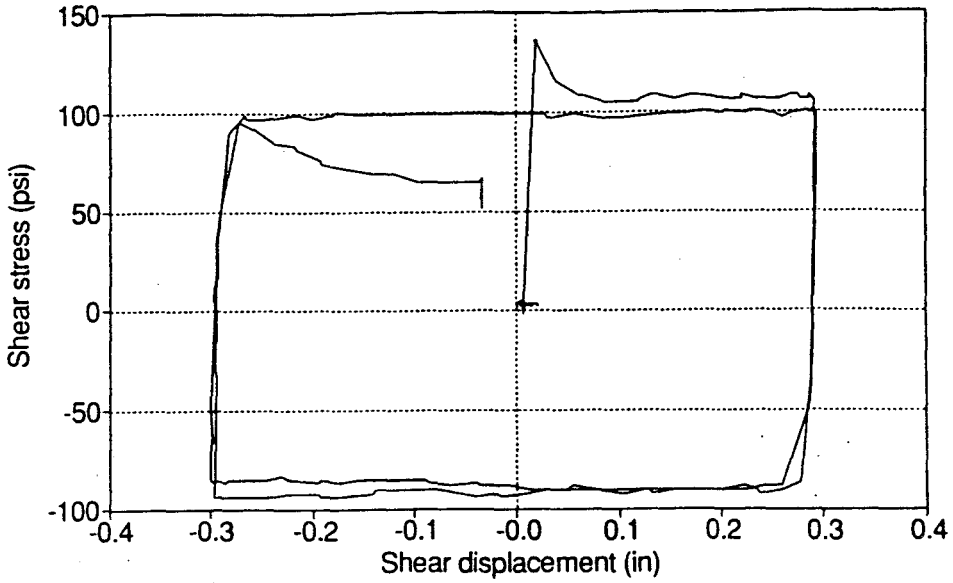

Figure 6.15. Shear Force-Shear Displacement Curve for Mortar Joint in Hollow Concrete Masonry under 100-psi Normal Stress (Experiment) .

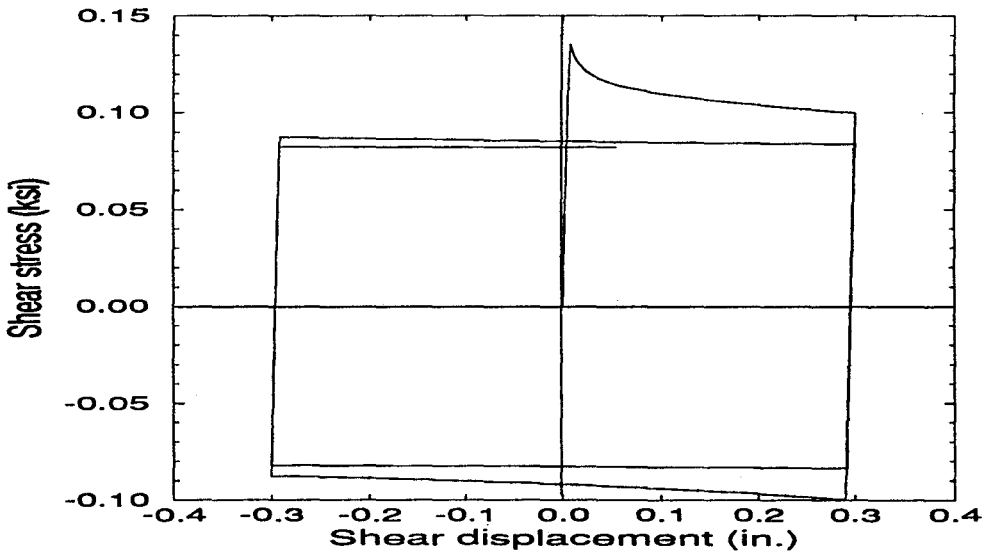

Figure 6.16. Shear Force-Shear Displacement Curve for Mortar Joint in Hollow Concrete Masonry under 100-psi Normal Stress (Numerical Result).

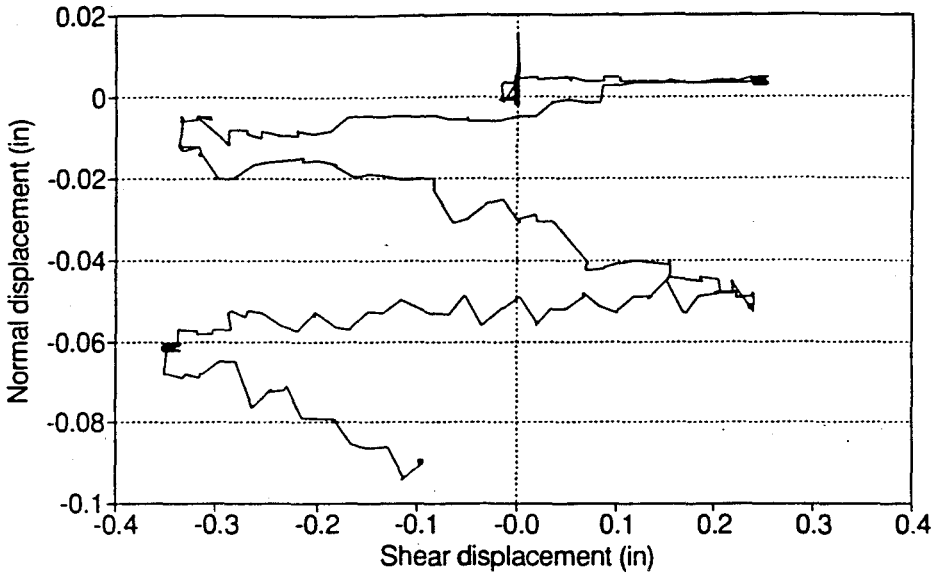

Figure 6.17. Normal Displacement-Shear Displacement Curve for Mortar Joint in Hollow Concrete Masonry under 100-psi Normal Stress (Experiment).

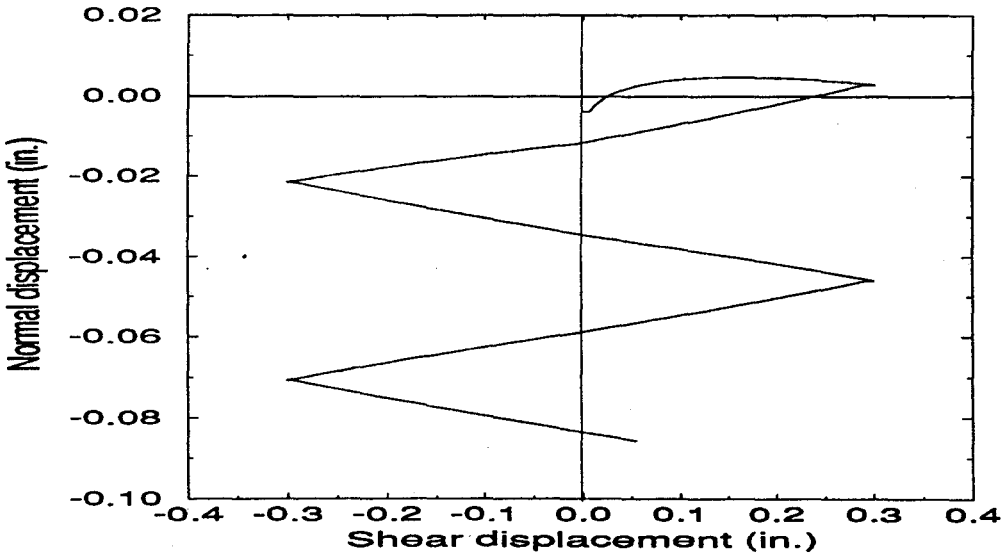

Figure 6.18. Normal Displacement-Shear Displacement Curve for Mortar Joint in Hollow Concrete Masonry under 100-psi Normal Stress (Numerical Result).

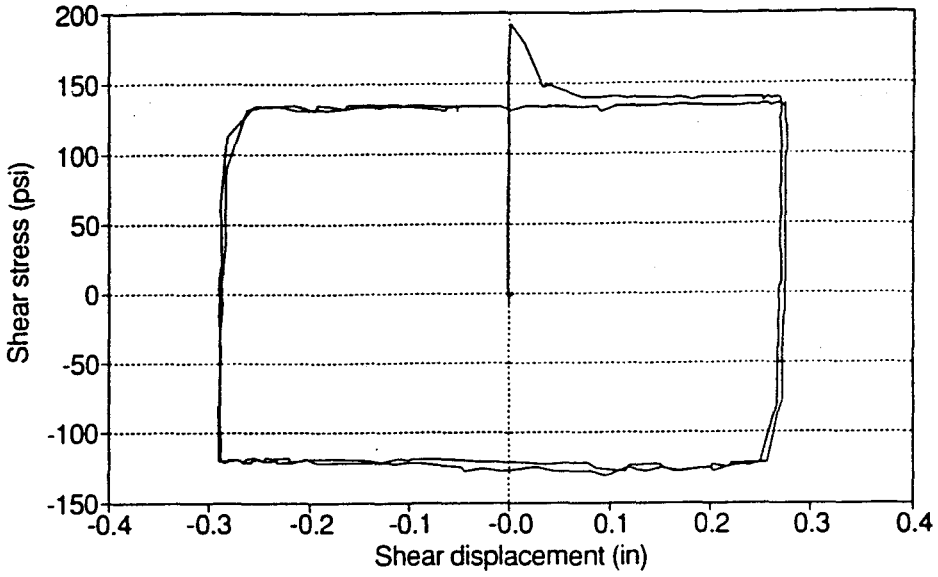

Figure 6.19. Shear Force-Shear Displacement Curve for Mortar joint in Solid Concrete Masonry under 150-psi Normal Stress (Experiment).

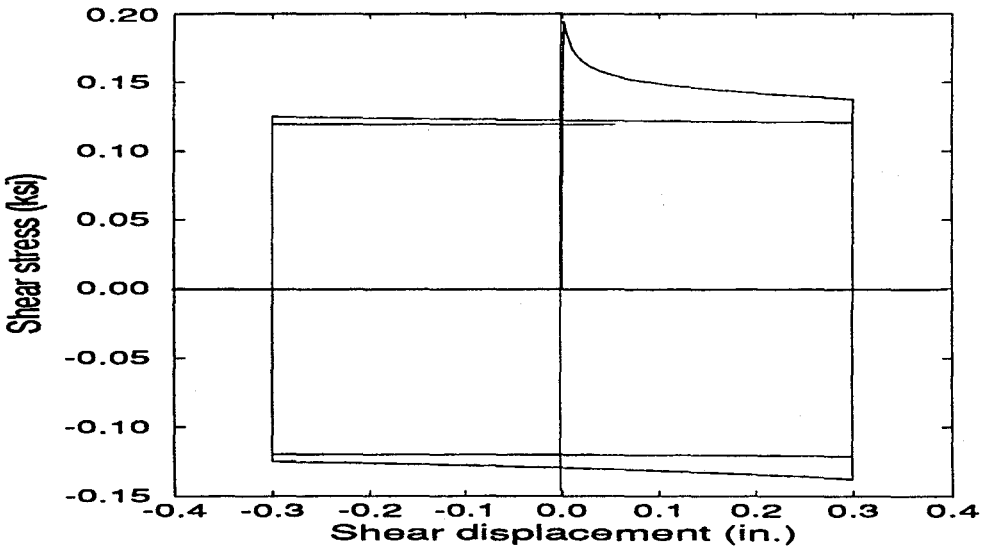

Figure 6.20. Shear Force-Shear Displacement Curve for Mortar Joint in Solid Concrete Masonry under 150-psi Normal Stress (Numerical Result).

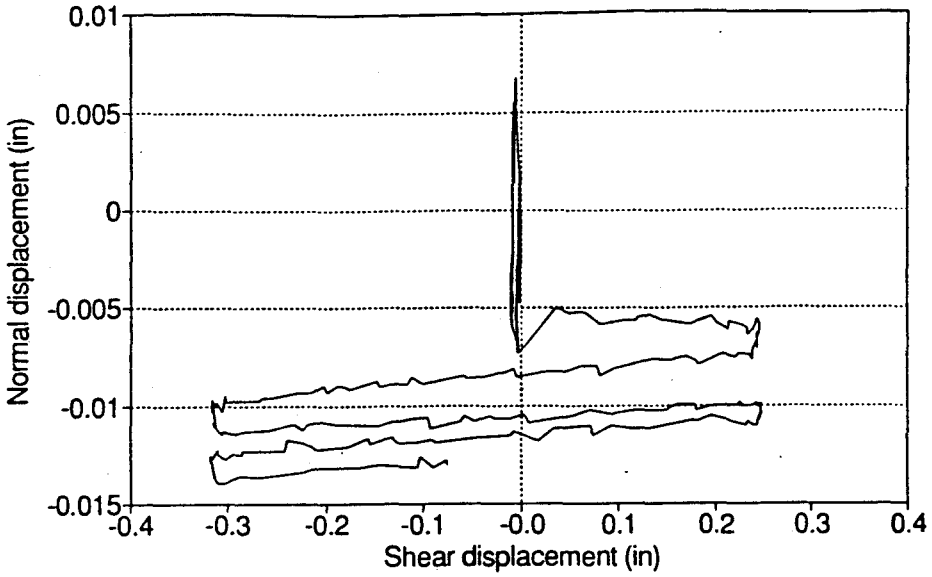

Figure 6.21. Normal Displacement-Shear Displacement Curve for Mortar Joint in Solid Concrete Masonry under 150-psi Normal Stress (Experiment).

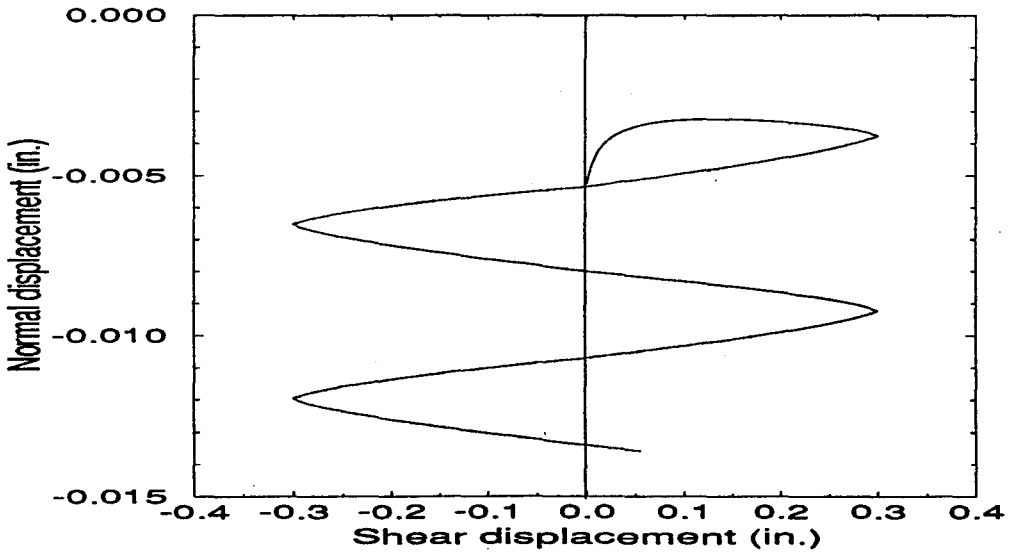

Figure 6.22. Normal Displacement-Shear Displacement Curve for Mortar Joint in Solid Concrete Masonry under 150-psi Normal Stress (Numerical Result).

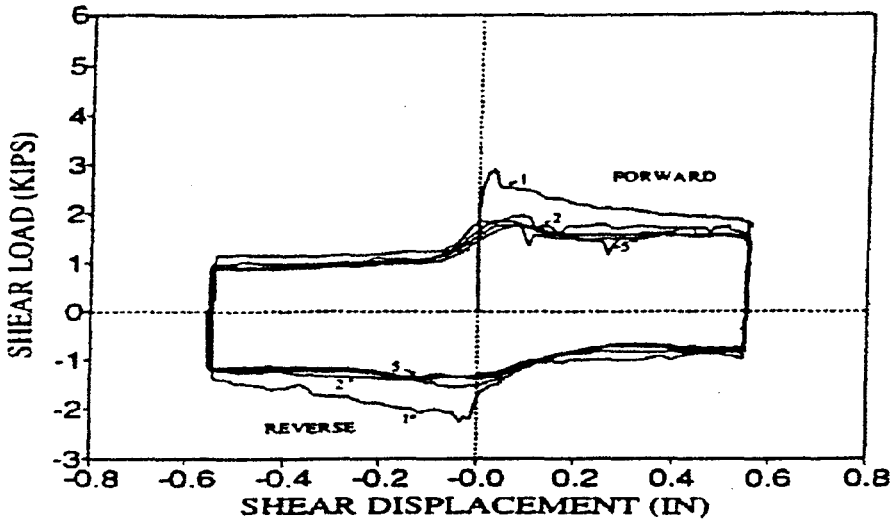

Figure 6.23. Shear Force-Shear Displacement Curve Obtained from Test of Rock Joint under 2.95-kip Normal Force (Experiment).

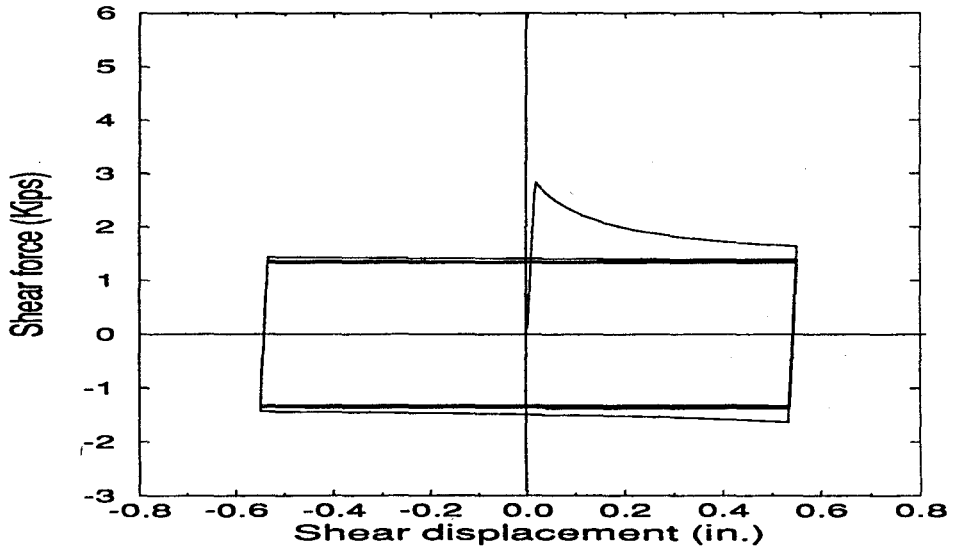

Figure 6.24. Shear Force-Shear Displacement Curve for Rock Joint under 2.95-kip Normal Force (Numerical Result).

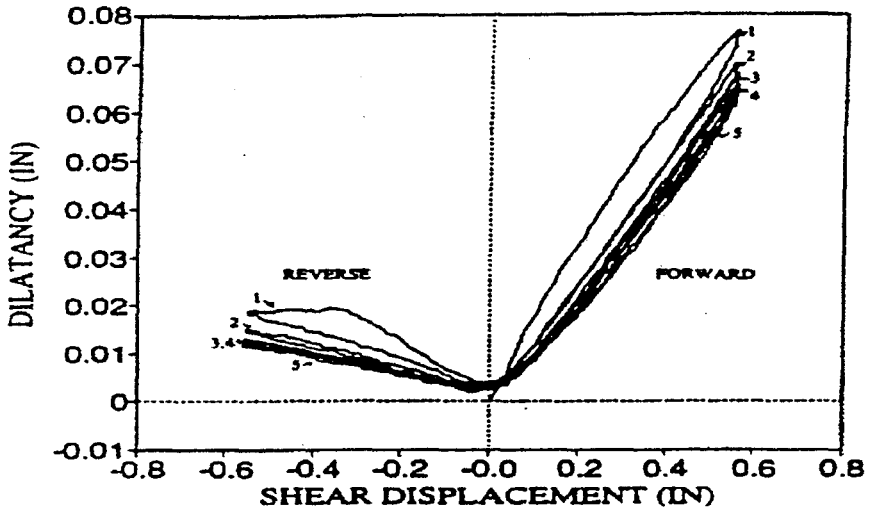

Figure 6.25. Normal Displacement-Shear Displacement Curve Obtained from Test of Rock Joint under 2.95-kip Normal Force (Experiment).

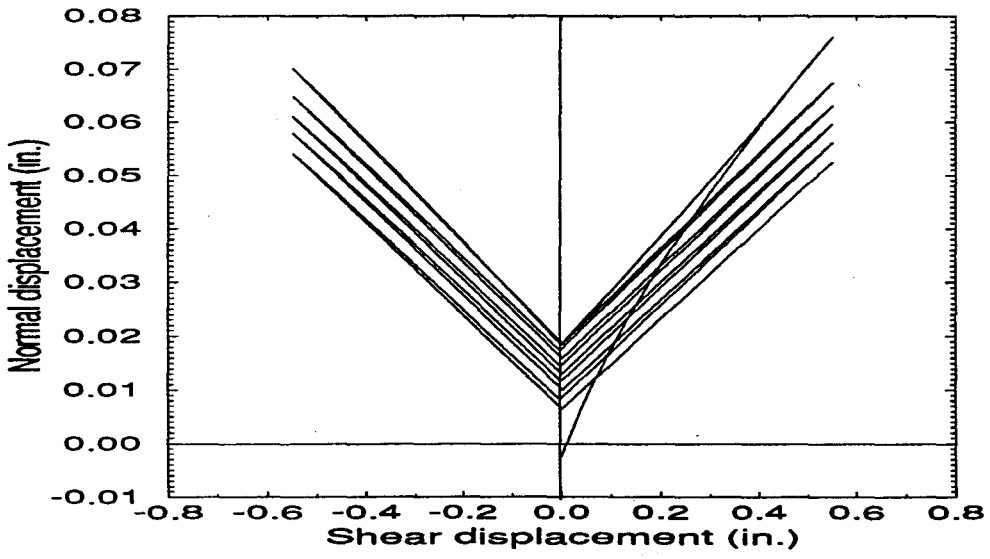

Figure 6.26. Normal Displacement-Shear Displacement Curve for Rock Joint under 2.95-kip Normal Force (Numerical Result).

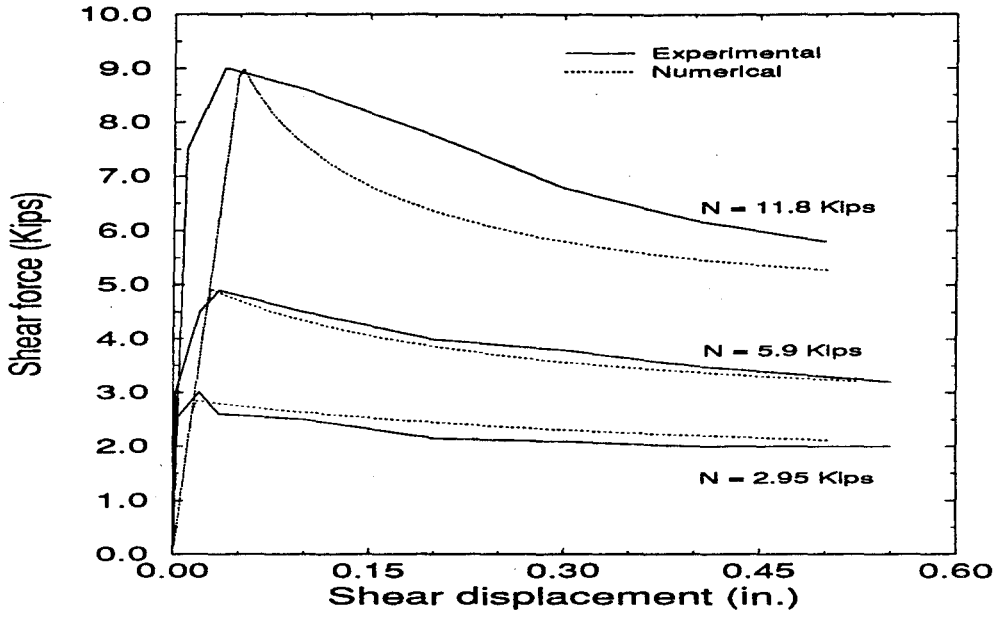

Figure 6.27. Shear Force-Shear Displacement Curves for Rock Joints under Three Different Normal Forces.

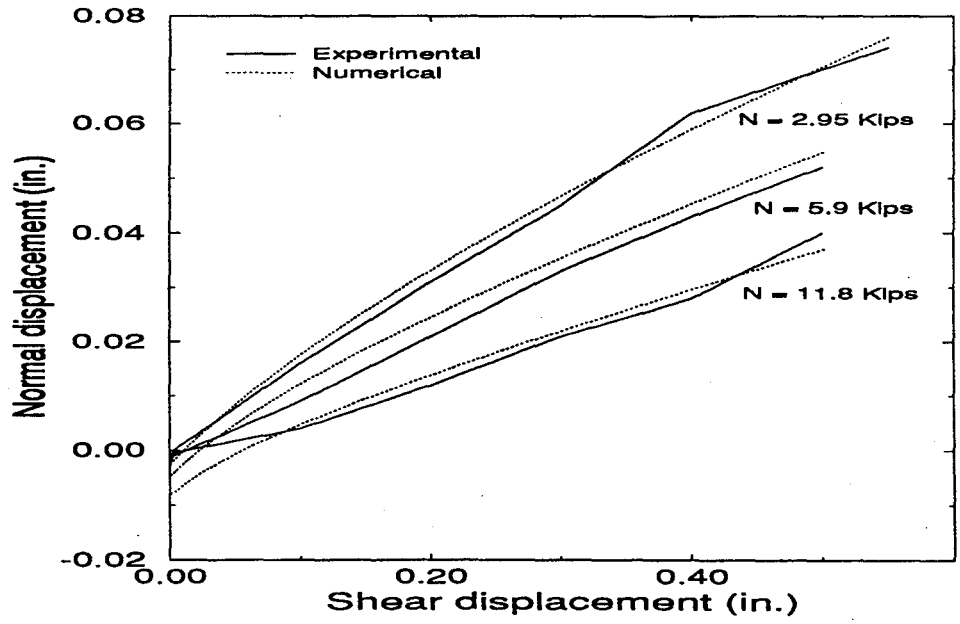

Figure 6.28. Normal Displacement-Shear Displacement Curves for Rock Joints under Three Different Normal Forces.

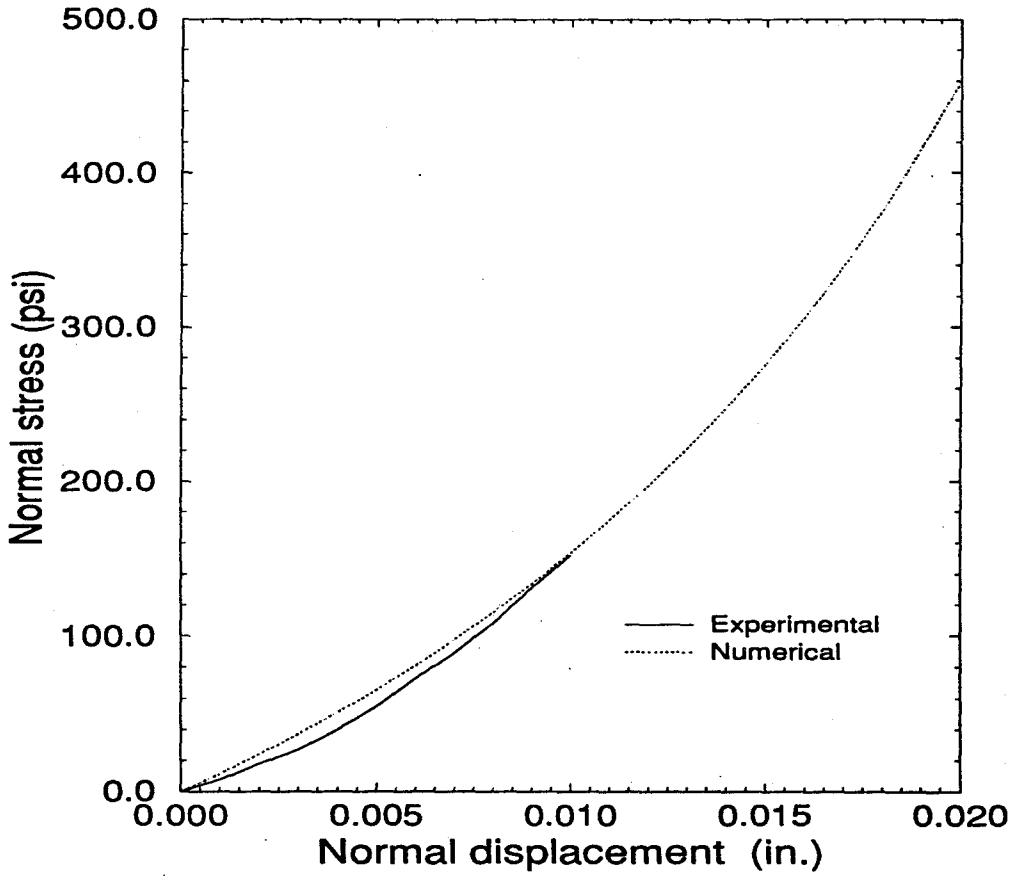

Figure 6.29. Normal Stress-Normal Displacement Curve for Mortar Joint under Pure Compression.

6.3.4 Conclusions. A plasticity-based constitutive model was proposed and successfully implemented for modeling the behavior of a large variety of interfaces including rock joints and mortar joints. In addition to separation and shear sliding, this model can simulate the nonlinear compressive behavior, reversible dilatancy, and compaction of an interface. The capability of the numerical model was validated with experimental results.

6.4 Bond-Slip Constitutive Model

6.4.1 Introduction. It has been generally recognized that the load carrying capacity and stiffness of a reinforced concrete structure depend on the bond between the steel reinforcement and concrete. In the simplified analysis of reinforced concrete structures, complete strain compatibility between the concrete and steel is usually assumed. This implies a perfect bond. The assumption of a perfect bond in cracked zones would require an infinitely high strain to account for a finite crack width, which would, therefore, prohibit a crack from opening under certain conditions. In reality, different amounts of straining develop in the concrete and reinforcing bars in the vicinity of a crack because of bond slip (Mehlhorn and Keuser 1985). The amount of slip is related to the bond stress developed at the bar-to-concrete interface.

The bond stress-slip relation involves several parameters. These include the deformation pattern of reinforcement, bar diameter, clear concrete cover, confining stresses, transverse reinforcement, the mechanical properties of concrete, concrete settlement, which sometimes leaves voids underneath the bar, and the failure mechanism of concrete surrounding the bars. The failure of concrete surrounding a reinforcing bar is usually in the form of splitting cracks or shearing and crushing of concrete keys between two consecutive steel ribs.

Developing an analytical relation incorporating all these parameters is a very difficult task. Several experimental investigations have been conducted on this subject, and different models have been proposed based on an empirical approach, or on micro- or macro-mechanical considerations. In this study, these models are reviewed and a simple and efficient bond-slip relation is selected. The constitutive model is implemented in a finite element model to capture bond slip. In this study, special considerations are paid to the bond-slip behavior of deformed bars.

6.4.2 Background on Bonding Mechanisms and Modeling.

The interaction between the concrete and deformed bars subjected to a pull-out force is characterized by a behavior consisting of four different stages (Gambarova et al. 1989). In Stage I, where the bond stress is very low, slip is prohibited by chemical adhesion. In Stage II, the bond stress is just large enough to break the chemical adhesion and the ribs of the bar exert large bearing stresses against the concrete. Transverse microcracks may originate at the tips of the ribs allowing the bar to slip a little, but the wedging action of the bars against the surrounding concrete remains limited. In Stage III, a considerable wedging action develops, which produces tensile hoop stresses in the surrounding concrete. As a result, a confining action is exerted by the concrete on the bars and the bond is provided by the bar-to-concrete interlock. Longitudinal crack initiates as a result of the hoop stress. In Stage IV, the longitudinal cracks (splitting cracks) propagate through the entire concrete cover and the bond may fail abruptly if no transverse reinforcement is provided. The presence of transverse reinforcement limits the opening of a splitting crack. Nevertheless, if the concrete cover is large, the bar spacing is large, and the confinement

pressure is high enough to resist the wedging action and the development of splitting cracks, the failure will be governed by the crushing and/or shearing of concrete keys between the steel ribs.

Effective Parameters

Among all possible parameters that may influence the bond behavior, the bar diameter, clear concrete cover, confining stress, transverse reinforcement, the mechanical properties of concrete, and load history are considered most important. The influence of other parameters, such as the end distance (the distance of the front face of the first steel rib from the loaded face of the surrounding concrete in a pull-out test), shear force causing the dowel action of the bars, bar surface condition, concrete settlement resulting in voids underneath the bars, and strain rate, are either not important or not well understood.

Bar Diameter. Giuriani et al. (1984) have carried out an experimental investigation on the bond-slip behavior of deformed bars in lightweight concrete. They have found that for small-diameter bars and a low amount of slip, the major part of the slip consists of the local crushing of concrete in front of steel ribs. In this case, larger bars resulted in a higher bond stiffness. On the other hand, for large-diameter bars and/or large slips, the splitting of concrete governs the failure. Furthermore, they have observed that the onset of splitting cracks, which is accompanied by a sudden change in stiffness, in large bars takes place at a lower bond stress than that in smaller bars.

Clear Cover. Clear cover influences the onset of the splitting of concrete. The smaller the clear cover is, the lower is the bond stress required for splitting. Morita and Kaku (1979) have noticed that increasing the clear

cover increases the ultimate bond strength but not proportionally. From the results of experimental investigations and finite element analysis, Hayashi and Kokusho (1985) have concluded that the thickness of the concrete cover does not affect the bond-slip behavior if a minimum cover of 2.5 times the bar diameter is provided.

Confining Stresses. The lateral pressure due to external lateral loadings or the confinement introduced by transverse reinforcement are the major sources of confining stresses. In any case, the confining stress increases the bond strength and provides a more ductile behavior by changing the failure mechanism from brittle splitting to ductile shearing (Robins and Standish 1984; La Borderie and Pijaudier-Cabot 1992). Morita and Kaku (1979) have observed from their experimental study that specimens having bars supported at the corners of the stirrups behaved in a more ductile manner than those with unsupported bars or with bars supported along the legs of the stirrups. Giuriani et al. (1991) have noticed that a small amount of transverse reinforcement is sufficient to prevent the splitting failure. McCabe and Darwin (1992) have explained that the ductile bond behavior in the presence of transverse reinforcement is due to the reduction of the crack width and the redistribution of the wedging forces of the bar as localized fracture occurs.

Concrete Mechanical Properties. The tensile and compressive strengths of concrete affect the onset of microcracking and splitting cracks, and the crushing/shearing of concrete keys. However, it has been observed that the bond strength is not directly proportional to the compressive strength. This is more evident for the case of splitting cracks where the tensile strength governs. The tensile strength of concrete is usually considered proportional to the square root

of its compressive strength. McCabe and Darwin (1992) have used the fracture mechanics approach to explain that in the case of high-strength concrete, the bond strength does not increase with the concrete compressive strength in the same way as in normal concrete. They explained that the fracture energy of concrete depends not only on the tensile strength of concrete, but also on the effective width of the fracture process zone over which the microcracks are assumed to be uniformly spread. The effective width is in turn proportional to the aggregate size (Bazant and Oh 1983). Although high-strength concrete is stronger in tension, it has generally a smaller aggregate size than normal concrete. The smaller the aggregate size is, the lower is the fracture energy for a constant tensile strength.

Load History. Morita and Kaku (1973) have observed that the local deterioration of a bond depends on the magnitude of the slip that have occurred previously. The larger the previous slip is, the greater is the reduction in the bond stress. The bond stiffness usually changes during unloading and reloading cycles. In general, if the bond stress in each cycle does not exceed 80% of the ultimate strength, the deterioration of the bond is slow (Giuriani et al. 1984).

Bond-Slip Relations

Several bond-slip relations have been developed to trace the bond behavior in the three different stages: adhesion, microcracking, and splitting/shearing. Most of these relations are empirical and have been calibrated with experimental results (Nilson 1968; Morita and Kaku 1973; Shipman and Gerstle 1977,1979; Mehlhorn and Keuser 1985). Some analytical relations have also been developed based on the micromechanics approach (Tepfers 1979;

Kemp and Wilhelm 1979). However, most of these analytical relations are developed only to define the critical limit states, such as the onset of the splitting crack or the failure load. There are also methods combining empirical relations with some theoretical aspects of micromechanics (Giuriani et al. 1991).

Empirical Relations

Various formulations have been proposed to represent experimentally derived bond-slip relations. Nilson (1968) and Houde (1973) have presented simple formulations expressing the bond stress as polynomial functions of average slip. In these relations, a set of coefficients have been calibrated to match the results of tests, and the various parameters mentioned above are not explicitly considered. Later, Nilson (1971) has modified his relation to account for the effect of the concrete strength and end distance. However, these formulations are not applicable to cases of large slips.

Morita and Kaku (1973) have proposed a bilinear relation based on their pull-out/push-in tests. They have also introduced unloading and reloading laws. The deterioration of the residual bond strength was based on the maximum level of slip that had occurred. The ultimate bond stress is not defined in this relation. Shipman and Gerstle (1977,1979) have modified this relation by using Nilson's simple polynomial relation for the behavior of the virgin bond. They have considered identical behavior for pull-out and push-in loads. Bond failure is assumed to occur with the opening of the splitting cracks in the absence of transverse reinforcement. In the presence of adequate transverse reinforcement, failure is assumed to be governed by the crushing of concrete in front of the steel ribs, or the shearing of the concrete keys. For behavior after failure, they have used a perfect plasticity for bars which are

supported by transverse reinforcement, and have assumed a total failure for bars not supported by transverse reinforcement. Noguchi (1985) have modified Morita and Kaku's relation by adding a criterion for the behavior after failure. Niwa et al. (1985) have used a single smooth function to express the behavior under loading, unloading and reloading. They have also introduced a residual slip and a residual bond for their relation. Mehlhorn and Keuser (1985) have used the bond stress-slip relationship originally proposed by Doerr (1978) to build their bond-slip constitutive model. Their relation starts with a smooth curve up to a maximum bond stress. The bond stress remains constant with increasing slip until the ultimate slip is reached. At this point, the bond stress drops to zero. The unloading-reloading condition is defined but the residual bond during unloading and reloading within previously attained slip limits is considered to be zero in both directions. However, none of these relations suggests an appropriate way to consider the dependency of the bond-slip behavior and the ultimate bond stress on the material properties. They do not distinguish the splitting mechanism from the shearing failure mechanism. Each of these relations has been calibrated with a special set of experiments for which it was developed. However, among these constitutive models, the relation proposed by Mehlhorn and Keuser (1985) possesses the appropriate simplicity to represent the bond behavior without loosing too much accuracy.

Gambarova et al. (1989) have developed a constitutive model for the bond behavior considering the presence of splitting cracks. The relation is for the bond behavior after the development of a full splitting crack.

Micromechanics Approach

Tepfers (1979) has considered the splitting of a concrete sleeve around

a steel bar as the bond failure mechanism. The wedging force which acts normal to the interface was considered as a hydrostatic pressure in a concrete pipe. The wall thickness of the pipe was assumed to be equal to the minimum concrete cover. Tepfers has derived the ultimate bond stress required for the cracking of the concrete along a bar. Reinhardt (1992) has modified Tepfers' model by considering concrete as a strain softening material. Kemp and Wilhelm (1979) have calibrated the coefficients of Tepfers' relation by matching with their experimental results. All these relations estimate the failure load for a pull-out test based on a splitting dominated mechanism with no transverse reinforcement. Robins and Standish (1984) have tried to relate the bond strength to the confining pressure based on micromechanical considerations. They have used Tepfers' (1979) relation to define the bond stress required for the splitting of the concrete cover. For a confining pressure of more than 30% of the compression strength of concrete, they have estimated that a shearing failure will occur under a constant bond stress of 1.8 times the tensile strength of concrete.

Giuriani et al. (1991) have used the empirical relations of Gambarova et al. (1989) for their constitutive model. In addition, they have also considered the effects of the transverse reinforcement and the residual tension of concrete on the confining pressure imposed on the longitudinal bars, after the opening of the splitting cracks, based on a micromechanics approach.

In spite of the accuracy of the micromechanical relations, they are too complicated to use in finite element modeling, specially in two-dimensional analysis.

Finite Element Models

For the finite element analysis of the bond-slip behavior, one can consider double-noded elements connecting steel to concrete. Although the bond-slip phenomenon is strongly three dimensional, most of the finite element analyses have been conducted in two dimensions, which cannot account for the splitting behavior of concrete in an appropriate manner.

The first bond-slip model used in the finite element analysis is a link element proposed by Ngo and Scordelis (1967). It consists of two orthogonal springs which connect concrete to a steel bar. The springs transfer shear and normal forces. Linear and non-linear constitutive relations, and different configurations of springs have been used for link elements. A bond-zone element has been developed by De Groot et al. (1981). This element idealizes the bond interface as a concrete sleeve with a finite dimension around a deformed bar. It accounts for both the frictional resistance and mechanical interlock between the steel and concrete. The third type of bond-slip element is an isoparametric interface element formulated and used by Mehlhorn and Keuser (1985). This element avoids the artificial discreteness of a bond link element. It represents a continuous bond over the entire steel-to-concrete interface. The element has no physical dimension normal to the interface. Linear, quadratic, and cubic interpolation rules can be used for this element by using two, three, and four double nodes, respectively. Figure 6.30 shows a quadratic interface element with three double nodes.

6.4.3 Proposed Finite Element Model. In this study, a one-dimensional isoparametric interface element is selected to model a bond interface. This is similar to the interface element proposed by Mehlhorn and

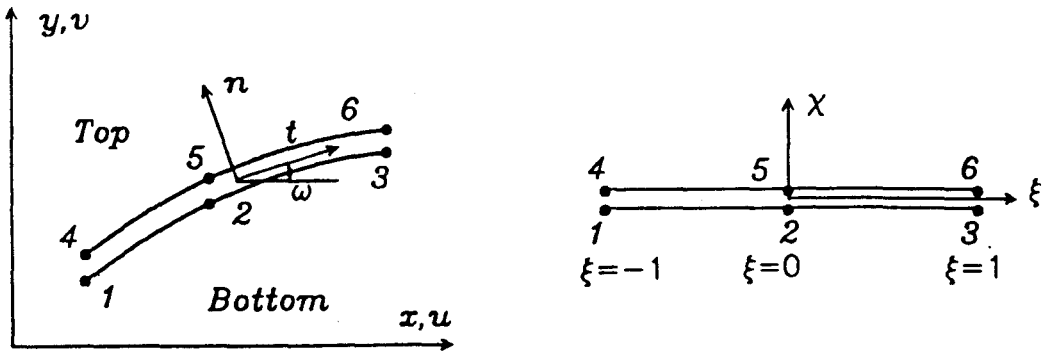

Figure 6.30. Interface Element with Local and Global Coordinates.

Keuser (1985). The relative displacement of double nodes is decomposed into two components: normal and tangential to the plane of the interface. This element is similar to the interface element used previously for mortar and rock joints.

Constitutive Model for Bond Interface

In this model, to restrict penetration and separation, a large constant stiffness is assumed for the direction normal to an interface. A nonlinear constitutive model with unloading and reloading laws, identical to the model proposed by Mehlhorn and Keuser (1985), is adopted for the bond-slip behavior. This relation is shown in Fig. 6.31. Furthermore, it is assumed that the stress-displacement relations are uncoupled in the normal and tangential directions. The bond stress-slip relation is represented by a third order polynomial curve as follows.

$$\frac{\tau_{br}}{f_{ct}} = \left\{ \begin{array}{ll} \alpha(5(\frac{\Delta_r}{\Delta_{r1}}) - 4.5(\frac{\Delta_r}{\Delta_{r1}})^2 + 1.4(\frac{\Delta_r}{\Delta_{r1}})^3) & \text{for } \Delta_r < \Delta_{r1} \\ 1.9\alpha & \text{for } \Delta_r > \Delta_{r1} \end{array} \right\} \qquad (6.41)$$

$$\alpha = \alpha_1 \alpha_2 \alpha_3 \alpha_4$$

in which τ_{br} is the bond stress, f_{ct} is the tensile strength of concrete, Δ_r is the relative tangential displacement (slip), and Δ_{r1} is the slip level at which the maximum bond stress is reached. The bond stress, τ_{br}, is defined the as bond force per unit length divided by the nominal circumference of the bar. The factor α in the above relation is intended to account for some of the physical parameters that may affect the bond behavior. α_1 is for the aggregate size, the consistency of concrete, and the position of concrete during casting; α_2 accounts for the geometry of the bar surface; α_3 takes into account the transverse pressure; and α_4 accounts for the effect of the local damage of concrete in the bond zone.

The maximum bond stress is reached at a slip level of Δ_{r1}, after which the bond stress remains constant. The bars are assumed to be confined by a large volume of concrete or a considerable amount of transverse reinforcement. Hence, the propagation of splitting cracks is constrained and the behavior is ductile. The unloading and reloading paths follow straight lines with a slope equal to the initial bond stiffness (shown by lines 2 and 3 in Fig. 6.31). Consequently, as it is shown in Fig. 6.31, the unloading of the bond stress from point A results in a residual slip equal to OB. During unloading and reloading at slip values between the previously attained limits, the bond stress is assumed to be zero. In reality, however, there are small residual stresses within this range, but their effect on the total behavior is negligible.

As it can be seen in Eq. 6.41, α affects both the ultimate bond stress and the initial bond stiffness. However, the effects of the physical parameters

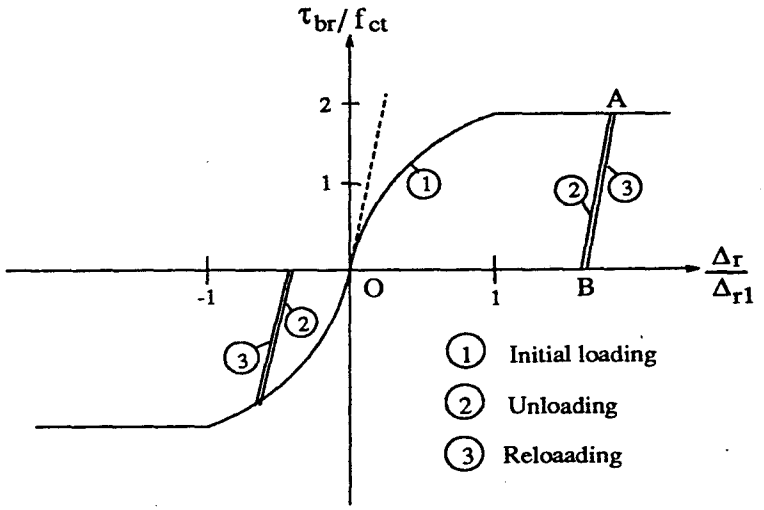

Figure 6.31. Bond Stress-Slip Relationship (Mehlhorn and Keuser 1985).

which are represented by α are either negligible or difficult to quantify. Therefore, α is assumed equal to one in this study. In a case that the ultimate bond stress and stiffness have been obtained experimentally, α can be approximately calibrated.

With α equal to one, the default value for the ultimate bond stress is $1.9f_{ct}$. It is an average value based on the empirical relations proposed by Nilson (1968), Wahla et al. (1971), Houde (1973), Mirza and MacGregor (1979), and Morita and Kaku (1973). These relations consider only deformed bars of normal sizes confined by transverse reinforcement or a large concrete cover.

For slip level Δ_{r1}, different values have been reported. They vary from 0.012 to 0.05 cm, leading to different values of bond stiffness. The default value for Δ_{r1} in the bond-slip relation is selected to be 0.04 cm. This is close to the values obtained from most of the empirical relations cited above. However, it is recognized that the bond stiffness varies with the bar diameter, specially

in the case where failure is governed by the crushing and shearing of concrete.

The proposed bond-slip constitutive model is shown by a numerical simulation in Fig. 6.32 for a single bond-slip interface.

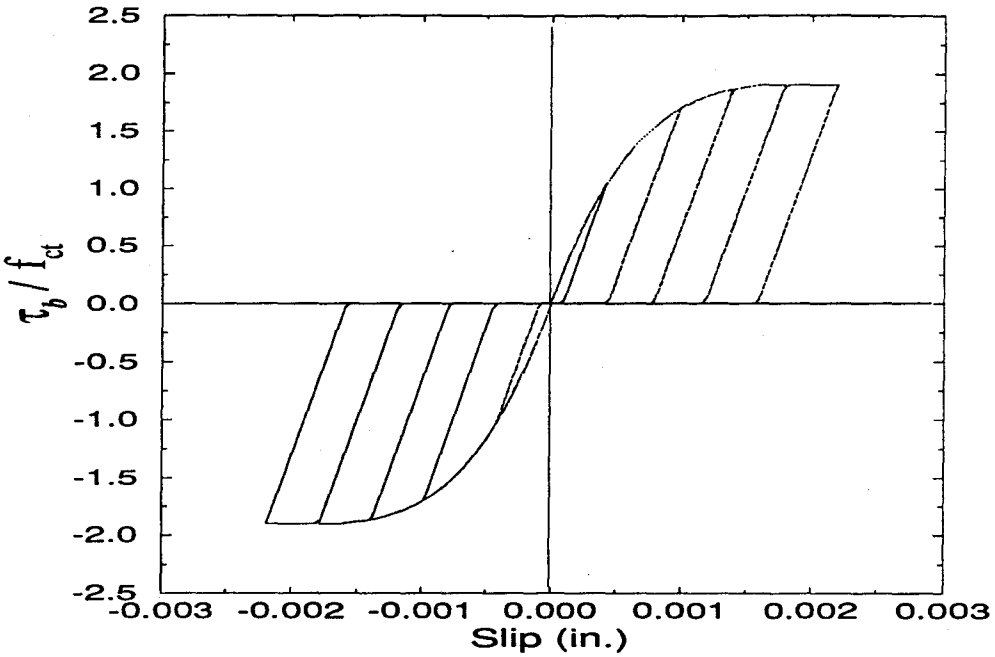

Figure 6.32. Bond Stress-Slip Relation.

6.4.4 Numerical Verifications. Hayashi and Kokusho (1985) have investigated the effect of the end distance on the bond behavior by conducting pull-out tests on 16-mm-diameter machined bars. In a pull-out test, the end distance is the distance of the front face of the first steel rib from the loaded face of the surrounding concrete. Three of their tests are intended to examine the capability of the bond-slip constitutive model. The embedment length in these specimens was 32 mm and the concrete cover was 2.5 times the bar diameter. The tensile strength of concrete was equal to 22.2 kg/cm^2. A typical specimen is shown in Fig. 6.33. The end distance, the embedment length of a bar, and the loaded face of a concrete specimen are shown in this

figure. The loaded face of a concrete specimen represents a crack face developed in an reinforced concrete member. Three specimens with end distances of 0.5d, 2.5d, and 5d, respectively, are selected, where d denotes the bar diameter. Since the model cannot account for effect of the end distance, slip level Δ_{r1} and the ultimate bond stress are extracted from the experimental curves directly in an empirical fashion. The ultimate bond stress of the specimens with end distances of 0.5d, 2.5d, and 5d are 65, 80, and 100 kg/cm^2, respectively. The values of Δ_{r1} are selected to be 0.08, 0.24, and 0.38 mm, respectively, to match the initial stiffnesses of the experimental curves. The model has been calibrated with these values and incorporated into the finite element program to model the bond-slip behavior. A single interface element has been used to model the bond behavior. A two-dimensional model is used. The experimental and numerical results for the specimens are shown in Fig. 6.34. Even though a good match between the experimental and numerical results can be obtained, it is evident that the model does not capture the degradation of the bond stress. The degradation is practically due to damage in concrete surrounding the bar. This cannot be modeled in a 2-dimensional analysis.

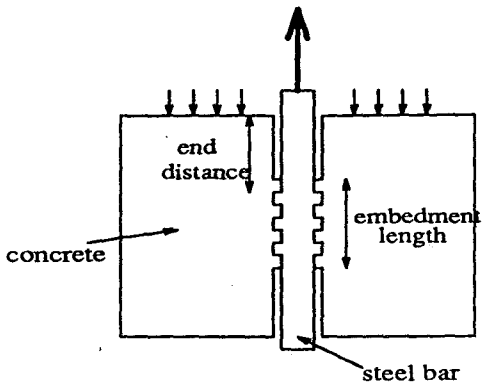

Figure 6.33. Typical Pull-Out Specimen with a Short Embedment Length.

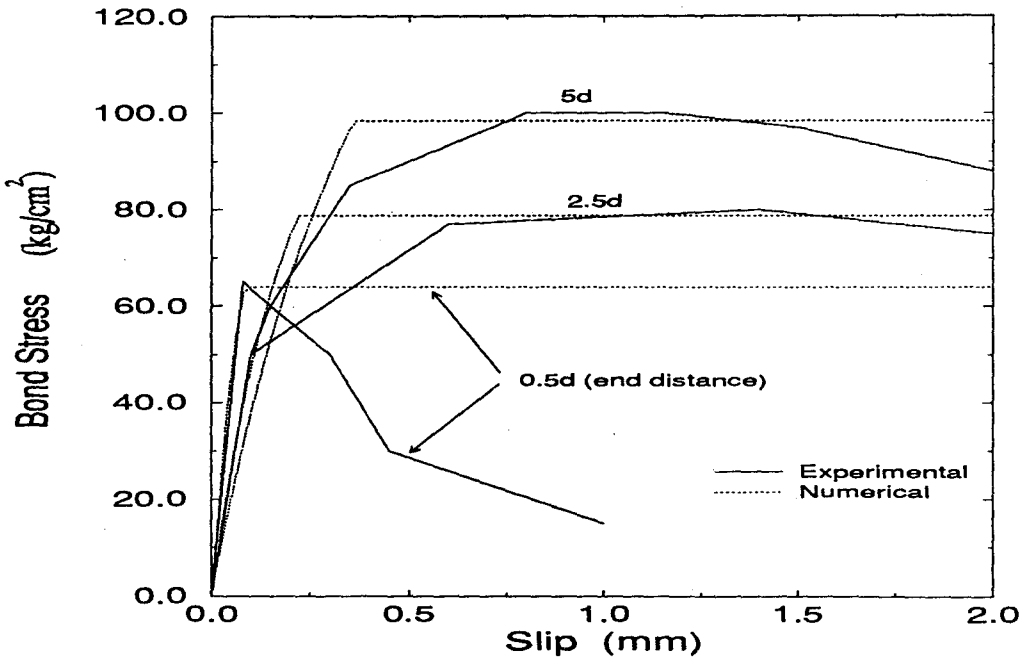

Figure 6.34. Bond-Slip Relations for Specimens with Different End Distances.

The calibrated model is also used to analyze a pull-out test with an embedment length of 112 mm. This specimen is shown in Fig. 6.35. The local bond stress and the local slip were measured at different locations along the bar corresponding to different end distances (see Fig. 6.35). This test has been conducted to study the effect of the end distance on the local bond behavior.

Figure 6.36 shows the experimental bond-slip curves. The curves are different from one another mainly because of the different damage levels in concrete at locations under consideration. The damage is higher near the end face of concrete and, therefore, the bond strength is lower in that vicinity. To simulate this test, a finite element analysis is conducted with a bond model calibrated previously for a large end distance (5 times the bar diameter). The steel bar was modeled by an elastic-hardening plastic bar element and the concrete was modeled by a smeared crack model, as presented previously in this chapter. As it is shown in Fig. 6.37, even with an identical model at different locations along the entire embedment length, the bond-slip behavior is different at different locations. This is due to the development of microcracks in the concrete and the deformation of the concrete itself. However, the numerical model cannot capture the true bond behavior influenced by the damage of the concrete. For a better agreement between experimental and numerical results, the bond stress in the model should be related to the damage level in concrete. Figure 6.38 shows the distribution of microcracks in the concrete obtained from the finite element analysis.

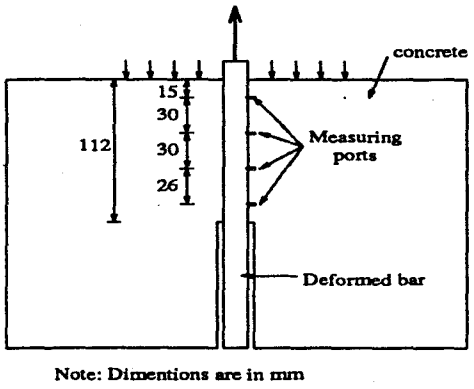

Figure 6.35. Pull-out Specimen with a Long Embedment Length.

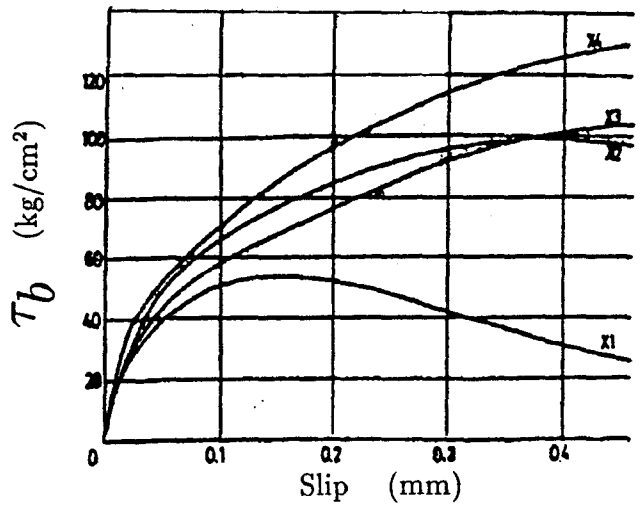

Figure 6.36. Experimental Results for the Local Bond Stress-Slip Relation in a Bar (Hayashi and Kokusho 1985).

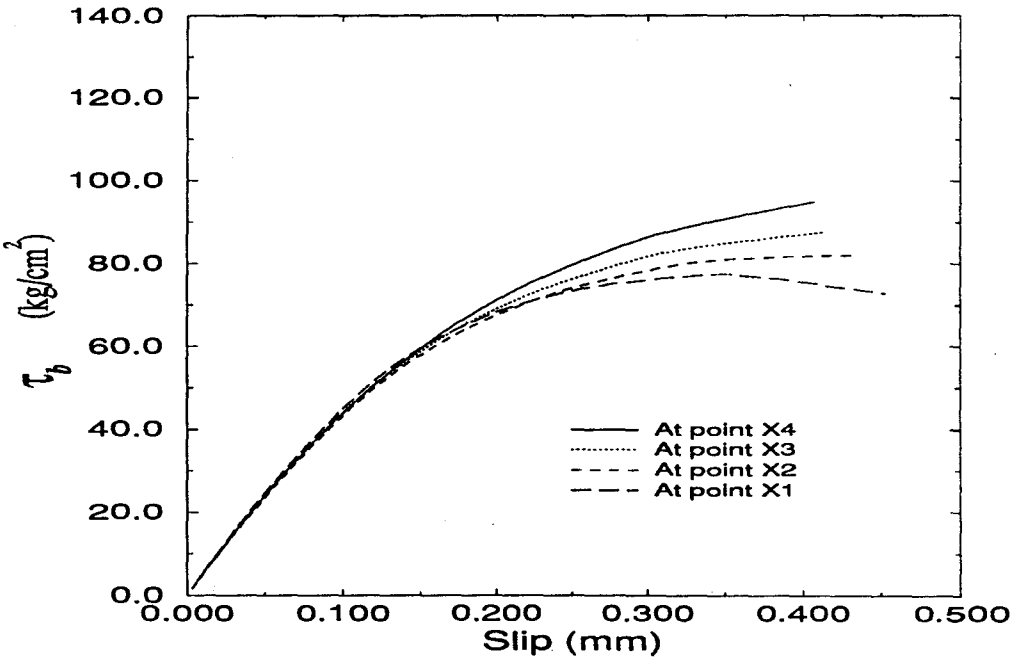

Figure 6.37. Numerical Results for the Local Bond Stress-Slip Relation in a Bar.

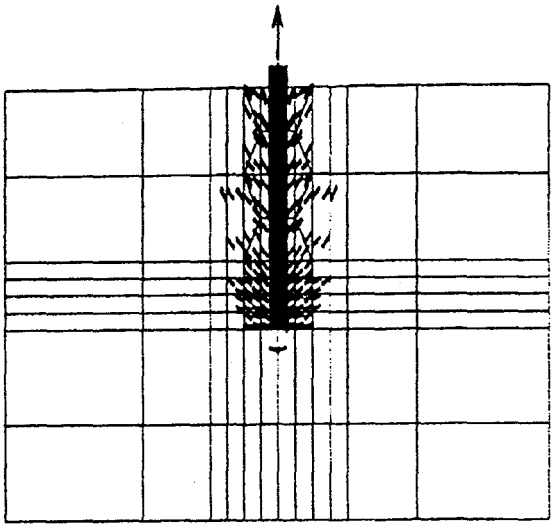

Figure 6.38. Crack Pattern obtained from F.E. Analysis.

6.4.5 Conclusions. A bond-slip constitutive model has been introduced for reinforced concrete structures based on the bond-slip relation proposed by Mehlhorn and Keuser (1985). The relation is simple and applicable to 2-dimensional analysis only. It is assumed that bond failure is governed by the crushing or shearing of concrete in front of steel ribs, which results in a ductile bond behavior. Therefore, this model is applicable only to the case of normal bar sizes with a large concrete cover (at least 2.5 times the bar diameter) or with the presence of a considerable amount of transverse reinforcement. This condition is true in most of the practical problems encountered in reinforced concrete structures.

6.5 Finite Element Analysis of Test Specimens

To examine the capability of the proposed models for simulating the behavior of infilled structures, five masonry-infilled R/C frames that were tested have been analyzed. These are Specimens 1, 8, and 9, which were tested

under monotonic lateral loads, and Specimens 6 and 7, which were tested under cyclic loads. The design details and test results have been discussed in Chapter 3 of this report. Specimen 1 was a bare frame specimen. Specimens 6 and 7 had strong frames, and were infilled with weak and strong panels, respectively. Specimens 8 and 9 had weak frames, and were infilled with weak and strong panels, respectively. All analyses were, however, conducted under monotonic loads. The concrete frames have been modeled with 9-node quadrilateral smeared crack elements, and the shear reinforcement has been smeared out over concrete elements. The longitudinal bars in the frame have been modeled with two-node bar elements. They are connected to the 9-node concrete elements at the two external nodes. For masonry units, 4 and 9-node smeared crack elements were used. The mortar joints in the masonry panels and along the interfaces between an infill and the frame have been modeled by 2-double-node interface elements. To model the possible shear failure of the columns, 3-double-node interface elements have been used at critical locations near the top and bottom sections of the columns. Two types of analyses have been conducted on Specimens 1, 8, and 9 with respect to the attachment of the longitudinal bars to the concrete. In the first, a perfect bond has been assumed between the reinforcing bars and the concrete. In the other, the steel has been attached to the concrete through bond-slip interface elements. Specimens 6 and 7 have been analyzed without bond-slip elements.

Calibration

The material models have been calibrated with the results of the material tests presented in Chapter 3 (Tables 3.2 and 3.3) as possible. Since no experimental data are available for the bond-slip behavior, the default values

mentioned previously have been used for the bond-slip parameters. For mortar joints, the calibration values presented in Tables 6.2 and 6.3 have been tried to be retained as possible. However, some of these parameters have to be adjusted to obtain a better match with the experimental results as well as to overcome convergence problems in the numerical solution. The complete set of parameters which have been used for the bed joints in these analyses are shown in Tables 6.5 and 6.6. Some of the values in the above tables have been modified to reflect weaker joints in the wall-to-beam interfaces as well as the behavior of head joints. For the top bed joints (the infill-to-beam interface) in Specimens 6 and 8, the tensile strength, s_0, has been reduced to 20 psi, and the initial and residual coefficients of frictions, μ_0 and μ_r, have been reduced to 0.8 and 0.7, respectively. For the head joints in these specimens, the initial normal and shear stiffnesses, K_{nn} and D_{tt}, have been reduced to 560 and 700 ksi, s_0 has been reduced to 10 psi, and μ_0 and μ_r, have been reduced to 0.8 and 0.7, respectively. The thicknesses of the bed joints, the infill-to-beam interface, and the head joints in Specimens 6 and 8 have been assumed to be 1.25, 1.4, and 1.25 in., respectively. These are based on the average thicknesses measured from the specimens. For the head joints in Specimens 7 and 9, the initial normal stiffness, K_{nn}, has been reduced to 350 ksi, s_0 has been reduced to 5 psi, and μ_0 and μ_r, have been reduced to 0.7 and 0.6, respectively. The thicknesses of the bed joints, the infill-to-beam interface, and the head joints in Specimens 7 and 9 have been assumed to be 3.5, 3.5, and 3 in., respectively. Material properties which are not available from the material tests, such as the tensile strength of the mortar joints, have been selected by trial and error to match the global behavior of an infilled frame.

Table 6.5. Material Parameters for Bed Joints in Specimens 6 and 8

K_{nn} (psi)	δ (in.)	D_{tt} (psi)	s_0 (psi)	G_f^I (psi-in.)	G_f^{II} (psi-in.)	μ_0	μ_r
740000	0.02	900000	40	1.61	16.1	0.9	0.75

α	r_0	r_r	β	ζ_0	ζ_r	γ	η
3	10	4	1.2	0.05	0.0003	0.1	15.7

Table 6.6. Material Parameters for Bed Joints in Specimens 7 and 9.

K_{nn} (psi)	δ (in.)	D_{tt} (psi)	s_0 (psi)	G_f^I (psi-in.)	G_f^{II} (psi-in.)	μ_0	μ_r
500000	0.02	500000	15	0.5	5	0.9	0.75

α	r_0	r_r	β	ζ_0	ζ_r	γ	η
2.5	10	4	1	0.05	0.0003	0.5	15.7

Numerical Results

Specimen 1 has been analyzed with and without bond-slip elements. Figure 6.39 shows the lateral load-lateral displacement curves obtained from these analyses as well as the experimental response. The numerical results indicate that the behavior of a bare frame is influenced significantly by bond

slip. The result with bond-slip elements is closer to the experimental load-displacement curve than that without bond-slip elements. The numerical result without bond-slip elements shows a large drop in post-peak resistance. This is due to the crushing of concrete in the compression zones of the columns. The bond slip in the tension bars relaxes the compression stress in concrete and, thereby, reduces the chance of sudden crushing.

Figure 6.40 shows the failure pattern of Specimen 1 obtained from the finite element analysis without bond-slip elements. This includes the deformed mesh, and the crack and crushing patterns. The finite element analysis has captured the actual failure mechanism of this specimen, as can be seen by comparing it with Fig. 3.28.

Analyses have been conducted for Specimen 8, which had a weak frame and a weak infill. The numerical results obtained with and without bond-slip elements are shown in Fig. 6.41, together with the experimental results. Using bond-slip elements for the longitudinal bars has not changed the behavior considerably. It has resulted in a slightly softer behavior and a better agreement with experimental results, which is hardly noticeable. Figure 6.42 shows the failure pattern for Specimen 8 obtained from the finite element analysis without bond-slip elements. This is similar to the actual failure of this specimen, as can be seen by comparing it with Fig. 3.35.

Specimen 9, which had a weak frame and a strong infill, has been analyzed in similar fashion as above. Figure 6.43 shows the numerical and experimental load-displacement curves of this specimen. The influence of bond-slip elements is insignificant for this specimen. The finite element analysis has captured the actual failure mechanism of this specimen, as can be seen by

comparing Fig. 6.44 with Fig. 3.36. The failure is governed by the shear failure of the infill (diagonal/sliding cracks) and the shear failure of the windward column.

Specimens 6 and 7, which had strong frames and were infilled with weak and strong panels, respectively, have been analyzed without bond-slip elements. The numerical load-displacement curve for Specimen 6 is compared to the hysteresis envelope curve obtained from the experiment in Fig. 6.45. The results show a good agreement in the initial stiffness, but the maximum lateral strength has been overestimated by the analysis as in the previous cases. Figure 6.46 shows the failure pattern obtained by the finite element analysis. This is similar to the experimental result shown in Fig. 3.33. The experimental and numerical load-displacement curves for Specimen 7 are shown in Fig. 6.47. In this case, the lateral resistance has been slightly underestimated. The failure pattern obtained from the finite element analysis is shown in Fig. 6.48.

6.6 Summary and Conclusions

A new constitutive model has been introduced for structural interfaces such as rock joints and mortar joints. Furthermore, a bond-slip constitutive model has been adopted for reinforced concrete structures. In each case, the applicability of the constitutive model has been validated with experimental results.

Finite element analyses have been conducted on one bare frame specimen and four masonry-infilled R/C frame specimens. It has been observed that bond-slip elements improve the analytical response of a bare frame considerably, whereas the influence of the bond-slip elements on the behavior of the infilled frames is insignificant. The results of the finite element analyses

have shown that the models can capture the true failure mechanisms of the infilled frames. The maximum lateral resistance and the initial stiffness of the specimens have been estimated fairly well.

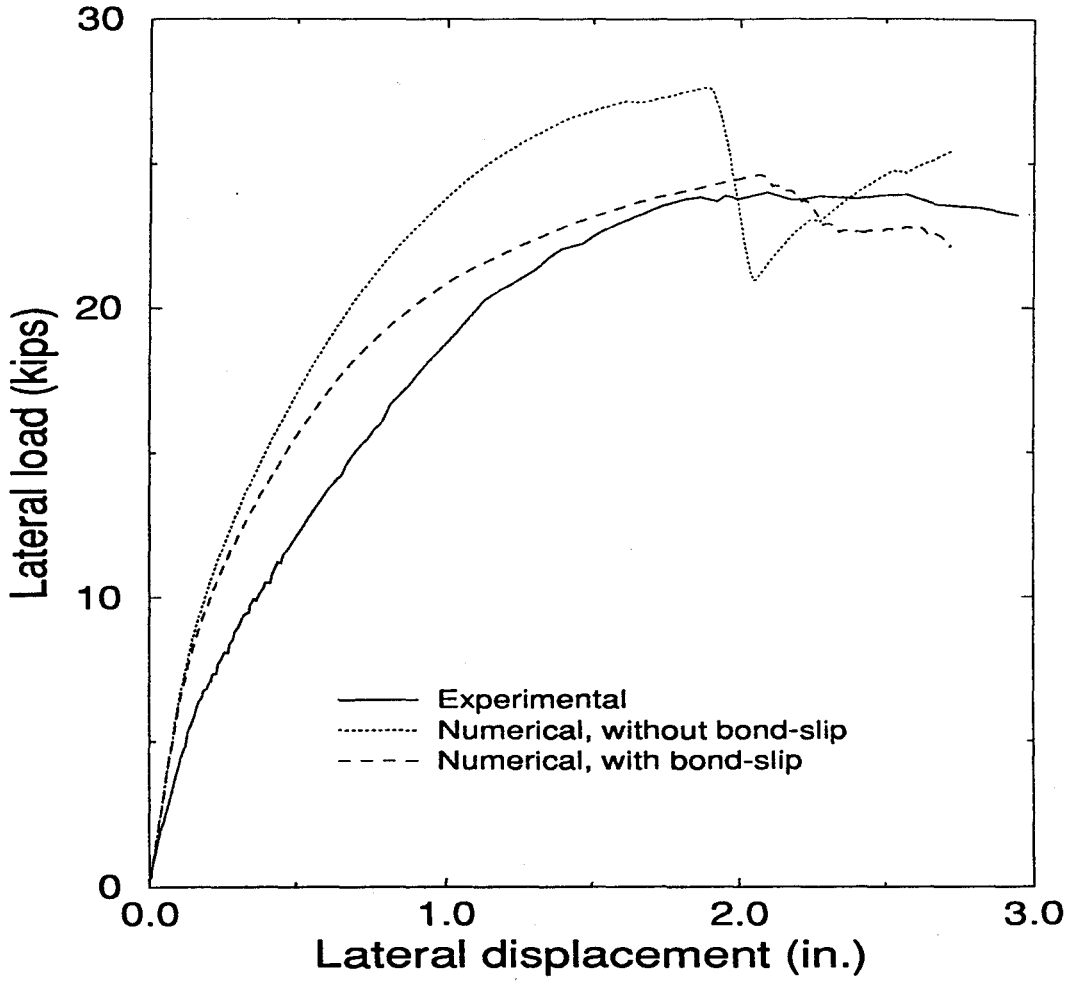

Figure 6.39. Lateral Load-Lateral Displacement Curves for Specimen 1.

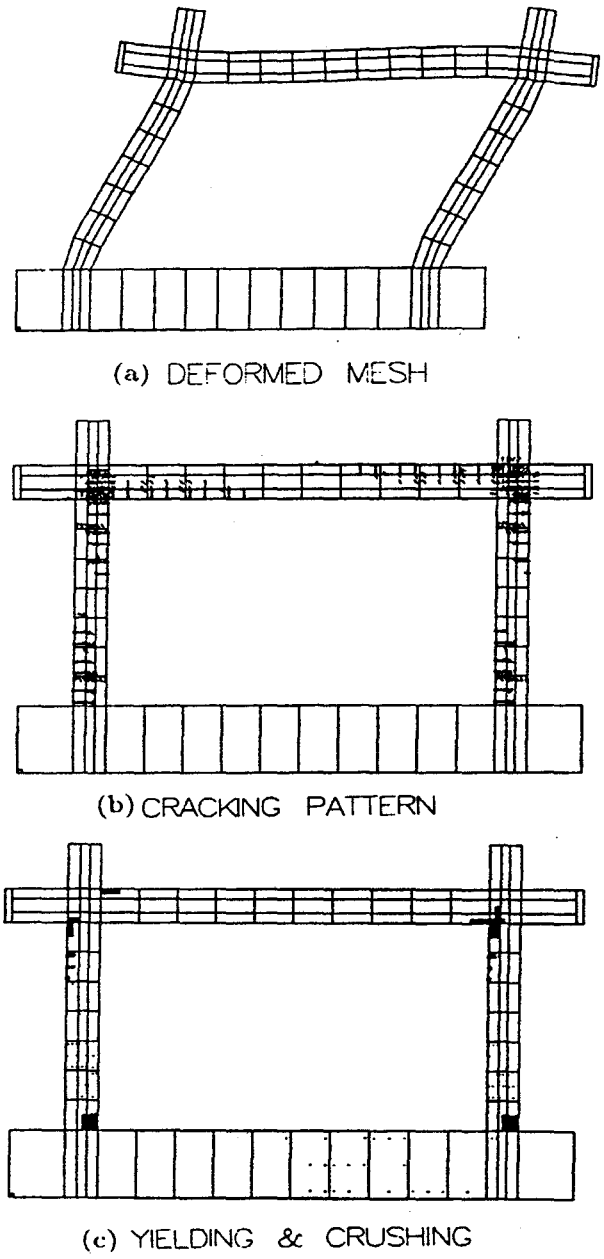

Figure 6.40. Failure Pattern of Specimen 1; a) Deformed Mesh; b) Crack Pattern; c) Crushing Pattern.

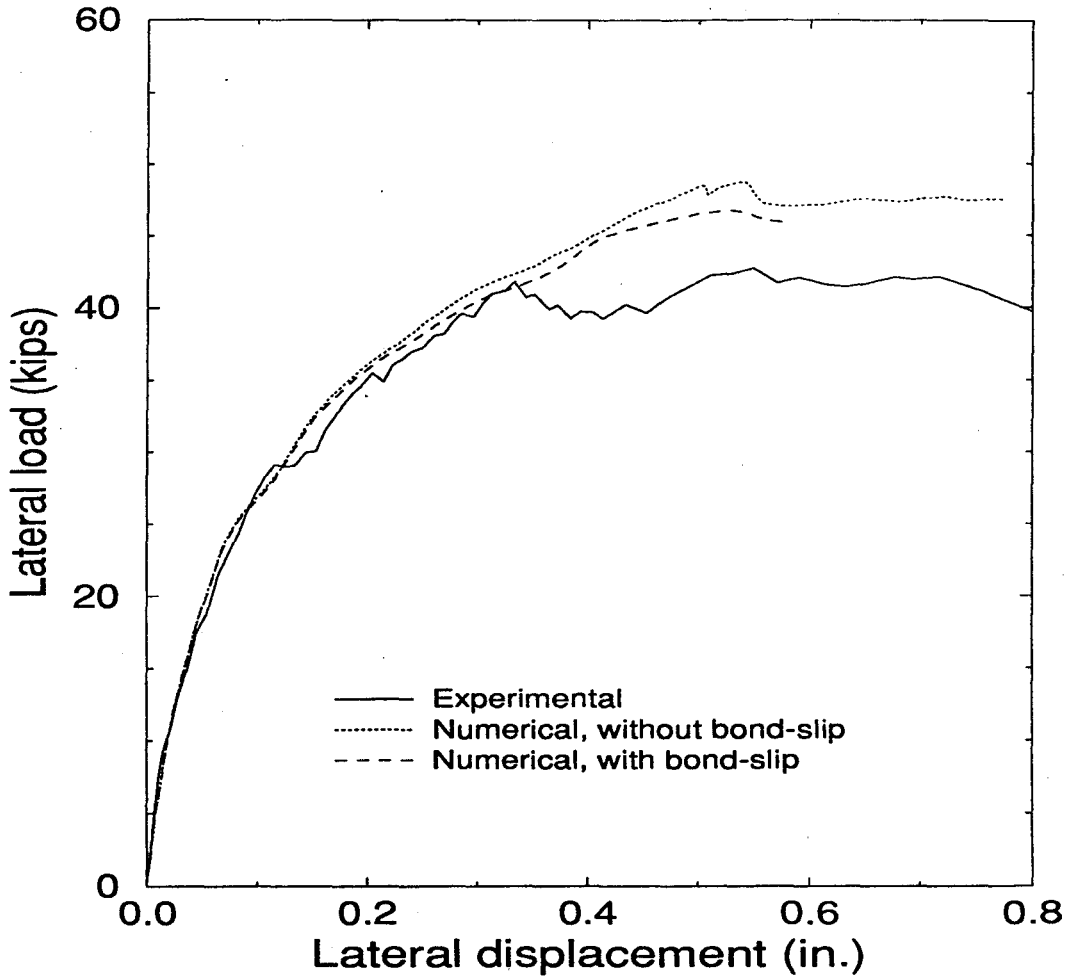

Figure 6.41. Lateral Load-Lateral Displacement Curves for Specimen 8.

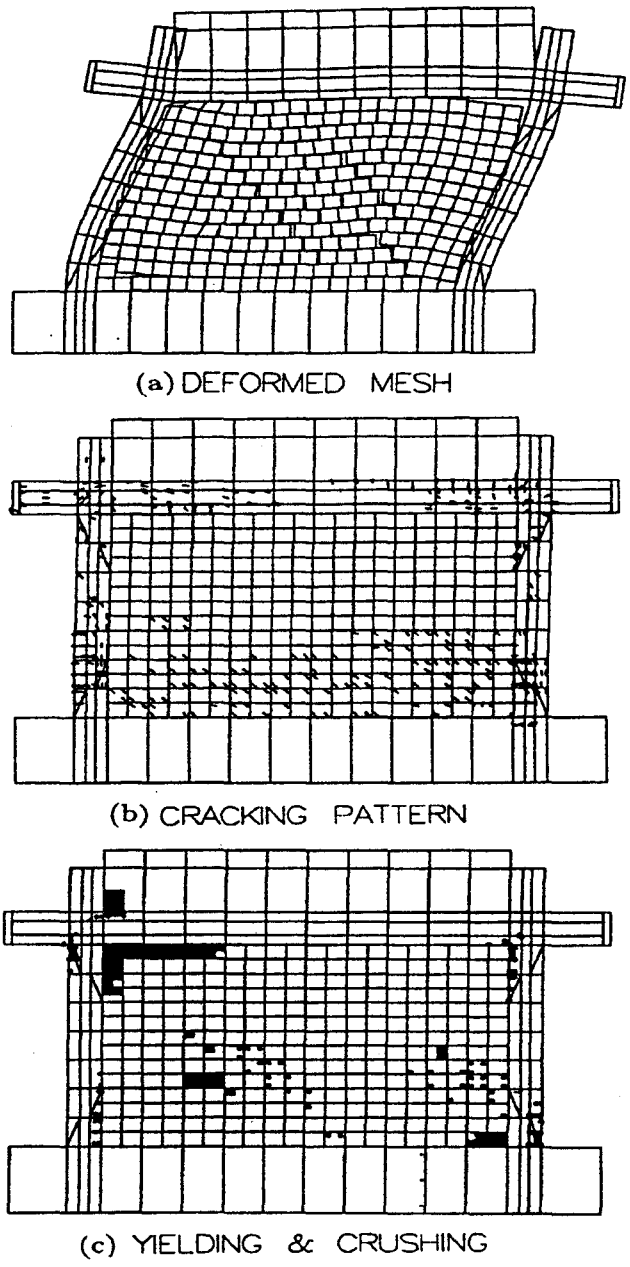

Figure 6.42. Failure Pattern of Specimen 8; a) Deformed Mesh; b) Crack Pattern; c) Crushing Pattern.

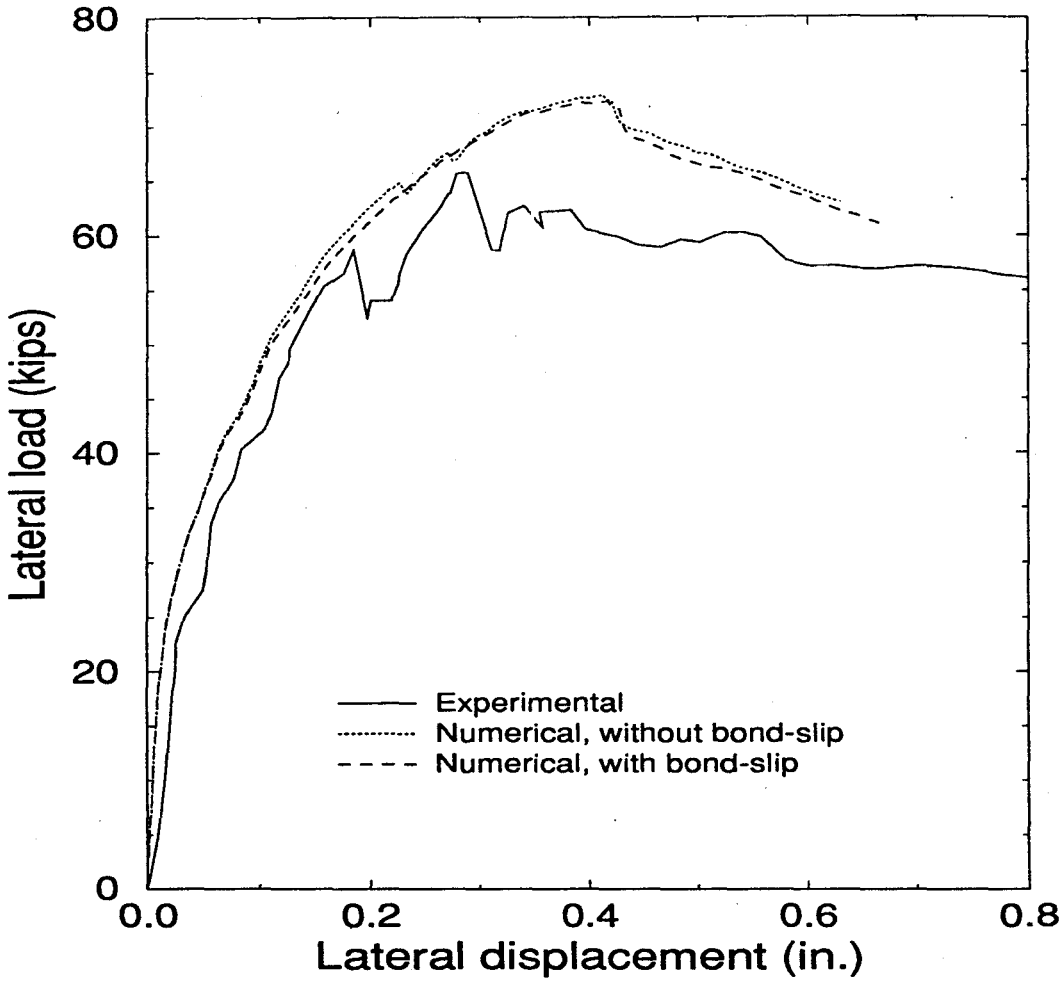

Figure 6.43: Lateral Load-Lateral Displacement Curves for Specimen 9.

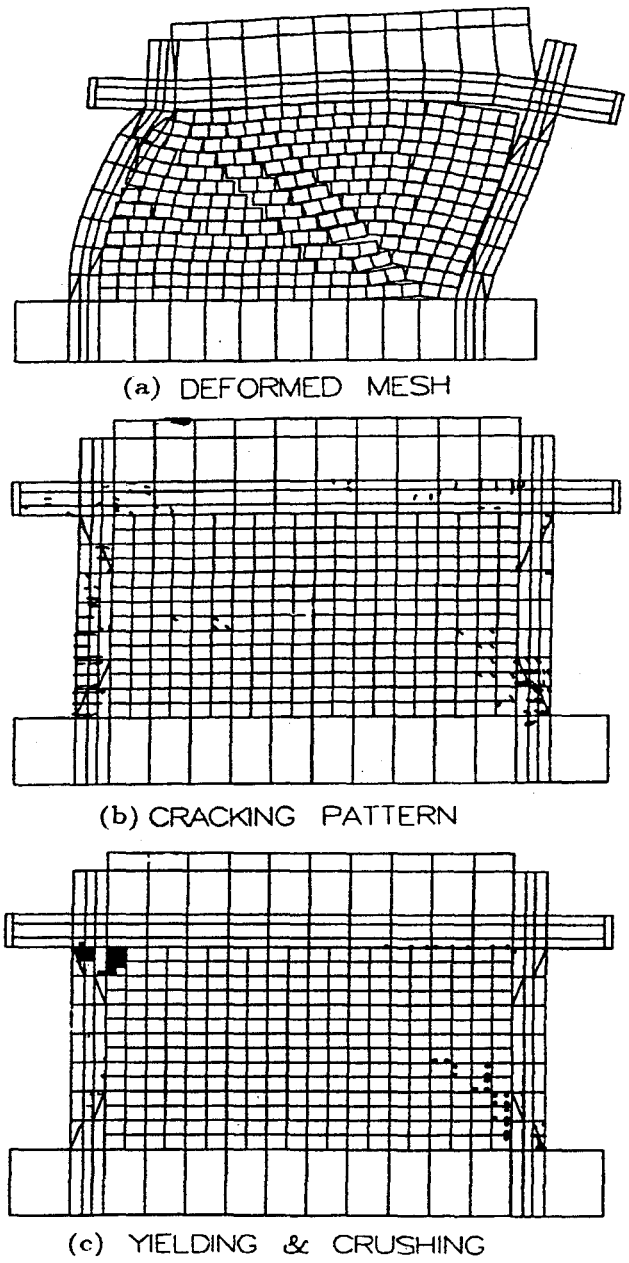

Figure 6.44. Failure Pattern of Specimen 9; a) Deformed Mesh; b) Crack Pattern; c) Crushing Pattern.

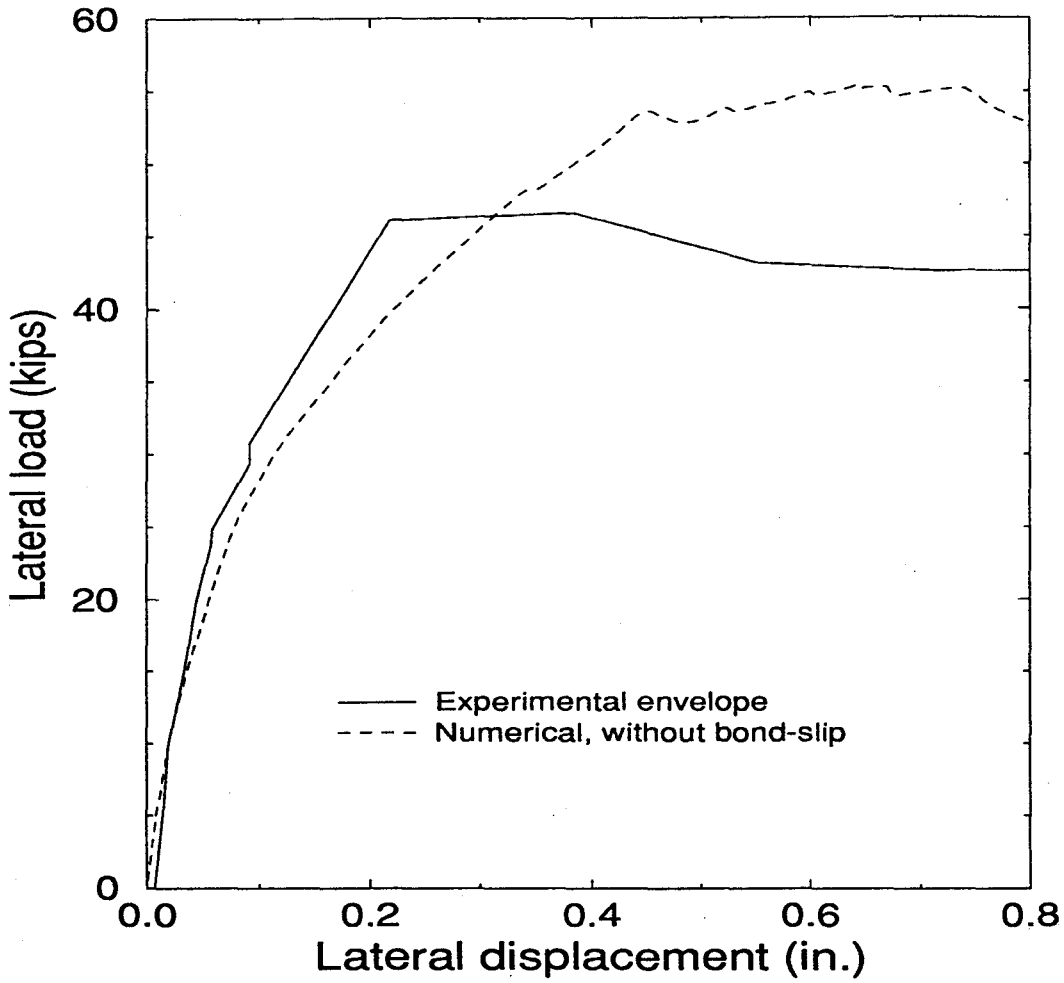

Figure 6.45. Lateral Load-Lateral Displacement Curves for Specimen 6.

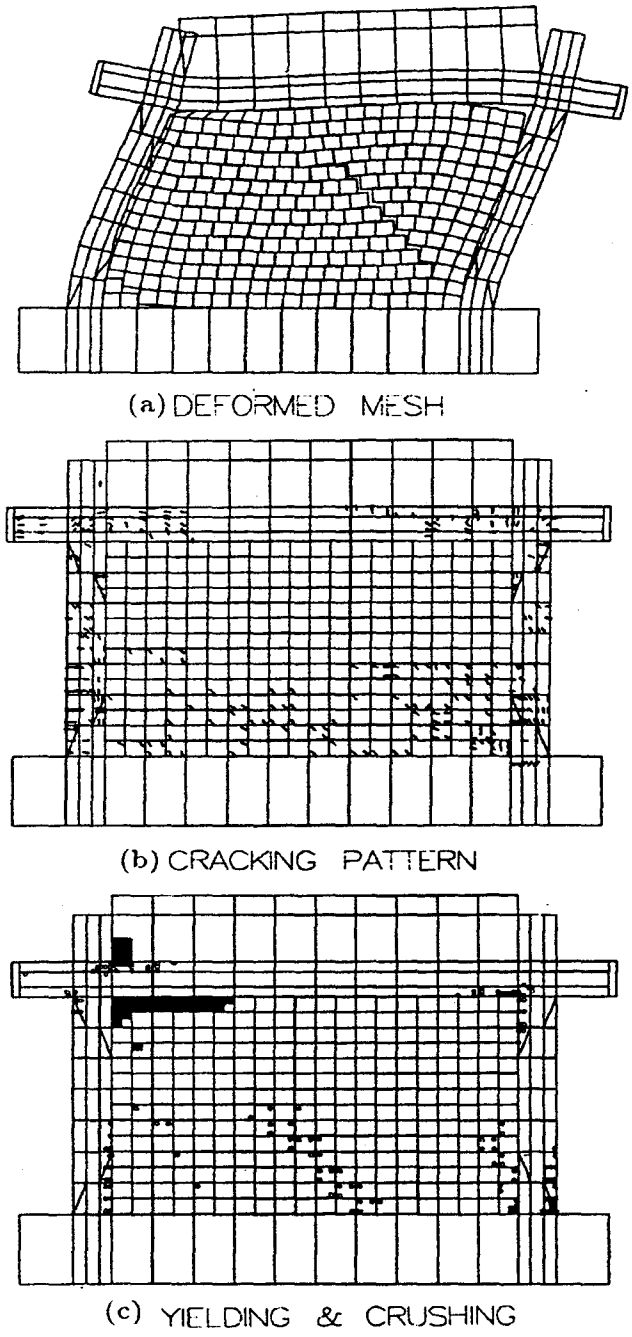

Figure 6.46. Failure Pattern of Specimen 6; a) Deformed Mesh; b) Crack Pattern; c) Crushing Pattern.

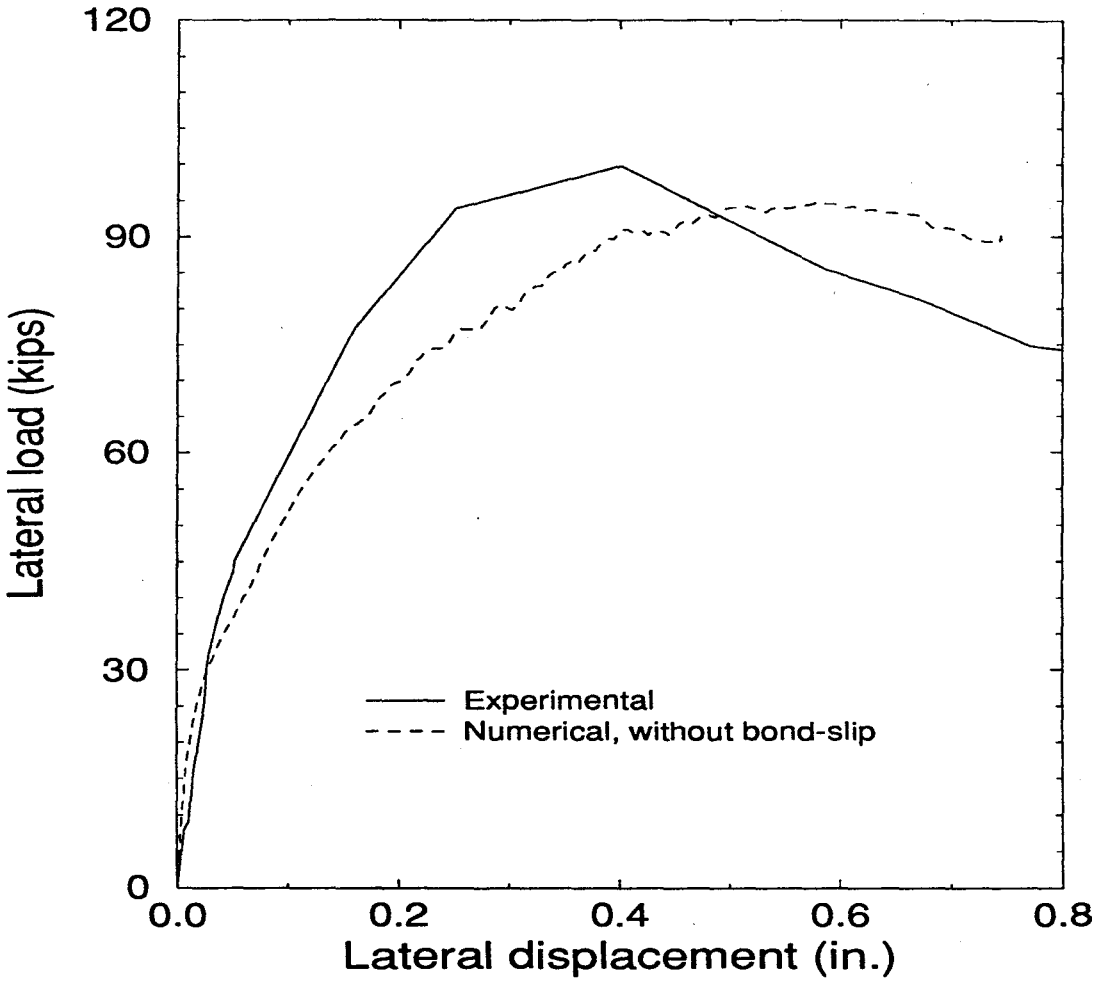

Figure 6.47. Lateral Load-Lateral Displacement Curves of Specimen 7.

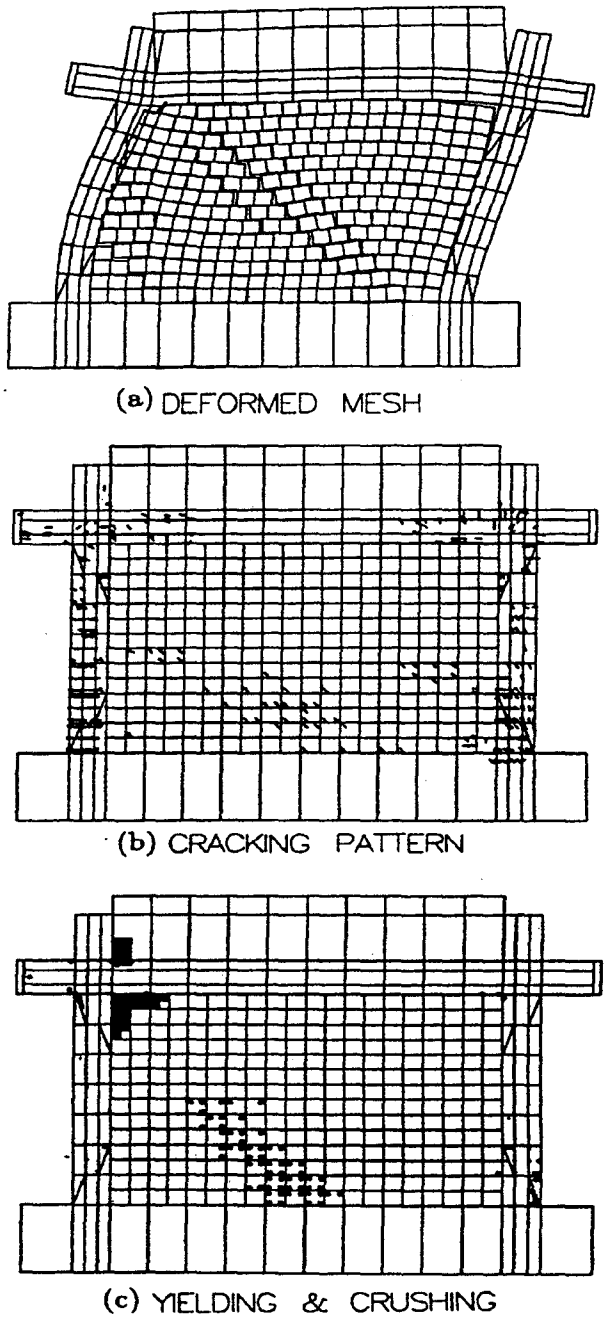

Figure 6.48. Failure Pattern of Specimen 7; a) Deformed Mesh; b) Crack Pattern; c) Crushing Pattern.

CHAPTER 7

CONCLUSIONS AND RECOMMENDATIONS

7.1 Summary

A literature review has been conducted to identify parameters which may influence the behavior of an infilled frame. Among the parameters identified, the influence of the relative strength and stiffness of an infill with respect to those of the bounding frame, the lateral load history, the panel aspect ratio, the vertical load level and its distribution, and the presence or absence of adjacent infilled bays have been selected for further investigation in this study. Furthermore, based on previous experimental observations, most of the possible failure mechanisms of infilled frames have been identified.

One bare frame and thirteen masonry-infilled R/C frames were tested in this study. Two of the infilled specimens were two-bay frames. The specimens were 1/2-scale models extracted from the first story of a six-story, three-bay, prototype frame, which represents an interior frame of a typical office building. The prototype frame has been designed for two types of lateral loadings: moderate wind loads and severe earthquake loads. These result in a weak-frame design and a strong-frame design, respectively. The former has a weak column-strong beam design, while the latter has a strong column-weak beam design. The frame specimens had aspect ratios of around 1/2 and 2/3, respectively. Two types of masonry units were used for the infill. They were hollow concrete blocks and solid concrete blocks, which resulted in different

panel strengths. The specimens were subjected to monotonic and cyclic lateral loadings. The vertical loads were applied onto the specimens with two different distributions. One had vertical loads only on the columns and the other had the loads distributed between the columns and the beam. The total vertical loads applied onto one of the single-bay specimens and the two two-bay specimens were 50% higher than those of the others.

In the analytical part of this study, a simple and rational method has been proposed to obtain the load resistance properties of a prototype frame based on the behavior of the scaled frame specimens. In this method, the prototype frame is idealized by an equivalent single-degree-of-freedom system based on the modal analysis technique. The idealized system has an elastic-perfectly plastic behavior with the yield resistance, yield displacement, and allowable displacement calculated from the experimental results. With the load resistance properties calculated, seismic analyses have been conducted on the prototype frame with and without infill.

To predict the lateral resistance of a single-bay, single-story infilled frame, a plastic analysis method has been developed. In addition to the load resistance mechanisms proposed by other investigators, this method accounts for the diagonal/sliding shear failure of the infill as well as the shear failure of the columns. The method has been used to analyze the specimens tested in this study. For the lateral stiffness of an infilled frame, the methods proposed by other researchers have been reviewed and evaluated.

The capability of the finite element method for predicting the behavior of infilled frames has been investigated. Two interface elements have been developed in this study. One is to simulate the behavior of the interfaces

between the frame and the infill as well as the behavior of the mortar joints within an infill. In addition to the separation and sliding modes of failure, this model is capable of simulating the nonlinear compression behavior, reversible shear dilatancy, and compaction of interfaces. The other element is to model the bond-slip behavior between the concrete and reinforcing bars. This model is applicable to bars of normal sizes that are adequately confined by transverse reinforcement. These models have been evaluated with existing experimental results in the literature. Finally, five of the specimens tested in this study have been analyzed with these elements.

7.2 Conclusions

In general, the experimental and analytical results have indicated that the addition of infill panels has a profound influence on the behavior of R/C frames. Infill increases both the lateral strength and stiffness of a bare frame, and improves the energy-dissipation capability of a structure significantly. This is more evident in the case of a strong panel.

Specimens subjected to cyclic loadings demonstrated a lower resistance and a faster strength degradation than those subjected to monotonic loadings. The panel aspect ratio, in the range considered in this study, had little influence on the lateral load resistance behavior. Increasing the vertical load increases the lateral resistance considerably, but the influence of the distribution of the vertical loads between the top beam and the columns was insignificant.

The two two-bay specimens with strong and weak panels exhibited lateral resistances that are 68 and 85% higher than those of the single-bay specimens with identical designs. Three different failure modes were observed

from all the specimens. Those with a weak panel had slips along the bed joints and plastic hinges in the frame. Brittle shear failure was observed in the windward columns of the specimens that had a weak frame and a strong panel. However, even in this case, the specimens sustained a considerable lateral load after shear failure had occurred in the columns, and they exhibited a good ductility due to the continued resistance provided by the infill. Furthermore, in the specimen that had a strong frame and a strong panel, the lateral strength was governed by the crushing of the infill. In this specimen, shear failure was prevented by a heavy column section and the shear reinforcement.

For all the cases considered in this study, it has been shown that the presence of infill panels improves the seismic performance of a frame. The stronger the infill and the frame is, the higher is the seismic resistance. However, to avoid the brittle shear failure of columns, which might jeopardize the stability and repairability of a structure, adequate shear reinforcement must be provided in the columns. The results also suggest that infill panels can be used for retrofitting existing R/C structures. In this case, new panels must be designed in such a way that their strength will be compatible with those of the columns.

The plastic analysis method proposed in this study has been able to capture the actual failure mechanisms in most cases. For these same cases, the lateral resistances calculated with the analysis method are in good agreement with the actual resistances measured. For the lateral stiffness of an infilled frame, the method based on an equivalent beam model results in a stiffness higher than the actual, while the equivalent strut model results in a lower stiffness.

Results of the finite element analyses have demonstrated the applicability of the proposed models for simulating the behavior of infilled frames. It has been observed that bond-slip elements are important for capturing the behavior of a bare frame, while the influence of these elements on the behavior of infilled frames is insignificant. The interface elements successfully capture the separation at the frame-to-panel interfaces and the crack propagation along mortar joints. The failure modes obtained with the finite element models are similar to the actual failure mechanisms of the specimens. The numerical results are also in good agreement with the load-displacement curves obtained from the experiments. The initial stiffness and the maximum resistance have been estimated fairly well.

7.3 Recommendations for Future Studies

The important findings of this study can be summarized as follows. The experimental and analytical results have indicated the beneficial influence of infill panels on the seismic resistance of R/C frames even though they were not engineered for such a purpose. The important influence of the vertical loads, the strengths of a panel and the bounding frame, and the adjacent infilled bays on the performance of this type of structures has been identified. Finite element models have been developed and validated for detailed analysis of such structures. The sophistication of these models provides a unique capability for the analysis and performance evaluation of infilled structures. Simple analytical models which account for the shear failure of R/C columns and the diagonal/sliding shear failure of an infill panel have been developed and validated. These models can be used as simple evaluation and design tools.

In spite of the above findings, additional research is required to address a number of remaining problems. Many infill panels in existing buildings have various forms of openings. Their influence on the lateral resistance capability of a structure is not well known. The damage of an infill panel due to in-plane loads can jeopardize its out-of-plane stability. Hence, it may be desirable to have light reinforcement in a panel to prevent the out-of-plane failure and also to increase its energy-dissipation capability under in-plane loads. Furthermore, to avoid irreparable damage, such as soft first stories, guidelines should be developed to match the strength of an infill panel to that of the bounding frame. These point to the development of engineered infill, which is especially useful for the retrofit of existing R/C frames. Additional experimental studies are needed to provide the above information. Furthermore, the finite element models developed here can be used for numerical parametric studies to supplement the experimental work. The simple analytical models developed here need to be further verified and generalized to encompass more failure mechanisms, in particular, for multiple infilled bays. Based on these results, new design and evaluation guidelines, which are simple enough for engineering practice, should be developed.

BIBLIOGRAPHY

[1] Amadei, B., Sture, S., and Saeb, S. (1989). "An Evaluation of Masonry Joint Shear Strength in Existing Buildings." *Report to N.S.F.*, Vol. I, Civil Engineering Department, University of Colorado, Boulder CO.

[2] American Concrete Institute (*ACI 318-89). Building Code Requirement for Reinforced Concrete.*

[3] Amrhein, J. E., Anderson, J. C., and Robles, V. M.(1985)."Masonry Saves Lives in Mexico earthquake." *Masonry Design West*, November-December.

[4] Angel, R., Abrams, D., Shapiro, D., Uzarski, J., and Webster, M. (1994). "Behavior of Reinforced Concrete Frames With Masonry Infills." *Technical Report UILU-ENG-94-2005,* Department of Civil Engineering, University of Illinois at Urbana-Champain, March.

[5] ASCE Task Committee, (1982). "State-fo-the-Art Report on Finite Element Analysis of Reinforced Concrete." *ASCE Publication*, New York, Chapter 3.

[6] Bazant, Z.P., and Oh, B.H. (1983). "Crack Band Theory for Fracture of Concrete." *Material and Structures*, Vol. 16, No. 93, pp. 155-177.

[7] Bazant, Z.P. (1983). "Comments on Orthotropic Models for Concrete and Geomaterials." *Journal of Engineering Mechanics,* ASCE, 109(3), pp. 849-865.

[8] Bertero, V.V., and Brokken, S. (1983). "Infills in Seismic Resistant Building." *J. of Structural Engineering*, ASCE, Vol 109, No. 6.

[9] Bertero, V.V., Mahin, S.A., and Herrera, R.A. (1978). "Aseismic Design Implications of Near-Fault San Fernardo Earthquake Records." *Earthquake Engineering and Structural Dynamics,* Vol. 6, pp. 31-42.

[10] Brokken,S.T.,and Bertero,V.V. (1981). "Studies on effects of infills in seismic resistant R/C construction." *UCB/EERC 81/12*, Earthquake Engineering Research Center, University of California, Berkely.

[11] Carol, I., and Prat, P. C. (1991). "Smeared Analysis of Concrete Fracture using a Microplane-Based Multicrack Model with Static Constraint." *Proceedings, International Conference on Fracture Processes in Brittle Disordered Materials*, J.G.M. von Mier et al., Eds., Chapman and Hall.

[12] Dawe,J.L., and Dukuze,A. (1992). "Parametric Study of Masonry Infilled Frames Subjected to Dynamic Loads." *Proceedings, 6-th Canadian Masonry Symposium*, pp. 351-363.

[13] Dawe,J.L., Dukuze,A., and Holder,J. (1992). "Dynamic Behavior of Masonry Infilled Steel Frames." *Proceedings, 6-th Canadian Masonry Symposium*, pp. 341-350.

[14] Dawe,J.L., and Seah,c.k. (1990). "Behavior of Masonry Infilled Steel Frames." *Journal of Canadian Society Civil Engineering, Excerpt*, Jan.

[15] De Groot, A.K., Kusters, G.M.A., and Monnier, T. (1981). " Numerical Modelling of Bond-Slip Behavior." *Heron Concrete Mechanics*, Vol. 26, No. 1B.

[16] Dhanasekar,M., and Page,A.W. (1986). "The influence of brick masonry infill properties on the behavior of infilled frames." *Proceedings of the Institute of Civil Engineers*, Part 2, 81, Dec., pp. 593-605.

[17] Dhanasekar,M., Kleeman, P.W., and Page,A.W. (1985). "Biaxial Stress-Strain Relation for Brick Masonry." *Journal of Structural Engineering*, ASCE, Vol. 111, No. 5, May.

[18] Doerr, K. (1978). " Bond Behavior of Ribbed Reinforcement under Transversal Pressure." *Proceedings, IASS Symposium*, Darmstadt, Germany, June.

[19] Fiorato, A.E., Sozen, M.A., and Gamble, W.L.(1970). "An investigation of the interaction of reinforced concrete frames with masonry filler walls." *Technical Report No. UILU-ENG 70-100*, University of Illinois, Urbana-Champaign, IL.

[20] Gambarova, P.G., Rosati, G.P., and Zasso, B. (1989). "Steel-to-Concrete Bond after Concrete Splitting: Test Results." *Materials and Structures*, Vol. 22, pp. 35-47.

[21] Gambarova, P.G., Rosati, G.P., and Zasso, B. (1989). "Steel-to-Concrete Bond after Concrete Splitting: Constitutive Laws and Interface Deterioration." *Materials and Structures*, Vol. 22, pp. 347-356.

[22] Giuriani, E., Migliacci, A., and Riva, P. (1984). "Experimental Investigation on the Local Bond-Slip Law in Structural Lightweight Concrete." *Studi e Ricerche*, School for the Design of R.C. Structures, Milan University of Technology, Vol. 6, pp. 203-230.

[23] Giuriani, E., Plizzari, G., Schumm, C. (1991). "Role of Stirrups and Residual Tensile Strength of Cracked Concrete on Bond." *Journal of Structural Engineering*, ASCE, Vol. 117, No. 1, pp. 1-18.

[24] Glogau, O. A.(1974)."Masonry performance in earthquakes." *Bulletin of the New Zealand National Society for Earthquake Engineering*, Vol. 7, No. 4.

[25] Habibullah, A., and Wilson, E. (1991). *SAP90, General Analysis and Design* Software, Computers & Structures Inc., Berkeley, California.

[26] Hayashi, S., and Kokusho, S. (1985). " Bond Behavior in the Neighborhood of Crack." *Proc. of the Seminar Sponsored by the Japan Society for the Promotion of Science and the U.S. National Science Foundation*, ASCE Publication, New York, pp. 364-373.

[27] Hobbs,B., and Samai,M.L. (1985). "A comparison of analytical methods for infilled frames." *International Symposium on Earthquake and Design Structures in Seismic Areas*, University of Constantine, Algeria.

[28] Hohberg, J. M. (1992). "Multimechanism Plasticity with Coupled Damage in Tension and Shear." *Proceedings, Third International Conference on Computational Plasticity*, Pineridge Press, Swansea, UK, 1503-1514.

[29] Holmes, M. (1961)."Steel frames with brickwork and concrete infilling." *Proceedings of the Institute of Civil Engineers*, Vol. 19, No. 6501, pp. 473-478.

[30] Houde, J. (1973). " Study of Force-Displacement relationships for the Finite Element Analysis of Reinforced Concrete." *Report No. 73-2*, Dept. of Civil Engineering and Applied Mechanics, McGill University, Montreal.

[31] Housner, G.W., and Jennings, P.C. (1982). *Earthquake Design Criteria.* Earthquake Engineering Research Institute, Berkeley, CA.

[32] Kahn,L.F., and Hanson,R.D. (1979). "Infilled walls for earthquake strengthening." *Journal of the Structural Division*, ASCE, Vol. 105, No. ST2.

[33] Kemp, E.L., and Wilhelm, W.J. (1979). "Investigation of the Parameters Influencing Bond Cracking." *Proceedings, American Concrete Institute Journal*, No. 76-3, pp. 47-71.

[34] Khouzam, M. (1977). " A Finite Element Investigation of Reinforced Concrete Beams." *Master Thesis*, McGill University, Montreal, Canada.

[35] Klinger,R.E., and Bertero,V.V. (1976). "Infilled frames in earthquake-resistant construction." *Report No. EERC 76-32*, University of California, Berkely.

[36] La Borderie, C., and Pijaudier-Cabot, G. (1992). " Influence of the State of Stress in Concrete on the Behavior of the Steel Concrete Interface." *Proceedings, First International Conference on Fracture Mechanics of Concrete Structures*, Elsevier Applied Science Publication, New York, pp. 830-835.

[37] Lefter,J., and Colville,J. (1974). "Reinforcing Existing Buildings To Resist Earthquake Forces." *Cento Symposium on Earthquake Engineering and Engineering Seismology*, Middle East Tachnical University, Ankara, Turkey.

[38] Liauw,T.C., and Kwan,K.H. (1983). "Plastic Theory of Non-Integral Infilled Frames." *Proceedings of Institute of Civil Engineers*, Part 2, sep. pp. 379-396.

[39] Liauw,T.C., and Kwan,K.H. (1985). "Unified plastic analysis for infilled frames." *Journal of Structural Engineering*, ASCE, Vol. 111, No. 7.

[40] Liauw,T.C., and Lo,C.Q. (1988). "Multibay infilled frames without shear connectors." *ACI Structural Journal*, July-Aug., pp. 423-428.

[41] Lotfi, H.R. (1992). "Finite Element Analysis of Fracture of Concrete and Masonry Structures." *Ph.D. Thesis*, Civil Engineering Department, University of Colorado at Boulder.

[42] Lotfi, H.R., and Shing, P.B. (1991). "An Appraisal of Smeared Crack Models for Masonry Shear Wall Analysis." *Computers and Structures,* 41(3), 413-425.

[43] Lotfi, H. R., and Shing, P. B. (1994). "An Interfaces Model Applied to Fracture of Masonry Structures." *Journal of Structural Engineering*, ASCE, Vol. 120, No. 1, pp. 63-80.

[44] Mahin, S.A, Bertero, V.V., Chopra, A.K., and Collins, R.G. (1976). "Response of the Olive View Hospital Main Building During the San Fernando Earthquake." *Report No. EERC 76-22*, Earthquake Engineering Research Center, University of California, Berkely.

[45] Mainstone, R.J. and Weeks, G.A. (1970)."The Influence of Bounding Frame on the Racking Stiffness and Strength of Brick Walls." *Proceedings, Second International Brick Masonry Conference*, Stoke-on-Trent, England, pp. 165-171.

[46] Mander, J.B., Nair, B., Wojtkowski, K., and Ma, J. (1993). "An Experimental Study on the Seismic Performance of Brick-Infilled Steel Frames With and Without Retrofit." *Technical Report No. NCEER-93-0001,* State University of New York at Buffalo.

[47] McCabe, S.L., and Darwin, D. (1992). " Fracture Mechanics Implications in the Bond and Development of Reinforcement in Concrete." *Proceedings, First International Conference on Fracture Mechanics of Concrete Structures*, Elsevier Applied Science Publication, New York, pp. 836-841.

[48] McDowel,E.L., McKee,K.E., and Sevin,E. (1956). "Arching Action Theory of Masonry Walls." *Journal of the Structural Division*, ASCE, Vol. 82, No. ST2, Paper 915.

[49] Mehlhorn, G., and Keuser, M. (1985). " Isoparametric Contact Elements for Reinforced Concrete." *Proceedings of the Seminar Sponsored by the Japan Society for the Promotion of Science and the U.S. National Science Foundation*, ASCE Publication, New York, pp. 329-347.

[50] Mirza, S.A., and MacGregor, J.G. (1979). "Variability of Mechanical Properties of Reinforced Bars." *Journal of Structural Division*, ASCE, Vol. 105, No. ST5, pp. 921-937.

[51] Morita, S., and Kaku, T. (1973). "Local Bond Stress-Slip Relationship Under Repeated Loading." *Preliminary Report, IABSE Symposium*, Lisbon, pp. 221-227.

[52] Morita, S., and Kaku, T. (1979). "Splitting Bond Failure of Large Deformed Reinforcing Bars." *Proceedings, American Concrete Institute Journal*, No. 76-5, pp. 93-110.

[53] Ngo, D., and Scordelis, A.C. (1967). " Finite Element Analysis of Reinforced Concrete Beams." *ACI Structural Journal*, Vol. 64, No. 3, pp. 152-163.

[54] Nilson, A.H. (1968). " Non-Linear Analysis of Reinforced Concrete by the Finite Element Method." *ACI Structural Journal*, Vol. 65, No. 9, pp. 757-766.

[55] Nilson, A.H. (1971). " Bond Stress-Slip Relations in Reinforced Concrete." *Report 345*, School of Civil and Environmental Engineering, Cornell University, Ithaca.

[56] Niwa, J., Chou, L., Shima, H., and Okamura, H. (1985). " Non-Linear Spring Element for Strain-Slip relationship of A Deformed Bar." *Proceedings of the Seminar Sponsored by the Japan Society for the Promotion of Science and the U.S. National Science Foundation*, ASCE Publication, New York, pp. 374-383.

[57] Noguchi, H. (1985). " Analytical Models for Cyclic Loading of RC Members." *Proceedings of the Seminar Sponsored by the Japan Society for the Promotion of Science and the U.S. National Science Foundation*, ASCE Publication, New York, pp. 486-502.

[58] Ortiz, M. (1981). "Topics in Constitutive Theory for Inelastic Solids." *Ph.D. Thesis*, Department of Civil Engineering, University of California, Berkeley.

[59] Ortiz, M., and Simo, J.C. (1986). "An Analysis of A New Class of Integration Algorithms for Elastoplastic Constitutive Relations." *International Journal for Numerical Methods in Engineering*, Vol. 23, 353-366.

[60] Pande, G.N., Beer, G., and Williams, J.R. (1990). *Numerical Methods in Rock Mechanics*, John Wiley & Sons LTD, Chichester, UK.

[61] Page, A.W. (1978). "Finite Element Model for Masonry." *Journal of Structural Engineering,* ASCE, 104(8), 1267-1285.

[62] Polyakov, S.V.(1960)."On the interaction between masonry filler walls and enclosing frame when loaded in the plane of the wall." *Construction in Seismic Regions*, Moscow, 1957, translation in *Earthquake Engineering, Earthquake Engineering Research Institute*, San Fransisco, pp. 36-42.

[63] Reinhardt, H.W. (1992). " Bond of Steel to Strain-Softening Concrete Taking Account of Loading Rate." *Proceedings, First International Conference on Fracture Mechanics of Concrete Structures*, Elsevier Applied Science Publication, New York, pp. 809-820.

[64] Rengers, N. (1970). "Influence of Surface Roughness on the Friction Properties of Rock Planes." *Proceedings, Second Congeress ISRM*, Belgrade, Vol. 1, pp. 229-234.

[65] Robins, P.J., and Standish, I.G. (1984). "The Influence of Lateral pressure upon Anchorage Bond." *Magazine of Concrete Research*, Vol. 36, No. 129, pp. 195-202.

[66] Rosenblueth, E., and Meli, R.(1986)."The 1985 earthquake: causes and effects in Mexico City." *Concrete International*, ACI.

[67] Schmidt,T.(1989). "An Approach of Modelling Masonry Infilled Frames by The F.E. Method and z Modified Equivalent Strut Method." *Darmstadt Concrete, Annual Journal on Concrete and Concrete Structures*, Vol. 4, Darmstadt, Germany.

[68] Schmidt,T.(1989). "Experiments on the nonlinear behavior of masonry infilled reinforced concrete frames." *Darmstadt Concrete, Annual J. on Concrete and Concrete Structures*, Vol. 4, Darmstadt, Germany.

[69] Seah,C.K. (1988). "Out-of-Plane Behavior of Concrete Masonry Infilled Panels.", *Master Thesis*, Department of Civil Engineering, University of New Brunswick, Canada.

[70] Shing, P. B., Mehrabi, A. B., Schuller, M., and Noland, J. L. (1994). "Experimental Evaluation and Finite Element Analysis of Masonry-Infilled R/C Frames." *ASCE Structures Congress '94*, Atlanta, Georgia, April 25-27, 1994.

[71] Shipman, J.M. , and Gerstle, K.H. (1977). "Bond Deterioration in Concrete Panels under Load Cycles." *ACI Annual Convention*, March 1977.

[72] Shipman, J.M. , and Gerstle, K.H. (1979). "Bond Deterioration in Concrete Panels under Load Cycles." *ACI Structural Journal*, Feb., pp. 311-325.

[73] Simo, J.C., and Ortiz, M. (1985). "A Unified Approach to Finite Deformation Elastoplastic Analysis Based on The Use of Hyperelastic Constitutive Equations." *Computer Methods in Applied Mechanics and Engineering*, 49, 221-245.

[74] Stafford Smith, B. (1962). "Lateral Stiffness of Infilled Frames." *Journal of Structural Division,* ASCE, Vol. 88, No. ST6.

[75] Stafford Smith, B.(1966). "Behavior of the square infilled frames." *Journal of Structural Division,* ASCE, Vol. 92, No. ST1.

[76] Stafford Smith, B. (1967). "Methods for Predicting the Lateral Stiffness and Strength of Multi-Story Infilled Frames." *Building Science,* Vol. 2, Pergamon Press, Great Britain, pp. 247-257.

[77] Stafford Smith, B. and Carter, C. (1969)."A Method of Analysis for Infilled Frames." *Proceedings of the Institute of Civil Engineers,* Vol. 44, No. 7218, pp. 31-48.

[78] Stafford Smith, B. and Riddington, J.R. (1978)."The Design of Masonry Infilled Steel Frames for Bracing Structures." *The Structural Engineer,* March, No. 1, Vol. 56B, pp. 1-7.

[79] Stankowski, T. (1990). "Numerical Simulation of Progressive Failure in Particle Composites." *Ph.D. Thesis*, University of Colorado, Boulder CO.

[80] Tepfers, R. (1979). "Cracking of Concrete Cover Along Anchored Deformed Reinforcing Bars." *Magazine of Concrete Research*, Vol. 31, No. 106, pp. 3-12.

[81] *Uniform Building Code (1991).* International Conference of Building Officials, Whottier, CA.

[82] Uzsoy, S. Z., and Citipitioglu, E.(1972)."Influence of infill walls on building frames: an example from the May 12, 1971 earthquake in Turkey." *Bulletin of the Seismological Society of America*, 62, 5, October.

[83] Wahla, M.I., Scott, N.R., and Nilson, A.H. (1971). "Direct Measurement of Bond Slip in Reinforced Concrete." *Trans. American Society of Agricultural Engineers,* Vol. 14, No. 4, pp. 762-767.

[84] Wibowo, J.T., Amadei, B., Sture, S., and Robertson, A.B. (1991). "Shear Response of A Rock Joint under Different Boundary Conditions: An Experimental Study." *Report to U.S. Department of Energy*, Civil Engineering Department, University of Colorado, Boulder CO.

[85] Wood,R.H. (1978). "Plasticity, Composite Action and Collapse Design of Reinforced Shear Wall Panel in Frames." *Proceedings of Institute of Civil Engineering*, 65, Part 2, pp. 381-411.

[86] Yow, Jr., J.L., and Goodman, R.E. (1987). "A Ground Reaction Curve Based upon Block Theory." *Rock Mechanics and Rock Engineering*, No. 20, pp. 167-190.

[87] Zarnic,R., and Tomazevic,M.(1990). "Behavior of repaired masonry infilled R/C frames." *A Report to U.S.-Yugoslav Joint Board on Scientific and Tech. Cooperation*, Institute for Testing and Research in Materials and Structures, Ljubljana, Yugoslavia.

[88] Zienkiewicz, O.C. (1989). *The Finite Element Method*, 4th Edition, McGraw-Hill, UK.

APPENDIX A

MATERIAL TEST DATA

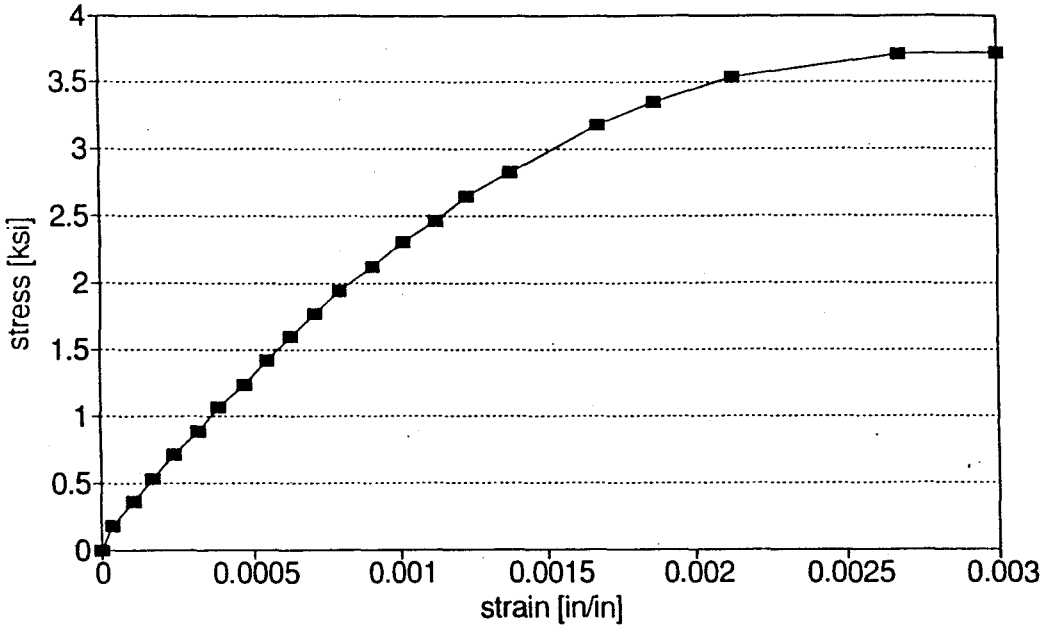

Figure A.1. Stress-Strain Curve for Compression Test of Concrete Cylinder (Specimen 11, Sample 1).

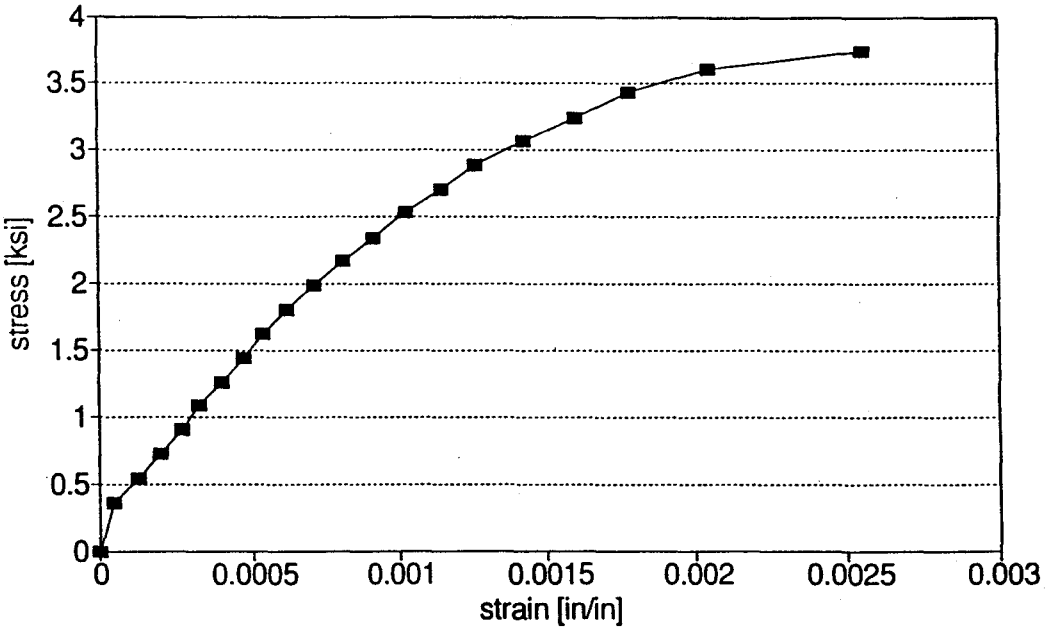

Figure A.2. Stress-Strain Curve for Compression Test of Concrete Cylinder (Specimen 11, Sample 2).

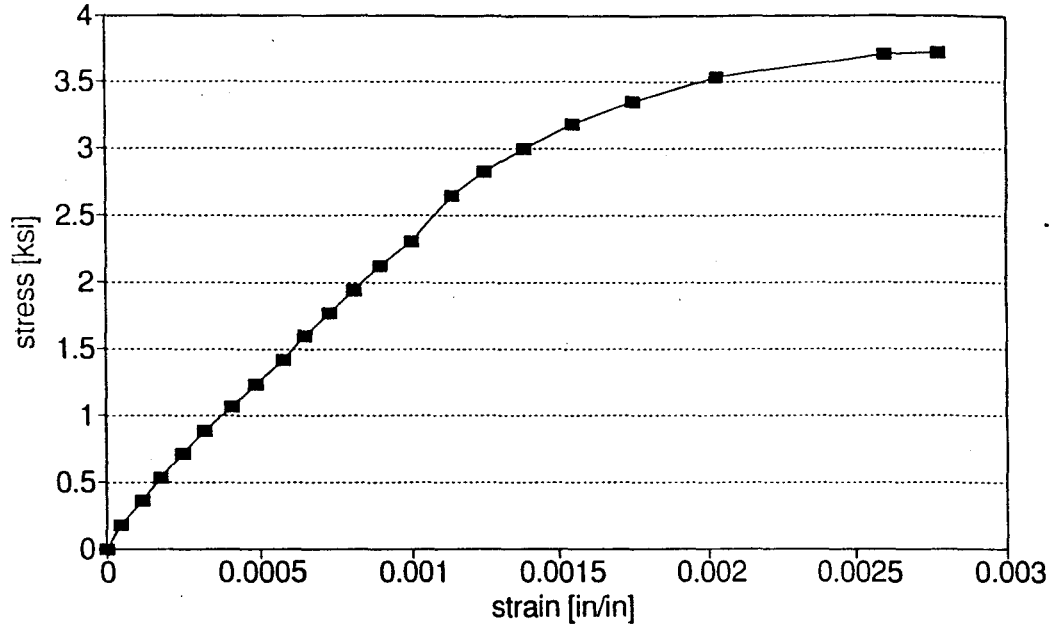

Figure A.3. Stress-Strain Curve for Compression Test of Concrete Cylinder (Specimen 11, Sample 3).

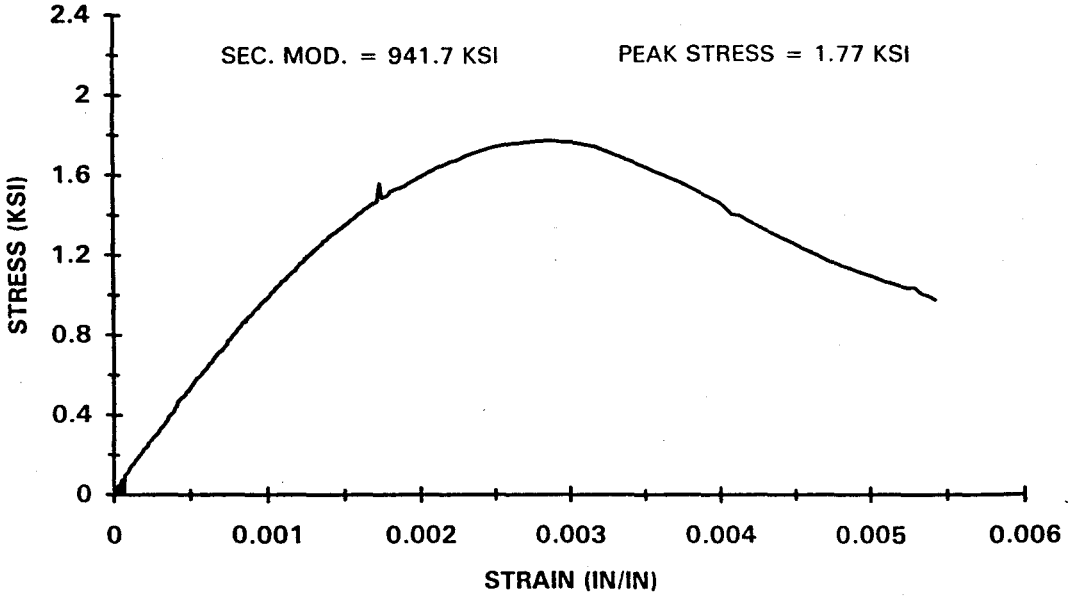

Figure A.4. Stress-Strain Curve for Compression Test of Masonry Prism (Specimen 12, Sample 1).

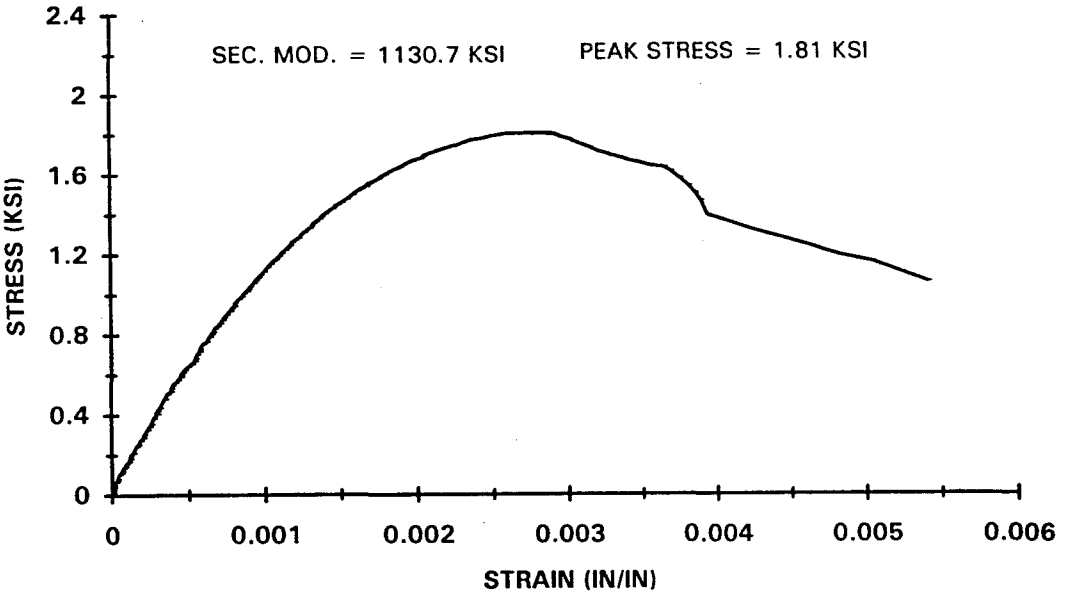

Figure A.5. Stress-Strain Curve for Compression Test of Masonry Prism (Specimen 12, Sample 2).

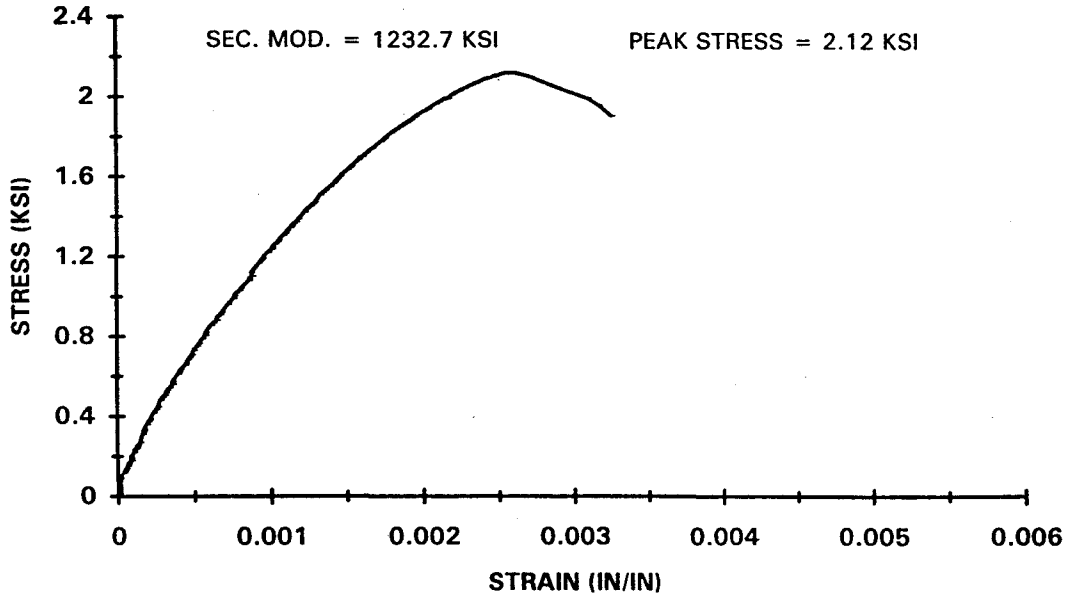

Figure A.6. Stress-Strain Curve for Compression Test of Masonry Prism (Specimen 12, Sample 3).

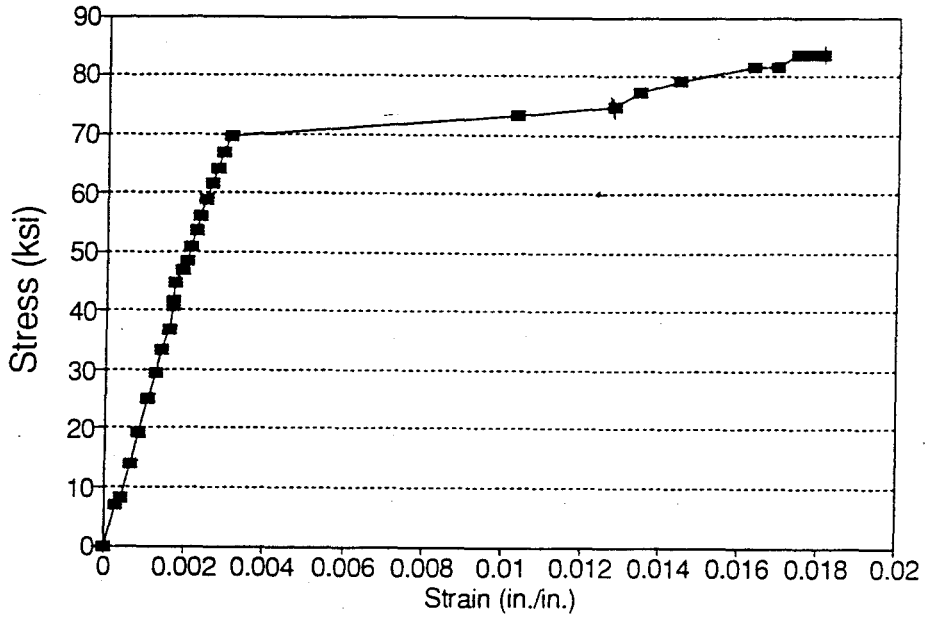

Figure A.7. Stress-Strain Curve for Tension Test of Reinforcing Bar (#5, bar Sample 1).

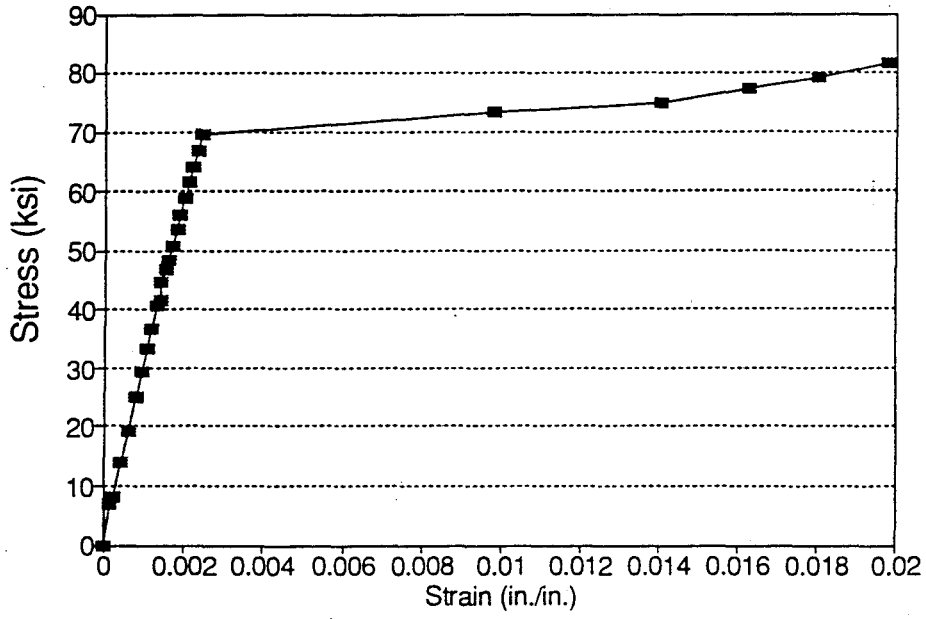

Figure A.8. Stress-Strain Curve for Tension Test of Reinforcing Bar (#5 bar, Sample 2).

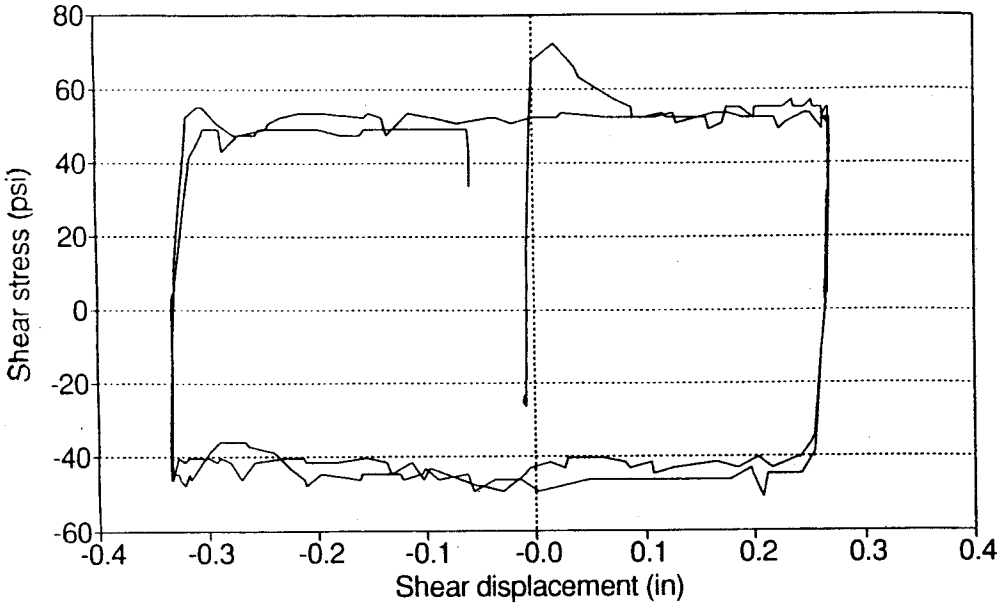

Figure A.9. Shear Stress-Shear Displacement Curve for Mortar Joint in Hollow Concrete Masonry under 50-psi Normal Stress.

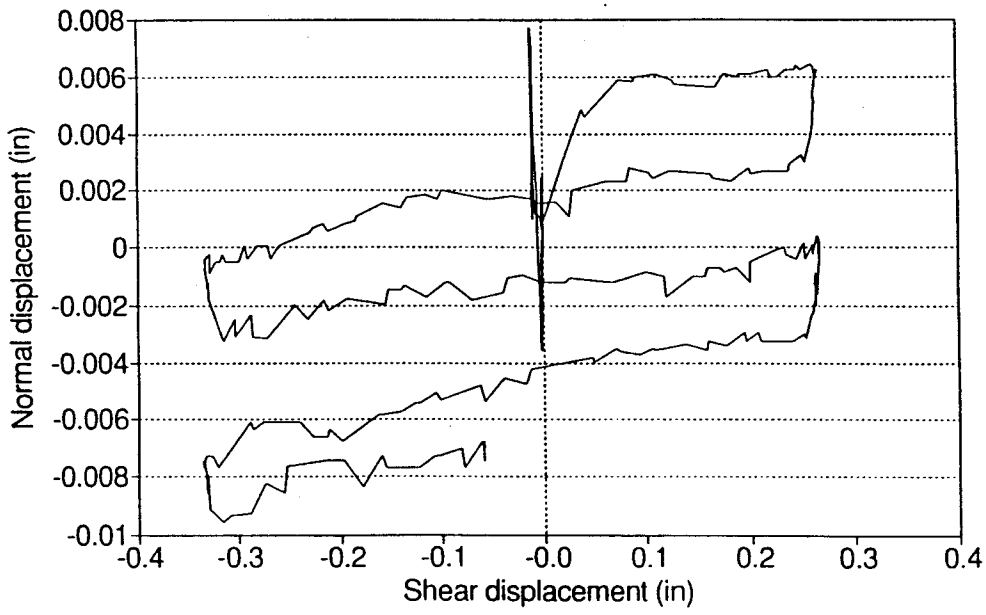

Figure A.10. Normal Displacement-Shear Displacement Curve for Mortar Joint in Hollow Concrete Masonry under 50-psi Normal Stress.

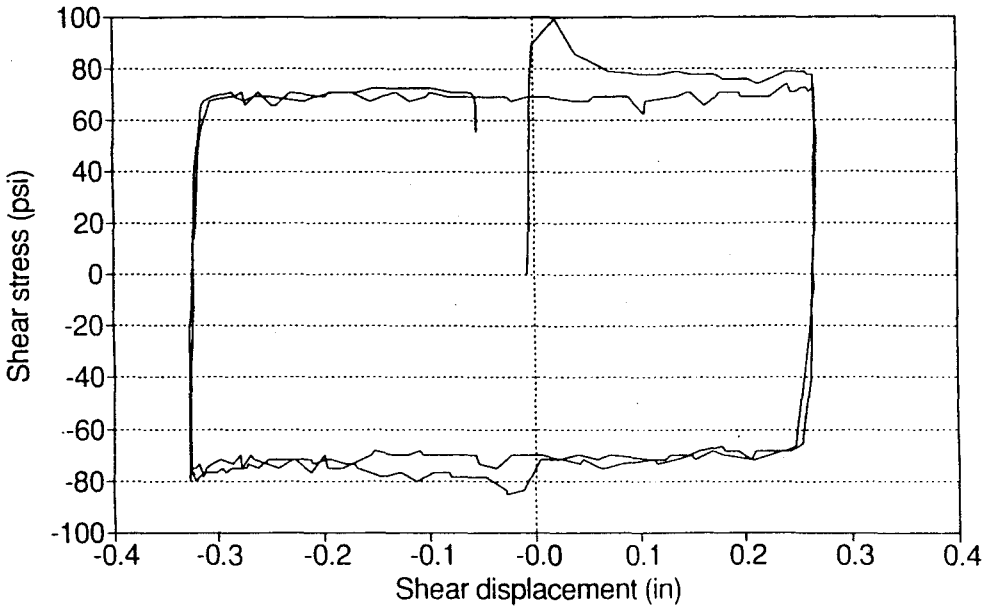

Figure A.11. Shear Stress-Shear Displacement Curve for Mortar Joint in Hollow Concrete Masonry under 75-psi Normal Stress.

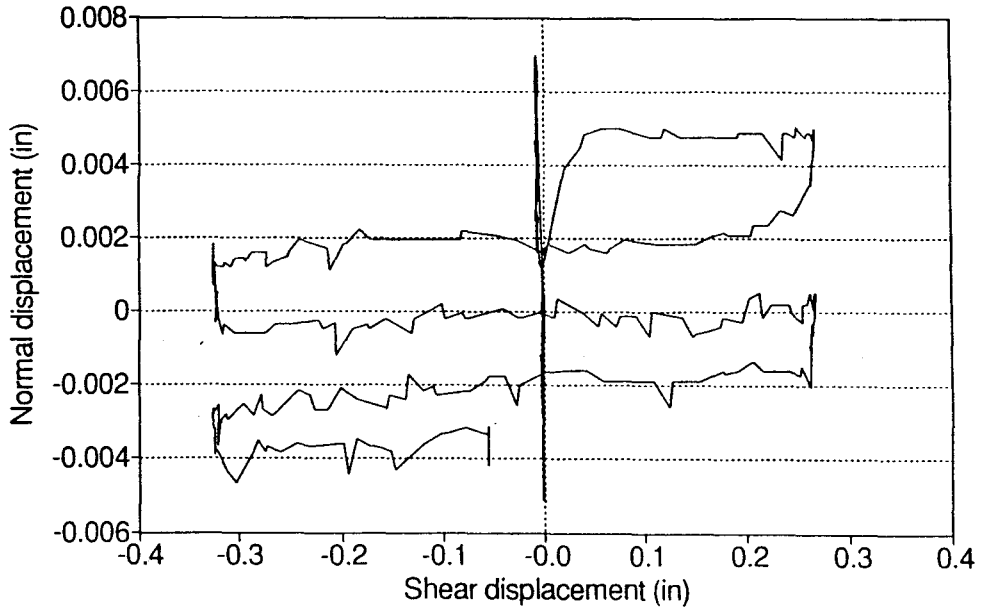

Figure A.12. Normal Displacement-Shear Displacement Curve for Mortar Joint in Hollow Concrete Masonry under 75-psi Normal Stress.

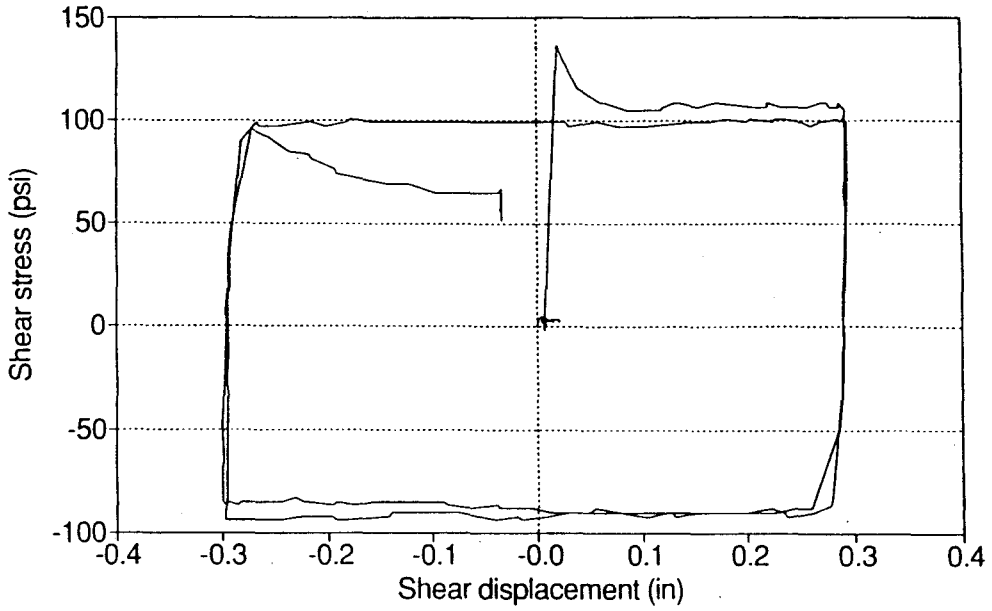

Figure A.13. Shear Stress-Shear Displacement Curve for Mortar Joint in Hollow Concrete Masonry under 100-psi Normal Stress.

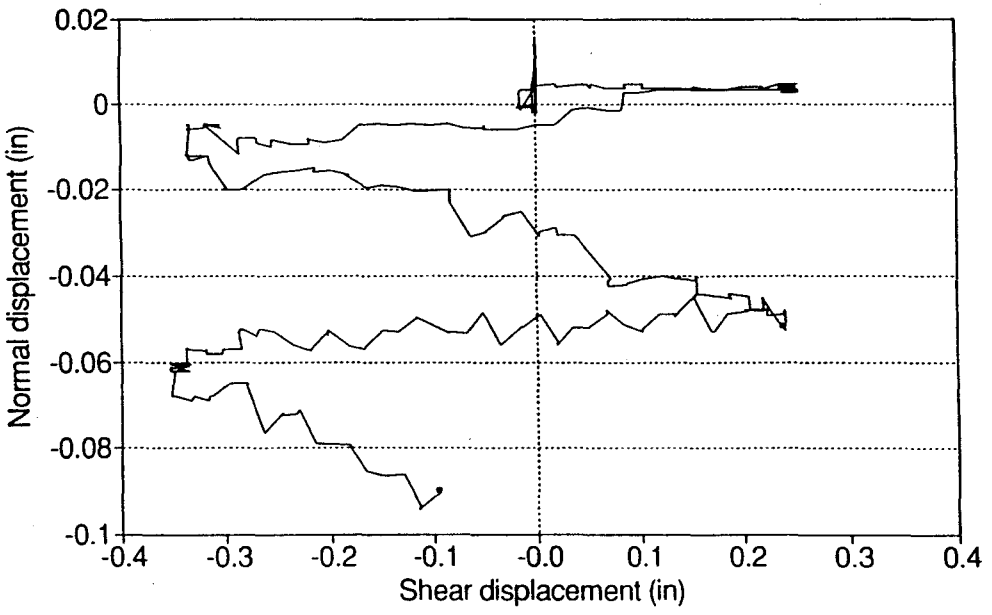

Figure A.14. Normal Displacement-Shear Displacement Curve for Mortar Joint in Hollow Concrete Masonry under 100-psi Normal Stress.

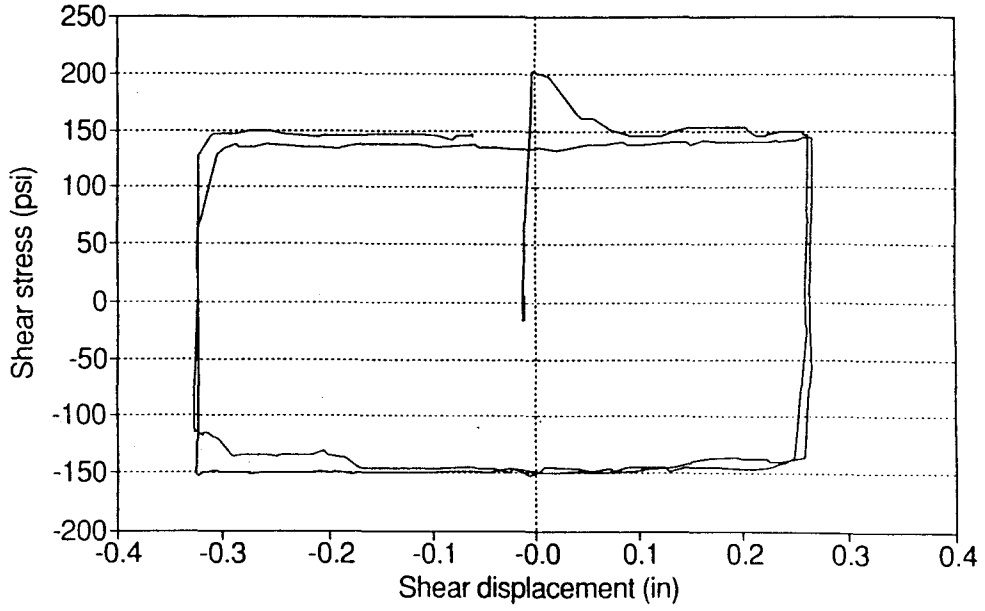

Figure A.15. Shear Stress-Shear Displacement Curve for Mortar Joint in Hollow Concrete Masonry under 150-psi Normal Stress.

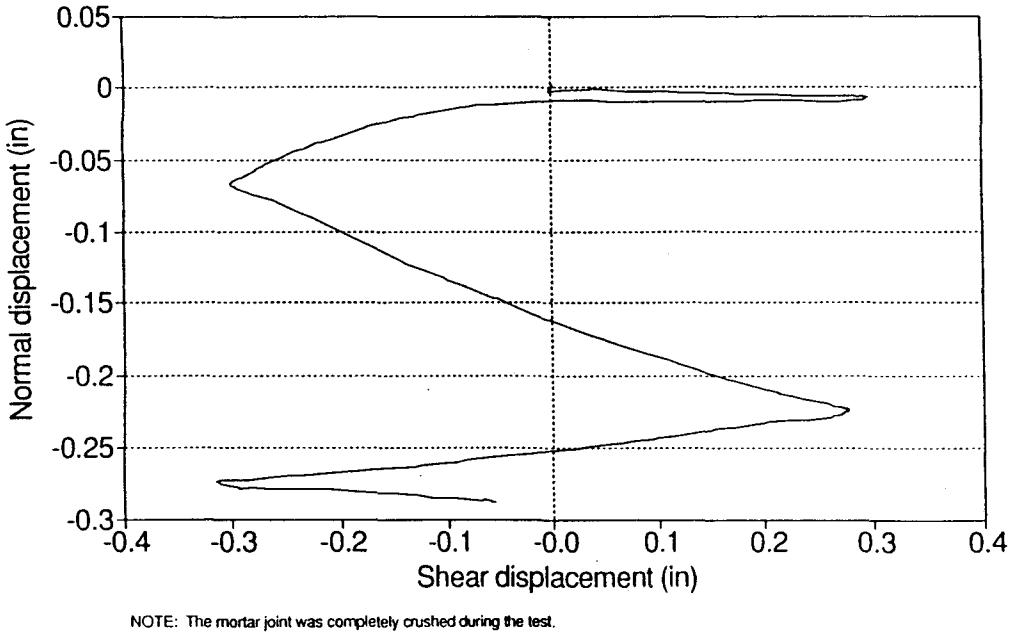

Figure A.16. Normal Displacement-Shear Displacement Curve for Mortar Joint in Hollow Concrete Masonry under 150-psi Normal Stress.

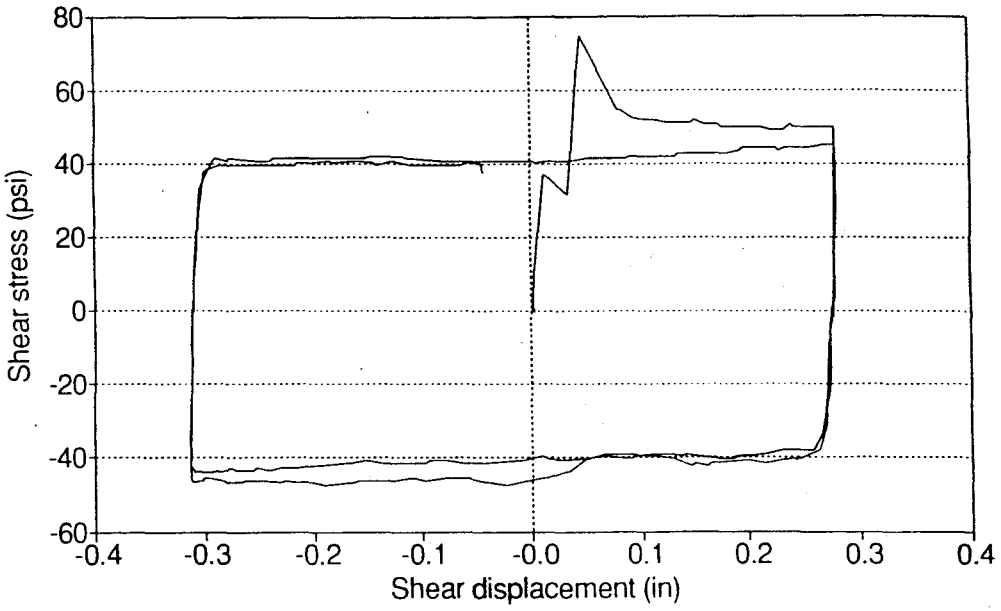

Figure A.17. Shear Stress-Shear Displacement Curve for Mortar Joint in Solid Concrete Masonry under 50-psi Normal Stress.

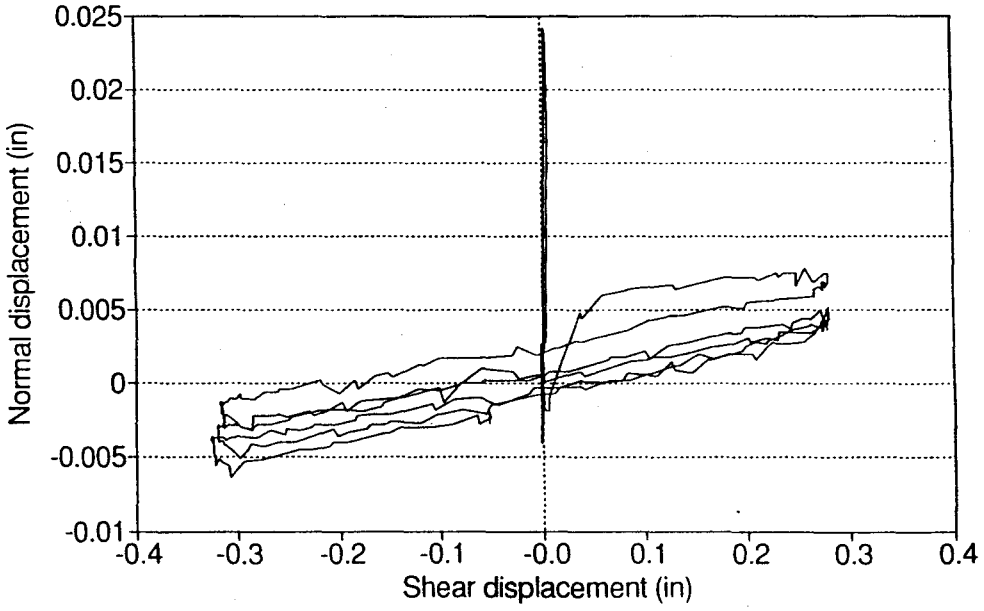

Figure A.18. Normal Displacement-Shear Displacement Curve for Mortar Joint in Solid Concrete Masonry under 50-psi Normal Stress.

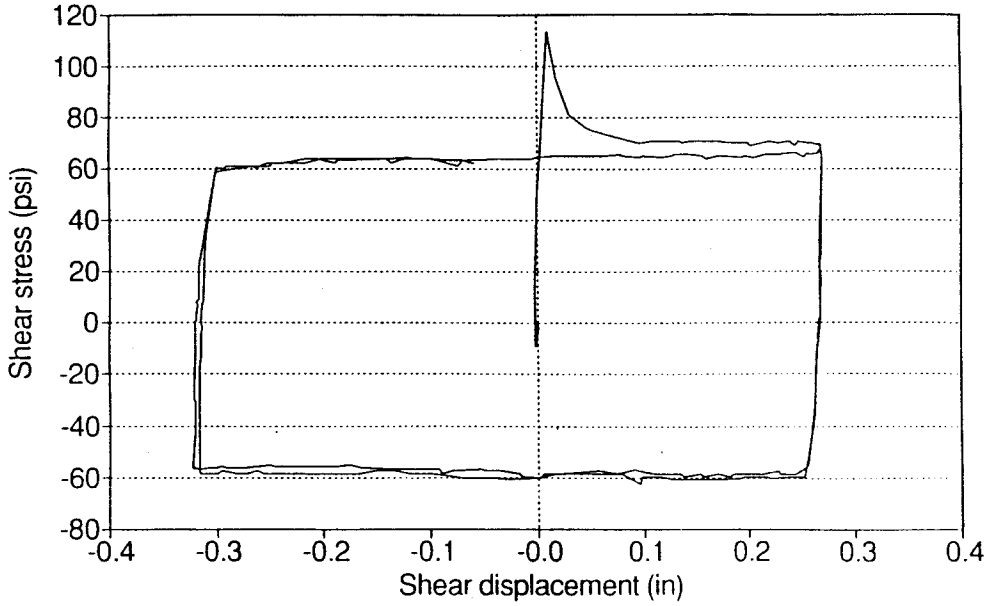

Figure A.19. Shear Stress-Shear Displacement Curve for Mortar Joint in Solid Concrete Masonry under 75-psi Normal Stress.

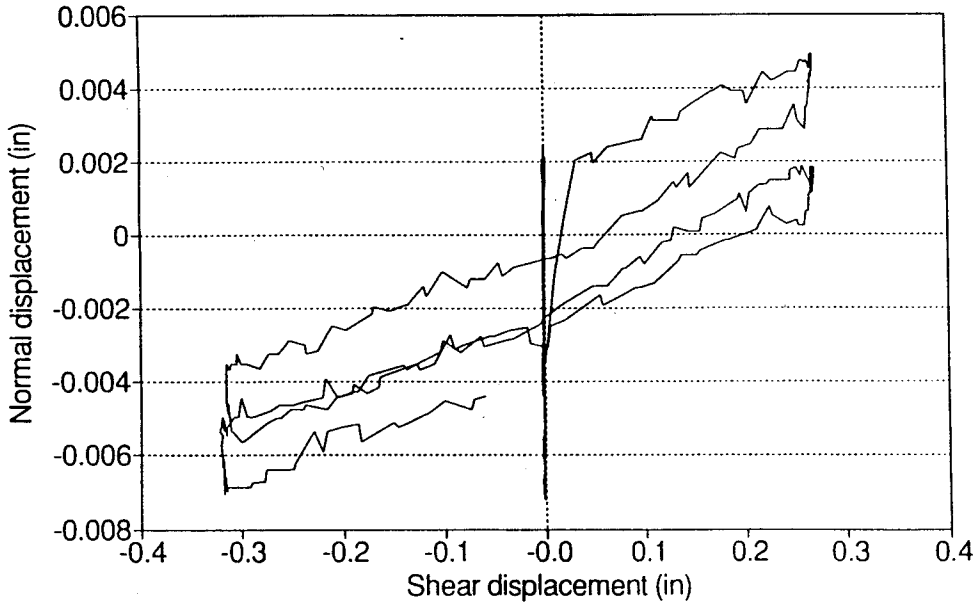

Figure A.20. Normal Displacement-Shear Displacement Curve for Mortar Joint in Solid Concrete Masonry under 75-psi Normal Stress.

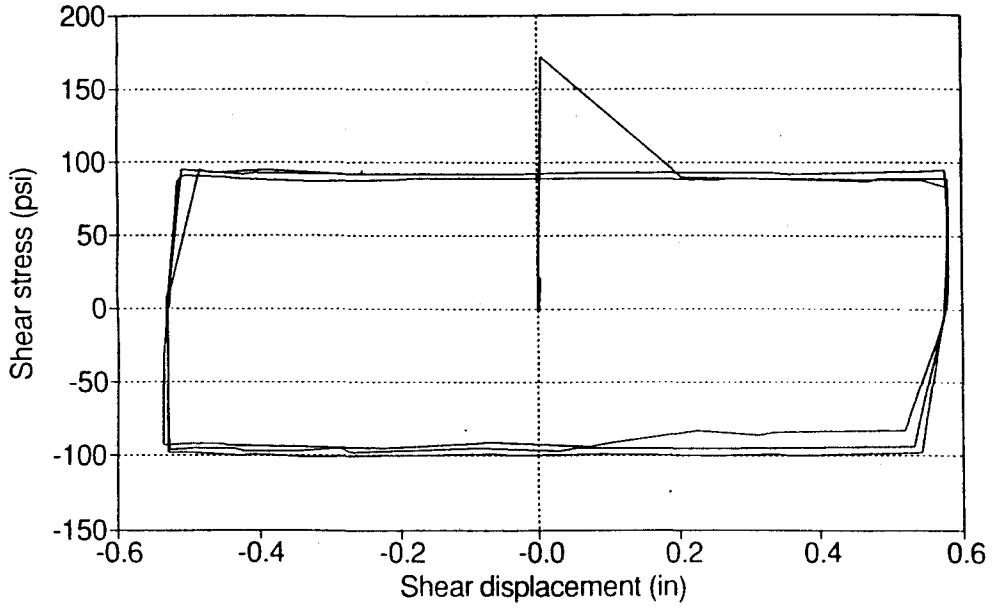

Figure A.21. Shear Stress-Shear Displacement Curve for Mortar Joint in Solid Concrete Masonry under 100-psi Normal Stress.

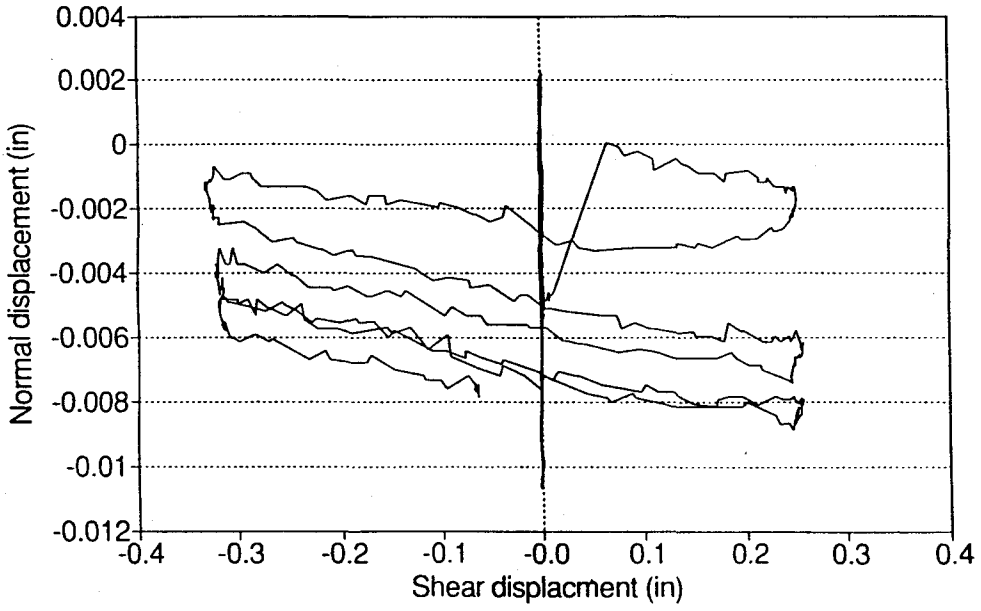

Figure A.22. Normal Displacement-Shear Displacement Curve for Mortar Joint in Solid Concrete Masonry under 100-psi Normal Stress.

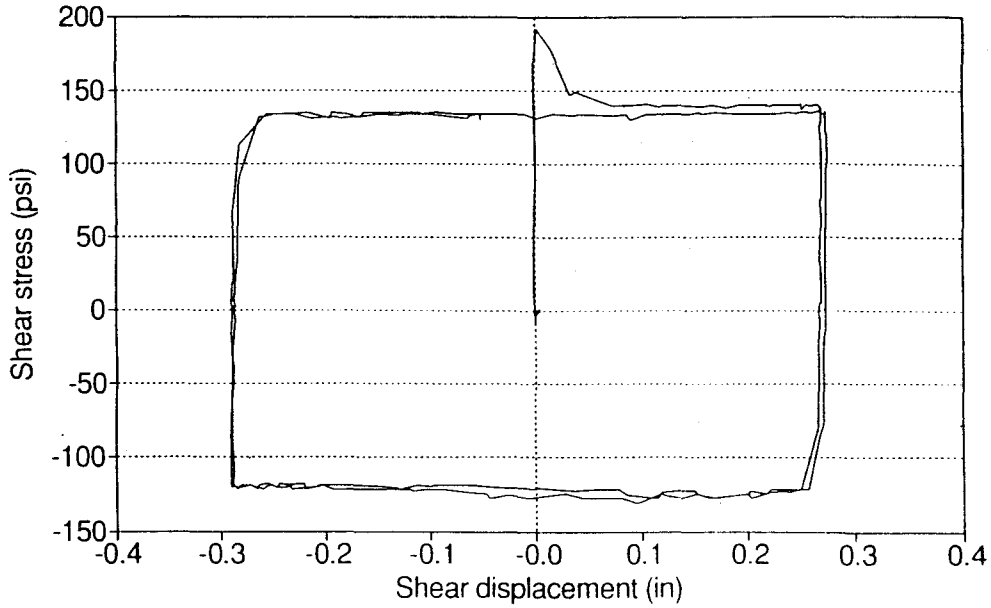

Figure A.23. Shear Stress-Shear Displacement Curve for Mortar Joint in Solid Concrete Masonry under 150-psi Normal Stress.

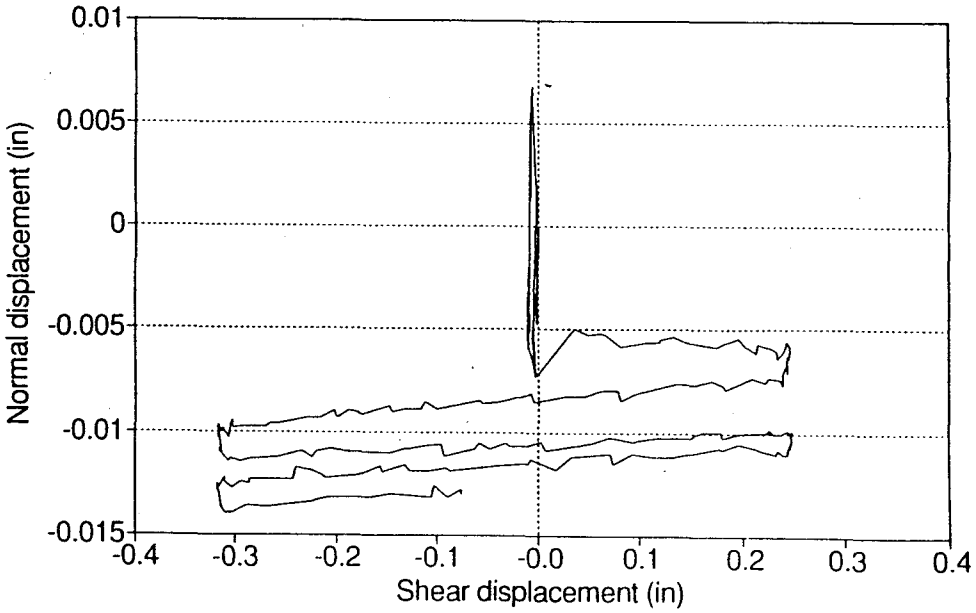

Figure A.24. Normal Displacement-Shear Displacement Curve for Mortar Joint in Solid Concrete Masonry under 150-psi Normal Stress.

APPENDIX B

TEST SETUP AND SPECIMEN DAMAGE PATTERNS

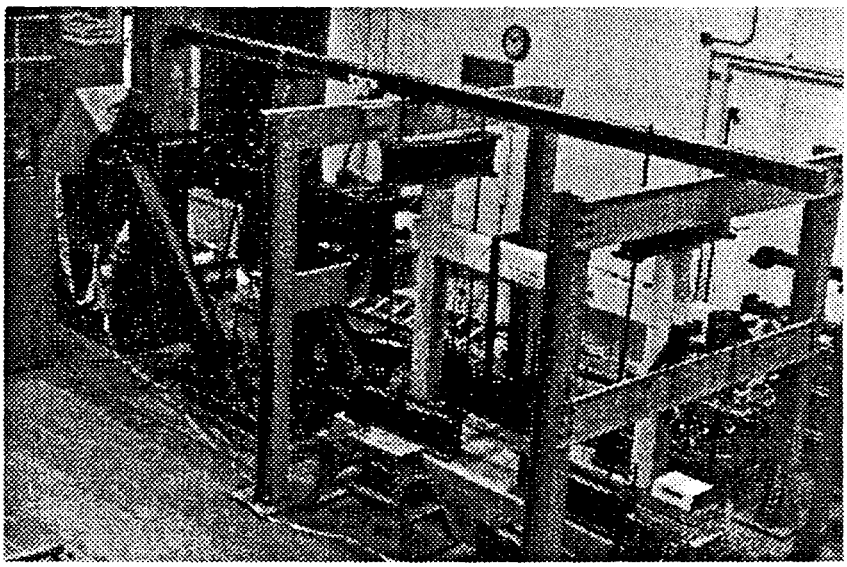

Figure B.1. Test Setup for Specimen 1..

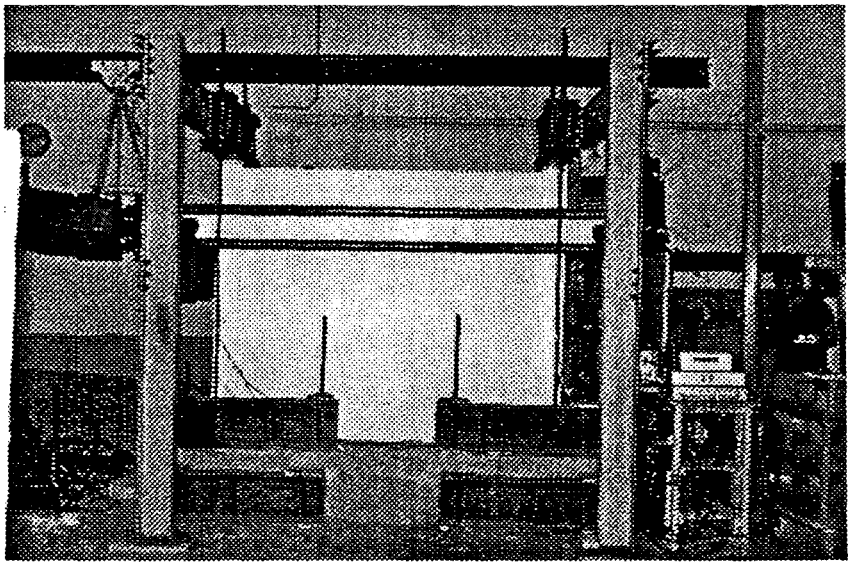

Figure B.2. Test Setup for Specimen 3.

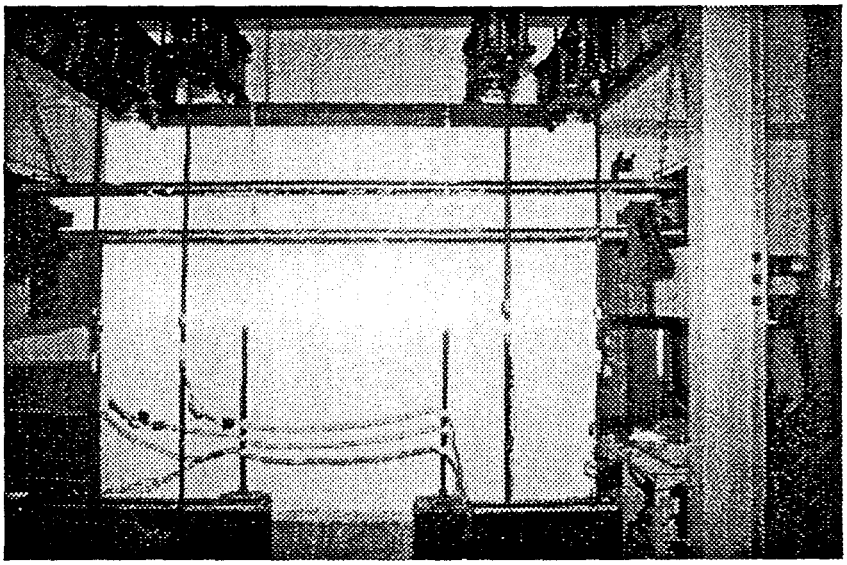

Figure B.3. Test Setup for Specimen 5.

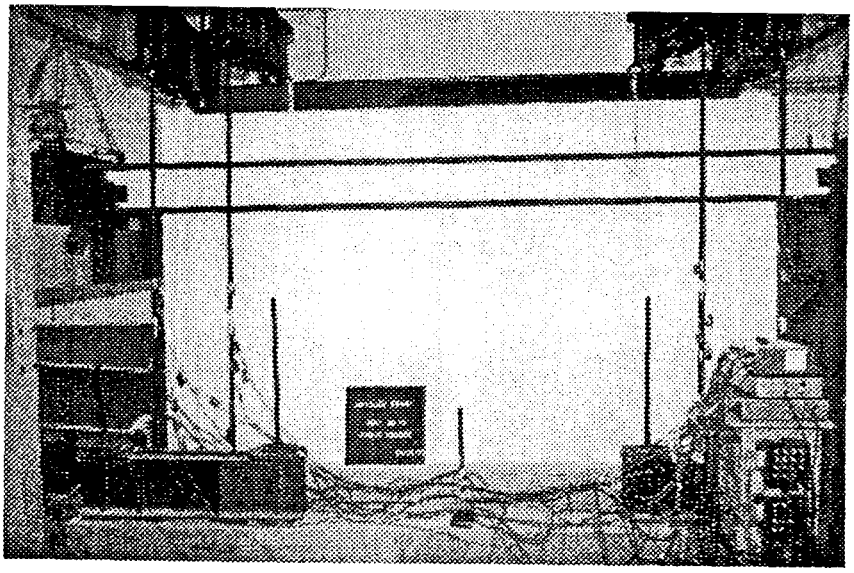

Figure B.4. Test Setup for Specimen 11.

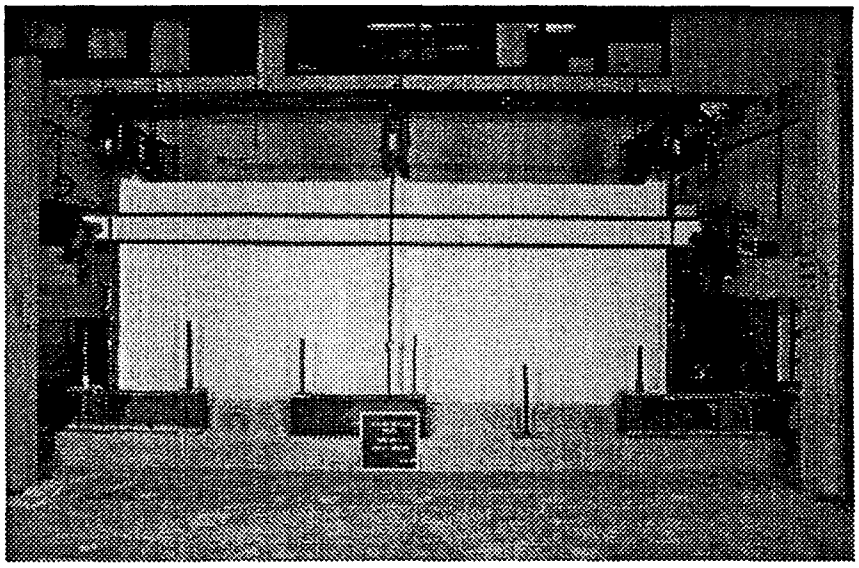

Figure B.5. Test Setup for Specimen 13.

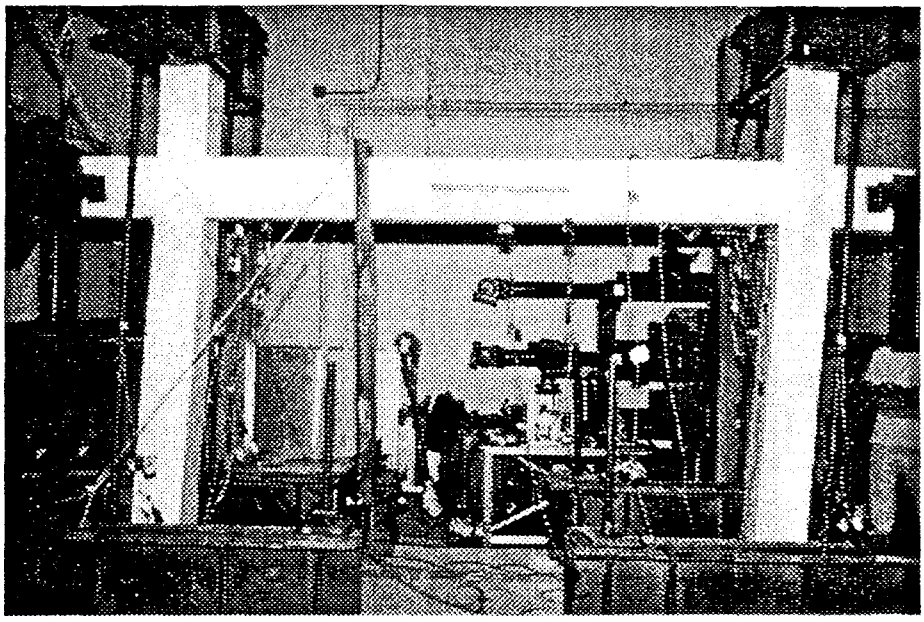

Figure B.6. Failure Pattern of Specimen 1.

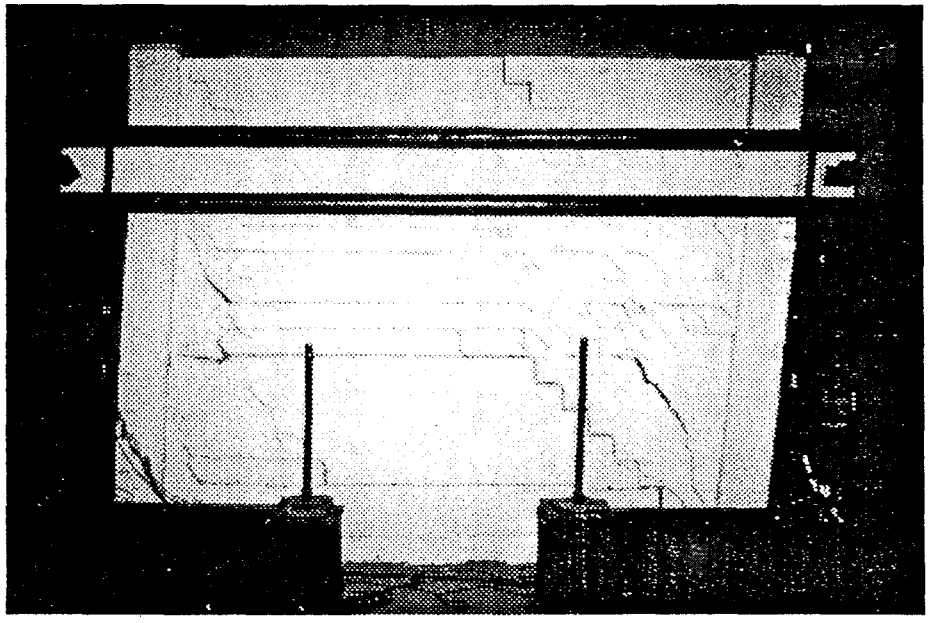

Figure B.7. Failure Pattern of Specimen 2.

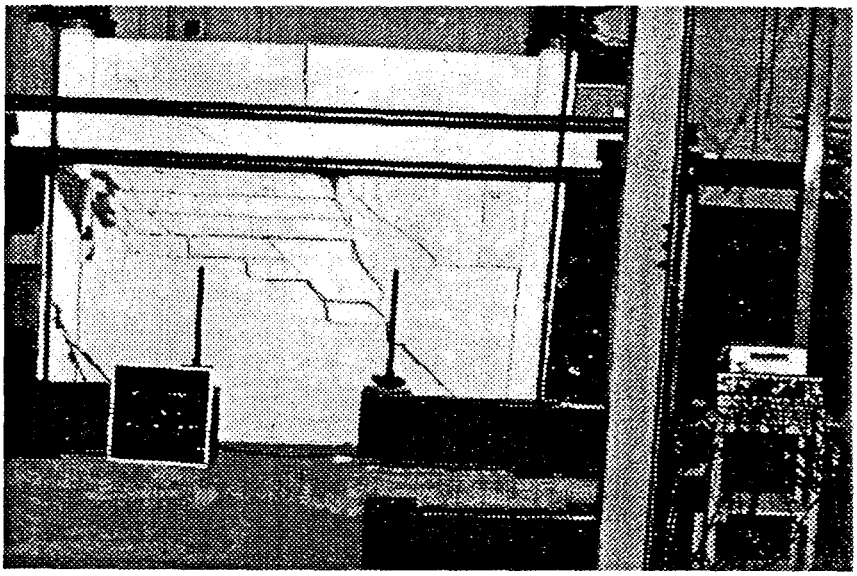

Figure B.8. Failure Pattern of Specimen 3.

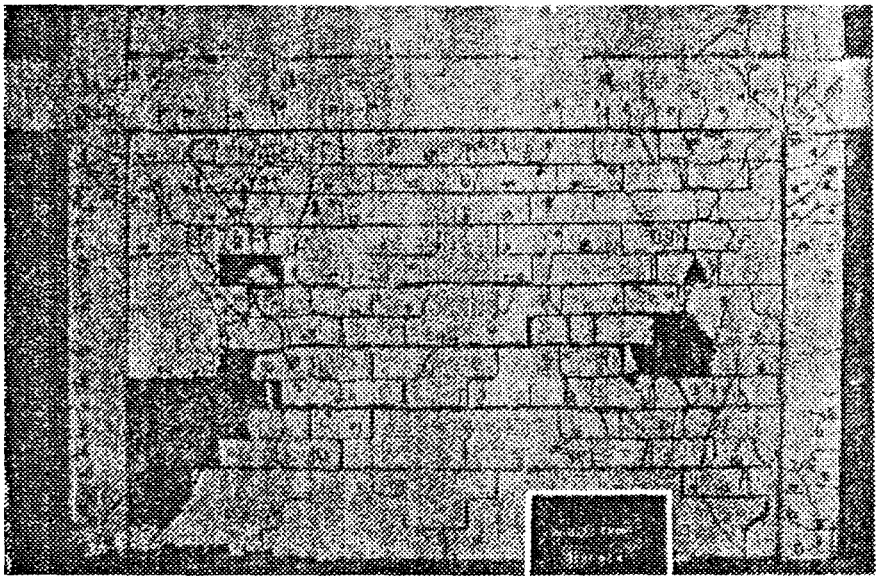

Figure B.9. Failure Pattern of Specimen 4.

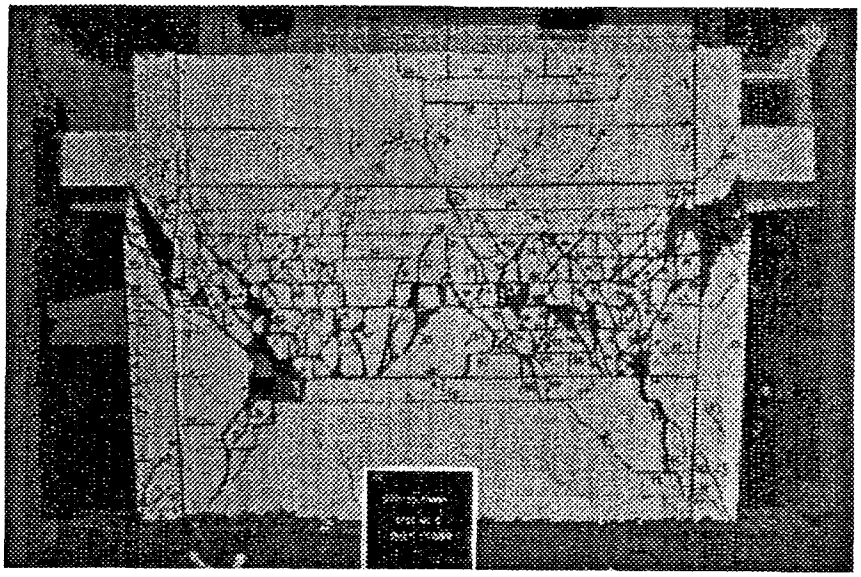

Figure B.10. Failure Pattern of Specimen 5.

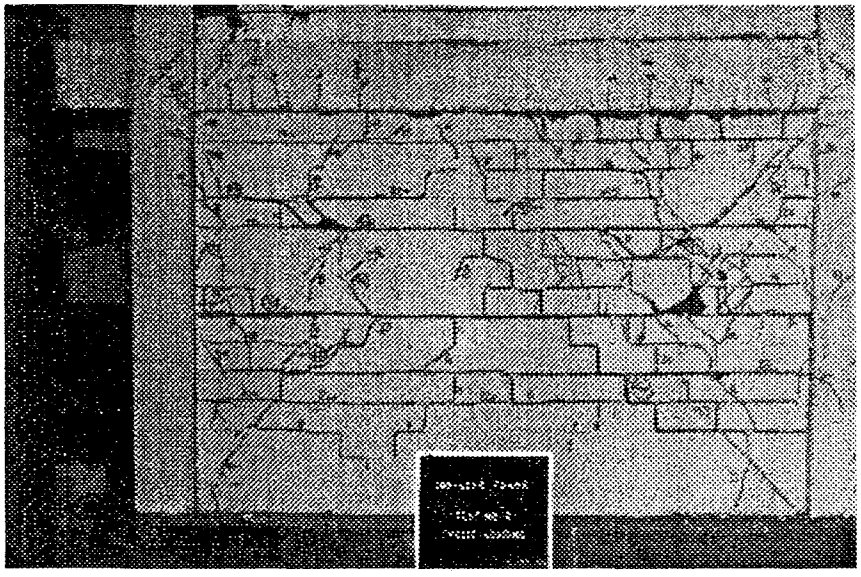

Figure B.11. Failure Pattern of Specimen 6.

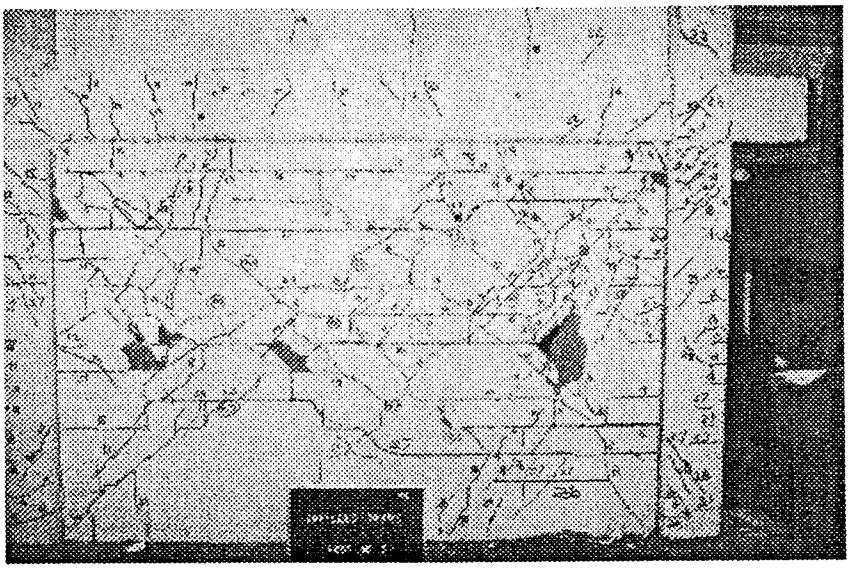

Figure B.12. Failure Pattern of Specimen 7.

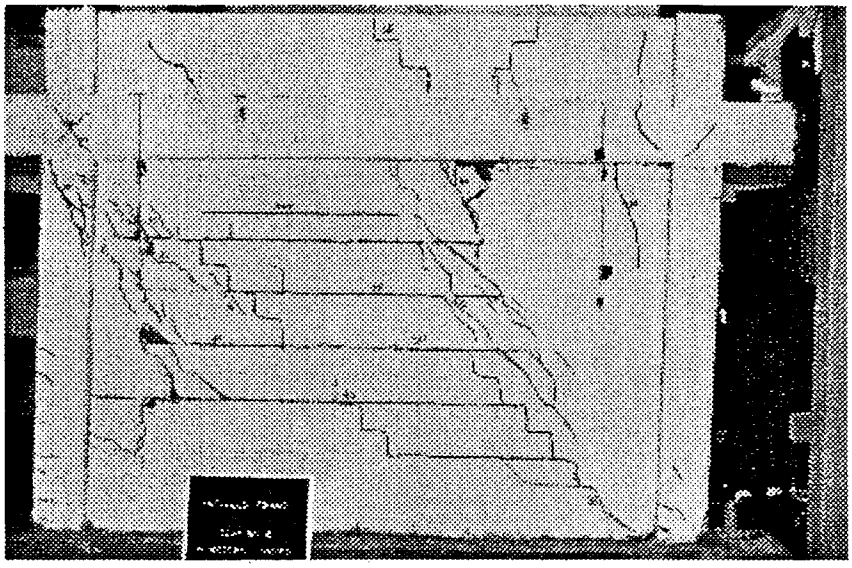

Figure B.13. Failure Pattern of Specimen 8.

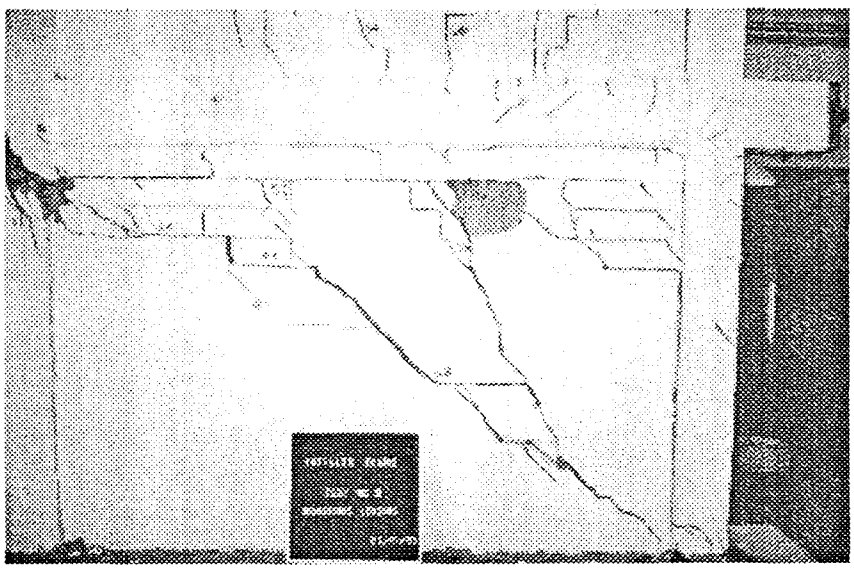

Figure B.14. Failure Pattern of Specimen 9.

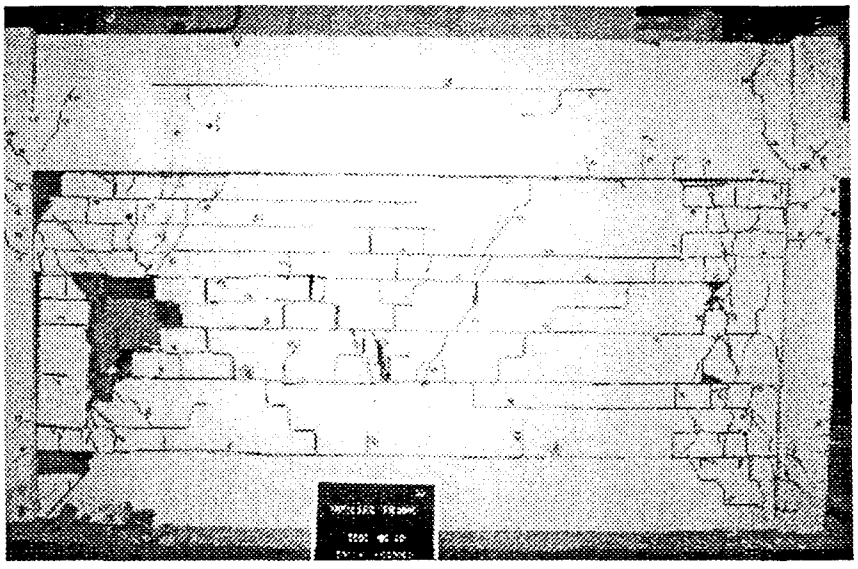

Figure B.15. Failure Pattern of Specimen 10.

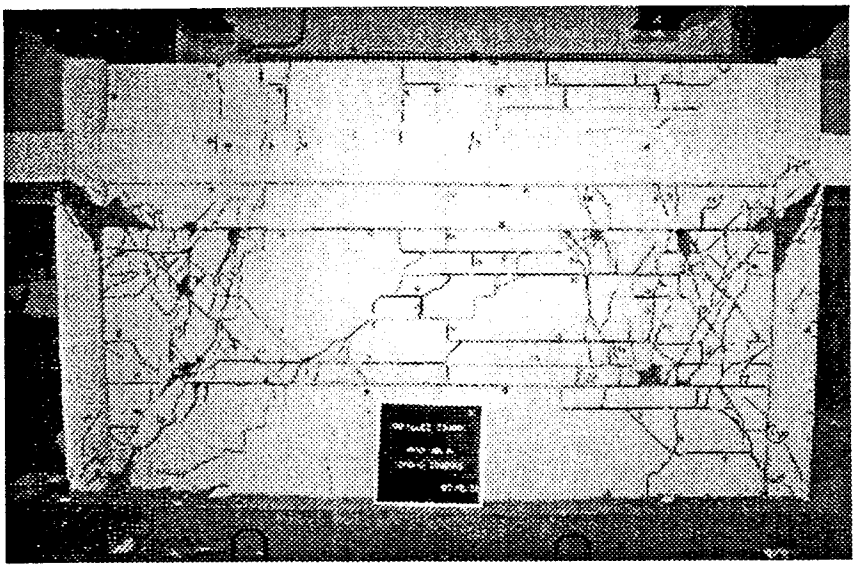

Figure B.16. Failure Pattern of Specimen 11.

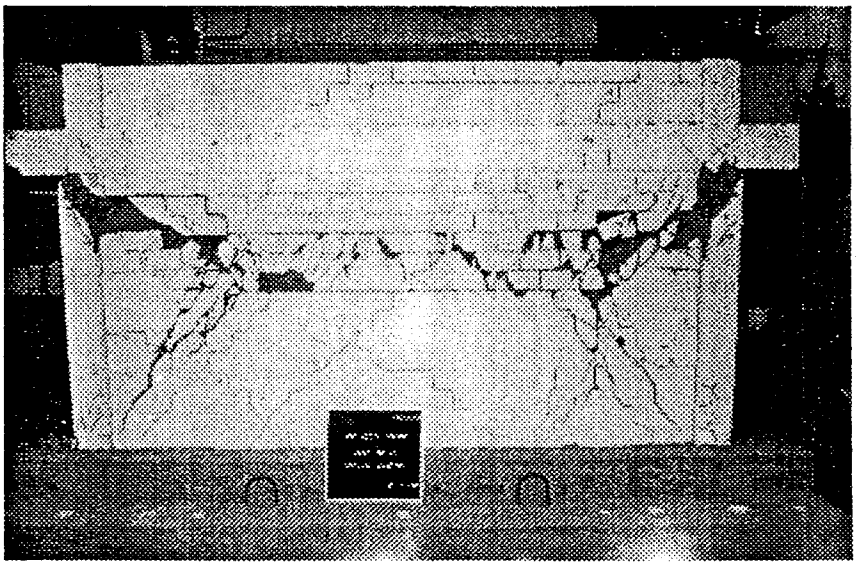

Figure B.17. Failure Pattern of Specimen 12.

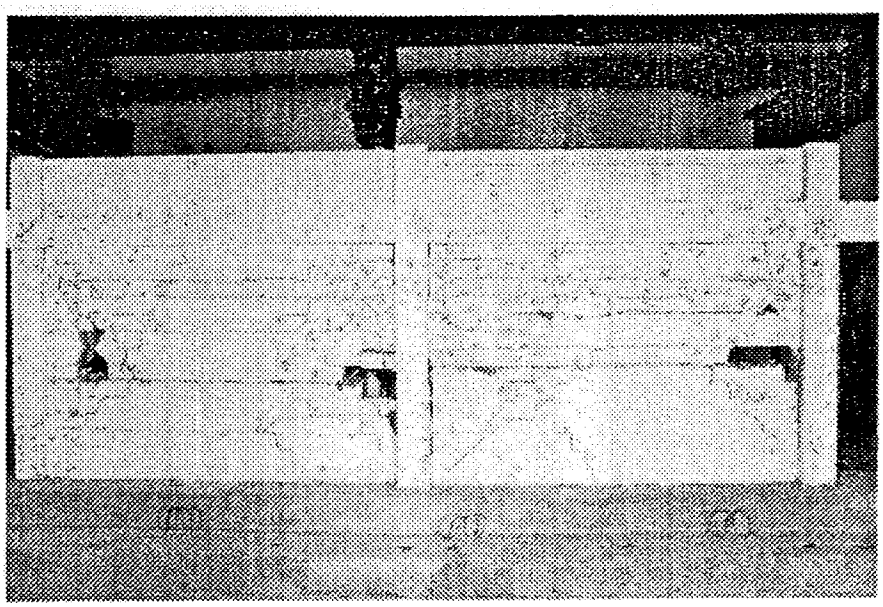

Figure B.18. Failure Pattern of Specimen 13.

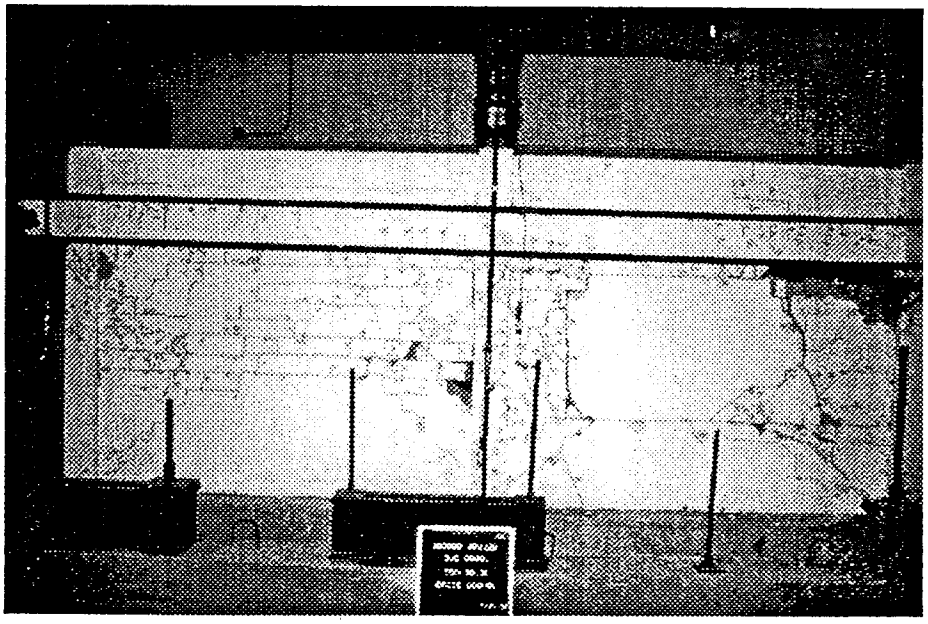

Figure B.19. Failure Pattern of Specimen 14.